

NUMERICAL AND EXPERIMENTAL STUDIES OF DROPLET-GAS FLOW

by

Aage Ingebret Jøsang

Department of Technology (HiT-TF)
Telemark University College
Kjølnes Ring 56, N-3914 Porsgrunn, Norway

Thesis submitted to
The Norwegian University of Science and Technology (NTNU),
for the degree of Dr. Ing.

Porsgrunn, September 2002

Abstract

This thesis considers droplet-gas flow by the use of numerical methods and experimental verification. A commercial vane separator was studied, both numerically and by experiment. In addition, some efforts are put into the numerical analysis of cyclones.

The experimental part contains detailed measurements of the flow field between a pair of vanes in a vane separator and droplet size measurements. LDA (Laser Doppler Anemometry) was used to measure the velocity in two dimensions and corresponding turbulence quantities. The results from the LDA measurements are considered to be of high quality and are compared to numerical results obtain from a CFD (Computational Fluid Dynamics) analysis. The simulations showed good agreement between the numerical and experimental results. Combinations of different turbulence models; the standard k- ϵ model and the Reynold Stress Model, different schemes; first order and higher order scheme, and different near wall treatment of the turbulence; the Law of the wall and the Two-Layer Zonal model, were used in the simulations. The Reynolds Stress Model together with a higher order scheme performed rather poorly. The resirculation in parts of the separator was overpredicted in this case. For the other cases the overall predictions are satisfactory.

PDA (Phase Doppler Anemometry) measurements were used to study the changes in the droplet size distribution through the vane separator. The PDA measurements show that smaller droplets are found at the outlet than present at the inlet. In the literature, there exists different mechanisms for explaining the re-entrainment and generation of new droplets. The re-entrainment mechanisms are divided into four groups, where droplet-droplet interaction, droplet break-up, splashing of impinging droplet and re-entrainment from the film are defined as the groups of re-entrainment mechanisms. Models for these groups are found in the literature, and these models are tested for re-entrainment using the operational conditions in the separator. This test shows that neither of these mechanisms can explain the generation of new droplets. An alternative mechanism is proposed to explain the generation of new droplets inside the vane separator. Based on this new mechanism new models for predicting re-entrainment are developed and tested. Using the new model improves the quality of the prediction of the droplet size distribution leaving the separator.

For the cyclones only numerical works have been done. Simulations are performed to differentiate between the use of Cartesian velocity components and cylindrical velocity components in the momentum equation for structured grids. In addition, two different turbulence models are used; the RNG k- ϵ model and the Reynolds Stress Model. The effect of increasing the order of the numerical scheme from a first order scheme to a higher order scheme was also investigated. The results show quite clearly that cylindrical components must be used when simulating cyclones by a structured grid. In addition, a simulation using the multiblock method shows satisfactorily predictions of the pressure drop and flow field by using Cartesian velocity components.

Acknowledgement

This work has been carried out at Telemark Technological Research and Development Center (Tel-Tek) and Telemark University College, Department of Technology (HIT-TF) under the supervision of professor Morten Chr. Melaaen. The work is financed through the PARFLU program, supported by the NFR (Norges Forsknings Råd)

First of all, I would like to express my deepest gratitude to my supervisor Morten Chr. Melaaen for outstanding advice in large-scale problems as well as small-scale problems related to this thesis. His engagement for his job is admirable, and it happened very often that Morten visited my office on a Friday afternoon asking for something to read during the weekend.

Then, I want to send lots of thanks to those who were helpful in the experiments. Talleiv Skredtveit for helping in the construction of the experimental set-up. Britt Halvorsen for always being there when she was needed. And a special thanks to Geir Elseth for helping me a lot with the laser measurements. I also want to thank the other co-workers in the Process Equipment Research Group: Qianpu Wang, Rune Engeskaug and Martin Siljan.

There are lots of people at Telemark University College, which has contributed to this thesis. Their contribution is however impossible to point out, but it is unquestionable that the fine and good attitude to all employees at the campus have added working spirit and positive thinking to this work. It has never been a day that I did not look forward to go to work!

I also want to thank the committee for constructive proposals in the finishing of this thesis.

Finally, I want to thank my wife, Siri, for coping with all the late working during the last year of writing. It is not possible to catch up with lost time, but I will try my best. Also lots of thanks to my children, Erlend and Mari, for making me understand the real proportion of life.

At last, always remember ‘Veien er målet’.

NUMERICAL AND EXPERIMENTAL STUDIES OF DROPLET-GAS FLOW

by

Aage Ingebret Jøsang

Department of Technology (HiT-TF)
Telemark University College
Kjølnes Ring 56, N-3914 Porsgrunn, Norway

Thesis submitted to
The Norwegian University of Science and Technology (NTNU),
for the degree of Dr. Ing.

Porsgrunn, September 2002

Abstract

This thesis considers droplet-gas flow by the use of numerical methods and experimental verification. A commercial vane separator was studied, both numerically and by experiment. In addition, some efforts are put into the numerical analysis of cyclones.

The experimental part contains detailed measurements of the flow field between a pair of vanes in a vane separator and droplet size measurements. LDA (Laser Doppler Anemometry) was used to measure the velocity in two dimensions and corresponding turbulence quantities. The results from the LDA measurements are considered to be of high quality and are compared to numerical results obtained from a CFD (Computational Fluid Dynamics) analysis. The simulations showed good agreement between the numerical and experimental results. Combinations of different turbulence models; the standard k - ϵ model and the Reynolds Stress Model, different schemes; first order and higher order scheme, and different near wall treatment of the turbulence; the Law of the wall and the Two-Layer Zonal model, were used in the simulations. The Reynolds Stress Model together with a higher order scheme performed rather poorly. The recirculation in parts of the separator was overpredicted in this case. For the other cases the overall predictions are satisfactory.

PDA (Phase Doppler anemometry) measurements were used to study the changes in the droplet size distribution through the vane separator. The PDA measurements show that smaller droplets are found at the outlet than present at the inlet. In the literature, there exist different mechanisms for explaining the re-entrainment and generation of new droplets. The re-entrainment mechanisms are divided into four groups, where droplet-droplet interaction, droplet break-up, splashing of impinging droplet and re-entrainment from the film are defined as the groups of re-entrainment mechanisms. Models for these groups are found in the literature, and these models are tested for re-entrainment using the operational conditions in the separator. This test shows that neither of these mechanisms can explain the generation of new droplets. An alternative mechanism is proposed to explain the generation of new droplets inside the vane separator. Based on this new mechanism new models for predicting re-entrainment are developed and tested. Using the new model improves the quality of the prediction of the droplet size distribution leaving the separator.

For the cyclones only numerical works have been done. Simulations are performed to differentiate between the use of Cartesian velocity components and cylindrical velocity components in the momentum equation for structured grids. In addition, two different turbulence models are used; the RNG k - ϵ model and the Reynolds Stress Model. The effect of increasing the order of the numerical scheme from a first order scheme to a higher order scheme was also investigated. The results show quite clearly that cylindrical components must be used when simulating cyclones by a structured grid. In addition, a simulation using the multiblock method shows satisfactorily predictions of the pressure drop and flow field by using Cartesian velocity components.

Acknowledgement

This work has been carried out at Telemark Technological Research and Development Center (Tel-Tek) and Telemark University College, Department of Technology (HIT-TF) under the supervision of professor Morten Chr. Melaaen. The work is financed through the PARFLU program, supported by the NFR (Norges Forsknings Råd)

First of all, I would like to express my deepest gratitude to my supervisor Morten Chr. Melaaen for outstanding advice in large-scale problems as well as small-scale problems related to this thesis. His engagement for his job is admirable, and it happened very often that Morten visited my office on a Friday afternoon asking for something to read during the weekend.

Then, I want to send lots of thanks to those who were helpful in the experiments. Talleiv Skredtveit for helping in the construction of the experimental set-up. Britt Halvorsen for always being there when she was needed. And a special thanks to Geir Elseth for helping me a lot with the laser measurements. I also want to thank the other co-workers in the Process Equipment Research Group: Qianpu Wang, Rune Engeskaug and Martin Siljan.

There are lots of people at Telemark University College, which has contributed to this thesis. Their contribution is however impossible to point out, but it is unquestionable that the fine and good attitude to all employees at the campus have added working spirit and positively thinking to this work. It has never been a day that I did not look forward to go to work!

I also want to thank the committee for constructive proposals in the finishing of this thesis.

Finally, I want to thank my wife, Siri, for coping with all the late working during the last year of writing. It is not possible to catch up with lost time, but I will try my best. Also lots of thanks to my children, Erlend and Mari, for making me understand the real proportion of life.

At last, always remember ‘Veien er målet’.

Table of contents

1 Introduction	1
1.1 Motivation for the thesis.	1
1.2 Goals of this thesis.	3
1.3 Outline of the thesis.	3
2 Governing equations and droplet theory.	5
2.1 Conservation equation	5
2.2 Turbulence modelling	6
2.2.1 The standard k- ϵ model.	7
2.2.2 The RNG k- ϵ model.	8
2.2.3 The Reynolds Stress Model (RSM)	9
2.3 Near wall models for turbulence.	11
2.3.1 Law of the wall.	11
2.3.2 Two-layer zonal model.	12
2.4 Discretisation.	13
2.4.1 Power law scheme.	13
2.4.2 First order upwind scheme.	13
2.4.3 Quadratic Upstream Interpolation for Convective Kinematics (QUICK).	14
2.5 Two-phase treatment in the simulations	15
2.5.1 Force balance.	15
2.5.2 Forces acting on droplet/particle in disperse systems.	15
2.5.2.1 Steady-state drag force.	15
2.5.2.2 Gravity.	16
2.5.2.3 Saffman lift force.	16
2.5.2.4 Magnus force.	17
2.5.2.5 Virtual mass force.	17
2.5.2.6 Basset force.	17
2.5.2.7 Global pressure force.	18
2.5.2.8 Additional forces.	18
2.5.3 Including the turbulence in the particle of the particle trajectory.	18
2.6 General droplet theory.	18
2.6.1 Shape of droplets.	19
2.6.2 Definitions of different droplet mean diameters.	19
2.6.3 The Rosin-Rammler size distribution.	20
3 LDA/PDA theory.	21
3.1 Measurement principle.	21
3.1.1 The laser beam.	21
3.1.2 The Doppler effect.	22
3.1.3 The measure volume.	24
3.1.4 Fringe model.	25
3.1.5 Frequency shift.	26
3.1.6 Bragg cell.	26
3.1.7 Signals from the detector.	27
3.1.8 Modes of scattering.	28
3.1.9 Definition of forward, side, and backscatter.	29

3.2 The LDA set-up used for the velocity measurements.	29
3.3 Phase Doppler Anemometry (PDA)	30
3.3.1 Basics for the PDA.	30
3.3.2 Light intensity properties for a water droplet in air	33
3.3.3 The PDA set-up for diameter measurements.	34
4 Description of the experimental rig and operational conditions.	35
4.1 Introduction to the experimental rigs.	35
4.2 Design of rig for measurements of velocity profiles.	35
4.3 Design of rig for measurements of droplet distributions.	37
4.4 Sources of error.	39
4.4.1 Physical error related to the rig.	39
4.4.2 The alignment of the laser.	39
4.4.3 Accuracy of the measurements.	39
4.5 Operational conditions.	39
4.6 Description of the measurements.	40
4.6.1 Velocity measurements.	41
4.6.2 Droplet distribution measurements.	44
5 Experimental results.	45
5.1 Observations and comments to the measurements.	45
5.1.1 Unstable flow inside the separator.	45
5.1.2 The unstable flow affects the size distributions.	46
5.1.3 Description of the film behaviour inside the separator.	47
5.1.4 Water injection trials.	48
5.2 The low mass flow rate case.	49
5.3 The medium mass flow rate case.	56
5.4 The high mass flow rate case.	61
5.5 Comparisons between the different mass flow rates.	66
5.5.1 Diameter comparisons.	66
5.5.2 Non-dimensional velocity profiles.	67
5.5.3 Non-dimensional rms velocity.	69
5.6 Overall comments and conclusions.	71
6 CFD simulations.	72
6.1 Several aspects in the problem definition.	72
6.1.1 Grid generation.	72
6.2 The effect of a mismatch between the grid and near wall model	74
6.3 Comparisons for the medium mass flow.	75
6.3.1 The pressure drop.	76
6.3.2 The profiles at $x = -50$ mm.	76
6.3.3 The profiles at $x = 50$ mm.	78
6.3.4 The profiles at $x = 68.75$ mm.	80
6.3.5 The profiles at $x = 87.5$ mm.	82
6.3.6 The profiles at $x = 112.5$ mm.	85
6.3.7 The profiles at $x = 137.5$ mm.	88
6.3.8 The profiles at $x = 165$ mm.	91
6.4 Discussion and conclusions from the predicted profiles.	94

7 Droplet generation mechanisms and existing models.	96
7.1 Introduction to droplet generation mechanisms.	96
7.1.1 Droplet-droplet interaction.	97
7.1.2 Droplet break up.	97
7.1.3 Splashing of impinging droplet.	99
7.1.4 Re-entrainment from the liquid film.	99
7.2 Models for splashing of impinging droplet.	100
7.2.1 The model from Park and Watkins.	100
7.2.2 The model from Mundo et al.	102
7.2.3 The model from Cossali et al.	102
7.2.4 The model from Schmehl et al.	103
7.2.5 The model from Stanton and Rutland.	103
7.2.6 Conclusions from splashing models.	104
7.3 Models for re-entrainment from the liquid film.	105
7.3.1 The model from Zaichik et al.	105
7.3.2 The model from Woodmansee and Hanratty.	106
7.3.3 Conclusions from the re-entrainment models.	107
8 Complete description of the new models.	108
8.1 Some general improvements used in the simulations	108
8.1.1 Droplet description on the wall instead of a continuous film.	108
8.1.2 Reflection at small angles.	109
8.2 Model 1 - Empirical model.	110
8.3 Model 2 - Constant We number model	112
8.4 Model 3 – Varying We number model.	114
9 Results from the new droplet models	115
9.1 Particle tracking procedure, properties and inlet conditions.	115
9.1.1 The different cases.	115
9.1.2 The Rosin-Rammler representation.	115
9.1.3 The discretized droplet distribution.	116
9.1.4 Different properties.	117
9.2 Results from the model 1 - Empirical model	118
9.2.1 Results from the Rosin-Rammler distribution.	119
9.2.2 Results from the discretized distribution	120
9.2.3 Conclusions from model 1 – Empirical model	122
9.3 Results from the model 2 – Constant We number model	122
9.3.1 Results from the Rosin-Rammler distribution.	122
9.3.2 Results from the discretized distribution.	123
9.3.3 Conclusions from model 2 – Constant We number model.	124
9.4 Results from the model 3 – Varying We number model	125
9.4.1 Results from the Rosin-Rammler distribution.	125
9.4.2 Results from the discretized distribution.	126
9.4.3 Conclusions from model 3 – Varying We number model	127
9.5 Conclusions from the new droplets models.	127
10 Cyclone simulations.	128
10.1 Cyclone information	128
10.1.1 Additional challenges when simulating cyclones.	128
10.2 Results from the structured cases.	129

10.2.1 The Qing cyclone.	130
10.2.2 The Stairmand cyclone.	136
10.3 Multiblock grid simulation	137
10.4 Results from the multiblock cases.	138
10.4.1 The Qing cyclone.	138
10.4.2 The Stairmand cyclone.	144
10.5 Conclusions from the cyclone simulations.	144
11 Conclusions and further work.	146
12 References.	149
Appendix.	154
A.1 Comparison from the low mass flow.	154
A.2 Comparison from the large mass flow.	164
A.3 The vane	174

Nomenclature

Latin symbols

A	Area, [m ²]
$A_{\mathcal{E}}$	Constant in Equation (2.36), $2 c_1$
A_{μ}	Constant in Equation (2.36), 70
a	Inlet height (cyclone), [m]
a_e	Coefficient in the discretisation equation
B	Dust outlet diameter (cyclone) [m]
B_k	Body force in Equation (2.2), [kg/(m ² s ²)]
b	Inlet width (cyclone) [m]
C	The wave velocity, [m/s]
C_1	Constant in Equation (2.27), 1.8
C_2	Constant in Equation (2.27), 0.6
$C_{1\mathcal{E}}$	Coefficient in Equation (2.12) and Equation (2.15)
$C_{2\mathcal{E}}$	Coefficient in Equation (2.12) and Equation (2.15)
C_D	Drag coefficient, [-]
C_{LR}	Lift coefficient due to rotation, [-]
C_{μ}	Coefficient in Equation (2.10), Equation (2.19) and Equation (2.2)
c	Speed of light, 3E8 m/s
c_1	Constant in Equation (2.36), $\kappa C_{\mu}^{-3/4}$
\overline{D}	Mean diameter, [m]
D	Diameter main body (cyclone) [m]; Diameter of particle, [m]
D_e	Diffusion conductance, $\Gamma/\delta x$; Diameter vortex finder (cyclone), [m]
D_{ij}	Diffusion term in Equation (2.21), [m ² /s ³]
D_l	Diameter of ligament, [m]
D_{Mean}	Mean diameter, [m]
D_w	Diameter of droplet at wall, [m]
d_0	Beam waist diameter, [m]
E	Constant in Equation (2.30), 9.81
e	The natural logarithmic, 2.718
\vec{e}_i	Unit vector
\vec{F}_{Basset}	Basset force, [kg m/s ²]
\vec{F}_D	Drag force, [kg m/s ²]
\vec{F}_G	Gravitational force, [kg m/s ²]
$\vec{F}_{L, \text{Magnus}}$	Magnus lift force, [kg m/s ²]
$\vec{F}_{L, \text{Saffman}}$	Saffman lift force, [kg m/s ²]
\vec{F}_p	Global pressure force, [kg m/s ²]
\vec{F}_{vm}	Virtual mass force, [kg m/s ²]
\vec{F}_x	Other optional force, [kg m/s ²]

F_e	Flow rate through a control-volume face, ρu , [kg/(m ² s)]
f_0	Frequency shift, [1/s]
f_s	Frequency, [1/s]
f_{vm}	Virtual mass coefficient, 0.5
G_k	Production rate of turbulent kinetic energy, [kg/(m s ³)]
g	Gravitational constant, [m/s ²]
H	Cyclone height (cyclone) [mm]
h	Film thickness, [m]; Cylinder height (cyclone) [mm]
K	Constant in Mundo et al's model Equation (7.6), $OhRe^{1.25}$
K_L	Constant in the model to Cossali et al. Equation (7.9), $Oh^{-0.4}We$
k	Turbulent kinetic energy, [m ² /s ²]
k_p	Turbulent kinetic energy in point P, [m ² /s ²]
L	Length, [m]
La	LaPlace number, $\frac{\rho \sigma D}{\mu^2}$, [-]
ℓ_μ	Length scale, [m]
M_D	Mass deposited in current cell, [kg]; Mass fraction in Equation (2.63), [-]
m	Mass, [kg]
m_p	Mass of particle, [kg]
N_f	Total number of fringes, [-]
N_{random}	Random number between 0 and 1, [-]
n	The spread diameter, [-]
n_1	The refractive index of the scattering medium, [-]
Oh	Ohnesorge number, $\frac{\mu_l}{\sqrt{\rho_l \sigma D_{db}}}$, [-]
P	Pressure, [Pa]
Pe	Peclet number, $\frac{\rho u L}{\Gamma}$, [-]
P_{ij}	Production term in Equation (2.21), [m ² /s ³]
R	Tube radius, [m]; Defined in Equation (2.19), [kg/(s ⁴ m)]
Re_y	Wall distance based Reynolds number, $\frac{\rho \sqrt{k} y}{\mu}$, [-]
Re_{shear}	Shear based Reynolds number, $\frac{D^2}{\nu} \frac{du}{dy}$, [-]
r	Droplet radius, [m]
r_f	$\frac{\overline{\phi_c}}{1 - \overline{\phi_c}}$, [-]
S	Vortex length (cyclone) [m]; Modulus of the rate-of-strain tensor, [1/s]
S_{ij}	Rate-of-strain tensor, [1/s]
s	Particle path distance, [m]
T	Time, [s]
t	Time, [s]

U	Particle velocity, [m/s]
u^*	$\frac{1}{\kappa} \ln(Ey^*), [-]$
u'	Fluctuating part of the mean velocity, [m/s]
u_i, u_k	Velocities in i- or k-direction, [m/s]
U_P	Mean velocity at point P, [m/s]; Particle velocity, [m/s]
V_p	Volume of particle, [m ³]
w	Gaussian distributed number, [-]
We	Weber number, $V^2 D \rho / \sigma$, [-]
x_i	Length in i-direction, [m]
y^*	$\frac{y_p C_\mu^{1/4} k_p^{1/2}}{\nu}, [-]$
y_P	Distance in y-direction from wall to point P, [m]
z	Distance from the beam waist, [m]

Greek symbols

$\overline{\rho u_i' u_k'}$	Reynolds stress, [N/m ²]
α	Angle, [rad]; Energy loss coefficient, [-]; The beam divergence, [-]
α_k	Inverse effective Prandtl/Schmidt numbers for k, [-]
β	Constant, 0.012
β_i	Geometrical factor
δ	The non-dimensional film thickness, (h/D_d) , [-]
δ_f	Fringe spacing, [m]
δ_{ik}	Kronecker delta, [-]
ε	Dissipation of turbulent kinetic energy, [m ² /s ³]
ε_{ij}	Dissipation rate in Equation (2.21), [m ² /s ³]
Φ_{ij}	Pressure-strain redistribution term in Equation (2.21), [m ² /s ³]
Φ_i	The phase difference of the Doppler bursts, [rad]
ϕ	General dependent variable subject to discretisation
$\overline{\phi_C}$	$\frac{\phi_C - \phi_L}{\phi_R - \phi_L}$
η	Sk/ε
η_0	Constant in Equation (2.19), 4.38
φ	General variable in Equation (2.5)
φ'	Fluctuating part of φ
$\overline{\varphi}$	Mean value of φ
φ	The scattering angle, [rad]
φ_{b0}	Brewster condition for reflected light, 73.7°
φ_{b2}	Brewster condition for 2 nd order refraction, 138.8°
φ_{c1}	Critical angle for refracted light, 82.9°

ϕ_{r2}	Rainbow angle for 2 nd order refraction, 138.0°
ϕ_{r3}	Rainbow angle for 3 rd order refraction, 128.8°
Γ	General diffusion coefficient
κ	Von Karmans constant, 0.42
λ	Wave length, [m]
μ	Dynamic viscosity, [kg/(m s)]
μ_t	Turbulent viscosity, [kg/(m s)]
μ_{eff}	$\mu + \mu_t$, [kg/(m s)]
ν	Kinematic Viscosity, [m ² /s]
π	Pi, 3.14
θ	Angle between incoming laser beams, [rad]; Impinging angle [rad]
ρ	Density, [kg/m ³]
σ	Surface tension, [N/m]
σ_ϵ	Turbulent diffusion of ϵ , 1.3
σ_k	Turbulent diffusion of k , 1.0
σ_{ik}	Fluid stress tensor in Equation (2.2), [kg/(m s ²)]
τ	Shear stress, [kg/(m s ²)]
τ_{ik}	Viscous stress tensor, [kg/(m s ²)]
τ_k	The characteristic kinematic time scale, [s]
$\psi(r_f)$	Bounding function defined according Equation (2.42)
$\overrightarrow{\omega_d}$	Particle rotation, [rad/s]
$\overrightarrow{\omega_r}$	Relative spin of droplet with respect to fluid, [rad/s]

Sub scripts

10	Arithmetic diameter mean
20	Area based diameter mean
30	Volume based diameter mean
32	Sauter mean diameter
a	After
b	Before
b0	Brewster condition for reflected light
b2	Brewster condition for 2 nd order refraction
c	Central; Critical
C	Central grid point
c1	Critical angle for refracted light
c2	Critical angle for 2 nd order refraction
D	Doppler-frequency
dn	Droplet normal
db	Droplet diameter before collision
e	East
f	Fringe; Film
FL	Far Left, Grid point left for the Left grid point
g	Gas
i	Direction; Inside, Incoming, Interface

j	Direction
k	Direction
<i>l</i>	Liquid; Direction
L	Left, Grid point to the left for central grid point
n	A large number; Normal
o	Outside
p	Particle
r	Right; Face value between the grid points C and R
R	Right; Grid point to the right for the central grid point
r2	Rainbow angle for 2 nd order refraction
r3	Rainbow angle for 3 rd order refraction
s	Scattered
t	Tangential
w	Wall
ϵ	Dissipation

Abbreviations

bfc	Body fitted coordinates
CFD	Computational Fluid Dynamics
LDA	Laser Doppler Anemometry
PDA	Phase Doppler Anemometry
PRESTO	PREssure Staggered Option
Quick	Quadratic Upstream Interpolation for Convective Kinematics
RNG	ReNormalization Group
rms	Root mean square
RSM	Reynolds Stress Model
Smart	Sharp and Monotonic Algorithm for Realistic Transport

Chapter 1

Introduction

1.1 Motivation for the thesis

Two-phase flows can be found in nearly every industrial process. There are many possible types of two-phase flow; some examples are liquid-gas, liquid-solid, liquid-liquid, and gas-solid. This work focuses on the gas-liquid types of two-phase flow, with focus on droplet-gas flow. The importance of gas-liquid flows can, for example, be seen in the light of Norwegian activity in the natural gas fields. Large contracts of selling natural gas to the continent are signed, and Norway will become a large export nation of natural gas. Natural gas is produced from fields, which also contains water, heavy hydrocarbons and sand. These components have to be removed in order to achieve pipeline transport specifications. Separation equipment is used in this process. But several onshore processes also deal with liquid-gas flows. In various reactors droplet-gas flows are found, such as a polypropylene reactor where propylene is the gas and the droplets are polypropylene. In electrical power generation facilities mist eliminators are used to prevent water and/or slurry droplets containing pollutants present in the gas scrubbing systems, from being released into the atmosphere. Another example is to recover valuable process chemicals and condensates, prevent contamination of downstream processes and guard the environment from possible pollution. Mist elimination, to remove the droplets from the gas, is also used in the prevention of water entering into turbine air intakes. Typical examples of types of separation equipment are cyclones and vane types, but in some instances wire-mesh types are used. Figure 1.1 shows some typical figures of the different types of droplet-gas separators.

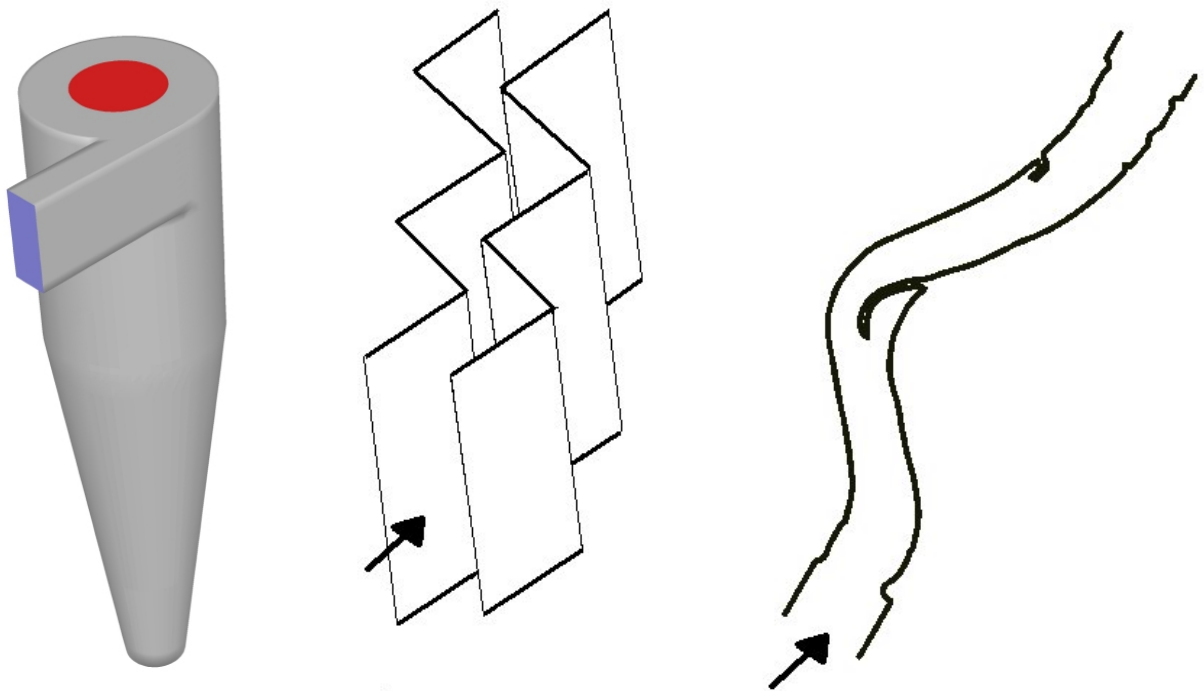


Figure 1.1: a) A typical cyclone (to the left), b) a zigzag type vane separator (in the middle), c) a curved vane (to the right).

The design of such demisters has mainly been done on an empirical basis. Long experience and best practice are commonly used in the design of the equipment. In order to make better and smaller equipment, detailed knowledge about the physics is needed. The need for smaller and better equipment arises from the fact that for instance, some natural gas fields are economical marginal. In order to exploit these fields, smaller equipment with cost and weight reduction can help the producers to make such fields economic profitable. It is also possible to use this knowledge to design equipment for onshore activities, such as in other problems related to droplet-gas flows.

In the development of new and improved process equipment during the last decades, the Computational Fluid Dynamics (CFD) has been playing a bigger role. The CFD codes have been developed to be robust, effective and easy to use, and so the marked has opened up to use CFD codes in the design of process equipment. CFD analysis is a powerful tool for analysing complex flows therein multiphase flows, and a useful model in the tracking of particles like droplets, bubbles and solid particles. There exist, however, few if any models that can be used in a CFD code that describes important features of the droplet-gas flow. The fate of a droplet hitting a wall inside the separator is of major importance. Will the droplet coalesce on the film or break up and create many small droplets? Measurements of the droplet size distribution before and after the separator will provide us with some information, and an analytical approach to the physics is necessary to understand the process of droplet-wall (film) interaction.

In this work, two types of demisters are studied. The vane type separator is primarily studied, but this work started by doing some work on cyclones. The cyclone simulations were intended to make a basis for further investigation of the droplet-wall interactions in cyclone separators. The work started with a comparison between predictions from the CFD code and measurements from the literature. The results from this comparison were satisfactorily, but when the Euler-Lagrangian was approach used on the un-structured version of the CFD code, the results was not promising. The results showed some discrepancy, and this effect was mainly because of the prediction of non-tangential velocities near the cyclone wall. It was then decided to shift focus from the cyclone type to the vane type separator. A typical vane separator consists of separate vanes, which forms a narrow passage where the gas with droplets must pass. Basic vanes are zigzag types but newer technology has made it possible to design vanes that are curved. Typical examples of the use and theory of common vane separators can be found in [7].

The vanes used in this study are commercial vanes from Munters, (<http://www.munters.com>) identical to the curved vanes shown in Figure 1.1. The curvature is somewhat sinusoidal, and some obstacles are added to the vane in order to increase the efficiency. The two hooks (or barbs) are added, and in addition, some small-scale grooves are added. The droplets in the carrier gas are heavier than the gas, and will consequently have a higher momentum. This is used as the separation force, and the increased momentum for the droplets forces the droplets to deviate from the streamlines of the carrier gas. Large droplets will collide with the vane, and deposit. The separation process is not trivial. The separated water may form a continuous film, or patches of water, or the deposition leads to excessive water loads in the current location, and results in re-entrainment of some of the water. These effects will be explained in the modelling section, where models are written to account for these effects in the CFD simulations of a droplet-gas flow. All the droplets have deviations from the streamlines, but for a certain size at a certain location, the deviations are not enough to force the droplet to collide with the vane. These droplets manage to escape from the separator. The efficiency of

the vane separator is, of course, the most important feature of the separator. The efficiency is connected to the pressure drop for the vane separator, and an increased efficiency leads to an increase in the pressure drop. The main objective is then to construct a high efficiency vane with the lowest possible pressure drop. New designs include curvature, and few bends, while earlier designs included zigzag types with many bends. Research and new technology have contributed to this innovation. In order to carry on the innovation, detailed knowledge of the gas flow within the vanes should be known. Few and insufficient references are found in the literature containing measured velocity vectors inside such a vane. The PhD thesis of Verlaan [64] contains one measured profile between a pair of zigzag vanes. Keshava Iyer et al [29] present some measured velocities in a vane package. Wang and James [66] perform simulations on a vane separator, and compare the predicted efficiency to measurements. Experimental work in order to find the efficiency of vane separators has been more popular and more references are found. These references contain efficiency measurements of a vane separator [6, 29, 30, 36, 37, 45, 46, 50, 61]. The laser technology has been used in some of these references to obtain the droplet size distribution before and after the separator in order to achieve information about the efficiency of the separator. Hence, the efficiency of such separators is well documented, but detailed measurements between sinusoidal vanes are not found in the literature.

1.2 Goals of this thesis

The main objective of this thesis is to obtain mathematical models that describe droplet interactions in a gas flow. The interactions can be of various types, but the main focus is the droplet wall interaction. The mathematical models are intended to be used in a commercial CFD code, and hence improve the possibilities and quality of droplet-gas flows simulations. In order to develop a mathematical model describing the physical phenomena involved, a comprehensive understanding of the underlying mechanisms are necessary. The best way to achieve a good insight to the proper mechanisms and physics involved in the droplet wall interaction is to perform measurements. The title of the thesis also implies an experimental part, and the experimental work shall reveal important features with the droplet wall interaction. The experimental work will use the LDA (Laser Doppler Anemometry) and PDA (Phase Doppler Anemometry) techniques to measure in detail the velocity distribution and droplet distribution on a chosen flow system. The experimental results will form a basis, which is important in two ways. Firstly, the CFD code can be checked and the quality are verified. The measured velocity field are compared with the predictions from the CFD code. Secondly, the experiments shall reveal information, such that a model can be developed. The combination of using experimental observations together with simulation is normally a safe way to a good result.

1.3 Outline of the thesis

This thesis can be considered to contain 5 different parts. The first chapter, ‘Chapter 1 Introduction’, and the last chapter, ‘Chapter 11 Conclusions and further work’ are chapters that contain moments with overall interest, and hence they are not part of any part. The rest of the chapters have the following classification:

Part I) Fundament and basis

This part contains the first four chapters, with the exception of this chapter ‘Chapter 1 Introduction’. The first chapter in this part is hence ‘Chapter 2 Governing equations and droplet theory’ which covers the fundamental theory of the CFD code. Then ‘Chapter 3 LDA/PDA theory’ presents the theory for the two measure techniques. ‘Chapter 4 Description

of the experimental rig and operational conditions’ describes the experimental set-up, operational conditions, and discuss several aspects with the measurements.

Part II) Results from the measurements and predictions

In ‘Chapter 5 Experimental results’ the experimental results are presented. The experimental work is performed on a vane separator. Velocities and rms (root mean square) velocities profiles are presented for seven different cross sections. ‘Chapter 6 CFD simulations’ shows the comparisons between experiments and simulations for a complete set of profiles from one of the three mass flows presented in the previous chapter.

Part III) Physical models of the droplet generation mechanism

In ‘Chapter 7 Droplet generation mechanisms and existing models’ the physics connected to the creation of new droplets inside the vane separator are identified. Some models for these mechanisms are found in the literature. These models are tested with operational conditions for the separator, and this analysis reveal that the existing models are not able to predict the generation of the new droplets. In ‘Chapter 8 Complete description of the new models’ the mathematical models developed in this work are presented. The models are shown and their basis is discussed. Three new models are presented, where one is empirical and the two others have a basis in a force balance.

Part IV) Results from the new models

This part contains only one chapter, ‘Chapter 9 Results from the new droplet models’. The new models presented in Chapter 8 are used together with the CFD code, and the differences in prediction of the droplet size distribution out of the separator are studied.

Part V) The Cyclone part

‘Chapter 10 Cyclone simulations’ covers the work done on cyclone simulations. Predictions from the CFD code, where compared with measurements found in the literature. This is a stand-alone part, and it is considered important to include this chapter in the thesis. The reason for including is that some amount of time was spent when simulating the cyclone, and cyclones are also used when separating gas and droplets. This time is nevertheless not wasted, since valuable experience using the CFD package was obtained.

Chapter 2

Governing equations and droplet theory

This chapter will present the governing equations for the CFD (Computational Fluid Dynamics) method and some additional theory for the droplets. The equations and theory for the CFD code are only briefly stated since the knowledge of these equations are well confirmed after years with research and analysis. Many commercial CFD codes exist, for example Phoenix, Flow3d, and Fluent, and in this work Fluent has been used [18]. The different aspects of the CFD code are presented, and special focus is given to models used later in the simulations. For the droplets additional theory is presented. This includes the shape of a droplet and different diameter means. However, the CFD theory first.

2.1 Conservation equation

The basis for a CFD code is the general equations for transient, compressible laminar flow. These equations are presented next, and these equations are well known and some references are listed [18, 28, 31, 49, 56]. The equations are written in Cartesian tensor notation. The first equation to be presented is the continuity equation

$$\frac{\partial \rho}{\partial t} + \frac{\partial}{\partial x_i}(\rho u_i) = 0 \quad (2.1)$$

Then the equation for the conservation of momentum in k^{th} -direction is given

$$\frac{\partial}{\partial t}(\rho u_k) + \frac{\partial}{\partial x_i}(\rho u_i u_k) = \frac{\partial}{\partial x_i} \sigma_{ik} + B_k \quad (2.2)$$

where σ_{ik} is the stress tensor and B_k is the body force in k^{th} -direction. The stress tensor is written

$$\sigma_{ik} = -p\delta_{ik} + \tau_{ik} = -(p + \frac{2}{3}\mu \frac{\partial u_l}{\partial x_l})\delta_{ik} + \mu(\frac{\partial u_k}{\partial x_i} + \frac{\partial u_i}{\partial x_k}) \quad (2.3)$$

If the equation for the stress tensor, Equation (2.3), is substituted into the momentum Equation (2.2) the Navier-Stokes equation is the result

$$\frac{\partial}{\partial t}(\rho u_k) + \frac{\partial}{\partial x_i}(\rho u_i u_k) = \frac{\partial}{\partial x_i}(-(p + \frac{2}{3}\mu \frac{\partial u_l}{\partial x_l})\delta_{ik} + \mu(\frac{\partial u_k}{\partial x_i} + \frac{\partial u_i}{\partial x_k})) + B_k \quad (2.4)$$

If the fluid is incompressible the term $\frac{2}{3}\mu \frac{\partial u_1}{\partial x_1}$ is zero.

2.2 Turbulence modelling

The Navier-Stokes equation is valid for turbulent flows. But the drawback is that the turbulent flow contains small-scale effects, which leads to an excessive fine grid in order to resolve these effects. In order to establish an understanding of the nature of the turbulence, a definition of turbulence done by Bradshaw [4] is worth quoting. Bradshaw: *"Turbulence is a three-dimensional time-dependent motion in which vortex stretching causes velocity fluctuations to spread to all wave-lengths between a minimum determined by viscous forces and a maximum determined by the boundary conditions of the flow. It is usual state of the fluid motion except at low Reynolds numbers."*

The development of turbulence models gives us the possibility to simulate turbulent flows, without needing to fully resolve the flow domain. This is accomplished by averaging the Navier-Stokes equations. Each variable is decomposed of a mean, $\bar{\varphi}$, and a fluctuating part, φ' . For variable φ

$$\varphi = \bar{\varphi} + \varphi' \quad (2.5)$$

For incompressible flow, which is the case for the simulations in this thesis, Reynolds average rule is used. If compressible flow is considered, density fluctuations are important, and Favre averaging is recommended. The averaged transport equations contain mean variables, and in addition an extra term. The modelling of the new term in the momentum equation is the objective of the turbulence models. If the averaged values are substituted into the momentum equation, the averaged momentum equation used in the CFD code for predicting turbulent flows are found. The averaged equations are then

$$\frac{\partial \rho}{\partial t} + \frac{\partial}{\partial x_i}(\rho u_i) = 0 \quad (2.6)$$

$$\frac{\partial}{\partial t}(\rho u_k) + \frac{\partial}{\partial x_i}(\rho u_i u_k) = \frac{\partial}{\partial x_i} \sigma_{ik} - \frac{\partial}{\partial x_i}(\overline{\rho u_i' u_k'}) + B_k \quad (2.7)$$

where u' are the fluctuating part, and u_i are now the mean values. This is consistent for the rest of this thesis. The new terms in the momentum equation, $(-\overline{\rho u_i' u_k'})$, are called the 'Reynolds stresses' and represent the effect of the turbulence. Note that $(-\overline{\rho u_i' u_k'})$ is a symmetric second order tensor, and hence:

$$\overline{\rho u_i' u_k'} = \overline{\rho u_k' u_i'} \quad (2.8)$$

The modelling of this term is the objective of the turbulence models, and three common turbulence models have been used in this work: the standard k- ϵ model, the Renormalization

Group (RNG) k- ϵ model, and the Reynolds Stress model (RSM). Turbulence modelling is not an object of this thesis, so the presentation of the turbulence models will be brief.

2.2.1 The standard k- ϵ model

The equation for modelling the Reynolds stresses is according to Hinze [22]

$$\overline{\rho u_i u_k} = \rho \frac{2}{3} k \delta_{ik} - \mu_t \left(\frac{\partial u_i}{\partial x_k} + \frac{\partial u_k}{\partial x_i} \right) + \frac{2}{3} \mu_t \frac{\partial u_l}{\partial x_l} \delta_{ik} \quad (2.9)$$

Equation (2.9) is based on the Boussinesq hypothesis, which assumes that the Reynolds stresses are proportional to the mean velocity gradients. The proportional constant is called the turbulent viscosity, μ_t . The evaluation of μ_t is obtained by assuming that it is a product of a turbulent velocity scale and a turbulent length scale. The length scales are then assumed as a function of the k and ϵ . The final equation for μ_t can be written as

$$\mu_t = \rho C_\mu \frac{k^2}{\epsilon} \quad (2.10)$$

where k is the turbulent kinetic energy and ϵ is the turbulent dissipation rate. The values for k and ϵ are given by respective transport equations

$$\frac{\partial}{\partial t}(\rho k) + \frac{\partial}{\partial x_i}(\rho u_i k) = \frac{\partial}{\partial x_i} \left(\frac{\mu_t}{\sigma_k} \frac{\partial k}{\partial x_i} \right) + G_k - \rho \epsilon \quad (2.11)$$

$$\frac{\partial}{\partial t}(\rho \epsilon) + \frac{\partial}{\partial x_i}(\rho u_i \epsilon) = \frac{\partial}{\partial x_i} \left(\frac{\mu_t}{\sigma_\epsilon} \frac{\partial \epsilon}{\partial x_i} \right) + C_{1\epsilon} \frac{\epsilon}{k} G_k - C_{2\epsilon} \rho \frac{\epsilon^2}{k} \quad (2.12)$$

G_k is the rate of production of turbulent kinetic energy, and is given by

$$G_k = \mu_t \left(\frac{\partial u_i}{\partial x_k} + \frac{\partial u_k}{\partial x_i} \right) \frac{\partial u_i}{\partial x_k} \quad (2.13)$$

In Equation (2.10), Equation (2.11) and Equation (2.12) various empirical constants appear, C_μ , $C_{1\epsilon}$, and $C_{2\epsilon}$. σ_k and σ_ϵ are Prandtl/Schmidt numbers representing the turbulent diffusion of k and ϵ compared to turbulent diffusion of momentum. Table 2.1 gives the numerical values of the empirical constants. The conservation equations for k and ϵ , and the values of the empirical constants, are according to the work of Launder and Spalding [33, 34].

Table 2.1: The empirical constants used in the standard k- ϵ model.

Constant	Value
$C_{1\epsilon}$	1.44
$C_{2\epsilon}$	1.92
C_μ	0.09
σ_k	1.0
σ_ϵ	1.3

The standard k- ϵ model has been tested and used for many years, and it is generally accepted that the performance for simple flows are satisfactorily. The main weakness with the k- ϵ model lies in the description of the anisotropic turbulence. Anisotropic turbulence exists for complex flows where there is more than one velocity gradient that dominates. This leads to the fact that in complex flows where the turbulence is expected not to be isotropic, the k- ϵ model may not be good enough. A typical example is a swirling flow inside a cyclone.

2.2.2 The RNG k- ϵ model

The turbulence in a swirling flow inside a cyclone has an anisotropic nature, and since the standard k- ϵ model is best on isotropic turbulence, the standard k- ϵ model is supposed to be inappropriate to use. An alternative turbulence model is used for the cyclones, and this is the RNG (ReNormalization Group) k- ϵ model [68]. The RNG k- ϵ model is a turbulence model, which is based on statistical mechanics rather than the continuum mechanics, and offer modifications that make this model useful on cyclones. When RNG theory is used on the turbulence this results in elimination of small scale eddies, which are assumed not to contribute to the turbulent kinetic energy. A statistical linked description of the length scales of the turbulence leads to an equation that describes the length scale as a function of the Reynolds number. The RNG k- ϵ model has similar equations for k and ϵ as the standard k- ϵ model, but with different values on the constants. Additional terms exist in the equation for ϵ , but modifications to the calculation of the effective viscosity are most significant. The effective viscosity is calculated from an ordinary differential equation, which includes the effect of swirl. The equation for turbulent kinetic energy, k, for the RNG k- ϵ model is [68]

$$\frac{\partial}{\partial t}(\rho k) + \frac{\partial}{\partial x_i}(\rho u_i k) = \frac{\partial}{\partial x_i}(\alpha_k \mu_{eff} \frac{\partial k}{\partial x_i}) + \mu_t S^2 - \rho \epsilon \quad (2.14)$$

and the equation for ϵ is

$$\frac{\partial}{\partial t}(\rho \epsilon) + \frac{\partial}{\partial x_i}(\rho u_i \epsilon) = \frac{\partial}{\partial x_i}(\alpha_\epsilon \mu_{eff} \frac{\partial \epsilon}{\partial x_i}) + C_{1\epsilon} \frac{\epsilon}{k} \mu_t S^2 - C_{2\epsilon} \rho \frac{\epsilon^2}{k} - R \quad (2.15)$$

where α_k and α_ϵ are the inverse effective Prandtl/Schmidt numbers for k and ϵ , and are computed using the following equation

$$\left| \frac{\alpha - 1.3929}{\alpha_0 - 1.3929} \right|^{0.6321} \left| \frac{\alpha + 2.3929}{\alpha_0 + 2.3929} \right|^{0.3679} = \frac{\mu_{mol}}{\mu_{eff}} \quad (2.16)$$

α is either α_k or α_ϵ , α_0 is equal to 1.0, and μ_{mol} is the molecular viscosity. S is the modulus of the mean rate-of-strain tensor, S_{ij} , which is defined as

$$S \equiv \sqrt{2S_{ij}S_{ij}} \quad (2.17)$$

where S_{ij} is defined

$$S_{ij} = \frac{1}{2} \left(\frac{\partial u_j}{\partial x_i} + \frac{\partial u_i}{\partial x_j} \right) \quad (2.18)$$

The R in the ε equation, Equation (2.15), is given by

$$R = \frac{C_\mu \rho \eta^3 (1 - \eta / \eta_0)}{1 + \beta \eta^3} \frac{\varepsilon^2}{k} \quad (2.19)$$

where $\eta \equiv Sk/\varepsilon$, $\eta_0 \approx 4.38$, $\beta = 0.012$. The calculation of the μ_t is almost similar as the calculation of μ_t for the k - ε model for the high Reynolds number limit $L \gg \ell_d$. L is the length scale for energy containing eddies, and ℓ_d is the Kolomogorov dissipation scale $L/Re^{3/4}$. The RNG k - ε model calculates the μ_{eff} beyond this high Reynolds number limit by integrating the variation of effective viscosity, and writing the resulting equation in terms of k and ε . A simplified algebraic form is given as

$$\mu_{eff} = \mu_{mol} \left[1 + \sqrt{\frac{C_\mu}{\mu_{mol}}} \frac{k}{\sqrt{\varepsilon}} \right]^2 \quad (2.20)$$

The empirical constants used in Equation (2.15) are shown in Table 2.2.

Table 2.2: The constants used in the RNG k - ε model.

Constant	Value
$C_{1\varepsilon}$	1.42
$C_{2\varepsilon}$	1.68
C_μ	0.0845

It is expected that the RNG k - ε model will have some weakness in the accuracy of calculating swirling flows, since it is still isotropic in its description of the turbulence. In order to get away from the isotropic description of the turbulence, the Reynolds Stress Model (RSM) is a natural choice.

2.2.3 The Reynolds Stress Model (RSM)

The major limitation of the k - ε model is that the description of the μ_t is isotropic, which implies that the turbulent length scales are equal in all directions. When large variations exist in the flow, the k - ε model performs rather bad and produces unrealistic flow fields. The RSM (Reynolds Stress Model) solves the individual Reynolds stresses by solving its respective transport equation. This model takes into account the anisotropy of the turbulence. The conservation equation can be written [32,35]

$$\frac{\partial}{\partial t}(\rho \overline{u'_i u'_j}) + \frac{\partial}{\partial x_i}(\rho u_k \overline{u'_i u'_j}) = D_{ij} + P_{ij} + \Phi_{ij} - \varepsilon_{ij} \quad (2.21)$$

On the left hand side the terms are the transient term and the convection term of $\overline{u'_i u'_j}$, and the first term on right hand side is the diffusion term, D_{ij} . The production term, P_{ij} , follows.

The two last terms are the pressure-strain redistribution, Φ_{ij} , and the dissipation rate, ε_{ij} .

These terms can from equation manipulation of the momentum equation, exactly be written like

$$D_{ij} = -\frac{\partial}{\partial x_k} \left[\left(\rho \overline{u'_i u'_j u'_k} \right) + \overline{p(\delta_{kj} u'_i + \delta_{ik} u'_j)} - \mu \frac{\partial}{\partial x_k} \left(\overline{u'_i u'_j} \right) \right] \quad (2.22)$$

$$P_{ij} = -\rho \overline{u'_i u'_k} \frac{\partial u_j}{\partial x_k} - \rho \overline{u'_j u'_k} \frac{\partial u_i}{\partial x_k} \quad (2.23)$$

$$\Phi_{ij} = p \left[\frac{\partial u'_i}{\partial x_j} + \frac{\partial u'_j}{\partial x_i} \right] \quad (2.24)$$

$$\varepsilon_{ij} = 2\mu \left[\frac{\partial u'_i}{\partial x_k} \frac{\partial u'_j}{\partial x_k} \right] \quad (2.25)$$

Based on the conservation equation for $\overline{u'_i u'_j}$, it is possible to calculate $\overline{u'_i u'_j}$. However, there are more unknown variables than equations. This is the closure problem. New models must be included so that it is the same number of variables and equations, and the models used are according to [32,35]. If the production term, P_{ij} , is studied, it appears that this term can be calculated directly since both u_i and $\overline{u'_i u'_j}$ already have conservation equations. However, the other three terms need models (D_{ij} , Φ_{ij} and ε_{ij}). A simple model for the diffusion term is [32]

$$D_{ij} = \frac{\partial}{\partial x_k} \left(\frac{\mu_t}{\sigma_k} \frac{\partial (\overline{u'_i u'_j})}{\partial x_k} \right) \quad (2.26)$$

The pressure-strain redistribution, Φ_{ij} , is modelled by

$$\Phi_{ij} = -C_1 \frac{\varepsilon \rho}{k} \left[\overline{u'_i u'_j} - \frac{2}{3} \delta_{ij} k \right] - C_2 \left[P_{ij} - \frac{2}{3} \delta_{ij} P - \frac{\rho}{2} \left(\frac{\partial u_j}{\partial x_i} + \frac{\partial u_i}{\partial x_j} \right) \right] \quad (2.27)$$

where $P = P_{ii} / 2$, $C_1 = 0.5$, $C_2 = 0.18$. The dissipation rate, ε_{ij} , is modelled by [53]

$$\varepsilon_{ij} = \frac{2}{3} \delta_{ij} \varepsilon \quad (2.28)$$

ε is not known and must be found. This can be done by solving a conservation equation for ε , similar to the one used in the k - ε turbulence model, Equation (2.12). Then the production term G is given by $G = P_{ii} / 2$. When the RSM model is selected instead of the k - ε turbulence model, the k -equation will not be solved, but instead equations for the cross moments, $\overline{u'_i u'_j}$, are solved. The turbulent kinetic energy is given by

$$k = \frac{\overline{u_i'^2 + u_j'^2 + u_k'^2}}{2} \quad (2.29)$$

The constants used in the RSM model are shown in Table 2.3.

Table 2.3: The constants used in the RSM model.

Constant	Value
C_1	1.8
C_2	0.6
σ_k	1.0

The advantage of the RSM model is the individual treatment of the different Reynolds stresses, but this is also the drawback with this model. The increased number of transport equations increases the computational effort in order to achieve a converged solution.

2.3 Near wall models for turbulence

Several methods for modelling the turbulence in the near wall region are presented in the literature, and two methods are tested in this work. These two methods deal with the near wall turbulence in quite different ways. The first method is called Law-of-the-wall, and in this approach the viscous layer is jumped over by the use of a simple equation. This reduces the number of the grid points in the wall region. If the grid is too fine, the wall adjacent cell will be inside the viscous layer, and the method will not be recommended. The other method resolves the viscous and the buffer layer, and a fine grid near the wall is hence needed. This method is called the Two-layer zonal model. Some important aspects for the two different methods will briefly be discussed. The differences between the two methods are discussed based on the k - ε model.

2.3.1 Law of the wall

The Law of the wall assumes a fully turbulent flow, and requires that the wall-adjacent cell is in the turbulent region. For the grid this implies a relatively coarse grid near the wall. Near the wall the following equation is used [34]

$$\frac{U_P C_\mu^{1/4} k_P^{1/2}}{(\tau/\rho)_w} = \frac{1}{\kappa} \ln(E y_P \frac{C_\mu^{1/4} k_P^{1/2}}{\nu}) \quad (2.30)$$

where $\kappa = 0.42$ (von Karmans constant), $E = 9.81$, U_P is the mean velocity at point P, $C_\mu = 0.09$, k_P is the turbulent kinetic energy at point P, subscript w means wall, y_P is the distance from the wall to point P. This is, as stated above, only valid in the turbulent region, and if the first grid point is too close to the wall, another equation is used. For $E y_P \frac{C_\mu^{1/4} k_P^{1/2}}{\nu} < 11.225$ the equation used is

$$\frac{U_P C_\mu^{1/4} k_P^{1/2}}{(\tau/\rho)_w} = y_P \frac{C_\mu^{1/4} k_P^{1/2}}{\nu} \quad (2.31)$$

These two last equations are often written as $u^* = \frac{1}{\kappa} \ln(Ey^*)$ and $u^* = y^*$.

The transport equation for k is solved throughout the whole domain, with a zero gradient as a boundary condition at the wall. The source terms in the k -equation, the production of k and its dissipation rate, have special treatments in the wall-adjacent cells. The ε -equation is not solved in the wall-adjacent cells. In the wall-adjacent cell ε is found from

$$\varepsilon_p = \frac{C_\mu^{3/4} k_p^{3/2}}{\kappa y_p} \quad (2.32)$$

2.3.2 Two-layer zonal model

For the Two-layer zonal model [9, 66] the viscous layer is discretised, and fully resolved. In the viscosity affected region, a length scale equation for the μ_t is implied [9, 66]. To separate the viscosity affected region from the fully turbulent region, a wall-distance based Reynolds number is used

$$Re_y = \frac{\rho \sqrt{k} y}{\mu} \quad (2.33)$$

For $Re_y > 200$ fully turbulent region is assumed. For $Re_y < 200$ viscous flow is assumed. When viscous flow is present, the turbulent viscosity is found through the use of

$$\mu_t = \rho C_\mu \sqrt{k} \ell_\mu \quad (2.34)$$

The ε -field is computed from

$$\varepsilon = \frac{k^{3/2}}{\ell_\varepsilon} \quad (2.35)$$

The length scales are

$$\ell_\mu = c_1 y \left[1 - e^{\left(-\frac{Re_y}{A_\mu} \right)} \right], \quad \ell_\varepsilon = c_1 y \left[1 - e^{\left(-\frac{Re_y}{A_\varepsilon} \right)} \right] \quad (2.36)$$

where c_1 is equal to $\kappa C_\mu^{-3/4}$, A_μ is equal to 70, and A_ε is equal to $2c_1$.

The grid considerations are then opposite as it was for the Law-of-the-wall, and a relatively fine grid is required. The Two-layer zonal model is not valid for the RSM model (Reynolds Stress Model), and hence this wall approach is only used for the k - ε model.

2.4 Discretisation

The simulations presented later in this thesis use different discretisation schemes: Power law, First order upwind and QUICK (Quadratic Upstream Interpolation for Convective Kinematics). The Power law and the First-order Upwind are discretisation methods, which produces an accuracy of 1st order, while the QUICK method is a higher order accuracy scheme.

2.4.1 Power law scheme

The power law scheme uses the exact solution of a one-dimensional convection-diffusion equation in order to interpolate the current variable at the face of the cell. The interpolated value varies with the current Peclet number, Pe , which is defined as

$$Pe = \frac{\rho u L}{\Gamma} \quad (2.37)$$

where L is a length, and Γ is a diffusion coefficient. The Peclet number is the ratio between convection and diffusion. The power law scheme differs in accuracy dependent on the numerical value of the Peclet number. At low Peclet numbers the power law scheme is reduced to central differencing, and at high Peclet numbers to the first order upwind scheme. Patankar [49] writes the compact form of the power law scheme as

$$a_e = D_e \left[\left[0, \left(1 - \frac{0.1 |F_e|}{D_e} \right)^5 \right] + \left[0, -F_e \right] \right] \quad (2.38)$$

where $F_e = \rho u$ and $D_e = \Gamma / \delta x$. a_e is the east coefficient in the discretisation equation. The notation $[[\cdot]]$ means the largest of the expressions contained within it.

2.4.2 First order upwind scheme

This discretisation scheme takes simply the cell centre value of the current variable, ϕ , and uses this value at the face of the cell in the upstream direction. Thus,

$$\phi_r = \phi_C \text{ if } u > 0 \quad (2.39)$$

and

$$\phi_r = \phi_R \text{ if } u < 0 \quad (2.40)$$

where ϕ_r is the wanted face value, ϕ_C is the value of variable ϕ in point C, and ϕ_R is the value of variable ϕ in point R. Figure 2.1 shows a principal sketch of the first order upwind scheme. ϕ_r is given by either ϕ_C or ϕ_R depending on the flow direction.

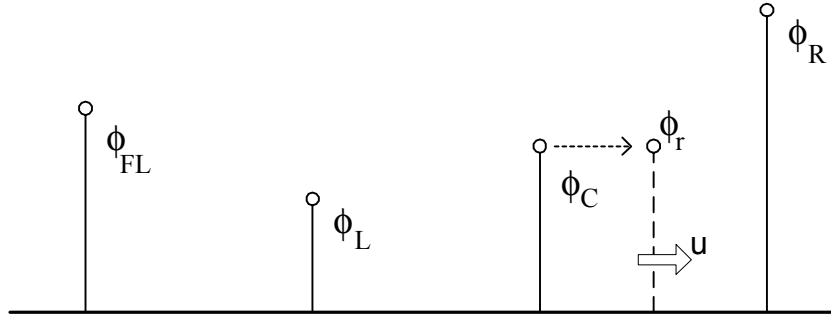


Figure 2.1: The First order upwind scheme.

2.4.3 Quadratic Upstream Interpolation for Convective Kinematics (QUICK)

QUICK uses a three-point upstream-weighted quadratic interpolation. The variable ϕ_t is then calculated as follows [18, 19, 39]

$$\phi_r = \phi_C + \frac{1}{4} \left[\frac{3}{2} \psi(r_f)(\phi_R - \phi_C) + \frac{1}{2} \psi\left(\frac{1}{r_f}\right)(\phi_C - \phi_L) \right] \quad (2.41)$$

where $r_f = \frac{\bar{\phi}_C}{1 - \bar{\phi}_C}$, and $\bar{\phi}_C = \frac{\phi_C - \phi_L}{\phi_R - \phi_L}$. Figure 2.2 shows the QUICK interpolation for ϕ_t . The $\psi(r_f)$ is the bounding function. The bounding function is needed to ensure a monotonic behaviour of the variables in regions of steep gradients. This is a typical draw back with the higher order schemes. Higher order schemes provide greater numerical accuracy, but numerical instabilities can occur. The bounding function used is the ‘Sharp and Monotonic Algorithm for Realistic Transport ‘ (SMART) where $\psi(r_f)$ is defined as

$$\psi(r_f) = \max[0, \min(2r_f, 0.75 + 0.25r_f, 2)] \quad (2.42)$$

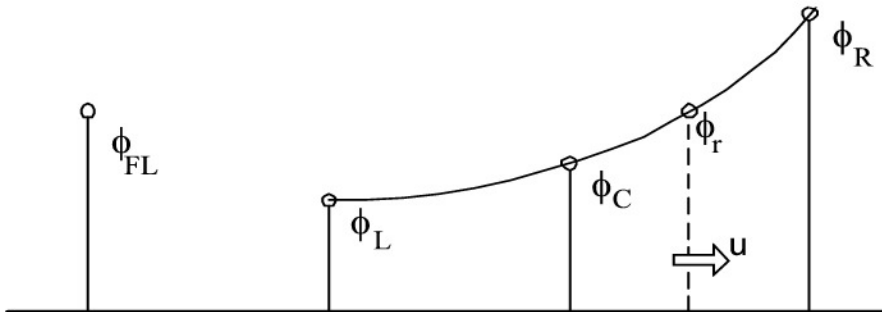


Figure 2.2: The QUICK interpolation scheme.

2.5 Two-phase treatment in the simulations

Two different two-phase methods are commonly used in numerical analysis today. These are called the Euler-Euler method or the Euler-Lagrangian method. The latter uses a force balance on the dispersed particle in a Lagrangian reference frame. The forces acting on a dispersed particle are described in the next section. The Euler-Euler method solves the respective transport equations for each phase completely. In the Euler-Euler method the phase boundary is represented by source/sink terms. The Euler-Euler method has not been used in this work, but the Euler-Lagrangian has, so the forces used in the force balance are discussed. Many of these forces are negligible in the current simulations in this thesis, but still included in this discussion.

2.5.1 Force balance

The force balance for a particle with a constant mass, m_p , is given as [18]

$$\frac{d\vec{u}_p}{dt} = (\vec{F}_D + \vec{F}_G + \vec{F}_x) / m_p \quad (2.43)$$

where \vec{F}_D is the drag force, \vec{F}_G is the force exerted from the gravity, and \vec{F}_x describes other optional forces. Typical examples of such forces are lift forces (both shear and rotational based), virtual mass force, Basset force, and pressure global force. In the next sub-sections models for the various forces are shown, and forces, which are considered insignificant, are neglected.

2.5.2 Forces acting on droplet/particles in dispersed systems

This section presents the various forces acting on a dispersed particle. The forces are presented and commented in light of the simulations for the applications in this thesis. It may be appropriate to mention that interactions between these forces are common, but in the simulations considered in this work this phenomena is neglected. The number of droplets is so small that interactions are negligible. This is further discussed in Chapter 7.1.

2.5.2.1 Steady-state drag force

This force is modelled as [12]

$$\vec{F}_D = \frac{1}{2} \rho_g C_D A |\vec{u}_g - \vec{u}_p| (\vec{u}_g - \vec{u}_p) \quad (2.44)$$

where ρ_g is the gas density, C_D is the drag coefficient, A is the representative projection area of a droplet, \vec{u}_g is the velocity of carrier gas, and \vec{u}_p is the velocity of the droplet. Typically the representative area is the projected area of the droplet in the direction of the relative velocity. The drag coefficient will depend on various parameters such as shape, orientation with respect to the flow, turbulence level, Reynolds number, and so on. For a sphere the drag coefficient is known to be variable with the relative Reynolds number. The relative Reynolds number is defined as

$$\text{Re}_g = \frac{\rho_g D |\vec{u}_g - \vec{u}_p|}{\mu_g} \quad (2.45)$$

where D is the diameter of the sphere, $|\vec{u}_g - \vec{u}_p|$ represent the relative velocity between the carrier gas and the droplet, and μ_g is the viscosity of the carrier gas. The drag coefficient follows a curve, as described in Figure 2.3, depending on the relative Reynolds number.

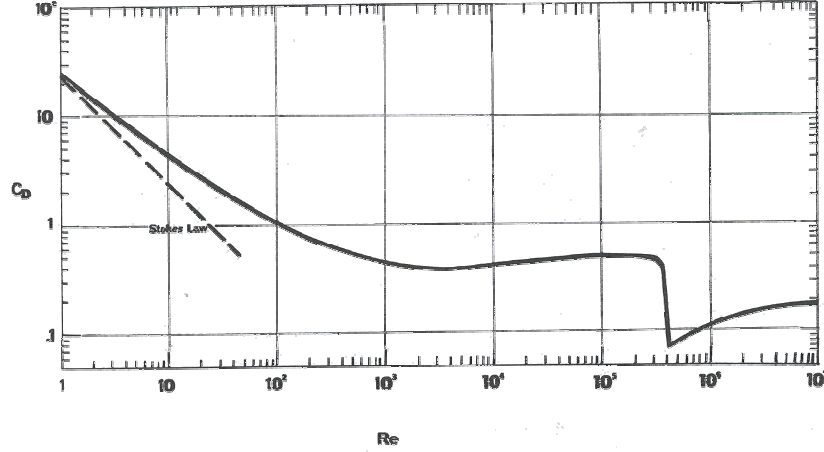


Figure 2.3: The drag coefficient as a function of Re. [10]

The drag coefficient, C_D , is defined according to Morsi and Alexander [41]. Several other drag laws were tested, but only minor deviations between the different drag laws were noted [10, 27, 30]. The drag law of Morsi and Alexander were used in the rest of the simulations.

2.5.2.2 Gravity

The gravity force is

$$\vec{F}_G = m_p \vec{g} \quad (2.46)$$

But it is wanted to include buoyancy effect into this force, and hence Equation (2.45) is re-written to

$$\vec{F}_G = m_p \vec{g} \left(\frac{\rho_p - \rho}{\rho_p} \right) \quad (2.47)$$

2.5.2.3 Saffman lift force

The Saffman lift force is caused by pressure differences developed on a droplet in a non-uniform velocity field. The higher velocity gives rise to a lift force, due to a low-pressure zone. Saffman [55] analysed this force, and for low Reynolds number, the following equation is used to model the lift force

$$\vec{F}_{L,Saffman} = 1.61 \mu_g D |\vec{u}_g - \vec{u}_p| \sqrt{\text{Re}_{shear}} \quad (2.48)$$

where the Re_{shear} is the shear Reynolds number defined as

$$\text{Re}_{\text{shear}} = \frac{D^2}{\nu} \frac{du}{dy} \quad (2.49)$$

where ν is the kinematic viscosity of the carrier gas. Physically this Reynolds number is based on the velocity difference between the top and the bottom of the droplet. If the relative velocity between the gas and the droplet is positive (the gas is moving faster than the droplet), the Saffman lift force will act in the direction of the higher velocity in the continuously phase. But if the relative velocity is negative, then the Saffman lift force will act in the direction of the lower velocity in the continuously phase. The Saffman lift force are tested in simulation of the vane separator, and showed no significant change in the particle trajectory. It is hence not included in the force balance.

2.5.2.4 Magnus force

The Magnus force is a lift experienced by the droplet due to rotation of the droplet. The rotation causes a velocity difference over the droplet, resulting in a pressure difference. This pressure difference creates the lift. The rotation also determines the direction of the lift. Rubinow and Keller [54] modelled the Magnus lift force as

$$\vec{F}_{L,Magnus} = \frac{1}{2} \rho_g |\vec{u}_g - \vec{u}_p| C_{LR} A \left(\frac{(\vec{u}_g - \vec{u}_p) \times \vec{\omega}_r}{\left| \vec{\omega}_d - \frac{1}{2} \nabla \times \vec{u}_g \right|} \right) \quad (2.50)$$

where C_{LR} is the lift coefficient due to rotation, and ω_r is the relative spin of the droplet with respect to the fluid ($\vec{\omega}_r = \vec{\omega}_d - \frac{1}{2} \nabla \times \vec{u}$). It has been numerous attempts to measure the spin coefficient, but fundamental results are yet to be made. However, it can be mentioned that for pipe flows the shear induced lift, Saffman, is significant larger than the rotational, Magnus [26]. Since the shear induced lift was shown to have no significant effect on the simulations, the Magnus force are neglected.

2.5.2.5 Virtual Mass force

This is one of the two forces, which has an unsteady nature. The virtual mass force relates to the force required to accelerate the surrounding fluid when the droplet is accelerated. In order to understand the virtual mass force it is necessary with a thorough analysis. This analysis is not done, and only the final result for the virtual mass force is mentioned [12]

$$\vec{F}_{vm} = f_{VM} \rho_g V_p \left(\frac{D\vec{u}_g}{Dt} - \frac{D\vec{u}_p}{Dt} \right) \quad (2.51)$$

where V_p is the volume of the particle, and f_{VM} is the virtual mass coefficient. According to [23] the value of f_{VM} lies between 0.25 and 0.75, and 0.5 is usually used.

2.5.2.6 Basset force

This force accounts for the viscous effects caused by acceleration. It is hard to evaluate the equation describing the Basset force, and is neglected in most trajectory analysis. The Basset force [3] is

$$\vec{F}_{Basset} = \frac{3}{2} d_p^2 \sqrt{\pi \rho_g \mu_g} \int_{t_0}^t \frac{(\frac{D\vec{u}_g}{Dt} - \frac{D\vec{u}_p}{Dt})}{\sqrt{t-t'}} dt' \quad (2.52)$$

2.5.2.7 Global pressure force

The net pressure force acting on a particle, where the pressure gradient is assumed constant over the volume of the particle, is given by [12, 24]

$$\vec{F}_p = -\nabla p V_p \quad (2.53)$$

For a gas-droplet flow where the densities ratio between the gas and particle is 10^{-3} , the global pressure force may be neglected.

2.5.2.8 Additional forces

This is a group of forces that may act on the droplet under certain circumstances. These forces can be electrostatic forces or adhesion forces. None of these forces are included in the trajectories performed, and hence neglected.

2.5.3 Including the turbulence in the prediction of the particle trajectory

The inclusion of turbulent dispersion is obtained by integrating the trajectory equations using the instantaneous velocity, $u = \bar{u} + u'$, along the particle path during the integration. If sufficient number of particles is calculated this way, the random effect of turbulence can be accounted for. The time spent in turbulent motion along the particle path is [18]

$$T = \int_0^\infty \frac{u'_p(t) u'_p(t+s)}{\overline{u'^2_p}} ds \quad (2.54)$$

where ds is the change in particle path. The instantaneous fluid velocity is found solving the Langevin equation [59, 62]

$$du_i = \frac{1}{T} u_i dt + \left(\frac{2 \overline{u'_i u'_i}}{T} \right)^{\frac{1}{2}} dw \quad (2.55)$$

where T is the integral time, and w is a Gaussian distributed number. A more thorough description of the Langevin equation can be found in [59, 62].

2.6 General droplet theory

Droplets in a gas stream can vary in shape, so the first sub-section of this chapter discuss different aspects of the shape of droplets. And to the end of this section a brief explanation to the different definitions of droplet mean diameters are given.

2.6.1 Shape of droplets

A quote from Clift et al. [10] is given: “When a fluid sphere exhibits little internal circulation, either because of high $\kappa = \frac{\mu_p}{\mu}$ or because of surface contaminants, the external flow is indistinguishable from that around a solid sphere at the same Re . For example, for water drops in air, a plot of C_D versus Re follows closely the curve for rigid spheres up to a Reynolds number of 200, corresponding to a droplet diameter of approximately 0.85 mm.” The droplets used in this work are mostly smaller than 0.85 mm, and for these droplets it is safe to assume spherical shape. But for larger droplets the droplets are droplet-shaped, and the drop tries to accomplish equilibrium according to the equation

$$1/r_1 + 1/r_2 = (P_i - P_o)/\sigma \quad (2.56)$$

where r_1 and r_2 is the principal radii at any point on drop surface, P_i and P_o is the pressure inside and outside the drop, and σ is the surface tension. This leads to, for a small droplet

$$2/r = (P_i - P_o)/\sigma \quad (2.57)$$

The reason for the sphere shape is because the surface tension wants to minimize itself, and a sphere has the smallest surface for a given volume. The surface tension is an important property for a droplet. The surface tension is responsible for the sphere shape, and its magnitude will influence the deformation when other forces influence the droplet. To determine the tension force of a liquid a simple experiment can be carried out. If droplet growth rate from a tube is very slow, and the elongation eventually go through a neck formation, and finally break-up, the kinetic contribution from the mass flow can be neglected. If this is the case, the droplet will rip itself from the tube when the gravity force is larger than surface force in the contact area of the liquid-droplet interface (the tube diameter). The following force balance is then used

$$2\pi R\sigma = mg \quad (2.58)$$

where R is the radius of the tube, m is the mass of the drop, and g is the gravitational constant. The mass of the droplet must be measured, and then the surface tension can be determined. [47].

2.6.2 Definitions of different droplet mean diameters

In a presentation of a droplet size distribution several different mean diameters can be given. The simplest is an arithmetic mean of the droplet diameter. This is called the D_{10} mean, and can be written as

$$D_{10} = \frac{1}{n} \sum_{i=1}^n D_i \quad (2.59)$$

where n is the total number of droplets in the sample. The area mean diameter can be found from the mean squared diameter, as shown in the next equation

$$D_{20} = \left(\frac{1}{n} \sum_{i=1}^n D_i^2 \right)^{1/2} \quad (2.60)$$

D_{20} is then the area mean diameter of the droplet distribution. A similar mean diameter can be defined on basis of the third power of the diameter, or in other words the volume

$$D_{30} = \left(\frac{1}{n} \sum_{i=1}^n D_i^3 \right)^{1/3} \quad (2.61)$$

D_{30} represents the volume mean diameter. Then the most used mean diameter can be defined on the basis of the volume mean diameter and the area mean diameter. The Sauter mean diameter, D_{32} , is defined as

$$D_{32} = \frac{\sum_{i=1}^n D_i^3}{\sum_{i=1}^n D_i^2} \quad (2.62)$$

2.6.3 The Rosin-Rammler size distribution

In later sections the measured droplet size distribution is presented as a Rosin-Rammler distribution. The Rosin-Rammler distribution function is based on the assumption that an exponential relationship exists between the droplet diameter, D , and the mass fraction of droplets with diameter greater than D , M_D . This relation can be written as

$$M_D = e^{-\left(\frac{D}{\bar{D}}\right)^n} \quad (2.63)$$

where \bar{D} is the mean diameter and n is the spread parameter. \bar{D} is found from a graphical presentation where the mass fraction M_D is plotted against the diameter, D . The value of \bar{D} is simply read from the graph where $M_D = e^{-1} = 0.368$. The spread diameter, n , is calculated from the following relation

$$n = \frac{\ln(-\ln M_D)}{\ln\left(\frac{D}{\bar{D}}\right)} \quad (2.64)$$

Chapter 3

LDA/PDA theory

The measuring technique used in this thesis is an optical laser method. The laser, which is available on the campus, can be rigged as both a LDA (Laser Doppler Anemometry) configuration and a PDA (Phase Doppler Anemometry) configuration. Both these techniques are used in the measurements. The theory of the LDA and PDA will be discussed in the following sections, and the set-up used for each method is presented. The main difference between the LDA and the PDA method is that the PDA method is capable of measuring velocities as well as sizes. The advantages of using optical methods in order to measure velocities and particle sizes are numerous. Compared to other known methods for measuring velocity, such as hot wire and pitot-tubes, the LDA technique offers several advantages; non-intrusive, high spatial resolution, fast dynamic response, well-defined velocity components, and to a certain degree no calibration needed. On the other hand, some disadvantages exist such as tracers needed, optical access, and expensive equipment. Additional information concerning the LDA technique can be found in the Ph.D. thesis of Elseth [17].

The history of using different laser techniques in order to achieve good measurements stretches back some decades. In 1964 Yeh and Cummins [69] demonstrated the LDA technique in practice. They used a set-up known as a reference beam method. Other references contain similar set-up, with slightly different optical arrangements. Some examples can be found in [5, 13, 40]. The development on the LDA measurement has been rather rapidly and contributions from numerous authors can be acknowledged. It is however important to mention the work of Durst and Zarè [16], which identified the phenomena that made it possible to measure the diameter of the passing particle. A reference of particular interest is the work of Durst et al. [15], which is known to be an excellent reference of the LDA-technique. Some general aspects to the laser light are given in the start of the next section. Then the theory and set-up of the LDA technique are presented, and finally the PDA method is presented.

3.1 Measurement principle

The measurement principle for any of the two optical laser methods is based on the crossing of two or more laser beams. In the crossing of two laser beams a volume forms, which becomes the measuring volume. When a particle passes the measuring volume, reflected or refracted light from the laser beams can be used to determine the velocity and size of the passing particle. The reflected or refracted light has experienced a shift because of interacting with the passing particle, and this information is used to determine the velocity and diameter. The measure principle is discussed on the basis of the LDA technique, and most of the theory presented in the following sections can be found in Dantec's user guide [13].

3.1.1 The laser beam

Laser is an acronym for "Light Amplification by Stimulated Emission of Radiation", and is much used in science because of its coherent nature. Coherent light means that the wave fronts in the beams move in unison. The source of the laser light is an Argon-gas laser. The Argon gas is energized, and the emitted light produces the laser light. The beam is not uniform in diameter, and contains a beam waist. The beam waist is located where the

diameter of the beam is at a minimum. In Figure 3.1 this is shown by d_0 . The importance of the beam waist is shown when the optimal performance of any LDA-equipment is wanted. The reason for this is that the wave fronts in the beam are straight in the beam waist, and slightly curved elsewhere in the beam. The straight wave front is assumed in the development of the calculations needed in order to use the optical signal, and hence a measurement performed at the beam waist will be optimal. The intensity across the diameter of the beam has a Gaussian distribution. The width of the beam is normally defined by the edge intensity being $1/e^2$ (13 %) of the core intensity. The intensity across the beam is shown in Figure 3.1, and termed $I(r)$. The beam divergence is given by α , and the equation for α is

$$\alpha = \frac{4\lambda}{\pi d_0} \quad (3.1)$$

where λ is the wavelength. The notation for Equation (3.1) follows from Figure 3.1. The beam diameter at a given distance from the beam waist, z , is [13]

$$d(z) = d_0 \sqrt{1 + \left(\frac{4\lambda z}{\pi d_0^2}\right)^2} \quad (3.2)$$

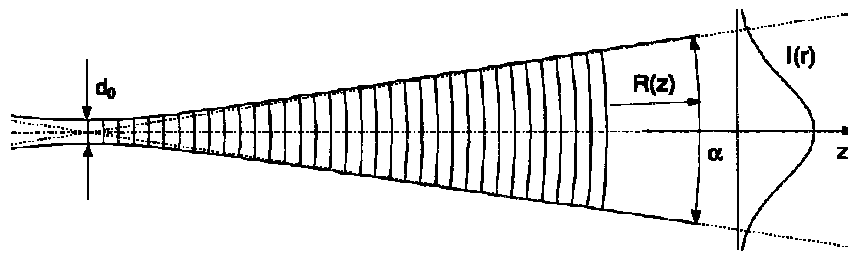


Figure 3.1: The beam waist at d_0 and other definitions of the laser beam.

3.1.2 The Doppler effect

The Doppler effect is a well-known and much studied effect. The Doppler effect states that a frequency shift for the light is noted when the source or the object moves relative to the medium. For the LDA measurements the light received by the receiver is shifted due to the Doppler effect. Figure 3.2 shows a principal sketch for a moving particle with incoming light, \vec{e}_i . The \vec{e}_s is the scattered light vector.

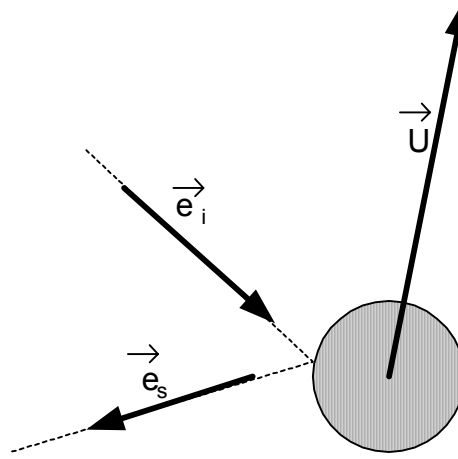


Figure 3.2 Light reflected from a moving particle.

The moving particle sees a light with different properties, and this light is reflected to the receiver. The particle acts as a moving transmitter, and creates a shift in the frequency, Doppler-shift. The light received at the receiver, can be expressed as

$$f_s = f_i \frac{1 - \vec{e}_i \cdot (\vec{U} / c)}{1 - \vec{e}_s \cdot (\vec{U} / c)} \cong f_i \left[1 + \frac{\vec{U}}{c} \cdot (\vec{e}_s - \vec{e}_i) \right] = f_i + \Delta f \quad (3.3)$$

where f_s is the frequency of the scattered light, f_i is the frequency of the incident light, \vec{e}_s is the unit vector for the scattered light, \vec{e}_i is the unit vector for the incident light, \vec{U} is the particle velocity, and c is the speed of light. The frequency change is in practice only measurable for particles with very high velocities. Therefore two intersecting laser beams are instead used as shown in Figure 3.3.

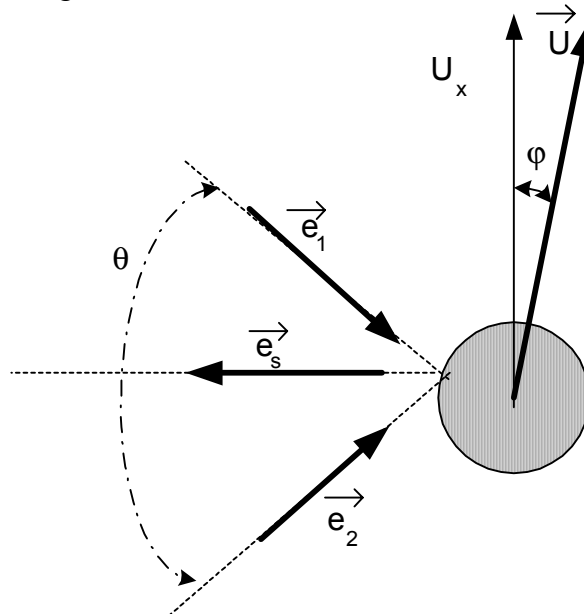


Figure 3.3: Light reflected from two different beams on a moving particle.

Now the light received by the receiver contains two slightly different frequencies due to different angles of the two beams. These frequencies are given by Equations (3.4) and (3.5).

$$f_{s,1} = f_i \left[1 + \frac{\vec{U}}{c} \cdot (\vec{e}_s - \vec{e}_1) \right] \quad (3.4)$$

$$f_{s,2} = f_i \left[1 + \frac{\vec{U}}{c} \cdot (\vec{e}_s - \vec{e}_2) \right] \quad (3.5)$$

The Doppler frequency, or the beat frequency, is obtained by superimposing the two reflected laser beams. This beat frequency is constructed when the beams interact constructively or destructively. The beat frequency corresponds to the difference between the two wave-frequencies. Equation for the Doppler frequency, f_D , or beat frequency, is obtained by the following equations

$$\begin{aligned} f_D &= f_{s,2} - f_{s,1} \\ &= f_i \left[1 + \frac{\vec{U}}{c} \cdot (\vec{e}_s - \vec{e}_2) \right] - f_i \left[1 + \frac{\vec{U}}{c} \cdot (\vec{e}_s - \vec{e}_1) \right] \\ &= f_i \left[\frac{\vec{U}}{c} \cdot (\vec{e}_1 - \vec{e}_2) \right] \\ &= \frac{f_i}{c} \left[|\vec{e}_1 - \vec{e}_2| \cdot |\vec{U}| \cdot \cos(\varphi) \right] \\ &= \frac{1}{\lambda} \cdot 2 \sin(\theta / 2) \cdot u_x \end{aligned} \quad (3.6)$$

The angle between the incoming laser beams is given by θ . The angle between the velocity vector \vec{U} and the direction of measurement are given by φ . The Doppler-frequency, f_D , is much lower than the frequency of the light. From Equation (3.6) it can be seen that the Doppler-frequency is directly proportional with the velocity, and hence the velocity can be calculated when the Doppler-frequency, f_D , is measured.

3.1.3 The measure volume

The two intersecting laser beams form a volume, where the measurements are carried out. The measuring volume is defined as the contour where the light intensity is $1/e^2$ or 13.5 % of the peak light intensity of the beam. The measuring volume is shown in Figure 3.4, and has the shape of an ellipsoid.

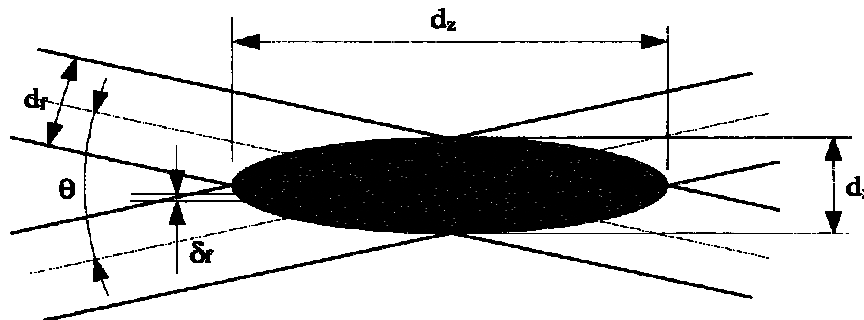


Figure 3.4: Two intersecting laser beams constructing the measure volume [13].

The volume, or the dimensions, of the ellipsoid can be calculated from the beam waist diameter, d_0 , and the angle between the beams

$$d_x = \frac{d_0}{\cos(\theta/2)} \quad (3.7)$$

$$d_y = d_0 \quad (3.8)$$

$$d_z = \frac{d_0}{\sin(\theta/2)} \quad (3.9)$$

The ellipsoid contains an interference pattern created by the intersecting laser beams. This produces straight planes of interference maximums and minimums, and these planes are called fringes. The theory of the fringe model is presented in the next section.

3.1.4 Fringe model

The fringes that exist in the ellipsoid-shaped measuring volume are shown in Figure 3.5.

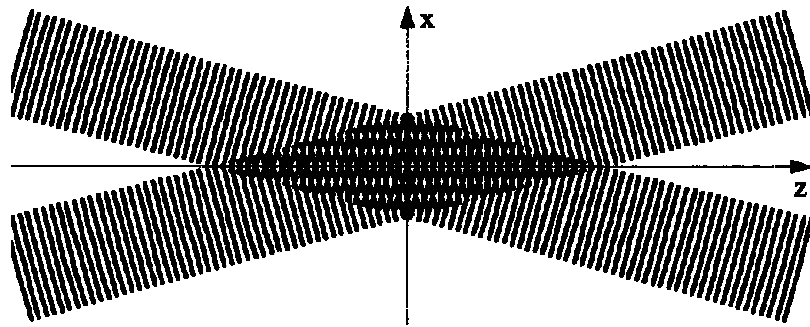


Figure 3.5: The fringes in the measuring volume [13].

The fringes are parallel to each other, and the distance between them, fringe spacing, is given by

$$\delta_f = \frac{\lambda}{2 \sin(\theta/2)} \quad (3.10)$$

It is important that the ellipsoid is placed in the beam waists of the laser beams, since the wave fronts are straight in the beam waist. If the location of the measuring volume is slightly offset, the wave fronts are curved, and the fringe spacing will vary. The total number of fringes in a measure volume can be calculated. The total number of fringes is given by

$$N_f = \frac{d_x}{\delta_f} = \frac{d_0 / \cos(\theta/2)}{\lambda / 2 \sin(\theta/2)} = \frac{2d_0}{\lambda} \tan(\theta/2) \quad (3.11)$$

The number of fringes passed by a moving particle varies depending on the entry to the measuring volume. If the particle moves in the middle of the volume, all the fringes in the volume are passed. But if the particle moves in the edge of the volume, fewer fringes are

passed. The number of fringes passed is an important factor, because of the number of fringes passed corresponds to the quality for the estimated Doppler-frequency.

3.1.5 Frequency shift

The set-up so far can produce a velocity from the measured Doppler frequency, but a major drawback is noted for the case of negative velocities. According to Equation (3.6) negative velocities will produce negative Doppler frequencies. But the receiver cannot distinguish between negative and positive frequencies, and so a directional ambiguity arises. This is shown in Figure 3.6.

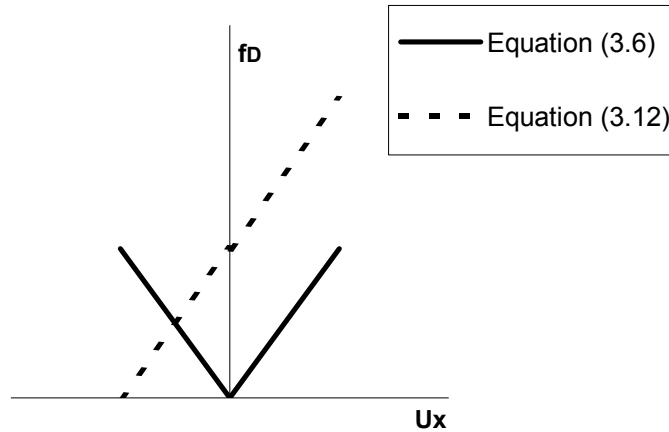


Figure 3.6: The directional ambiguity for negative velocity.

In order to make it possible to measure negative velocities, the intersection for the f_D -line in Figure 3.6 is altered. If an offset of this line is made, so that the f_D -line crosses the axis on a negative u_x value, a successful measurement of the negative velocity is accomplished. Adding a frequency shift to one of the laser beams makes this offset. The fringe, which was stationary, moves now with a constant velocity. If the fringes move across the measure volume with a velocity higher than the magnitude of the negative velocity, a unique relation between the measure Doppler-shift and the corresponding velocity are obtained. The unique relation between the velocity and the measured Doppler-frequency is given by

$$f_D = \left| f_0 + \frac{2 \sin(\theta / 2)}{\lambda} u_x \right| \quad (3.12)$$

where f_0 is the frequency shift.

3.1.6 Bragg cell

The frequency shift added to one of the laser beams in the previous section, f_0 , is done in the Bragg cell. The Bragg cell is a slab of glass with an electro-mechanical transducer on one side, and is shown in Figure 3.7. The electro-mechanical transducer produces an acoustic wave propagating through the slab generating a periodic moving pattern of high and low density. When the light enters the slab, the waves produced by the electro-mechanical device, acts as a thick grating. The interference pattern generated is emitted in many directions, but by adjusting the acoustic signal intensity and the tilt angle of the Bragg cell, the intensity balance between the direct beam and the first order of diffraction can be adjusted. The Bragg cell adds a fixed frequency shift to the diffracted beam according to Equation (3.12). The ambiguity in

Figure 3.6 is avoided as long as the negative velocity does not become larger in magnitude of the corresponding Doppler-shift than the frequency shift given by the Bragg cell. In Figure 3.6 f_I is the incoming frequency, f_0 is the frequency shift, θ_B is the Bragg cell angle.

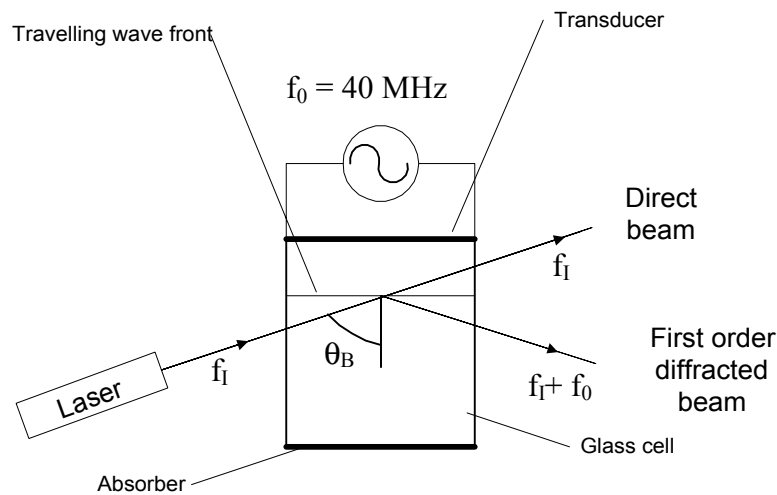


Figure 3.7: A principle sketch of the Bragg cell [13].

3.1.7 Signals from the detector

The detector receives the incoming light, and the result is a pulse containing information related to the velocity of the particle passing the measure volume. Some noise is also included in the signal coming from the detector. The noise might origin from several sources; noise related to the detection process and noise related to other light sources. The noise related to the detection process origins from that the interaction between the optical field and the photosensitive material, which unavoidably causes some fluctuation or noise in the mean photocurrent. The noise coming from the undesired light is of course an important noise source. Some additional noise sources are the secondary electron noise from the photo multiplier dynode chain and preamplifier thermal noise in the signal processor. Several means are used to minimise the noise level, this including the power of the laser light, bandwidth, seeding particle size and optical system parameters.

Another property, which is important for the quality of the signal, is the number of particles present simultaneously in the measure volume. If on average much less than one particle is present in the measure volume, the signal detected are said to be a burst type Doppler signal. The Figure 3.8 shows a typical Doppler burst signal (to the left), and the filtered signal (to the right). The filtered signal is fed into the signal processor. If more than one particle is in the measure volume, the result is a multi-particle signal. The contributions from each particle are added to the total, causing a Doppler signal of random character. A single-particle burst is most common used in signal processors.

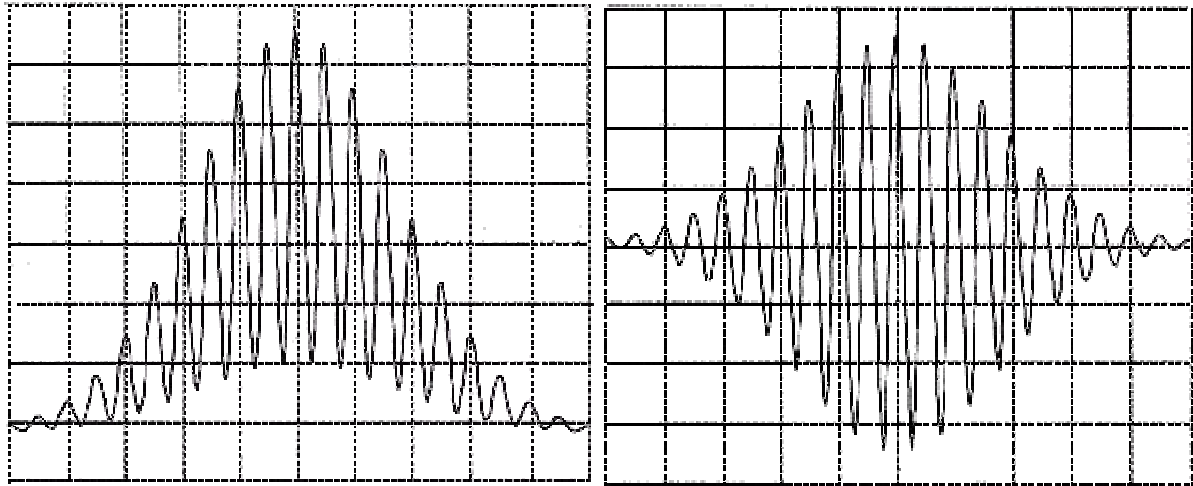


Figure 3.8: The Doppler-burst (to the left), and the filtered signal (to the right).

3.1.8 Modes of scattering

Figure 3.9 shows three different kinds of scattering possible for a water droplet in air. Higher order refraction modes are neglected in this figure, and only 2nd order refraction is included. The importance of knowing which scattering mode one wants to use in the measurements arises from the fact that the scattering mode is included in Equation (3.13) for β_i . This dependency on the scattering mode can lead to error if the detectors receive scattered light from different modes. It is hence necessary to rig the PDA set-up in such a way that only one scattering mode dominates.

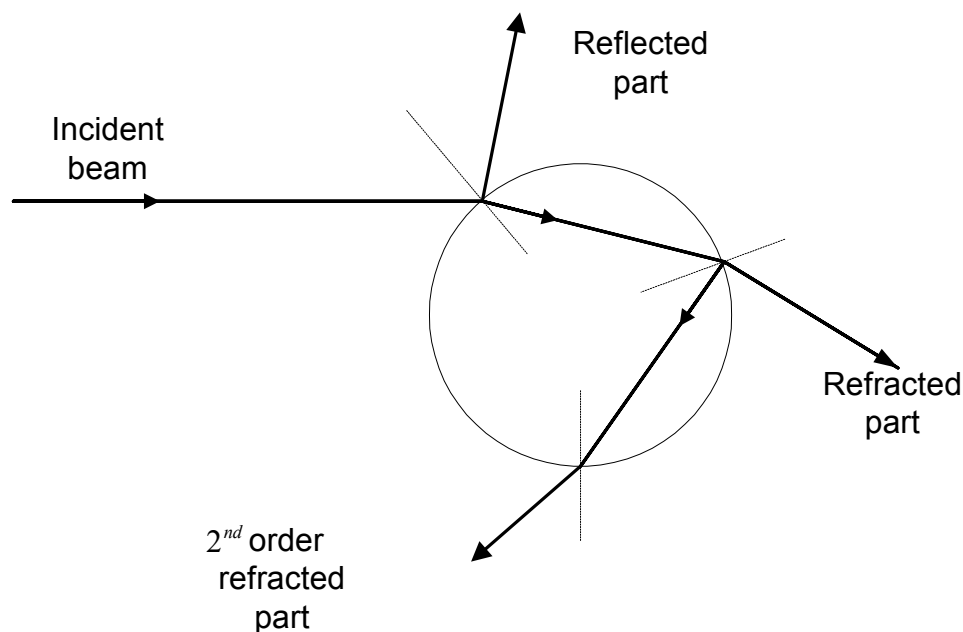


Figure 3.9: Different scattering modes for a water droplet in air [13].

3.1.8 Definition of forward, side, and backscatter

It is found necessary to include the Figure 3.10, which defines the terms used for different scattering angles. Figure 3.10 shows the forward scatter, side scatter, and the backscatter regimes. ϕ is the scattering angle. Forward scatter refers often to scattering angles between 0° and 80° , which typically represent 1st order refracted light. Side scatter contains normally reflected light, and represent scattering angles between 80° and 110° . Second order refraction lies in the backscatter regime, and contains scattering angles typically between 150° and 180° . The backscatter regime for PDA should normally be avoided, and only used when all other alternatives are impossible.

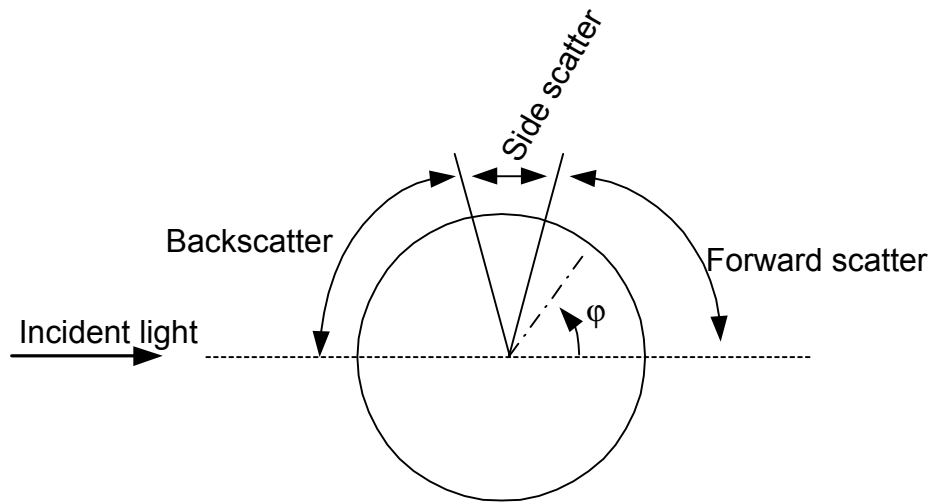


Figure 3.10: The name of the different scattering areas. ϕ is the scattering angle. [13]

3.2 The LDA set-up used for the velocity measurements

The Figure 3.11 shows a principal sketch of the set-up for the velocity measurements. The laser beam generated in the laser generator is led into a beam splitter. The beam splitter splits the beam into two parts. Then one of the beams, just previously split, enters the Bragg cell. The Bragg cell add the frequency shift to one of the laser beams, and the result is that the pair of laser beams now consists of one shifted and one un-shifted beam.

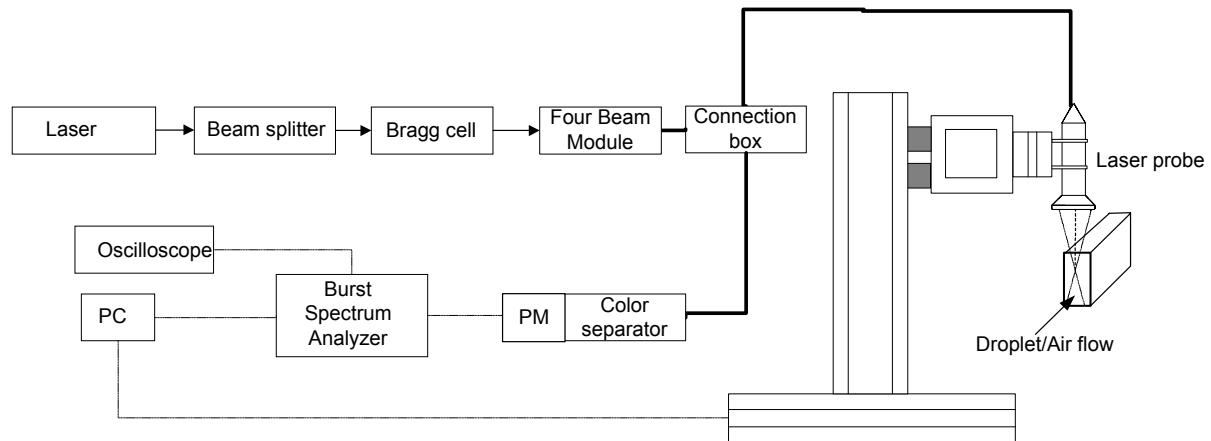


Figure 3.11: The LDA set-up used in the velocity measurements.

The selected equipment was for a couple of years ago expanded to make 2D measurements, and hence two sets of laser beams are used. The beam splitter splits the laser pair into a green and a blue set. The green pair has the wavelength 514.5 nm, and the blue pair 488 nm. So far the laser light has been travelling in the open air, but at the exit of the Four beam module the beams are directed into the optical fibre leading to the laser probe. In Figure 3.11 lines with arrowhead shows the air-borne laser light, while the thick line shows the optical fibre. The lens mounted at the end of the laser probe determines the focal point. For the velocity measurements, a lens with focal length of 310 mm was used. In this backscatter mode, the light scattered from the droplets in the air stream, is transferred back to the connection box. The scattered light is directed into the two detectors (one for the green and one for the blue light), photo multiplier tubes (PM), and the produced electrical signals are fed into the Burst Spectrum Analyser (BSA). The BSA converts the received electrical signals into a velocity.

3.3 Phase Doppler Anemometry (PDA)

So far the velocity is measured, but what is needed in order to be able to make a size measurement of the moving particle? The Doppler-frequency determines the velocity for the particle, but there is more information from the scattered light that can be used. For a one-dimensional velocity measurement a single detector for each colour is enough. If a second detector for each colour is added, it is found that the phase difference of the scattered light represents the diameter of a spherical moving particle. This is the basis for the PDA technique, further presented in the following section. Durst & Zaré first presented this idea and method already in 1975 [16].

3.3.1 Basics for the PDA

In Figure 3.12 a sketch of the scattering process in two detector directions is shown. The incident beams enter to the left in the figure, and it can be seen that there is a slight difference on the scattered light that enters the two detectors. This difference is a phase difference, and can be used to determine the diameter of the scattering particle.

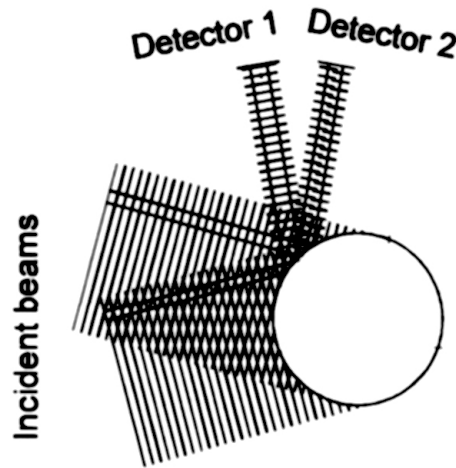


Figure 3.12: A phase difference is noted for the scattered light.

The phase difference of the Doppler bursts received at the detectors can be written mathematically as

$$\Phi_i = \pi \frac{n_1}{\lambda} D \cdot \beta_i \quad (3.13)$$

where n_1 is the refractive index of the scattering medium, λ is the wavelength of the laser light, D is the particle diameter, and β_i is a geometrical factor. β_i depends on the scattering mode (reflection, refraction, or 2nd order refraction), the angle between the laser beams, and the angles between the measure volume and the detectors. β_i for reflection and 1st order refraction is given by exact equations, but the equation for β_i for 2nd order refraction must be solved numerically. Figure 3.13 shows how the particle size affects the phase difference. An increased particle size results in an increased phase difference.

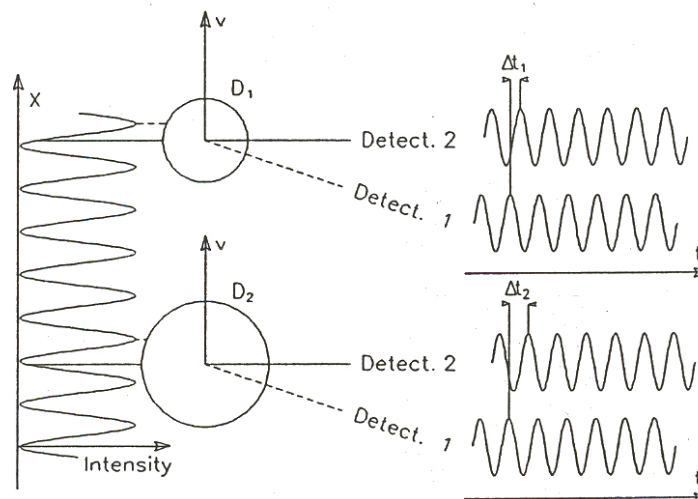


Figure 3.13: Increasing phase difference with increasing particle size. [13]

The phase difference has a linear correlation to the particle diameter, and an idealized relation is shown in Figure 3.14.

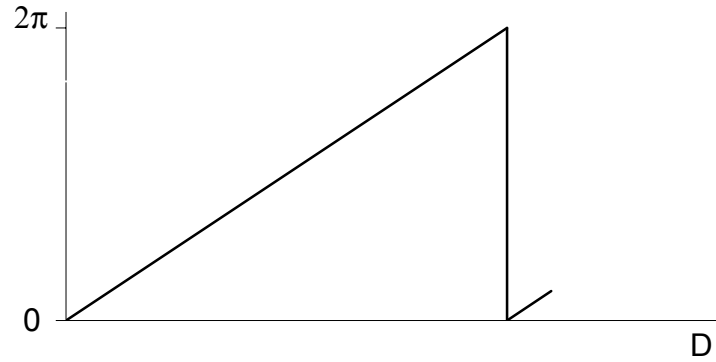


Figure 3.14: Phase-diameter relation for the PDA.

As mentioned before the measurement is dependent on the angles between the detectors and the measure volume. In fact the sensitivity and the size range are affected when the angles are altered. The angles cannot, however, be set by coincidence. The angles must strictly follow constraints set-up by the particular scattering mode, practical limits, or to keep a good signal-to-noise ratio.

The 2π -ambiguity is a new challenge to overcome. For a particular diameter one and only one phase difference should be acceptable. But different diameter can give the same phase difference, and hence a phase difference does not give a unique diameter. This is called the 2π -ambiguity, and is solved by the use of an additional detector. The three detectors forms now two pairs of phase differences, and if these two pairs are given different properties the 2π -ambiguity is solved. This is shown in Figure 3.15.

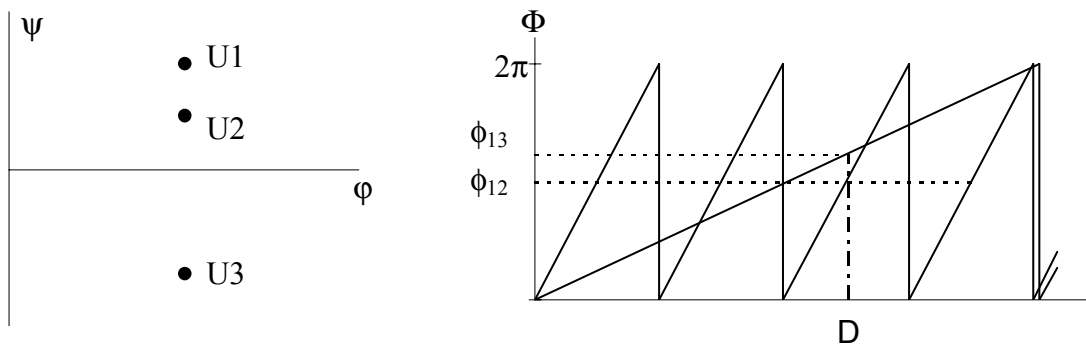


Figure 3.15: The phase difference from two sets of detectors results in one diameter.

In Figure 3.15 the phase difference between the detectors 1 and 2, ϕ_{12} , results in a relation between the measured phase difference and the diameter that is characterised by high resolution, but small range for the diameter. The other phase difference, ϕ_{13} , is characterised by a low resolution, but a wide working range for the diameter. Together these two phase differences complement each other, resulting in a measurement containing the advantages of both high resolution and wide working range. It happens sometimes that discrepancies exist between the predicted diameters from the two detector pairs. One validation criterion performed in the software is the ΔD obtained in such cases. This validation is known as deviation from sphericity. If the ΔD is larger than the defined limit, the sample is rejected.

3.3.2 Light intensity properties for a water droplet in air

The scattered light from a water droplet in air varies in intensity due to scattering angle, scattering mode, and polarization of the incoming laser beam. Figure 3.16 shows the scattering properties for a water droplet in air. The upper half of the circle gives the intensity of the perpendicular polarized light as a function of the scattering angle. The lower gives the parallel polarization. For scattering angles up to 30° , 1st order refraction dominates for both the polarizations. Which means that measurements can be performed for these scattering angles for both the polarizations. For scattering angles $>30^\circ$ the two polarizations are quite different. For perpendicular polarization the refraction gets less dominant, but for the parallel polarization refraction gets more dominant. 2nd order scattering exists for backscatter angles, approximately at $>138^\circ$, for both the polarization modes. From Figure 3.16, recommended angles of receiving optics are listed in Table 3.1. The diameter measurements were performed with parallel polarization and a scattering angel at 30° .

Table 3.1: Recommended angles of the receiving optics.

	Useful range	Polarization
Refraction	30° to 75°	Parallel
Reflection	83° to 115°	Perpendicular
2nd order refraction	144° to 149°	Parallel/Perpendicular

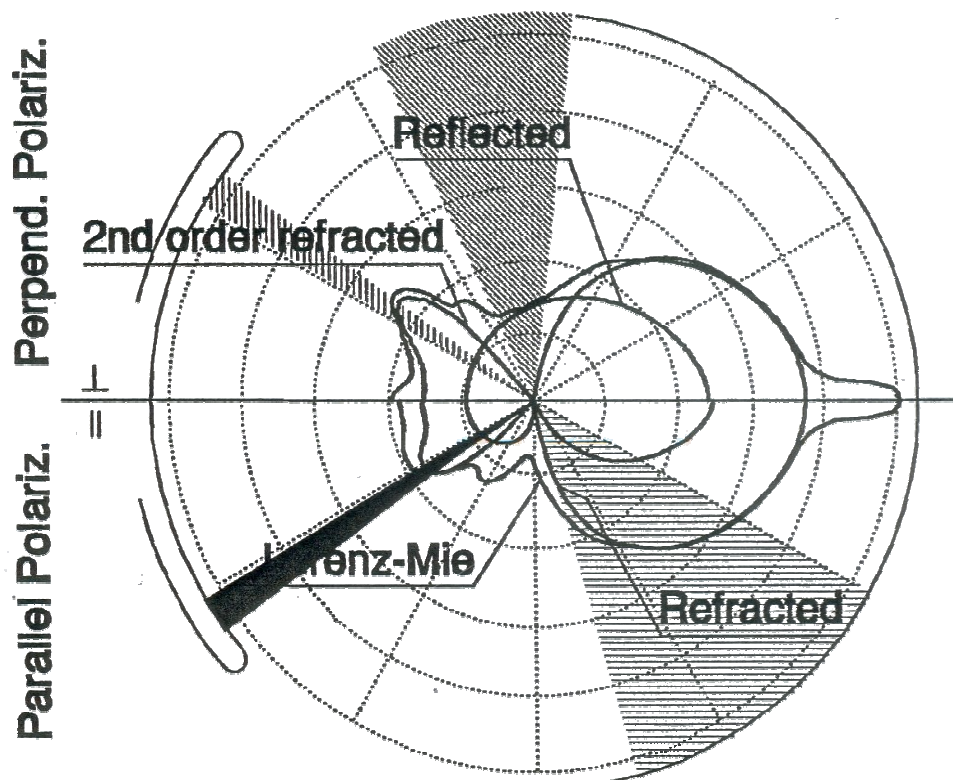


Figure 3.16: Intensity chart for a water droplet in air [13].

3.3.3 The PDA set-up for diameter measurements

It was noted in the previous section that the scattering angle was 30° . This corresponds to a forward scattering type, and Figure 3.17 shows the set-up for the diameter measurements. The laser probe is rotated, so that the incident laser light is coming from the side of the flow channel. On the opposite side of the channel the receiver are mounted. The focal length of the lens used for the receiver was 310 mm, and the lens on the laser probe is 160 mm. The generation of the laser beams are analogue with the LDA set-up, only a slight change for the laser beam on their way to the laser probe. The connection box is removed, and the receiver is included. The receiver consists of four detectors, drawn in Figure 3.18 as grey circles. In this work only 1D velocity measurements are performed simultaneously with the diameter measurements. Three detectors are then enough, but the system is capable of measuring 2D velocities along with the diameters.

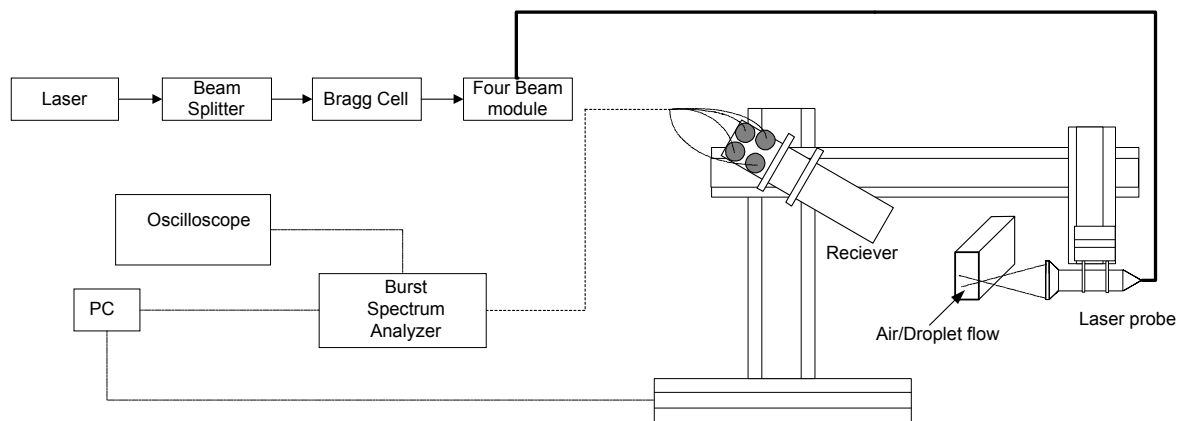


Figure 3.17: A principal sketch of the PDA set-up for the diameter measurements.

Chapter 4

Description of the experimental rig and operational conditions

This chapter contains the description of the experimental set-up and the operational conditions for the experiments carried out on the vane separator. It was noted in the introduction to the thesis, that the motivation for making measurements were many. It was necessary to perform experiments to establish a data set to verify the simulations and the new models, as well as to create a physical understanding of the underlying mechanisms. The measurements were performed on two different experimental rigs, which will be thoroughly presented in the next sections. At the end of this chapter a discussion considering different aspects of the measured profiles are carried out. But first an introduction to the experimental rigs is given.

4.1 Introduction to the experimental rigs

The need for two different set-ups of the experimental rig is to be found in the measuring technique. For the velocity measurements, a LDA technique is used. This technique requires fluid flow containing tracer particles, with good optical access to the measuring volume. The velocity field between the vanes is wanted, and hence in this case the optical access to the narrow passage between two vanes has to be ensured. For the droplet distribution studies, a different laser technique is used, PDA. The droplet size distribution on the inlet contains large droplets that are possible to remove. The single passage rig, which is used in the velocity measurements, causes the droplet size distribution to change towards smaller droplet diameters. The reason for the decreased droplet size is the presence of the walls. This effect is minimised by increasing the number of passages, and hence reduce the effect of the walls. This is the motivation for constructing a second experimental rig to ensure a stable droplet size distribution upstream the separator. The two experimental rigs are discussed in details in the following sections.

4.2 Design of rig for measurements of the velocity profiles

The experimental rig consists of several parts and each part will be briefly discussed. Figure 4.1 shows a sketch of the experimental rig. The P in Figure 4.1 indicates pressure measurements, and F indicates flow measurements. The main parts of the rig are the vane separator located far to the right in Figure 4.1. The different parts in the rig following the air/water flow are presented next. The parameters measured are pressure and flow, and the positioning of the meters is shown in Figure 4.1.

The fan

There are two sources of air, the fan and the compressed air used in the nozzle. The fan, model CK 200 from Östberg (<http://www.ostberg.com>), can deliver large amounts of air, but the pressure build-up is relatively small. The fan was used in cases where the air flow through the nozzle did not produce enough mass flow of air through the channel. A frequency regulator regulated the fan. This regulator did not work with a sufficient accuracy. This was

worked around by reducing the inlet area of the fan. This is, of course, a crude way of regulating the fan, but it was surprisingly stable and repeatable.

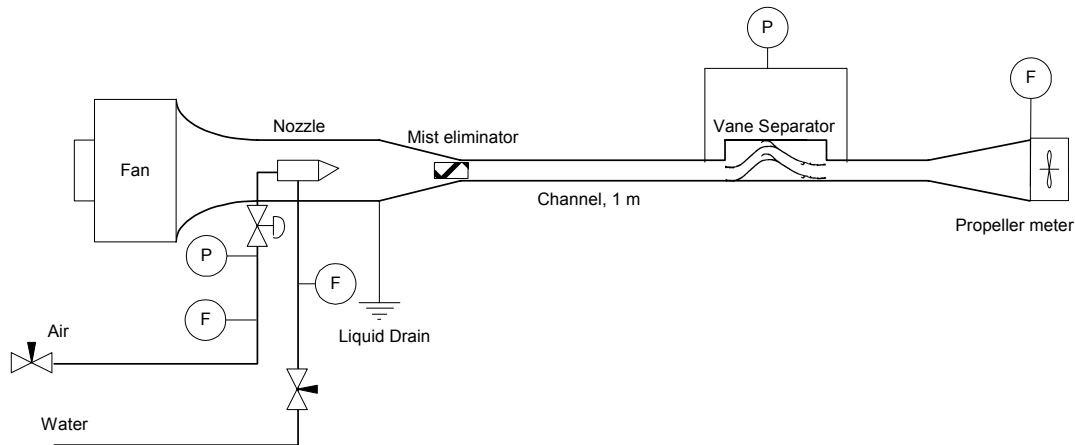


Figure 4.1: A sketch of the experimental rig for the LDA measurements (top view).

High-pressure air

Air is delivered to the nozzle by the compressed air system mounted on the campus. A regulation was placed between the manometer and the high-pressure pipe. This valve reduced the pressure in the pipe leading to the nozzle, and this valve was necessary in order to reduce pressure variations from the high-pressure system. The pressure upstream the valve was 6.7 bar, while the pressure downstream the valve was 3 bar. A second control valve was placed right after the manometer, and was used to control the airflow. The manometer on the air supply line was somewhat futile, since the airflow was altered by the fan.

Water source

The water is taken directly from the supply pipe, and a filter is used in order to prevent plugging of the fine orifices in the nozzle. A rotameter with a build-in needle valve was used to regulate the water flow to the nozzle. The regulation of the water is very important seen in light of the velocity measurements. The water amount must be sufficient to seed the airflow with enough droplets in order to get enough samples in the measurements. On the other hand, the water flow must be small enough that deposition does not occur. Deposition destroys the optical access, and makes measurements impossible. It is hence important to avoid deposition, and a slight decrease in the water flow to the nozzle stops further deposition. Typical procedure was to start with a dry channel, and slowly increase the water flow. At first sight of deposition the water flow was decreased slightly, and operational conditions for the velocity measurements are achieved.

Nozzle

An ultrasonic nozzle from PNR (<http://www.pnr-nozzles.com>) is selected. The MAD 0331 is chosen, and adapter type A is found most relevant. According to the vendor this will produce a narrow spectre of droplets at given flow conditions. At the operational conditions used in the measurements, the droplet distribution showed a Sauter mean of 60-70 μm . The nozzle was mounted in a 100 mm aluminium pipe, and a flexible hose guided the flow over to the rectangular channel. At the end of the hose, right before the channel starts, a liquid drain is placed. This liquid drain is placed right before the mist eliminator.

Mist eliminator

The mist eliminator is important in the velocity measurements. The objective of the mist eliminator is to remove nearly all the big droplets, and hence most of the water. The mist eliminator chosen is a mesh type. This type has a large pressure drop, but is highly effective. This is of importance, because the aim is to seed the airflow with few small droplets. Droplets, particles or other fragments are needed in a flow, to scatter light that makes it possible to use the laser. A perfectly clean flow, would not give any scatter of the laser light, and hence no measurements. By the use of an effective mesh eliminator inside the hose, an air stream seeded with small droplets was achieved. A PDA analysis performed on the droplet distribution generated with the mesh eliminator showed a Sauter mean diameter of 7 μm . Observations from the experiments state that little or no activity was noted on the vanes during the velocity measurements. This observation supports a view that the droplets are so small that they can be assumed to follow the air stream almost perfectly.

The channel

The channel, which leads to the separator, is made of plexiglas. This channel is 1 m long, in order to achieve fully developed flow. Ideal airflow will have a hydrodynamic entry length of about 0.3 m, so it can be safely assumed that a fully developed flow is achieved. The channel is 25 mm wide and 108 mm high, and the plexiglas used in the walls, roof and floor is 6 mm thick. For the velocity measurements, no deposition is noted on the channel walls.

The separator unit

The vanes are inserted directly into the channel, and are sealed, so the Plexi glass forms a box around the vanes. The vanes are placed vertically and touch both the roof and the floor, and all gaps are sealed so no leakage occurs. Details of the vane geometry are listed in Appendix 3 – A3 Details from the experimental set-up. The height of the vanes was 108 mm, and the measurement is performed in the middle of the separator, that is 50 mm from the top. Only a single passage is mounted in the channel. A pressure manometer measures the static pressure over the separator. The static taps were localized 50 mm before and after the vanes.

The outlet

An extension of the channel forms the outlet. This leads to a flexible hose, and the propeller meter is mounted in the flexible hose. The outlet is vented directly to the atmosphere, and to a drain for the separated water. The propeller meter, an AV6 100 mm Hd. from Airflow Developments Limited (<http://www.airflow.co.uk>), placed at the outlet of the rig measures the mass flow of air through the channel.

4.3 Design of the rig for measurements of droplet distributions

If a droplet size measurement is carried out on the rig presented in the previous section, except that the mist eliminator right after the nozzle is removed, it shows that the droplet size distribution is altered as it flows through the channel. The presence of the walls, and the high water load, leads to some deposition of water along the channel walls. The result is that the droplet size distribution reaching the separator has a Sauter mean diameter around 20 μm . This droplet size distribution is not well suited to determine the efficiency of the separator. A droplet size distribution entering the separator with a higher Sauter mean diameter is more suitable, in order to achieve information about efficiency and re-entrainment. Hence, some modifications to the velocity measurement rig are made. Figure 4.2 shows a sketch of the rig used for the droplet size distribution. The only modification is that the channel is made wider,

and the number of vanes inside the separator is increased to four. The number of passages has, consequently, increased to three. This modification makes the flow less influenced by the walls, and the deposition rate is reduced. A positive side effect is that the PDA measurements are easier to carry out. The decreased deposition rate causes less disruption of the optical access, and a simple wiping technique is used when the depositions ruins the optical access. In the flowing film in the bottom of the channel, a thin piece of metal is placed. This metal piece is used together with a magnet to wipe away any deposition when needed. During measurements, typical two or three wiping was needed before the separator, but no wiping was needed after the separator.

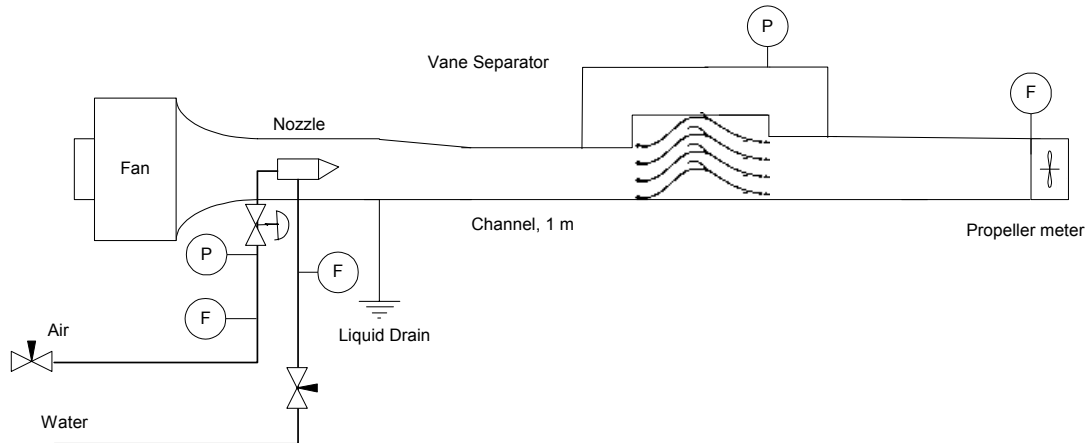


Figure 4.2: A sketch showing the experimental set up for the PDA measurements (top view).

Figure 4.3 shows a photo taken of the rig and the laser equipment while carrying out diameter measurements. The laser set-up described in the previous chapter can easily be spotted. The angle between the transmitting and receiving optics is 30° . The receiving optic is to the right and the transmitting laser probe to the left. The droplet-laden air can be seen leaving the channel.



Figure 4.3: A photo of the rig and the laser equipment.

4.4 Sources of error

It is natural to discuss the different sources of error in the experimental set-up. The sources of errors are divided into appropriate sub-sections.

4.4.1 Physical error related to the rig

One of the largest sources of error arises from the physical design of the rig. Small deviations in the vanes, in the channel width and in the box surrounding the vanes cause discrepancies, which is not included in the computational model. These small deviations can lead to a cross-section, which theoretically should have width of 21 mm, is measured to have a width of 20 mm. For most of the measured profiles, the discrepancy was relatively small, and hence no correction is performed. In position $x = 165$ mm, it was found necessary to modify the predicted profile from the CFD code, in order to obtain the same width of the profile. By using the physical width and the theoretical width, a relative error of 4 % is found in this location.

4.4.2 The alignment of the laser

Another important source of error can be the alignment of the laser probe. The alignment was first performed by the aid of rulers, and then a check of the measured y-velocity was done in the channel where fully developed flow exists. The y-velocity was found to be low, less than 1% of the x-velocity, and the alignment were assumed correct.

4.4.3 Accuracy of the measurements

The laser techniques used in this work are known to be accurate and reliable. In the documentation to the laser equipment [13] the expected accuracy is claimed to be ± 0.5 % for the velocity measurements. That is for a very well aligned and tuned system, and is often hard to achieve. The statistical determination of the appropriate number of samples in each measurement ensures a stable value. To estimate the new accuracy level due to deviations in the system set-up is a difficult task. The propeller meter has a reported accuracy of 1 %, and the author's impression is that the accuracy of the laser measurement is better than the propeller meter.

For the droplet diameter measurements the same accuracy as given for the velocity measurements is expected [13]. The droplet diameter measurements are difficult, and lots of tuning of parameters is needed to ensure a good measurement. It is hence necessary to assume that the accuracy for the current measurement is slightly worse. For the droplet diameter measurement it is even more difficult to estimate the systems overall accuracy. It is assumed safe to estimate the accuracy to be better than ± 10 %.

4.5 Operational conditions

The normal inlet velocity for the vanes is given by the vendor to be between 2 m/s and 6 m/s. The mass flow in the three experimental series is chosen to be in that area. In Table 4.1 the operational conditions for the three different series are given. ΔP is the static pressure drop over the vane.

Table 4.1: The operational conditions for the different experimental series.

	ΔP [Pa]	Inlet velocity [m/s]
Low mass flow	18	2.46
Middle mass flow	40	3.54
High mass flow	60	4.54

The inlet velocity in Table 4.1 is the mean integrated velocity obtained from the inlet measurement of the fully developed channel flow. The inlet velocity profile is integrated numerically by the use of the trapezoid method, and the mean velocity is obtained. The mean velocity from the propeller meter deviates from the integrated velocity. The deviation was from 4 % to 10 %, which is within the accuracy limit of a propeller. The laser measurement is used as the inlet condition in the CFD simulations. The used inlet velocity then produced a good match between the inlet condition and the measurements. The deviation for the propeller meter comes most likely from the traces of water, which increase the momentum of the flow. The deviation is greatest in the high water load experiments and droplet size studies, which supports this theory.

Table 4.2 shows the conditions for the nozzle for all the experiments of the three mass flows. The column ‘Inlet velocity’ is the integrated mean velocity for each mass flow rate. In short, the only difference between the velocity and the droplet size distribution measurements is the water flow. For the velocity measurements the water flows are minimal, while for the droplet size distribution measurements the water flow is 0.4 l/min.

Table 4.2: The operational conditions for the nozzle.

Mass flow rate	Set-up	Water flow [l/min]	Air pressure [bar]	Fan	Inlet velocity [m/s]
Low	LDA	Low	3	Off	2.46
	PDA	0.4	3	Off	2.46
Medium	LDA	Low	3	On, 10 %	3.54
	PDA	0.4	3	On, 10 %	3.54
High	LDA	Low	3	On, 30 %	4.54
	PDA	0.4	3	On, 30 %	4.54

For the velocity measurements, the mist eliminator was present and separated out most of the water. The drainage right before the mist eliminator was used to drain the separated water. For the droplet size distribution measurements, the mist eliminator was removed. This resulted in some deposition and film generation on the walls of the channel. Some of the water was already in the film when then water reached the vane separator. A liquid film was formed on the bottom of the channel, and moved through the separator.

4.6 Description of the measurements

Velocity measurements were carried out in 7 different positions in the separator, and droplet size measurements were performed before and after the separator. Different problems were met in the measurements, and this section discusses the problems and solutions. It is found necessary to divide this section into two parts. One section covering the velocity measurements and one section covering the droplet size distribution measurements. Each of these sections will describe the experimental process in order to make appropriate measurements.

4.6.1 Velocity measurements

To obtain a complete velocity profile in one position several measurements are performed. Due to problems when entering the laser beams into the separator, three series are measured at each position. The problems of entering the laser beams origin from the curvature of the vanes. In Figure 4.4, this is visualised. The sketch to the left in Figure 4.4 shows the channel seen from above. The sketch shows that for the near wall measurement, one of the beams is hindered by the presence of the vane. The measurements are not possible in such cases. By giving the laser light a slight incident angel, α , this problem is solved. This is shown to the right in Figure 4.4, which shows the laser beam track through the top plane of the passage between the vanes. The refraction of the beam pair drawn in Figure 4.4 is not destroying the measurement, but causes only a displacement offset of the x-velocity measure volume. For the other pair, the y-velocity, the refraction of the laser pair is different, hence a good measurement is not possible, and only the x-direction is measured near the walls.

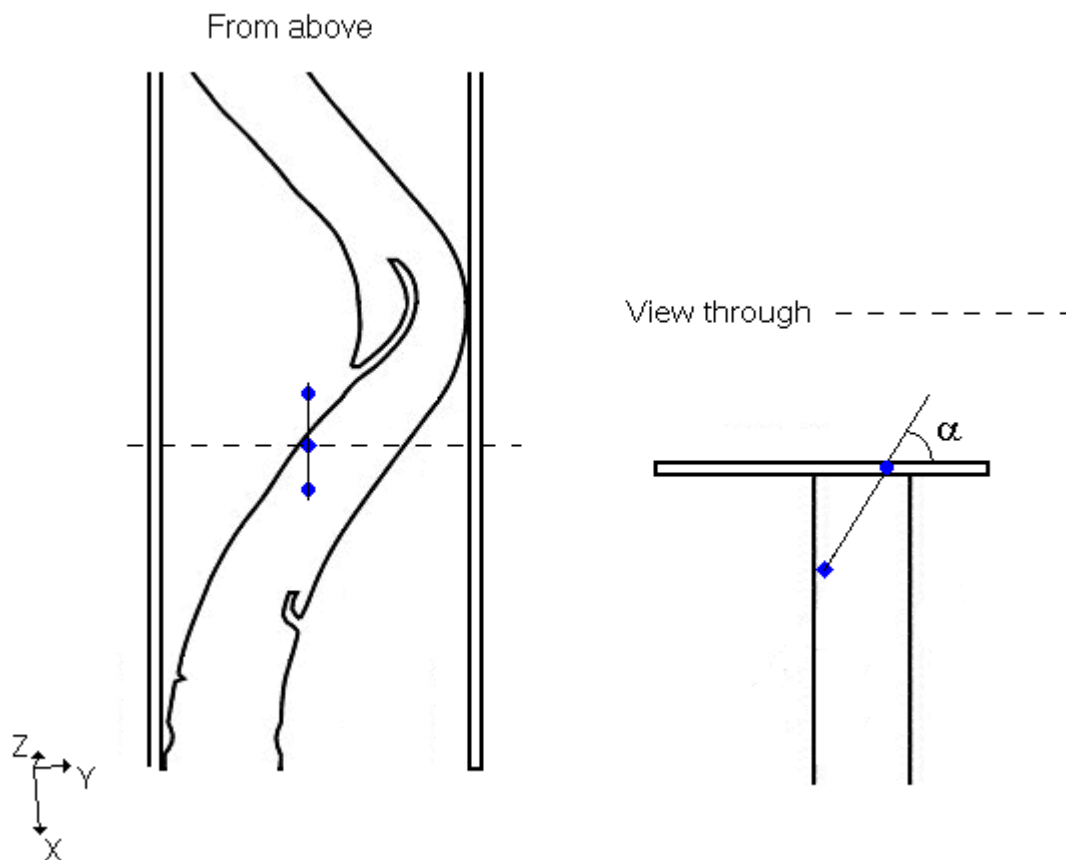


Figure 4.4: Sketch over the entering problems near the walls.

Two of the three series measured at every x-location, origin from each of the walls. The third series is measured in the middle of the channel, and differs slightly from the two others. The laser light for the third series enters the channel normal through the plexiglas top, and a 2D velocity measurement is carried out in the middle of the channel. Only x-velocities are measured near the walls. Figure 4.5 shows the three series in the channel. It is noted that the profiles are taken on the same position, and the difference in x-position of the different profiles is merely there for the visualisation.

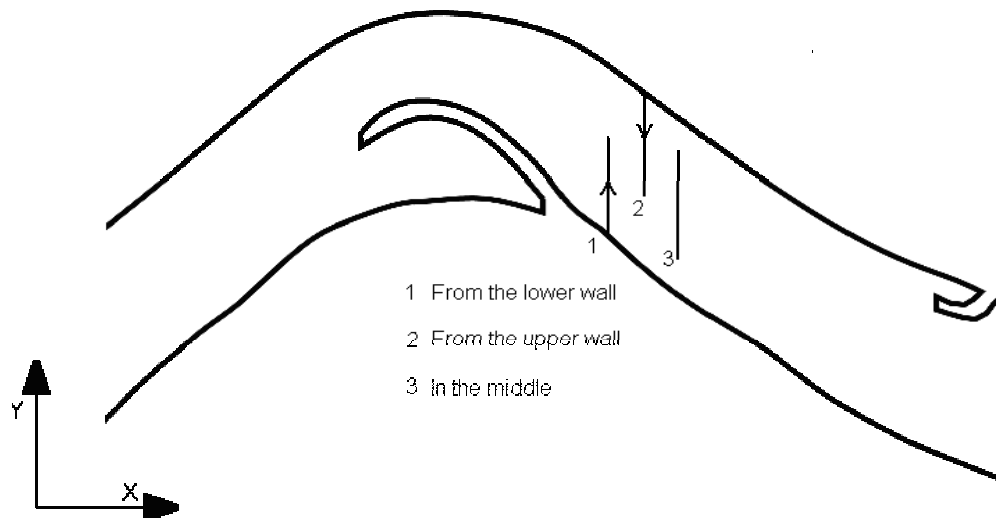


Figure 4.5: The three series measured at each position.

The profiles are measured in seven different positions in the separator. All these positions are shown in Figure 4.6.

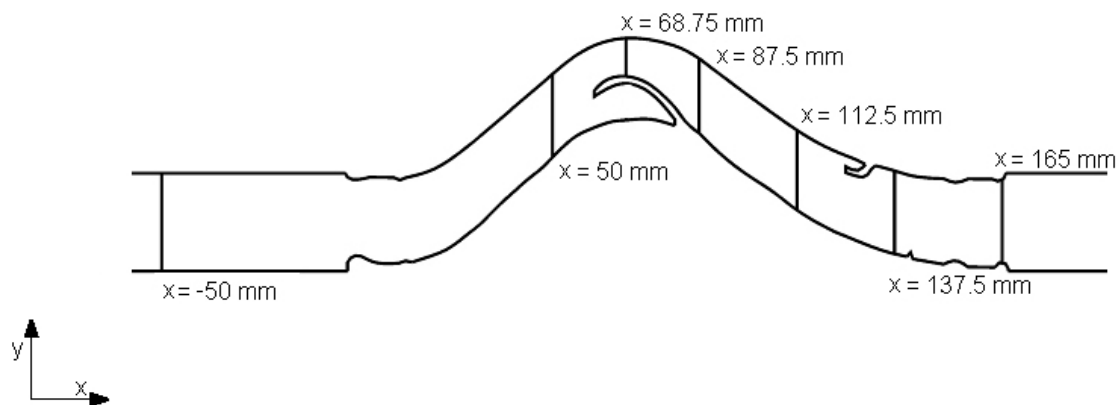


Figure 4.6: The positions of the profiles for the velocity measurements.

All the measurements are carried out far away from the top of the channel, and hence effects from the roof can be neglected. A check for this is performed, and Figure 4.7 shows the variations in the x-velocity in position $x = -50 \text{ mm}$ for the high mass flow case. In Figure 4.7, the abscissa denotes the traversed length from the top wall in z-direction (direction normal to the plane shown in Figure 4.6). It is seen that the effects from the top of the channel are negligible due to constant x-velocities in the level where the measurements were carried out. The wall effects from the roof extend only a couple of millimetres into the flow area.

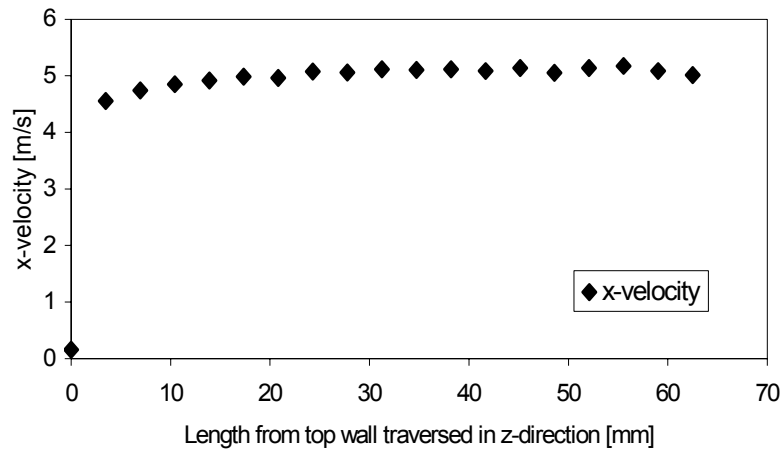


Figure 4.7: The x-velocity profile in the z-direction for the high mass flow rate.

Variations in the histograms of the velocity measurements are dependent on the current position in the vane. If the flow is straight forward, such as at the inlet position $x = -50$ mm, the histograms are very narrow, and the peaks are high. The thin grey line in Figure 4.8 represents a typical histogram for the inlet velocity. The fluctuations in velocity are small. In addition, three different positions for $x = 137.5$ mm for the middle mass flow case are added to Figure 4.8. The histograms for the positions located at $y = 9$ mm and $y = 19$ mm are relatively narrow, and the fluctuations in the velocity are small. For the point located at $y = 15$ mm the fluctuations are bigger, and this leads to a wide peak for the histogram. The level of turbulence is a function of fluctuations in the velocity, and hence the turbulence in this position is high.

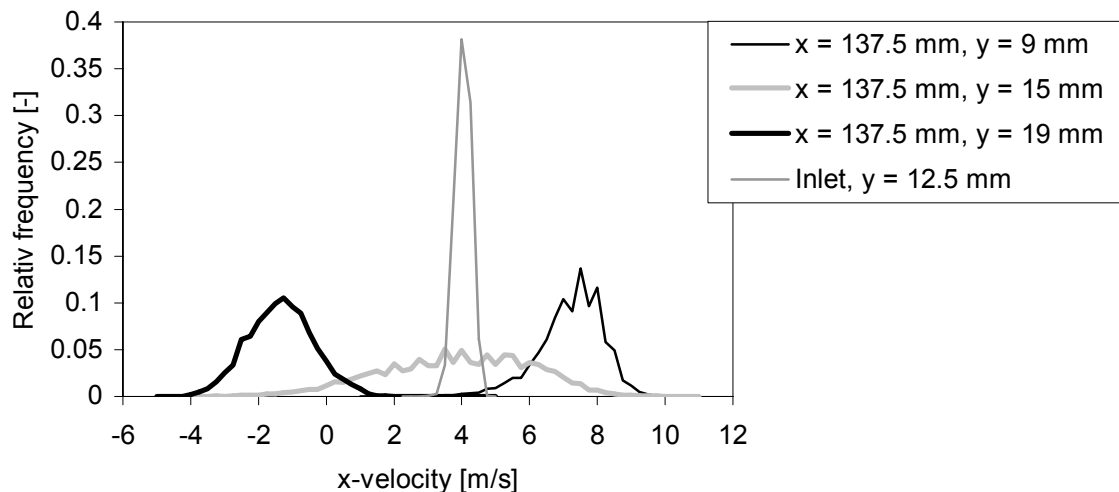


Figure 4.8: Different histograms of velocity measurements for the middle mass flow case.

The number of samples required to achieve a good representative measurement is determined from experience. The mean velocity is noted after 5000 samples, and then the measurement continues. After 10 000 samples the mean velocity is noted again, and these two measurements are compared. If these velocities differ, further samples are needed. Hardly any difference was noted between the two measurements at 5000 and 10 000 samples in any part

of the separator. However, due to possible long-term fluctuations, a safety margin was added, so the number of samples used on each position is 25 000. The total time of measurement on each position was set to 200 s, and on some of the near wall positions, the time stopped the measurements.

4.6.2 Droplet distribution measurements

Droplet distribution was measured at two positions. The positions are 50 mm upstream and downstream of the vane separator. Problems with the film, and problems with entering the laser contributes to the fact that the measurements are not carried out inside the vane separator. Although some deposition and film are generated on the walls, and influence the laser beams entering the flow, measurements are obtained. The selected positions are marked in Figure 4.9.

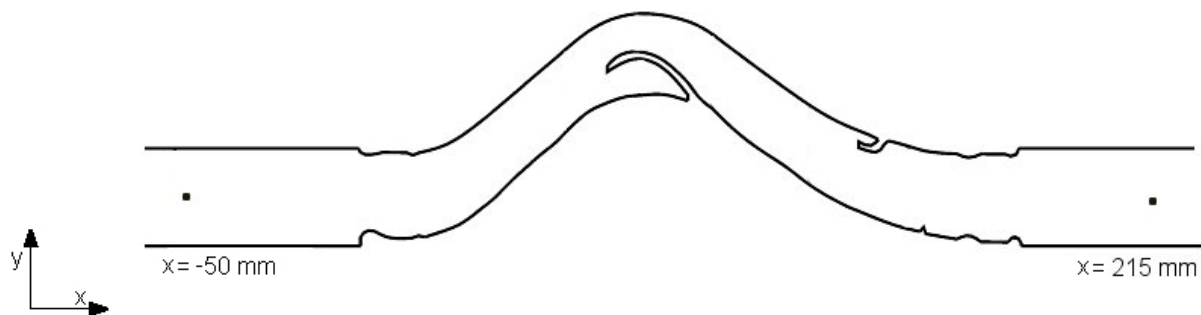


Figure 4.9: The black dots show the position of the PDA analysis.

To test the quality of the PDA measurements, the phase plot is used. In Figure 4.10, a typical phase plot is shown. The solid line gives the ideal correlation between the two phase differences, in Figure 4.10 given as P1-2 and P1-3. Each sample is given by a dot. The dashed lines indicate the validation criterion. For a measurement to be validated and accepted, the measurement must lie within the two dashed lines. This phase plot shows that most of the measurements are within the selected validation criterion. The number of samples needed is determined by experience. The number of samples used for the diameter are approximately 10 000.

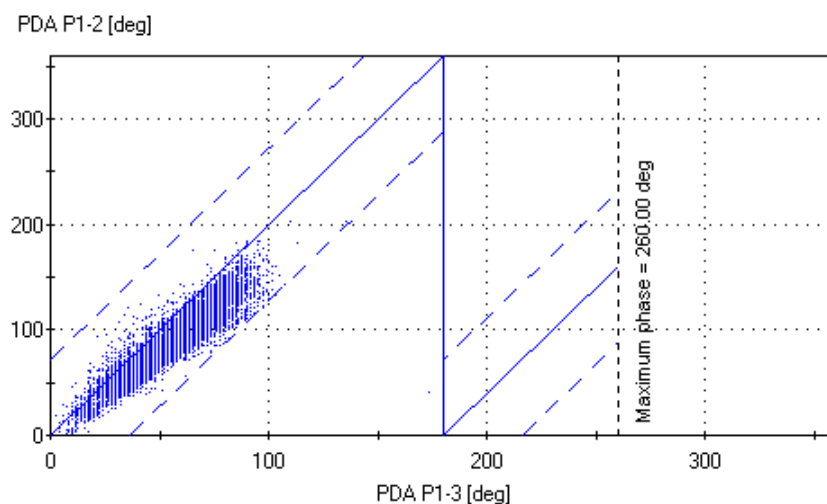


Figure 4.10: Typical phase plot from the PDA measurements.

Chapter 5

Experimental results

The results from the measurements performed on the two experimental rigs are presented in this chapter. Three different mass flow rates are used in the measurements, and the measurements are divided on the basis of the mass flow rate. The different mass flow rates are called small, medium and high mass flow rate. Each mass flow rate consists of complete profiles in several positions in the separator, and droplet size measurements. The profiles presented are the velocity in x-direction (x-velocity), the velocity in y-direction (y-velocity), the x directed rms velocity (x-rms velocity) and the y directed rms velocity (y-rms velocity). The droplet size measurement is a measurement of the droplet size distribution before and after the separator. In addition, some observations are presented in this chapter, and these are organised and presented in a separate section. The structure of the chapter is such that the observation section is next to follow, and then the experimental results from the different mass flow rates are presented.

5.1 Observations and comments to the measurements

This section contains some information that is not directly useable in the comparison to the CFD predictions. The reason for including this information is that it increases the general knowledge of the vane separator. This information concerns with a flow phenomena, which is discovered on the rig for measurements of the droplet distribution, and an experiment that is carried out to investigate the possibility of film re-entrainment in the vane separator.

5.1.1 Unstable flow inside the separator

If velocity profiles were measured on the rig for measurements of the droplet distribution, an unstable flow was measured. Figure 5.1 shows the measured x-velocity in a fixed point at the $x = 165$ mm position. $X = 165$ mm is located at the end of the separator. Figure 5.1 shows that the velocity is varying in time. The minimum velocity was measured to be around 2 m/s while the maximum was at 5 m/s. Each of these mean sample numbers represent a mean of the samples gathered for a time of 60 seconds (approximately 4000 individual samples). The fluctuations in x-velocity are slow, and in order to obtain a useful mean value, the time scale for this point is large. The total time for the measurement performed in Figure 5.1 is 45 minutes. The time scale for the fluctuations suggests a long measuring time needed to ensure a good mean value. The unstable flow can arise from pressure variations or unstable phenomena caused by the increased number of vanes. For the velocity measure rig, the vanes are mounted directly in connection with the channel walls, and hence the low pressure behind the little hook is bounded to the channel. For the efficiency measurement rig, this is valid for only two of the four vanes. For the two vanes mounted in the middle of the channel the case is different. The low-pressure region, in which some backflow are noted, causes suction of air from other regions, and hence the unstable conditions may appear. The unstable conditions lead to fluctuations in the velocity. This instability is noted in several places in the separator, but not in the first part of the separator. For the velocity measurement rig, with the single passage, this phenomenon was not present. Thus it can be concluded that the air flow from the fan and nozzle is stable, and cannot explain the instability.

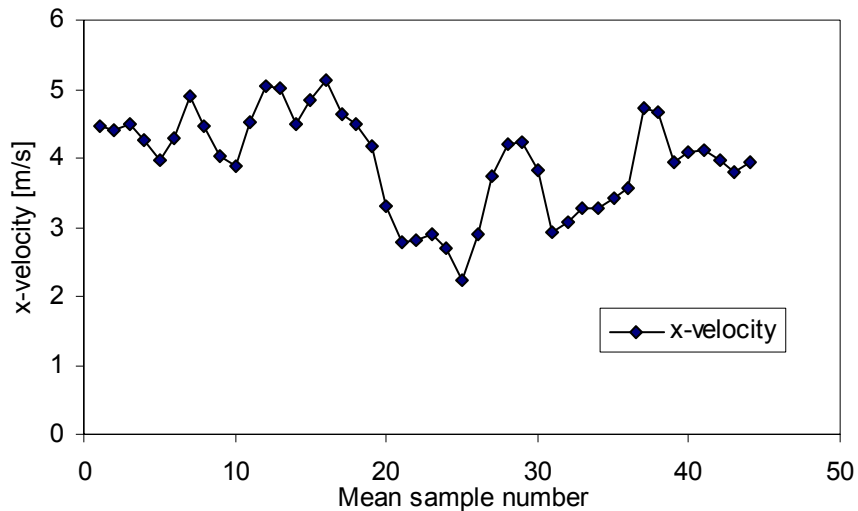


Figure 5.1: Fluctuations in the x-velocity at $y = 18$ mm in the $x = 165$ mm position for the droplet distribution rig.

The fluctuation of the x-velocity noted in Figure 5.1 is for a fixed point in the cross-section at $x = 165$ mm. A full profile for this position is presented in Figure 5.2 for four different parallels. The parallels are identical, and show that the x-velocity is varying all over the cross-section. Some discrepancy is noted between the parallels, and this implies that the flow might have a transient behaviour in this position.

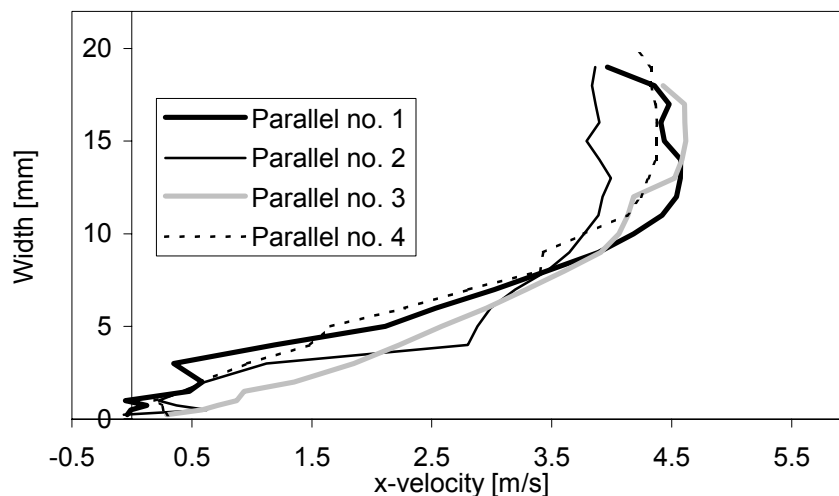


Figure 5.2: The x-velocity in several different parallels for $x = 165$ mm for the droplet distribution rig.

The conclusion from this observation is that the rig for measurements of the droplet distribution is not useable for velocity measurements. The time needed to obtain stable and repeatable measurement is considerable longer than acceptable. In addition, a design improvement can be suggested from the shown phenomena. In order to ensure more stable conditions all through the separator, one might increase the length of the vanes at the end.

5.1.2 The unstable flow affects the size distribution

The droplet size distribution leaving the separator is affected by the unstable flow. This can be easily visualised. In Figure 5.3 all the samples for the medium mass flow rate are drawn in a

scattering diagram, using the sample number for the x-axis, and the diameter on the y-axis. The variation in the droplet diameter is quite easy to see. The minimum droplet size is close to $1\text{ }\mu\text{m}$. For certain sample numbers, for example approximately 2100 and 8000, the minimum droplet size is considerably bigger. The reason for the shift in the droplet size must be found in the fluctuating nature of the flow. Different flow properties produce different droplet sizes, and hence this finding is not surprising. However, it is quite interesting that the difference in the generated droplet inside the separator varies so much in size.

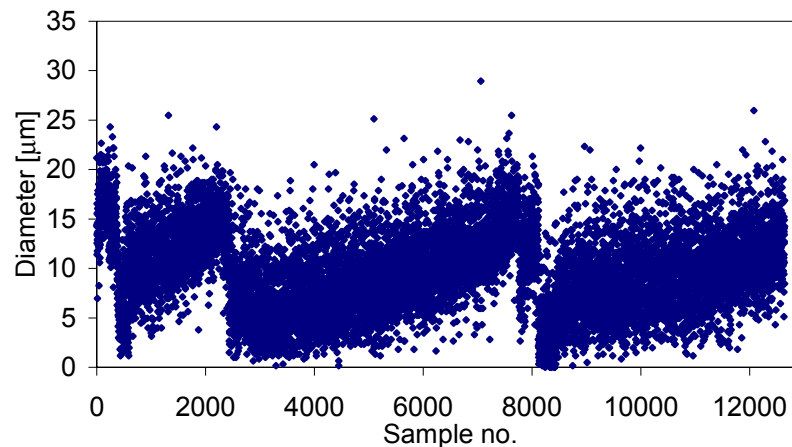


Figure 5.3: Sample number plotted against the droplet diameter.

5.1.3 Description of the film behaviour inside the separator

During the experiments the film generated at the vanes was non-continuous and dynamic. A droplet that is big enough to be separated will collide with the wall. The droplet will deposit on the wall, or coalesce with any pre-existing fluid. For the case of a droplet hitting the dry wall, the droplet may splash on its own. For the case of a droplet hitting a wall where there exists some water, the droplet may induce splashing of the pre-existing water. A secondary effect is that the new droplet add so much fluid to the pre-existing fluid that the gravitational forces overcome the adhesive forces, and the water will start to flow downward the vane. This is called drainage, and leaves an almost dry surface behind its track. The pre-existing fluid has the shape of a half droplet. A crude analysis was carried out to find the maximum radius of the half droplet before drainage started. A slide calliper was used to measure the maximum radius, and it was found to be about 1 mm . During operational conditions several drainage rivers existed, varying in position and drainage velocity. The drainage occurred not straight down, but was affected by the passing gas causing the drainage to be skew. The number of drainage streams decreased along the flow direction in the separator. This non-continuous and dynamic nature of the film makes it difficult to obtain a mean film thickness.

The Figure 5.4 shows the different states a droplet patch can have in these experiments. Figure 5.4 a) shows the state before the drainage starts. The droplets grow by the addition of new fluid from incoming droplets. When the droplet reaches a critical size, it starts to drain. On its way, the drainage river may coalesce with other droplets, increasing in size, and accelerates. After the drainage, the track is almost dry, but some small droplets are noted in the drainage track. This is visualised in Figure 5.4 b). No continuous film was observed, even though the activity on the first curve on the vane was high. The only continuous film that was noted appeared at the bottom of the channel.

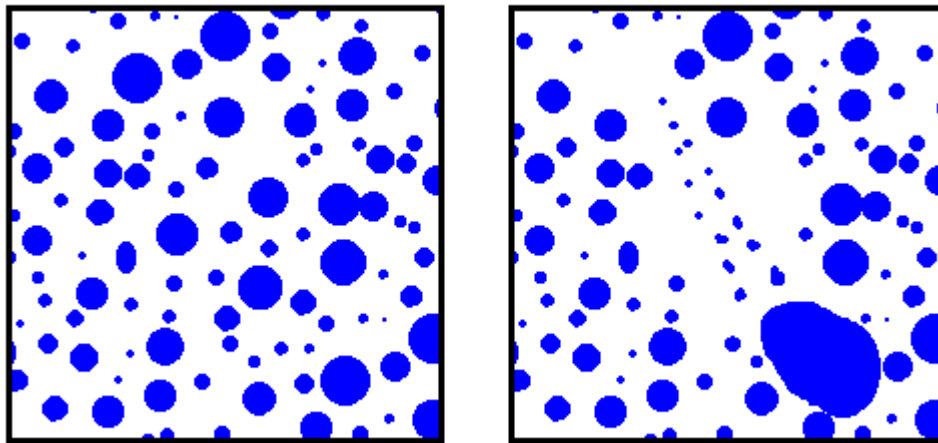


Figure 5.4: a) stable droplets at the vanes (left), and b) after drainage has started (right).

5.1.4 Water injection trials

In Chapter 7, the re-entrainment from already deposited water is studied. In order to identify the mechanisms that explain the droplet generation within the separator, a close look at the re-entrainment from the film is made. In this section, an experiment has been carried to investigate the possibility of film re-entrainment in the separator. The velocity measurement rig is used, and some small injection slots are made. The slots are orientated parallel to the vane and through the top of the channel. The Figure 5.5 shows the positions of the injection slots.

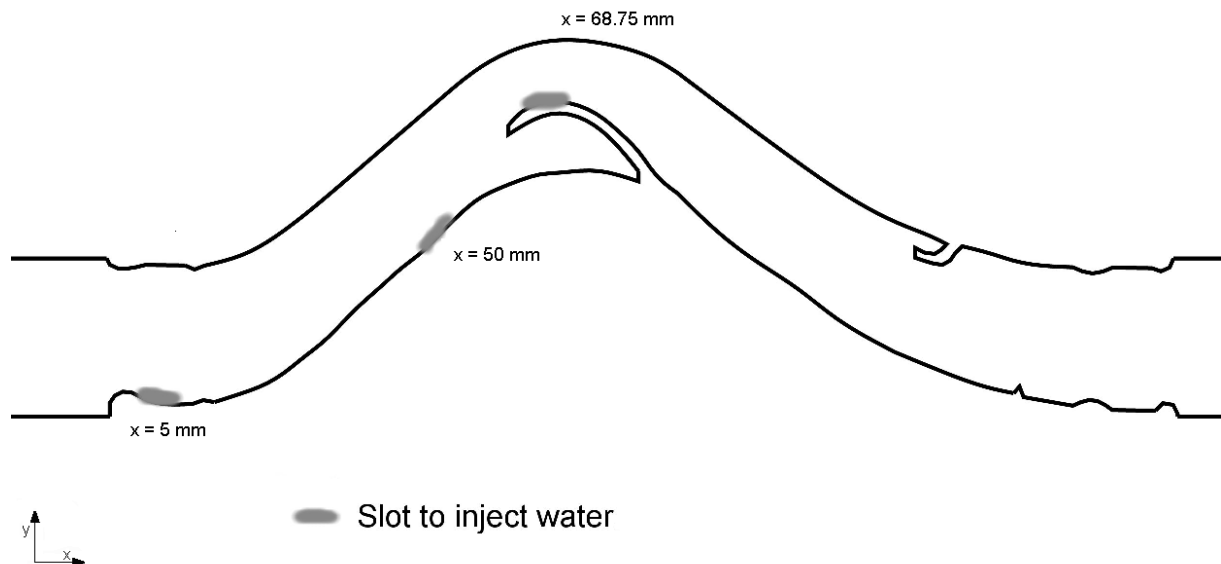


Figure 5.5: The injection slots used to inject water to the vanes.

A 5 mm hose was fitted exactly in these slots, and water was injected from a water reservoir. A water flow of about 1 l/min was injected. The fan was used as the air supply. The three

injections were located at $x = 5$ mm, $x = 50$ mm and at $x = 68.75$ mm. The observations will be discussed in order of the slots since the properties varied for each position.

Slot at $x = 5$ mm

At this position, no re-entrainment was observed at normal mass flow rates. If the mass flow rate was increased beyond the vendor guidelines, inlet velocity > 6 m/s, then certain re-entrainment was observed. Especially, this appeared near the interface between the film at the bottom of the rig and the vane. Atomisation from the falling film was not observed.

Slot at $x = 50$ mm

At $x = 50$ mm the observations were analogue with the observations from the slot at $x=5$ mm. No re-entrainment was noted from the falling film, but some re-entrainment can be noted from the film at the bottom of the separator. Lots of re-entrainment was noted if the water injected detaches the vanes, and enters in the middle of the cross-section. The detached water flow hits the hook, and lots of re-entrainment is noted. Relatively large droplets, approximately 1 mm, but also 'mist' like droplets, down to micron size diameters, are observed.

Slot at $x = 68.75$ mm

At this position, small changes in the water flow injection lead to large influence of the re-entrainment process. If the water was injected as a falling film downwards the vanes, some re-entrainment was noted. This re-entrainment was small in amount and size. If the water injected detached the vane, lots of re-entrainment was noted. The water stream was highly destroyed by the flowing air, and nearly the entire water stream was re-entered. The sizes of the re-entered droplets were large, approximately in mm size. Lots of action, deposition and drainage were noted on the plexiglas walls immediately after the separator. Some droplets left the separator, and could be collected at the outlet. However, these droplets were bigger than the droplets found during normal operational conditions.

The conclusions from these experiments are that the re-entrainment from the film attached to the vanes is almost negligible. The re-entrainment from the film occurred only at the top of the big hook, but during normal operational conditions there are not continuous film in this position. The re-entrainment is quite different when the water is injected in the middle of the passage. The water that enters in the middle of the channel breaks up, and the droplets leaving the separator are bigger than at normal operational conditions.

5.2 The low mass flow rate case

This section presents the measurements from the low mass flow rate. The Table 5.1 shows a brief overview over the operational conditions for this mass flow rate.

Table 5.1: Properties for the low mass flow rate measurements.

Pressure drop	18 Pa
Inlet velocity	2.46 m/s

The operational conditions were stable, even though minor deviations exist. These deviations were typical, for the propeller meter, in the range ± 0.02 m/s. Lots of readings over several minutes give the mean value for the propeller. In addition, the propeller meter was checked during the measurement of the current velocity profile, and if the deviation was larger than

0.05 m/s, adjustment was carried out. The profiles measured for this mass flow are marked in Figure 5.6.

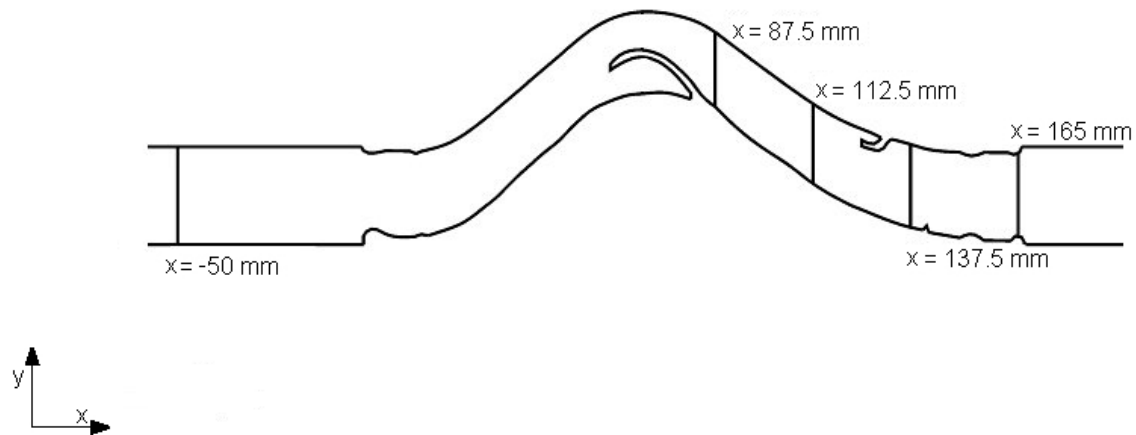


Figure 5.6: The different positions measured for the low mass flow.

The velocity profiles are presented in Figures 5.7 and 5.8, and each of these velocity profiles are composed of three parallels. The three parallels that each profile is composed from are discussed in Section 4.6. Generally it is impossible to distinguish the 3 different measurements in the velocity profiles, and hence this implies that the measurements have a high quality. The profiles are presented from the start of the separator and towards the end of the separator.

The first profile presented is the fully developed velocity profile measured 50 mm upstream the vanes, $x = -50$ mm. The velocity is well represented and stable measurements are obtained. The profile is relatively flat and implies a turbulent flow. The Reynolds number based on the hydraulic diameter is 6600 for this mass flow rate. This velocity profile is the basis for the mean velocity used in the simulations for this mass flow rate. The trapezoid rule is used for integrating this profile, and gives a mean velocity of 2.46 m/s. The integrated mean velocity is added to the figure, and represented by the dashed line.

The next profile shows the velocities at $x = 87.5$ mm, and the resirculating zone behind the large hook are shown. The x-velocities show some minor scattering at the maximum velocity. This is probably caused by minor fluctuations in the velocity field. The next profile is the velocity profile at $x = 112.5$ mm. The most interesting fact with this profile is that the shape of both the x- and y-velocity are the same, only the magnitude is different. In Figure 5.8 the first profile is the velocities at $x = 137.5$ mm. A wide resirculating zone is noted on the upper wall. This corresponds to a region behind the small hook. The y-velocity shows again a similar shape as the x-velocity, though a difference in the magnitude exists. For the outlet, $x = 165$ mm, a narrow area with negative x-velocities are noted near the upper wall. The resirculating zone present in position $x = 137.5$ mm is stretching into this position. The measured y-velocities are small in this position, and this is expected as the flow is close to straightened again.

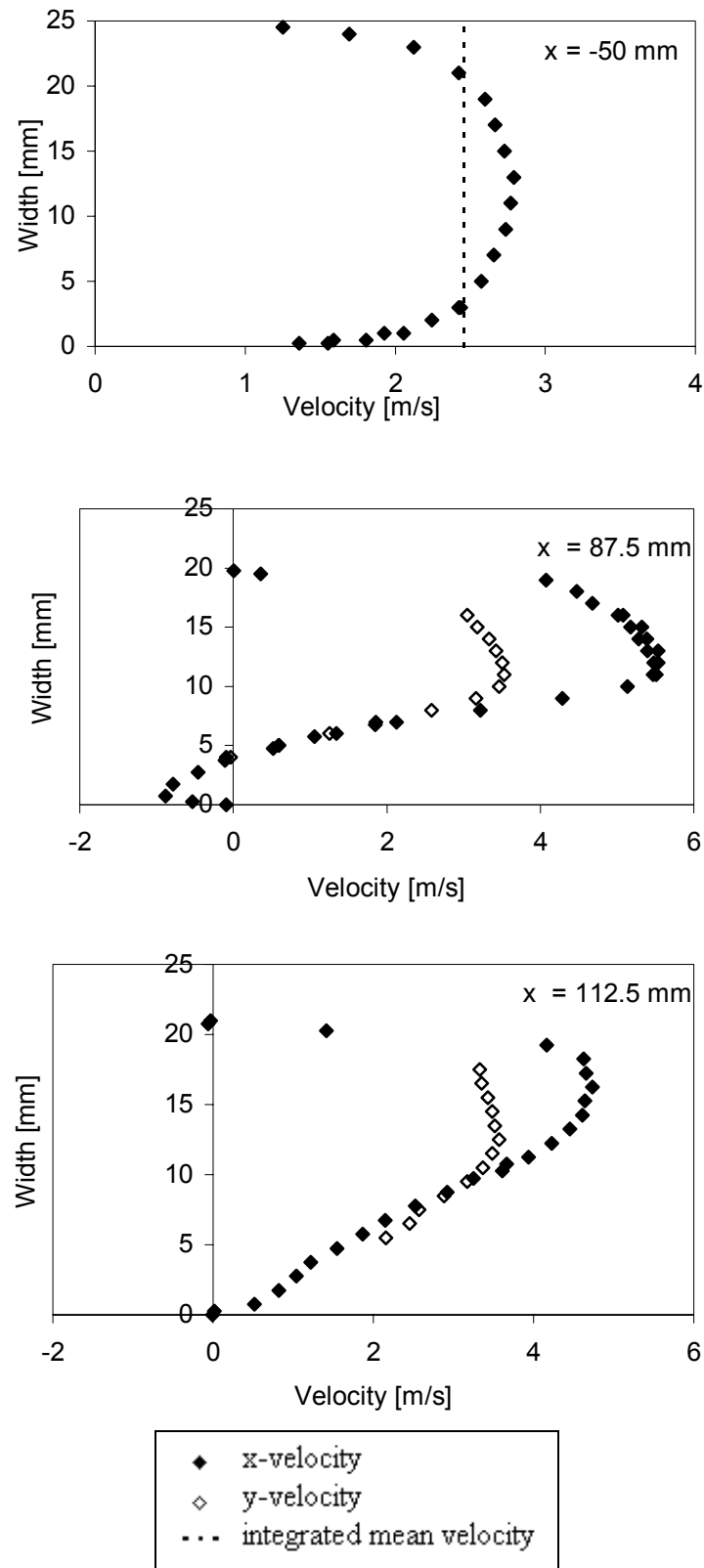


Figure 5.7: Measured velocity profiles at different positions for the low mass flow rate.

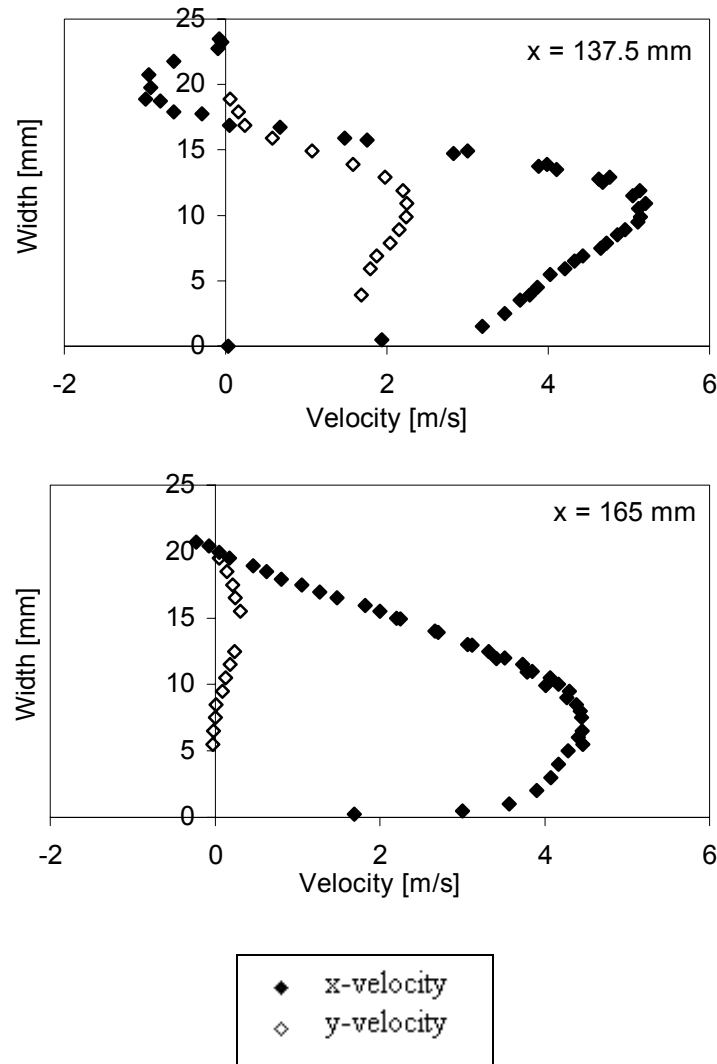


Figure 5.8: Measured velocity profiles at different positions for the low mass flow rate.

The measured root mean square (rms) velocities are given in Figures 5.9 and 5.10. For the fully developed flow, $x = -50$ mm, only the x directed rms velocities (x -rms velocity) are measured. The profile is smooth, and corresponds to the expected shape. The variation of the measured rms-velocities in $x = 87.5$ mm is large, and both rms velocities give a S-shaped profile. The y directed rms velocity (y -rms velocity) has more variation than the x -rms velocity. The increased level in turbulence for the y -rms velocity may be caused by fluctuations in the recirculation zone. The same trends are observed in the next profile, $x = 112.5$ mm. The level of the y -rms velocity is higher than the x -rms velocity. For the $x = 137.5$ mm profile high values of the x -rms velocity are measured. Some scattering is noted between the different series for the x -rms values in this profile. This implies that the measurements are carried out a bit shorter than necessary to obtain stable rms values. On the other hand it might be possible that stable rms values are more or less impossible to obtain. The profiles at the outlet, $x = 165$ mm, show that the x -rms and the y -rms velocities are nearly identical, and only a small difference between the magnitudes is noted.

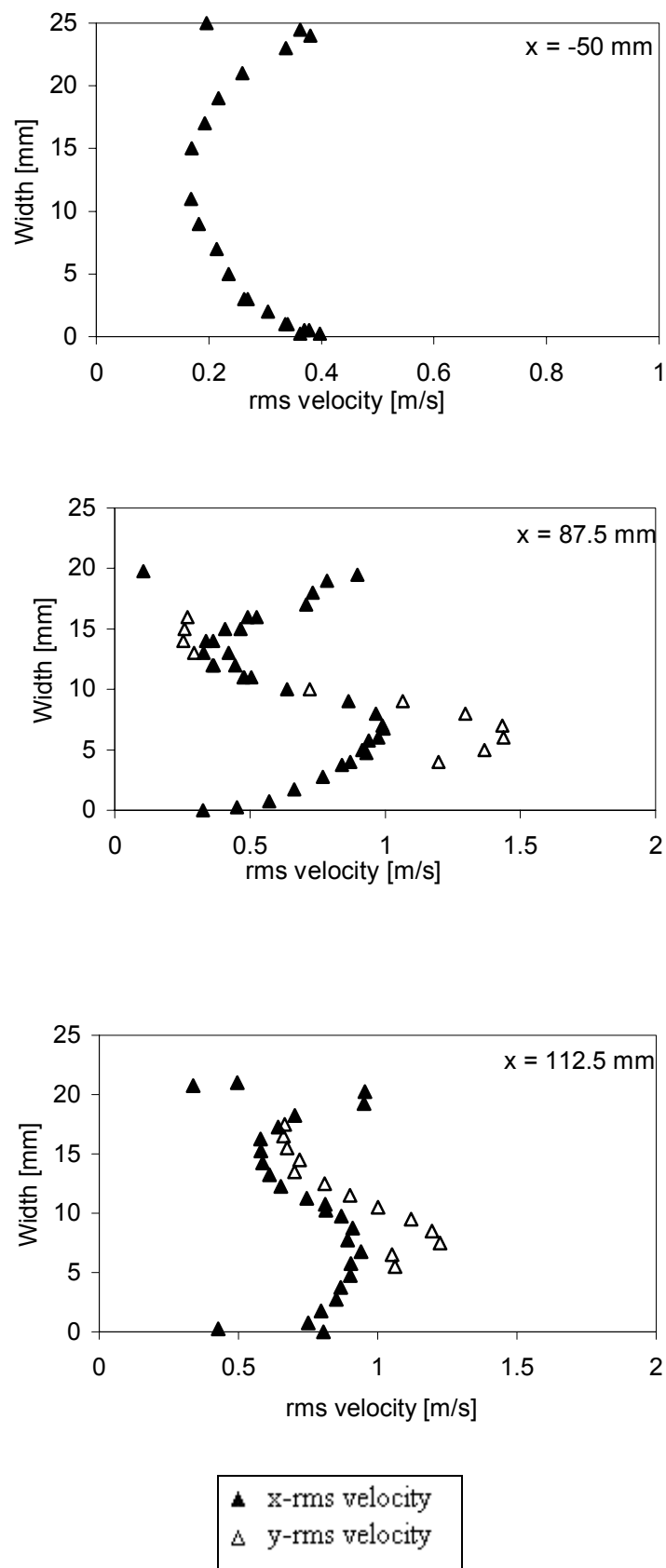


Figure 5.9: Measured rms velocities at different positions for the low mass flow rate.

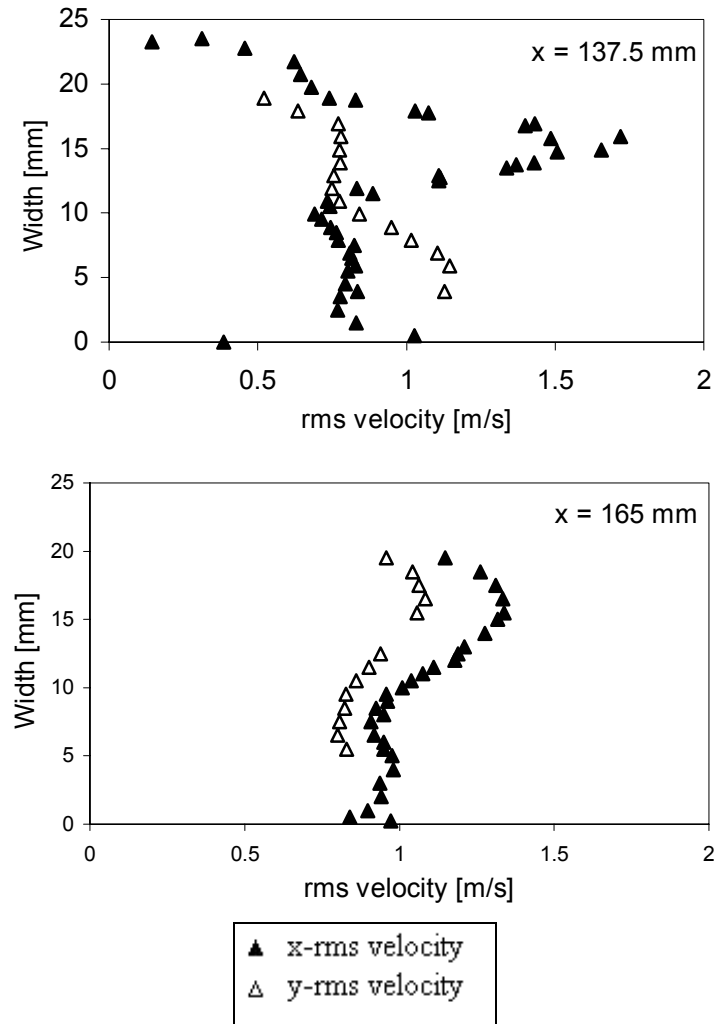


Figure 5.10: Measured rms velocities at different positions for the low mass flow rate.

Some interesting observations can be noted if the velocity and the corresponding rms velocity are plotted in the same figure. This is done for the $x = 137.5$ mm location in Figure 5.11. Approximately 17 mm from the lower wall, the flow changes direction. The x-velocity shifts from positive to negative values. In the same area the largest x-rms values are found. In this area, it is hard to obtain good measurements because of the low velocity, and the small tracer droplets can fluctuate between a positive and a negative value.

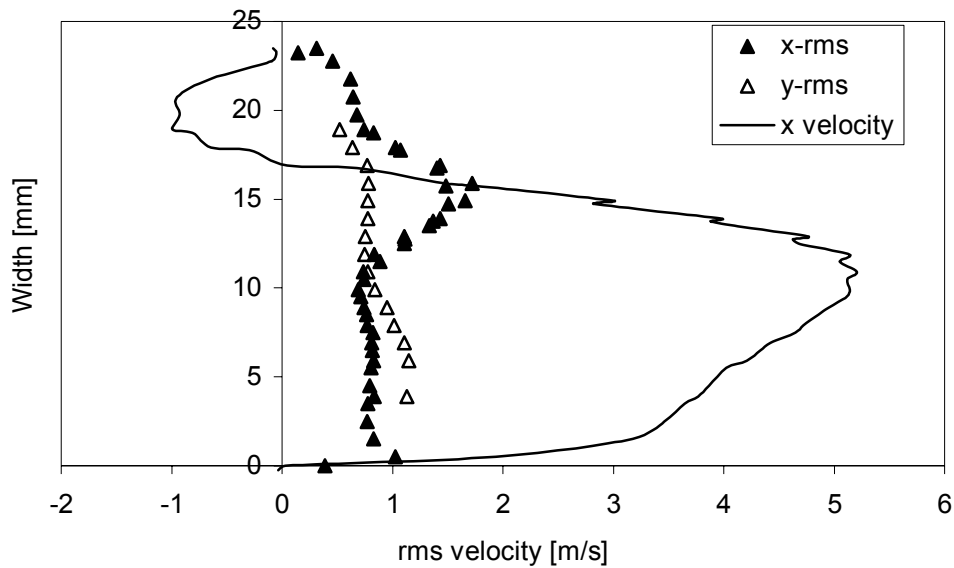


Figure 5.11: The rms profiles and x-velocity at $x = 137.5$ mm for the low mass flow.

The measured droplet size distributions before and after the separator are presented in the next figure, Figure 5.12. The x-axis is the diameter of the droplets in micron, while the y-axis represents the probability density function. The difference between these two graphs shows clearly the effect of the separator. The large droplets are removed, and the number of small droplets is increased. These droplets must have been generated inside the separator.

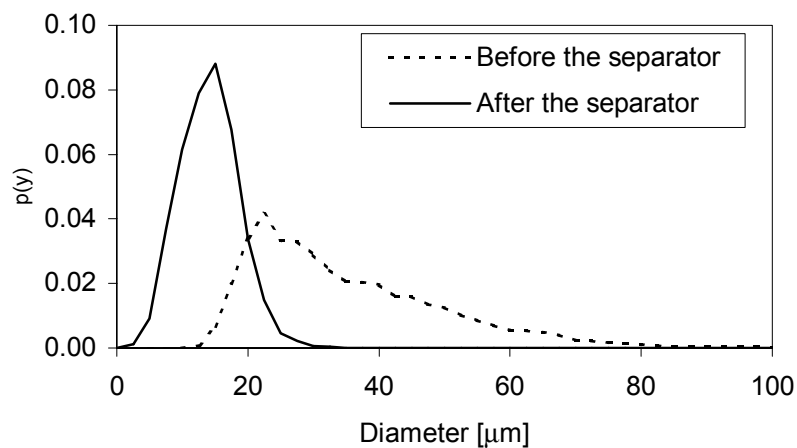


Figure 5.12: Droplet size distributions for the low mass flow rate.

Some statistics from the PDA measurements for the low mass flow case can be found in Table 5.2. The different means are defined in the theory chapter. The Sauter mean has been lowered from $48.9 \mu\text{m}$ at the inlet of the separator to $15.7 \mu\text{m}$ at the outlet of the separator. The Sauter mean has been lowered by 67.8 %, and the majority of the droplets at the outlet are generated inside the separator.

Table 5.2: Diameter statistics from the low mass flow rate case.

Variable	Before the Separator	After the Separator
	[μm]	[μm]
D_{10}	34.1	12.9
D_{20}	37.4	13.6
D_{30}	40.9	14.3
D_{32}	48.9	15.7
D_{max}	127.8	34.2

5.3 The medium mass flow rate case

The mass flow rate through the separator is increased, and the operational conditions for the medium mass flow rate are summarised in the Table 5.3. Stable operational conditions were achieved. In comparison with the low mass flow rate case, the integrated mean velocity is increased approximately 1 m/s, and the pressure drop is increased from 18 Pa to 40 Pa.

Table 5.3: The properties from the middle mass flow case.

Pressure drop	40 Pa
Inlet velocity	3.54 m/s

The measured positions coincide with the measured positions from the previous case, with the inclusion of the profiles at $x = 50$ mm and $x = 68.75$ mm, and all profiles are presented in Figure 5.13 and 5.14. The profiles are briefly commented, and the fully developed velocity profile at $x = -50$ mm is the first to be studied. The velocity profile is well represented by the measurements, because of stable measurements and small differences between the series. The Reynolds number for this flow is 9530. For $x = 50$ mm the x-velocity is flattened, and more sharper towards the walls, with the highest velocity by the upper wall. At the top of the vane, $x = 68.75$ mm, the passage is only approximately 10 mm wide, and hence the x-velocity is much higher than for the rest of the locations. The x-velocity in this position is nearly 10 m/s for the parts of the profile near the lower wall, but a decrease in the magnitude is noted towards the upper wall. The profile located at $x = 87.5$ mm shows a resirculating zone near the lower wall. The zone extends 5 mm into the passage between the vanes. The velocity magnitude is high in this position, since the resirculating zone reduces the effective area for the flow. The y-velocity measurement in the middle of the channel indicates the same shape as for the x-velocity. Near the wall, the y-velocity is believed to deviate from the x-velocities.

The next profile presented is the velocities at position $x = 112.5$ mm given in Figure 5.14. The resirculating zone present at the previous position, $x = 87.5$ mm, is not present at this position. The x-velocity is positive, but some deviation on the x-velocity is noted compared with an ideal profile. The x-velocity shows the build up of a new boundary layer towards the lower wall. The measured profile shows some minor scattering. The y-velocity in the middle of the channel suggests a similar shape of the profile, but with a different magnitude. For the position $x = 137.5$ mm a resirculating zone near the upper wall is noted. The resirculating zone is right after the little hook. The y-velocity in this profile has the same shape as the x-velocity, but differs in magnitude. For $x = 165$ mm a small resirculating zone present at the upper wall is shown. The negative x-velocity noted near the upper wall, is quite surprising, and will cause suction from the passage that is located right above. However, the walls present in this experimental rig restrict the suction, but unstable conditions were noted when multi-passes were tested.

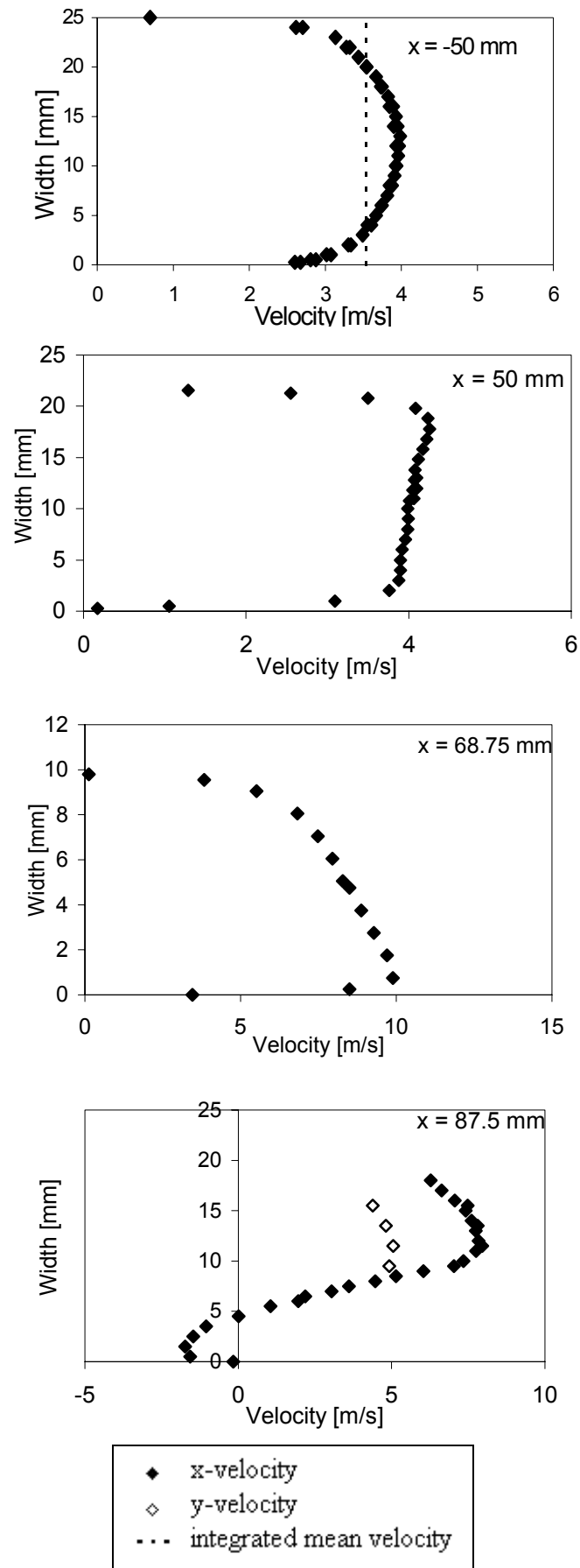


Figure 5.13: Measured velocity profiles at different positions for the middle mass flow rate.

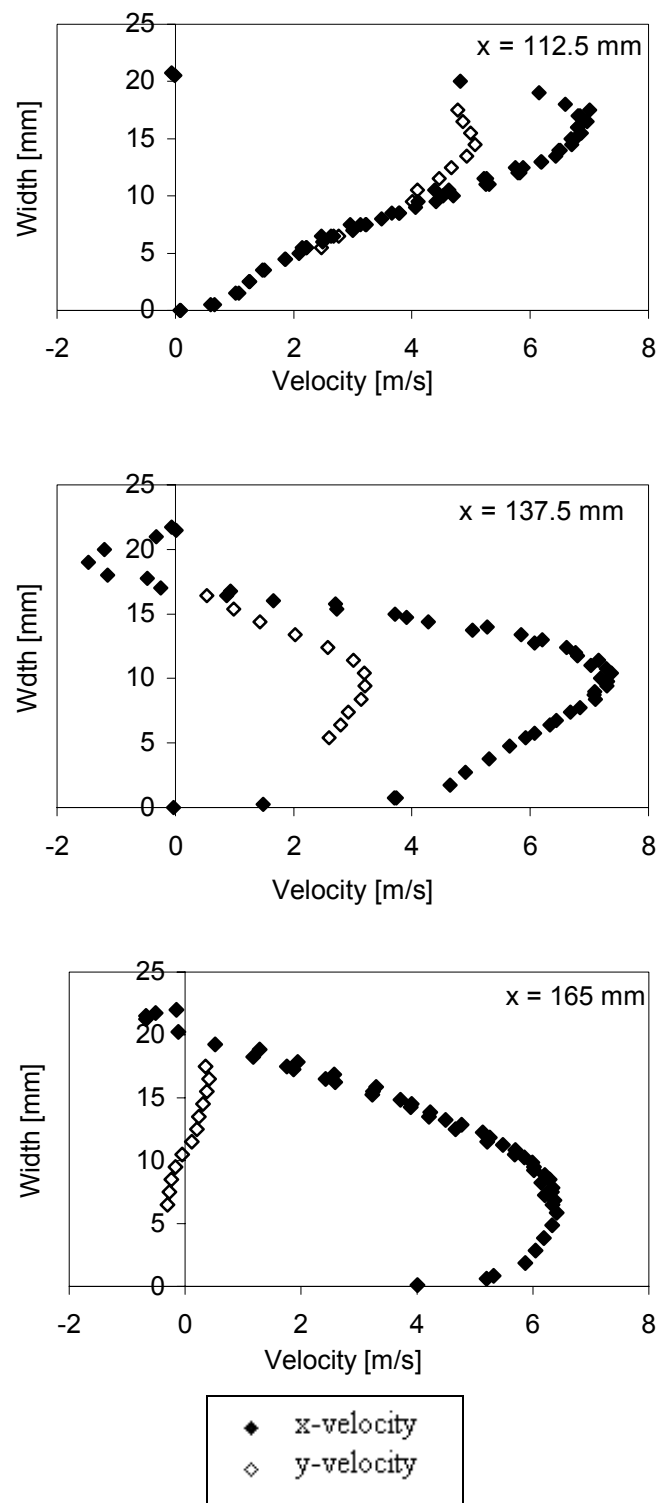


Figure 5.14: Measured velocity profiles at different positions for the middle mass flow rate.

The rms velocities are presented in Figure 5.15 and 5.16. The measured rms velocities are well represented, although some scattering exists in certain positions on different profiles. Especially, some scattering in the rms velocities is found on the profiles located near the end of the separator, typically $x = 112.5$ mm, $x = 137.5$ mm and $x = 165$ mm. It can also be useful to compare the rms measurements from this mass flow to the measurements from the low

mass flow. The profiles will be similar, but a change in the magnitude of rms velocity is noted.

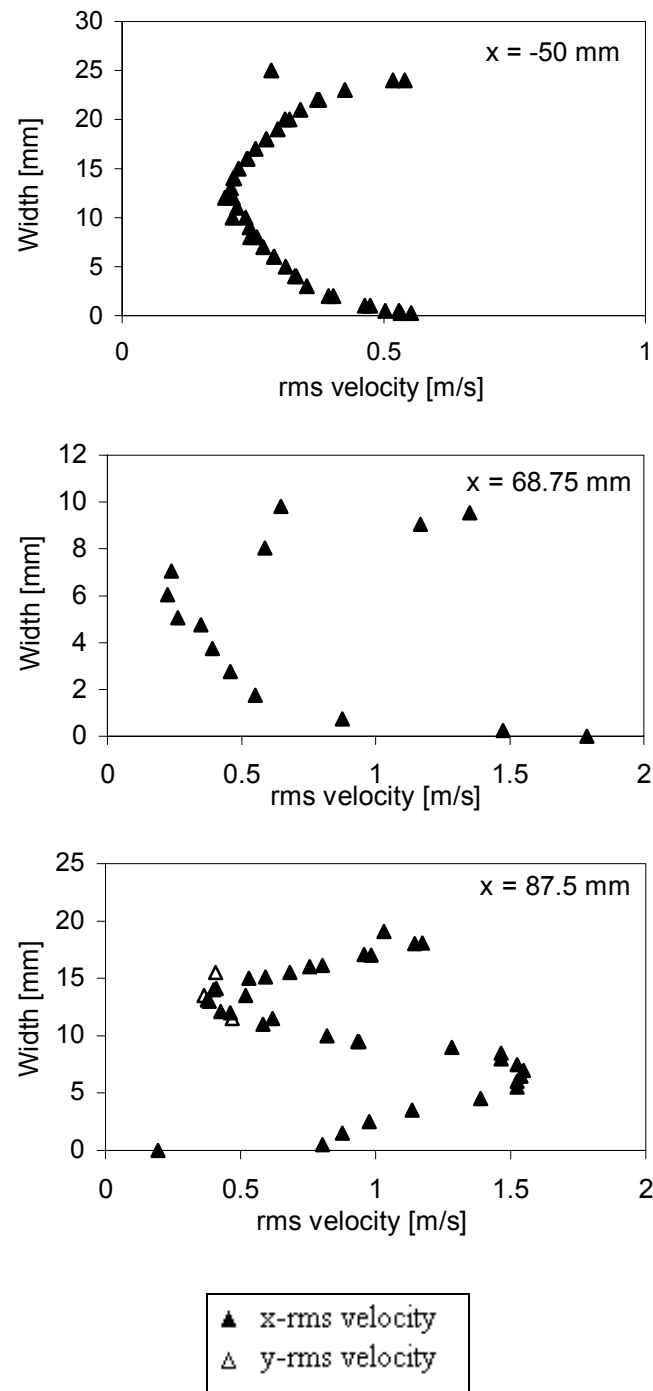


Figure 5.15: Measured rms velocities at different positions for the middle mass flow rate.

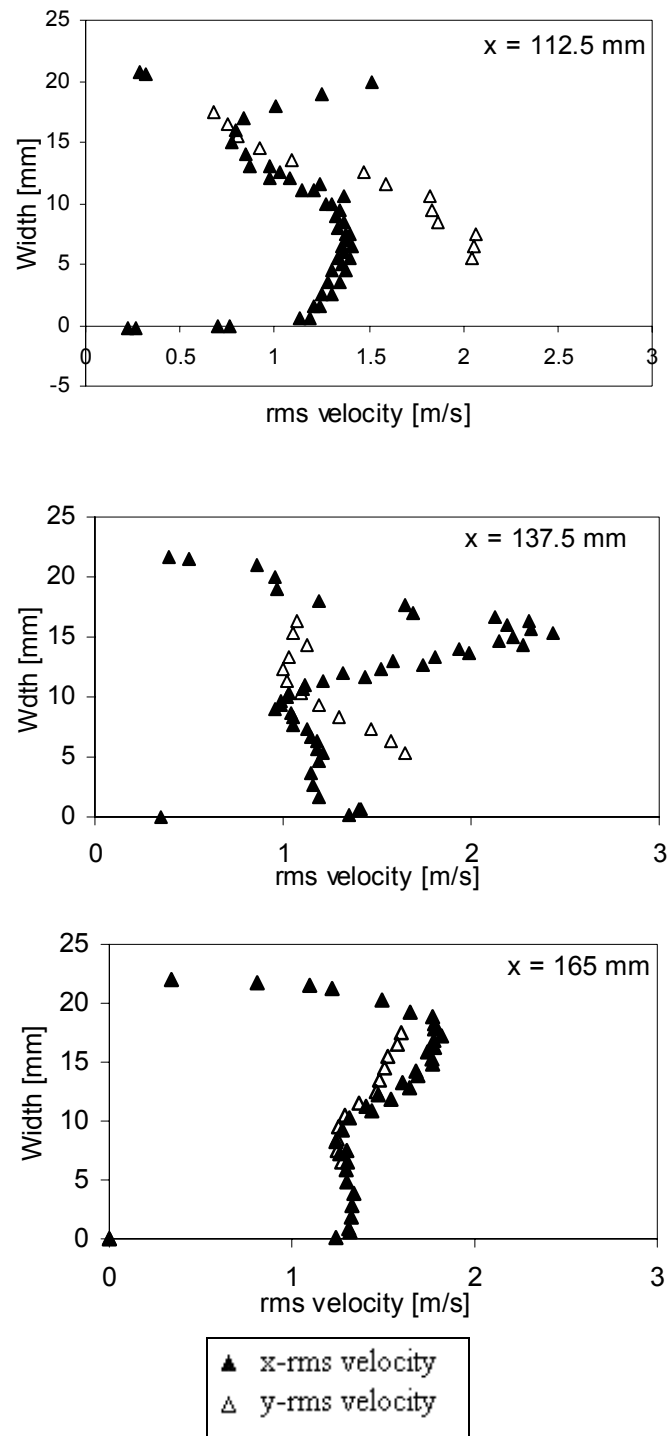


Figure 5.16: Measured rms velocities at different positions for the middle mass flow.

A PDA analysis similar as for the low mass flow rate case is carried out. The efficiency of the separator is shown in Figure 5.17, and the generation of new droplets below 20 μm are clearly present.

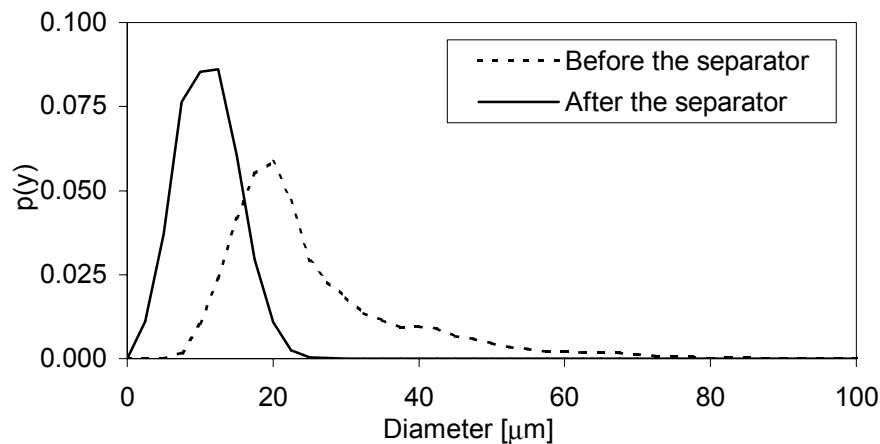


Figure 5.17: The droplet size distributions for the middle mass flow rate.

The diameter statistics for the middle mass flow case are summarized in Table 5.4. The Sauter mean, D_{32} , is lowered from 42.2 μm to 12.8 μm , which is a lowering of 69.7 %.

Table 5.4: Diameter statistics from the middle mass flow.

Variable	Before the separator [μm]	After the separator [μm]
D_{10}	24.6	9.8
D_{20}	28.0	10.6
D_{30}	32.1	11.3
D_{32}	42.2	12.8
D_{Max}	131.3	29.0

5.4 The high mass flow rate case

The inlet velocity is further increased, and a pressure drop over the separator of 60 Pa is noted, Table 5.5. The integrated mean velocity, based on the x-velocity, is equal to 4.54 m/s.

Table 5.5: Properties for the high mass flow rate case.

Pressure drop	60 Pa
Inlet velocity	4.54 m/s

The increased mass flow rate is the only difference in comparison with the other experiments, and compared with the medium mass flow rate case the inlet velocity is increased by 1 m/s. The pressure drop increases from 40 Pa to 60 Pa, and the Reynolds number is 12200. The positions that are measured for the high mass flow rate case are similar to the positions for the low mass flow rate, Figure 5.6. The profiles are presented in Figure 5.18 and 5.19. The profile at $x = -50$ mm contains the x- and the y-velocity for this position. The y-velocities are very small. The measured y-velocities are negative and positive, typical in the range ± 0.025 m/s, and the mean is 0.0008 m/s. This indicates good alignment of the laser probe. The profiles measured at $x = 87.5$ mm shows that the x- and y-velocity profile is similar but differs in

magnitude. A strong resirculating zone is seen near the lower wall. This resirculating zone is not present in the profile located at $x = 112.5$ mm. The similarity between the x - and y -velocity for the profile at $x = 112.5$ mm is strong, and they differ only in magnitude. For $x = 137.5$ mm the backflow is present at the upper wall right after the small hook. The x - and y -velocity show again a similarity, but differ in magnitude. For $x = 165$ mm the measurements are good, and no resirculation is present.

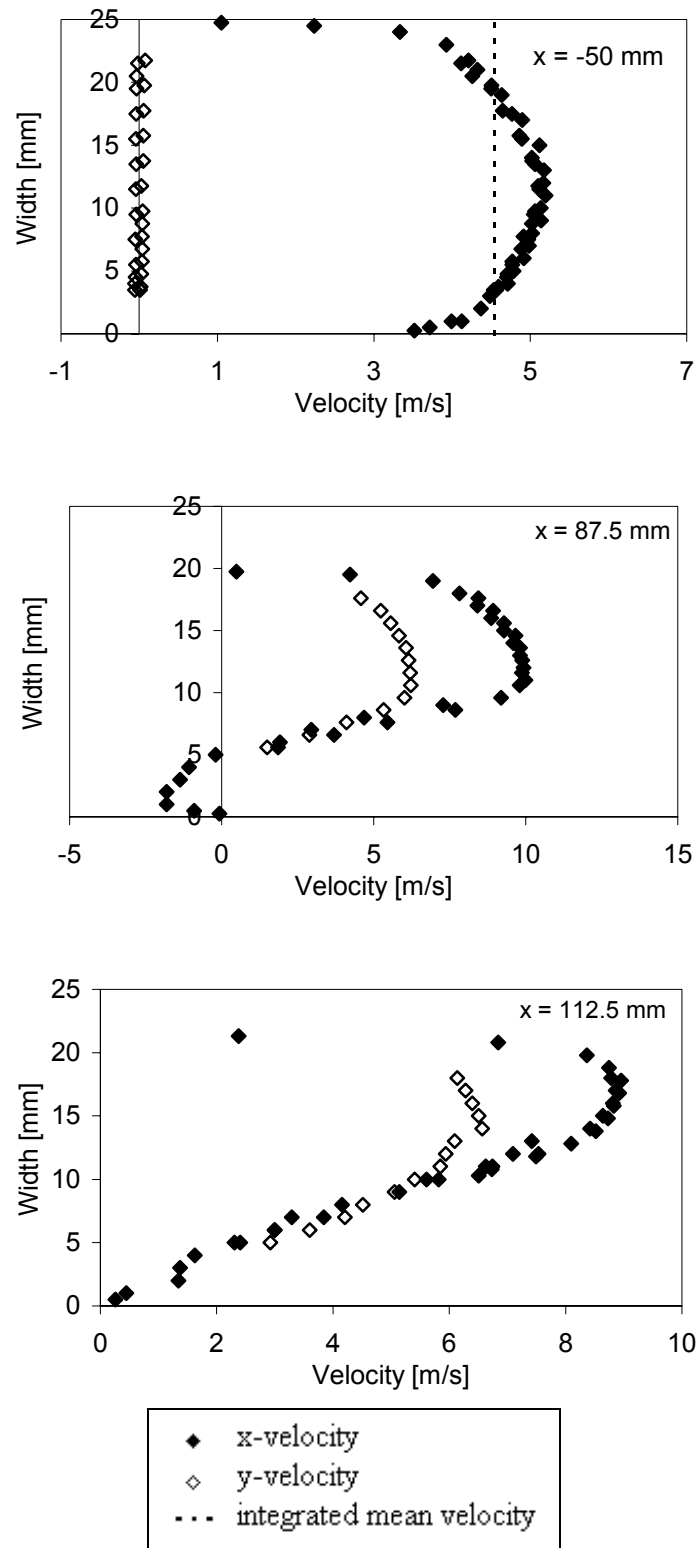


Figure 5.18: Measured velocity profiles at different positions for the high mass flow rate.

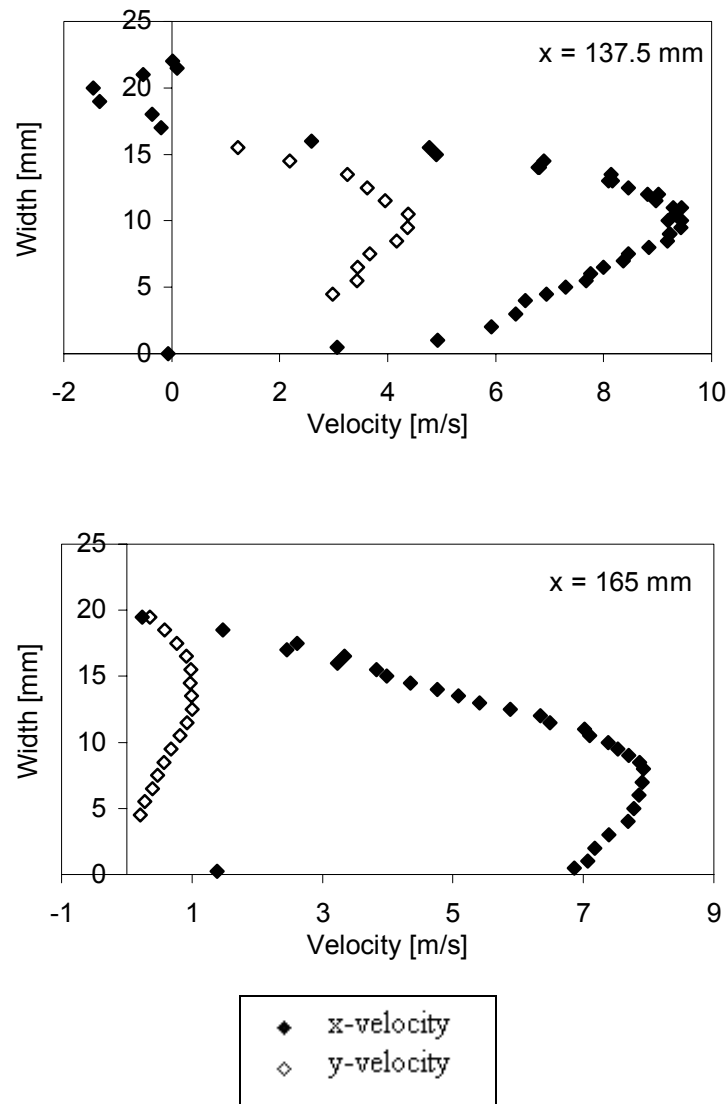


Figure 5.19: Measured velocity profiles at different positions for the high mass flow rate.

The rms velocity profiles from the high mass flow rate are presented in Figures 5.20 and 5.21. For the inlet profile, $x = -50$ mm, the x-rms shows expected shape. For $x = -50$ mm the y-rms velocities are measured, because this case was used to verify the alignment of the laser probe. The absolute values are higher than for the other mass flow rates, and indicate an increased level of turbulence. The measured rms velocities show analogue results as for the other mass flow rates. Generally, some deviations exist between the different measurement parallels, but these deviations are not too large.

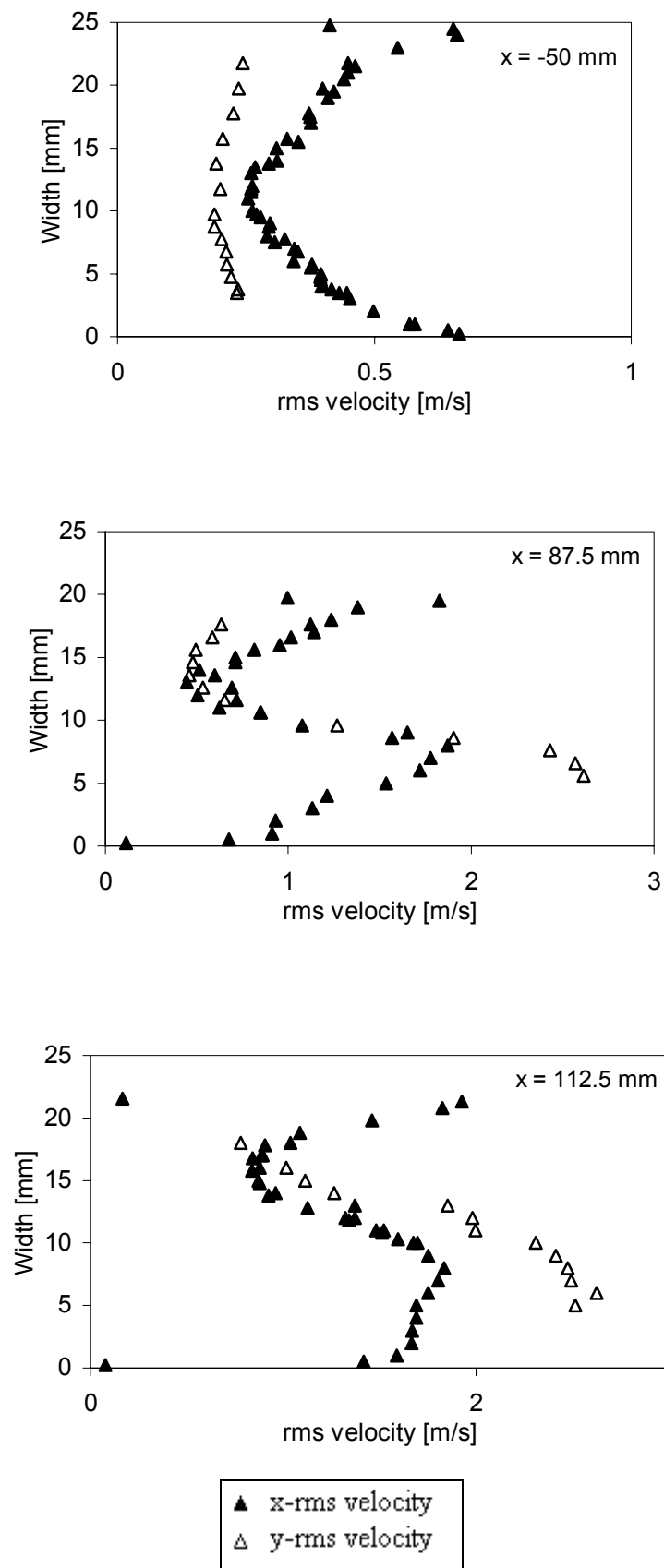


Figure 5.20: Measured rms velocities at different positions for the high mass flow rate.

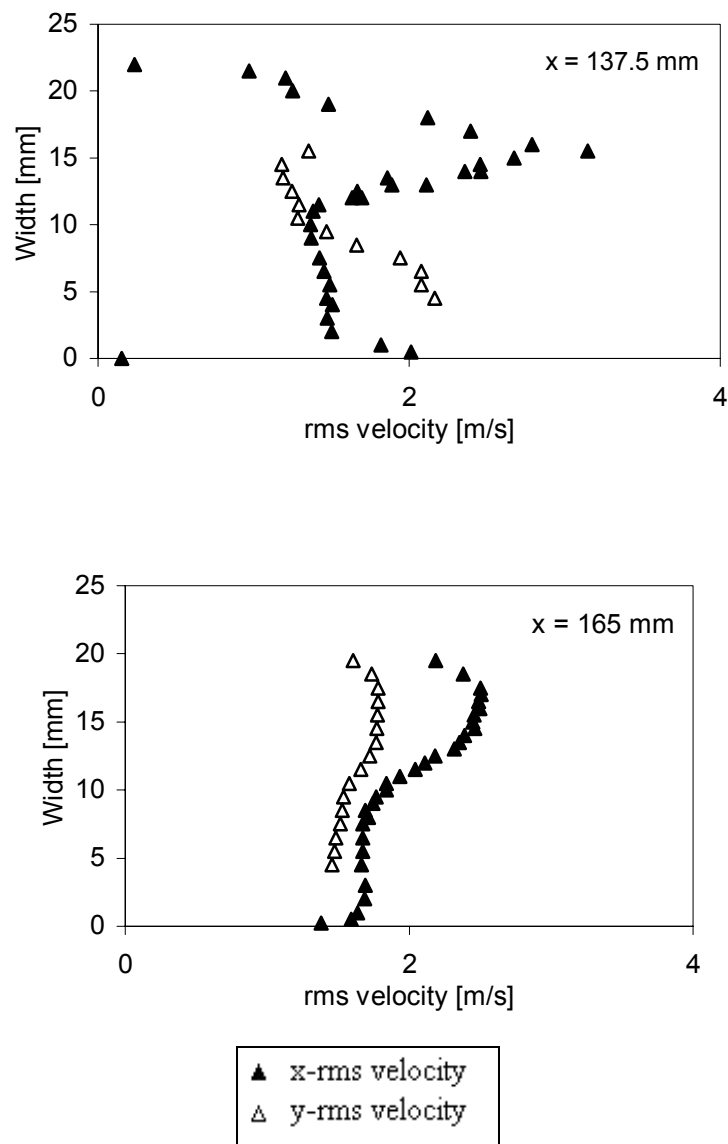


Figure 5.21: Measured rms velocities at different positions for the high mass flow rate.

The efficiency of the separator seen in light of the difference between the inlet and outlet droplet size distributions is presented in Figure 5.22. The effect of the separator is quite easy to identify, and lots of droplets are generated in the range below $20\text{ }\mu\text{m}$.

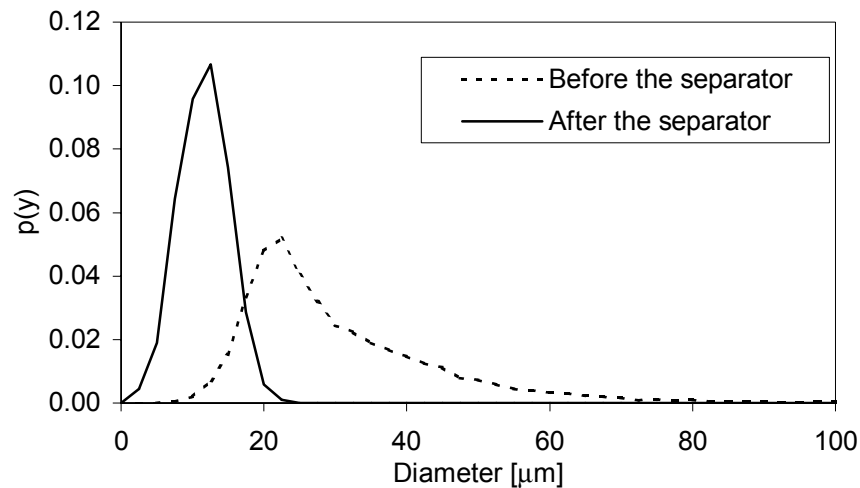


Figure 5.22: The droplet size distribution in and out of the separator for the high mass flow.

The droplet statistics from the PDA measurements for the high mass flow are summarised in Table 5.6. The Sauter mean has been lowered 72.1 %.

Table 5.6: Diameter statistics from the high mass flow.

Variable	Before the separator [μm]	After the separator [μm]
D_{10}	29.3	10.4
D_{20}	32.5	10.9
D_{30}	36.2	11.4
D_{32}	44.8	12.5
D_{Max}	125.1	23.9

5.5 Comparisons between the different mass flow rates

Some additional information can be noted if comparisons between the different mass flow rates are carried out. In this section, comparisons for the mean diameters, non-dimensional velocity profiles, and turbulent quantities are compared. These comparisons are divided into each separate section.

5.5.1 Diameter comparisons

The decrease in Sauter mean diameter for the different mass flows is presented in Table 5.7. The effect of increased mass flow is clearly spotted on the Sauter mean diameter. An increase in the mass flow leads to a higher decrease in the Sauter mean diameter.

Table 5.7: Comparison of the Sauter mean diameter for the different mass flows.

	Decrease in Sauter mean diameter [%]
Low mass flow rate	67.8
Medium mass flow rate	69.7
High mass flow rate	72.1

The Sauter mean diameter for all the mass flow rates are shown in Figure 5.23. The bars to the left show the Sauter mean diameters before the separator. The Sauter mean diameter for the different mass flow rates is not constant before the separator. This can be caused by different operational conditions for the nozzle, but also by different properties of the flow in the channel. For the low mass flow rate case, less turbulence exists, and it is more likely that a droplet reaches the separator without being in contact with the walls. For increased turbulence, or mass flow rate, the probability increases for a droplet-wall interaction, which can lead to a change in the Sauter mean diameter for the droplet distribution. When the droplet reaches the wall and adheres to the wall, re-entrainment is possible, and the re-entered droplets cause a change in the droplet size distribution.

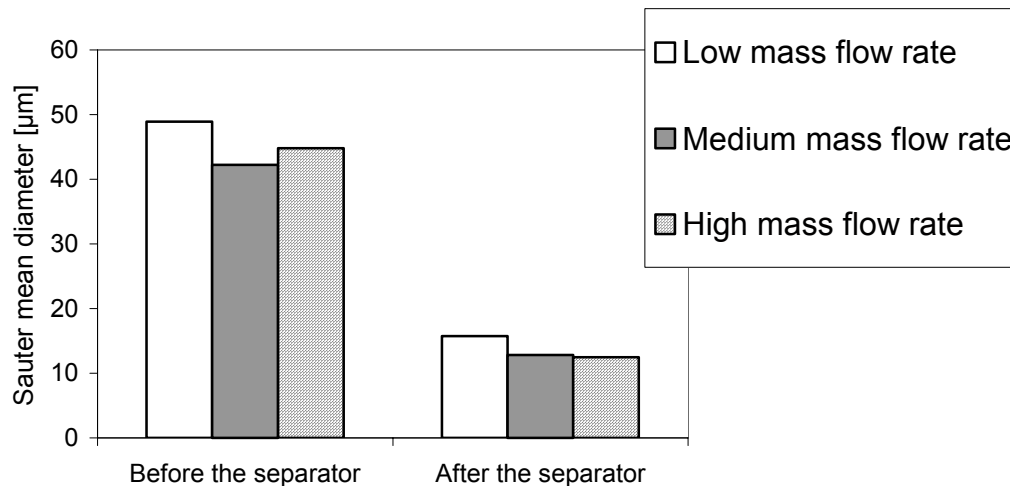


Figure 5.23: The Sauter mean diameter before and after the separator.

5.5.2 Non-dimensional velocity profiles

The velocities are made dimensionless by the use of the integrated mean velocity associated with the respective mass flow rates. The non-dimensional velocities show a remarkable similarity between the different mass flow rates. Only in the resirculating zones some deviations are present.

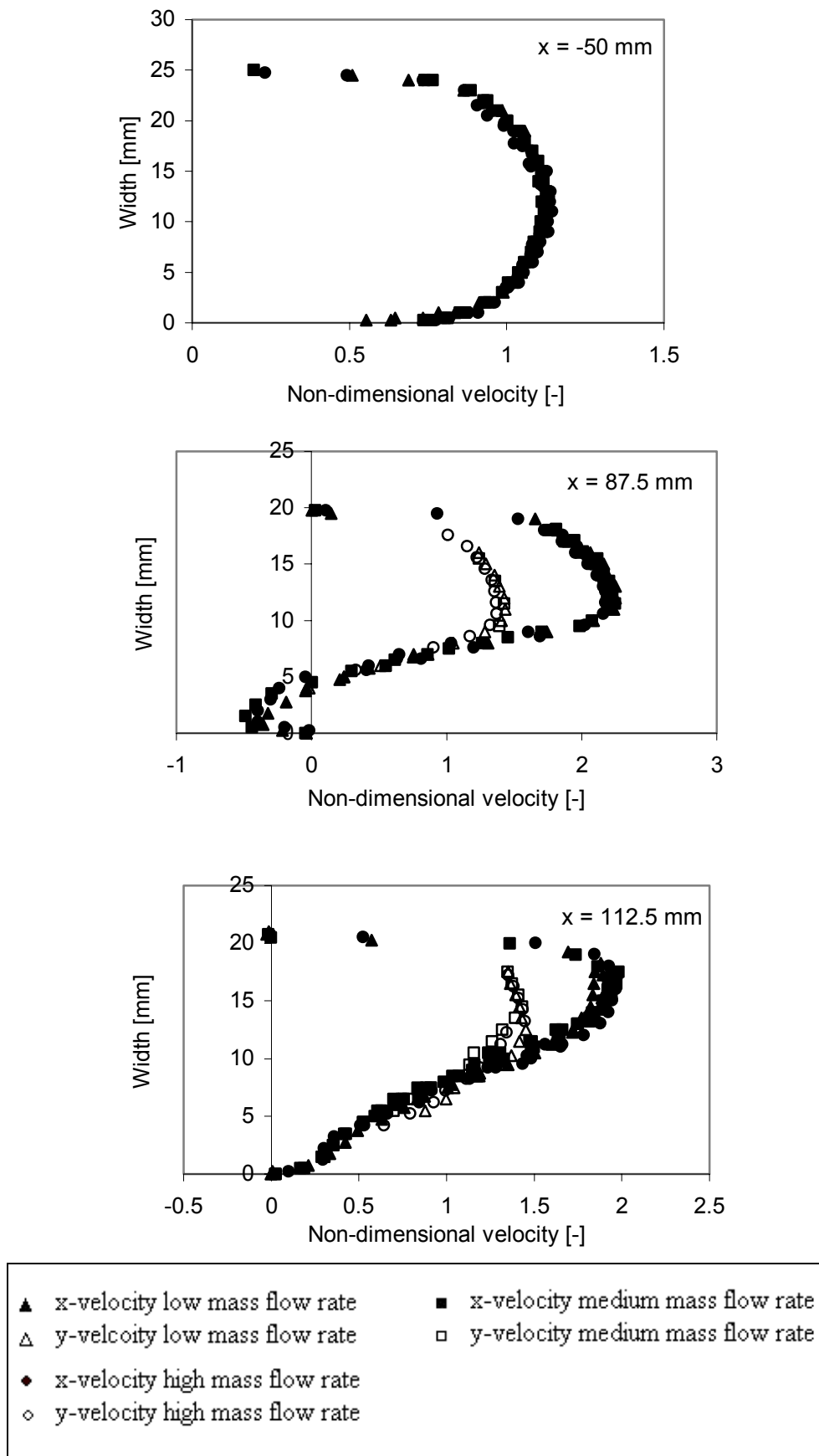


Figure 5.24: Non-dimensional x- and y-velocity profiles for the different mass flow rates.

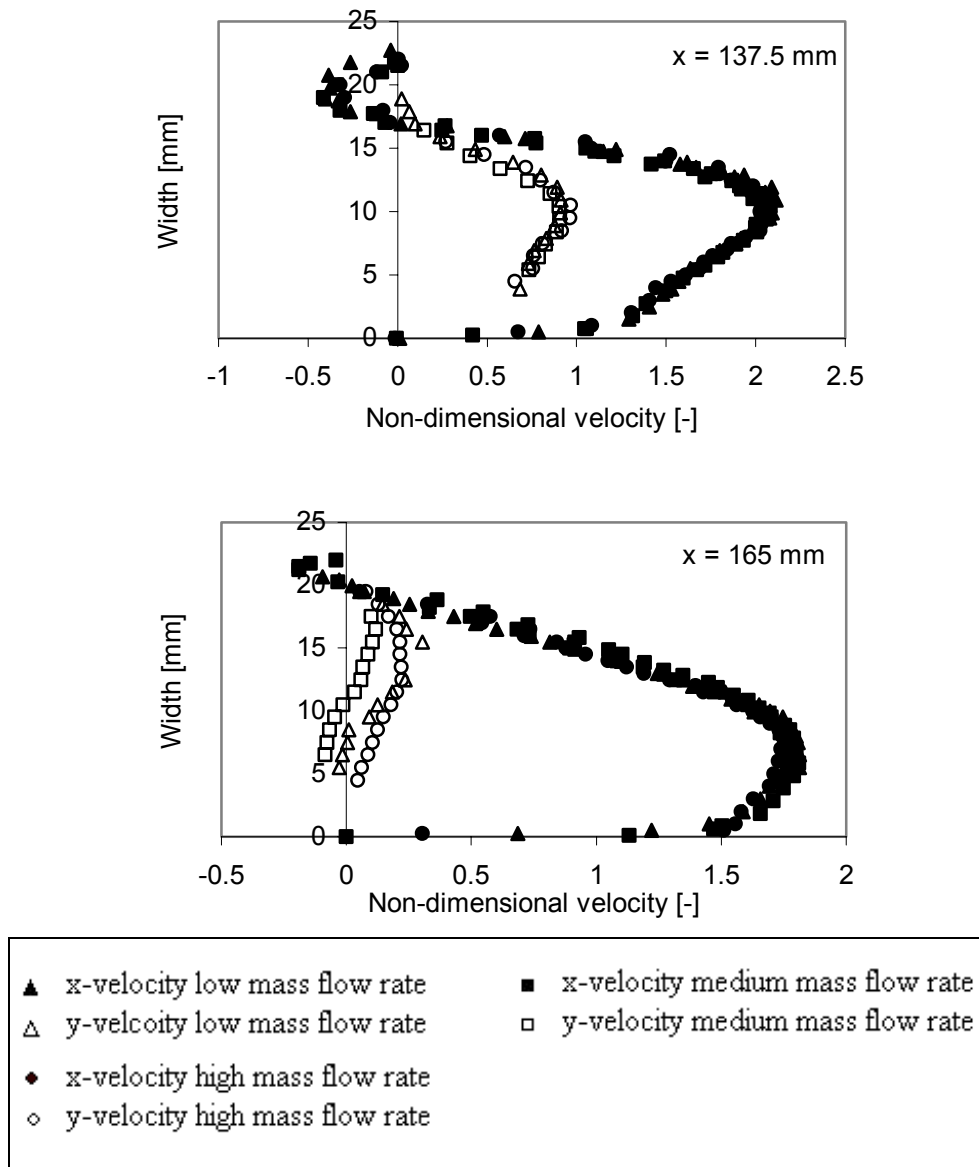


Figure 5.25: Non-dimensional x- and y-velocity profiles for the different mass flow rates.

5.5.3 Non-dimensional rms velocities

In Figure 5.26 and 5.27 the non-dimensional rms velocities are shown. The rms velocities are made dimensionless by the use of the maximum rms velocity in the respective profile. The non-dimensional profiles show similarity between the different mass flows, however this is not easy to see in the figures due to some scattering of the rms velocities. The trends for the various profiles indicate however that similarity exists for the rms velocities.

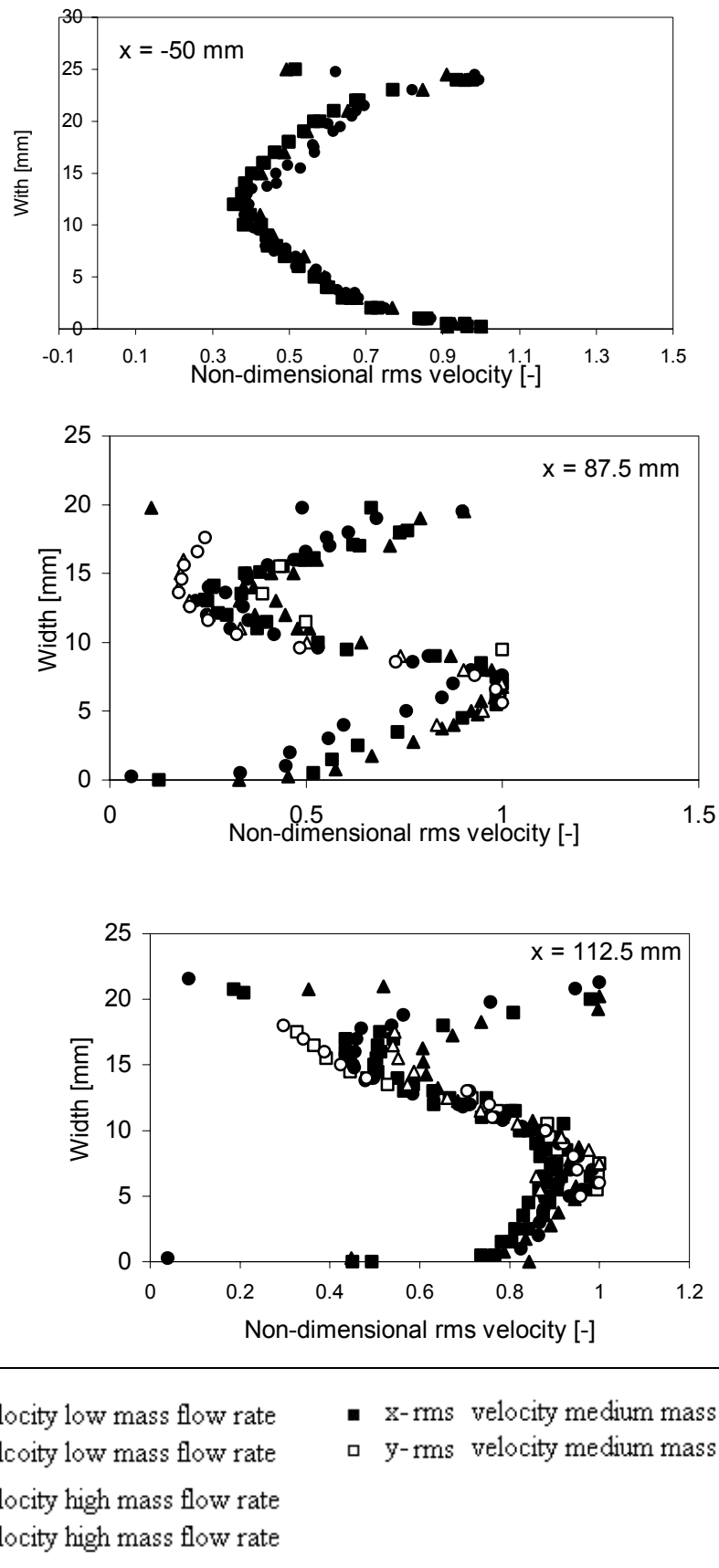


Figure 5.26: Non-dimensional x- and y-rms velocity profiles for the different mass flow rates.

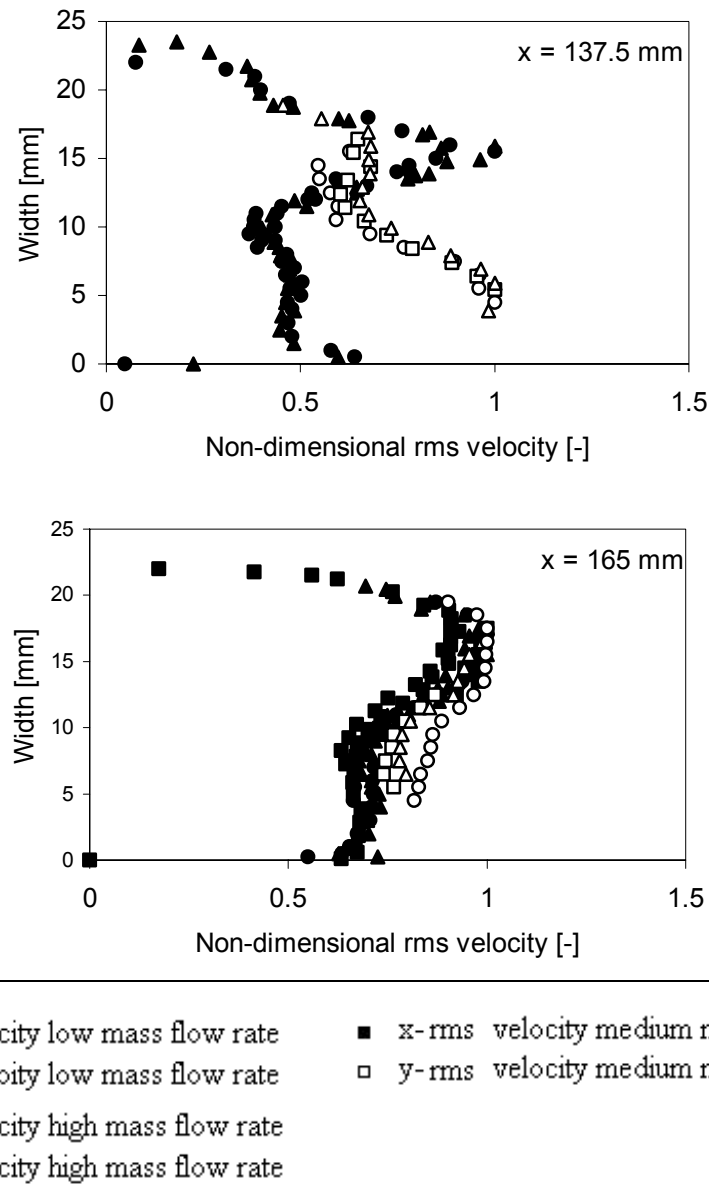


Figure 5.27: Non-dimensional x- and y-rms velocity profiles for the different mass flow rates.

5.6 Overall comments and conclusions

The measurements presented in this chapter are highly reproducible and reliable. Each profile consists of minimum two series, but most frequent are three series in each profile. The velocity profiles seems to be continuous and smooth, and it is hard to see that each velocity profile consists of 3 individual parallels. It is on this basis that it is concluded that the measurements are reproducible and reliable. Some scattering is found in few of the profiles, but this is most occasionally for the rms velocity profiles. The reason for more scattering in the rms velocities is increased statistical requirement on the measurements in order to achieve a stable measurement. Some scattering also exists on the high mass flow rate velocities, and this may be caused by a more unstable flow, which increases the statistical requirements. The measurements are overall satisfactorily to be used as a basis for comparison with predictions from a CFD code.

Chapter 6

CFD simulations

The measured profiles of velocity, turbulence, and the droplet diameter distribution are the basis for comparisons with the predicted values obtained by CFD simulations. The different aspects, or methods used in the CFD simulations are described in Chapter 2. However, a short section is presented in this chapter to refresh the different aspects, and to define the different cases used in the simulations. The rest of this chapter compares the simulations of the middle mass flow, and presents comparisons between the measured velocities, turbulence, and pressure drop. The measured droplet size distribution is compared with predicted values in Chapter 9 ‘Results from the new droplet models’. Comparisons for the small and the high mass flows are presented in Appendix 1 and 2.

6.1 Several aspects in the problem definition

There are several aspects in the problem definition that need extra attention. These aspects are discussed in this section. It is found necessary to divide this section into sub-sections, and a natural starting point becomes the generation of the grid for the geometry.

6.1.1 Grid generation

The first moment to consider in a CFD analysis is the grid. The grid shall represent the geometry of the object for analysis. The transformation of the physical geometry into the computational domain must be of such character that important features of the flow are brought along. Details that are important must be resolved in the geometrical representation in the grid. The method used for the vanes to ensure a best as possible representation of the vane, was to make a photographic copy of the vane. Then the co-ordinates of the vane were read out from the copy. If the representation was copied onto a millimetre-scale paper, the deciphering of the vane was a straightforward process. The co-ordinates were fed into the grid generator, Gambit, and lines were drawn on the basis of the co-ordinates. This method produces only the vane, and not the passage, which is the actual computational domain. The passage was made by copying all the points 25 mm in the y-direction. The rest of the channel is trivial to generate. Only a 2-dimensional (2D) representation of the vane separator is used in the simulations. The geometrical representation is the same for the two different versions of Fluent, but the grid is quite different. In Figure 6.1, the geometry representing one vane in 2D is shown.

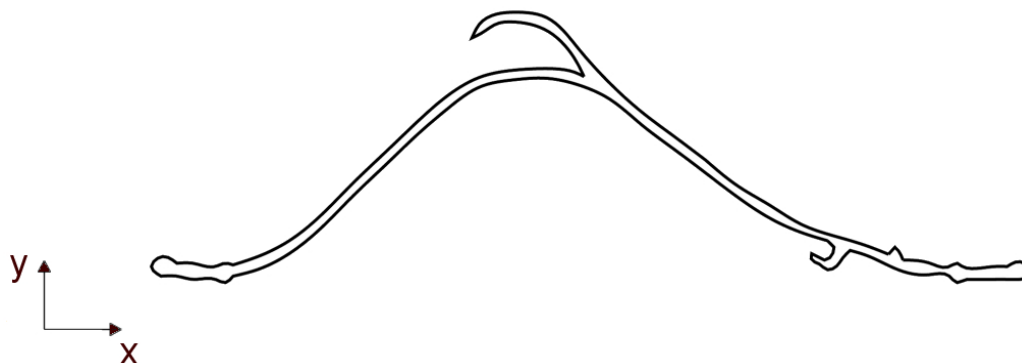


Figure 6.1: The geometry of the vane.

The resolution of the grid is important. It should be fine enough to resolve all the important flow details, but on the other hand it should be so coarse that the computational requirements do not become too high. For the structured grid some requirements are important. First of all the grid-lines must be continuous within the computational domain. The grid lines cannot terminate inside the domain. The cells are squared, and for a body fitted co-ordinate (bfc) grid the grid lines follow the geometry. The bfc cells can be deformed, and a smooth representation of a complex physical domain can be represented. A detail from the structured bfc grid for the passage between the vanes is given in Figure 6.2. The grid lines are continuous through the domain, and the cells are deformed along with the body fitted grid lines.

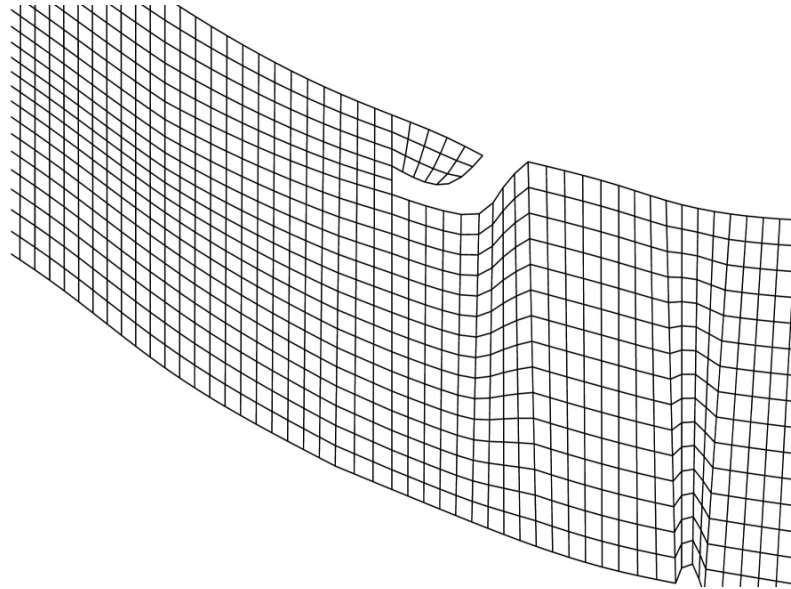


Figure 6.2: Details of the structured grid of the passage between the vanes.

The constraints that existed for the structured grid are not valid for the un-structured grid. Grid lines may terminate or new grid lines can be started within the computational domain. For un-structured grid it is possible to use triangles as well as rectangles in the grid. A part of the un-structured grid for the passage is given in Figure 6.3.

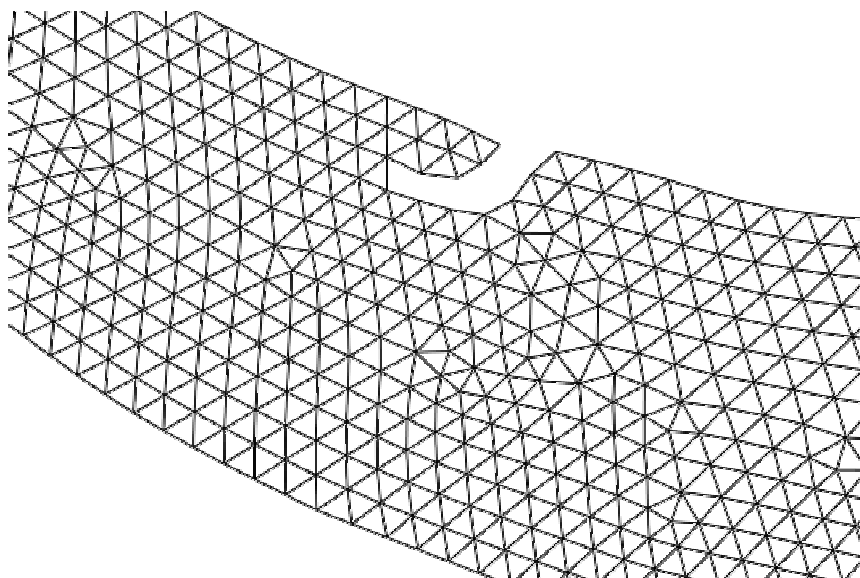


Figure 6.3: Details of the un-structured grid of the passage between the vanes.

It is interesting to perform simulations on both types of grid, in order to achieve information about the quality of the predictions from the different grids. The un-structured grids have many advantages compared to the structured grid, and hence it must be investigated if an un-structured grid is appropriate. The structured grid has been used for many years, and the performance of this grid type is well documented. In the generation of the grid, some attention to the density of cells near the walls is important. The density of the cells must be seen in the light of the current near wall model used for the turbulence. In the theory chapter, it was mentioned that the near wall models for the turbulence have different grid requirements. Basically the 'Two-layer zonal model' requires a fully resolved near wall region, which means lots of cells near the wall. For the 'Law-of-the-wall' the requirements states that the first cell adjacent to the wall must be located so that $y^+ > 30$. The number of cells is considerable higher for the simulations with the Two-layer zonal model compared by the Law-of-the-wall since a fine grid is needed by the wall.

For the structured simulations (Fluent v4.5) the grid size was 875x32 (28000) cells for the Law-of-the-wall case, and 1440x52 (74880) cells for the Two-layer zonal model. For the un-structured simulations (Fluent v5.3) the Law-of-the-wall grid consisted of 30202 cells, and for the Two-layer zonal model the un-structured grid consisted of 52528 cells. For the structured case the grid was doubled, and the new simulations showed no major changes, and hence a grid impendent solution was achieved. For the un-structured grid a refine mesh was performed resulting in increased cells, but this did not influence the solution.

6.2 The effect of a mismatch between the grid and near wall model

Before starting with presentation of the results from the simulations of the middle mass flow, a brief glance at the effect of a mismatch between the near wall treatment of the turbulence and the grid is given. A typical mismatch is a fine grid in near wall regions for the 'Law-of-the-wall', or too few cells near the wall for the 'Two-layer zonal model'. In Figure 6.4 the results from a simulation where there has been a mismatch between the grid and the current near wall treatment of the turbulence is presented. Figure 6.4 shows the results from the structured cases, but the same trends are observed for the un-structured cases. When the 'Law-of-the-wall' is used on a grid that is too fine, i.e. the cell density is too high in the near wall regions, the resulting profile for the inlet velocity contains discrepancies. If a coarse grid where used together with the 'Two-layer zonal model', only minor deviations where noted. But when the grid and the current method for near wall treatment are matched, the simulated profiles differ little from case to case, and the predicted velocity profile on the inlet is satisfactory.

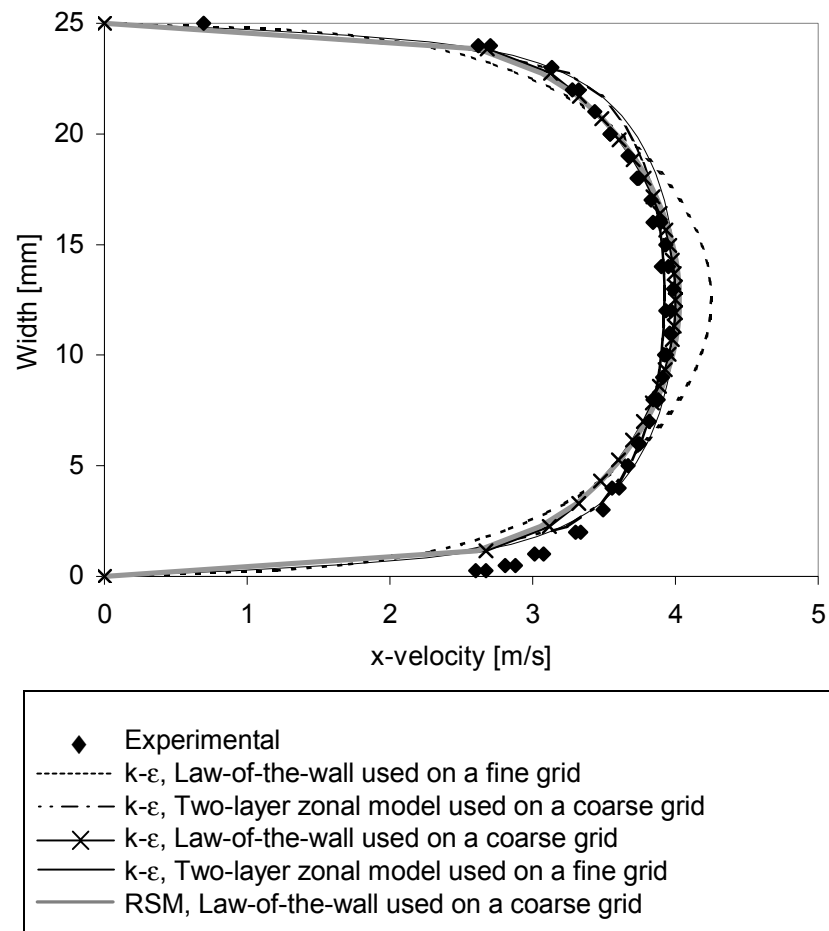


Figure 6.4: The effect of near wall treatment and a matching (or mismatching) grid.

For the rest of the simulations performed in this work, a check is done to ensure that a too fine grid is avoided for the 'Law-of-the-wall'. If any doubt arises about the choice of a correct near wall treatment of the turbulence, it seems safer to use the 'Two-layer zonal model' since this method performs well even though the grid matching is inappropriate.

6.3 Comparisons for the medium mass flow rate

As mentioned in the introduction to this chapter only the simulations for the medium mass flow rate are presented in this section. First, the pressure drops are presented, and in the same table a description of each case is given. After the presentation of the pressure drop the comparisons between the measured and predicted profiles follows. The different cross-sections are briefly commented, and more thorough discussion is found in 'Chapter 6.4 Discussion and conclusion from the predicted profiles'.

6.3.1 The pressure drop

The pressure drop for the different cases is shown in Table 6.1. The simulated cases are numbered from 1 to 12, while the experimental case is number 0. The predicted pressure drops show that the RSM model always overpredicts the pressure drop. The overprediction is from 13 % to 54 %. Using a higher order scheme together with the RSM model causes the structured case to improve, while the un-structured case becomes worse. For the k- ϵ cases the higher order scheme slightly improves on the un-structured cases, while a slight decrease in the accuracy are noted for the structured cases. However, the k- ϵ cases predict satisfactorily, in the area of ± 13 %.

Table 6.1: Pressure drop for the medium mass flow.

Case no. [#]	Type of grid	Turbulence model	Numerical Scheme	Near-wall treatment	Δp [Pa]	Deviation [%]
0	Experimental				40.0	
1	Structured	k- ϵ	Power law	Law-of-the-wall	43.1	7.8
2	Structured	RSM	Power law	Law-of-the-wall	48.7	21.8
3	Structured	k- ϵ	Power law	Two-layer Zonal model	38.0	-5.0
4	Structured	k- ϵ	Quick	Law-of-the-wall	35.0	-12.5
5	Structured	RSM	Quick	Law-of-the-wall	45.1	12.8
6	Structured	k- ϵ	Quick	Two-layer Zonal model	36.4	-9.0
7	Un-structured	k- ϵ	1st order upwind	Law-of-the-wall	44.4	11.0
8	Un-structured	RSM	1st order upwind	Law-of-the-wall	50.8	27.0
9	Un-structured	k- ϵ	1st order upwind	Two-layer Zonal model	43.9	9.8
10	Un-structured	k- ϵ	Quick	Law-of-the-wall	42.8	7.0
11	Un-structured	RSM	Quick	Law-of-the-wall	61.7	54.3
12	Un-structured	k- ϵ	Quick	Two-layer Zonal model	36.9	-7.8

6.3.2 The profiles at $x = -50$ mm

The cases at $x = -50$ mm are shown in Figure 6.5. The abscissa denotes the x-velocity, and the ordinate gives the channel width. The structured cases are given in the figure to the left, while the un-structured cases are given to the right. Some deviation is noted near the lower wall, but these deviations are considered to be offset errors in the measurements. First order scheme is used in the cases to the left in the legend for Figure 6.5.

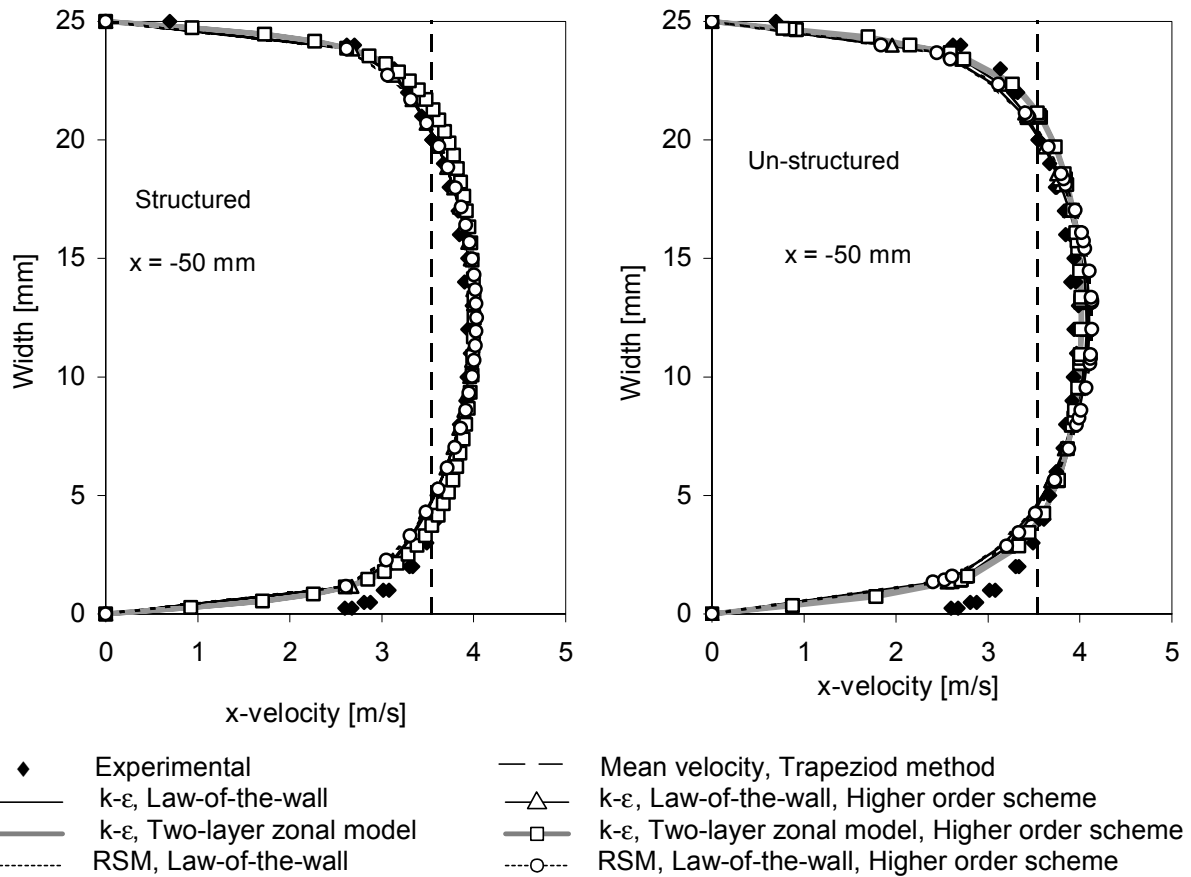


Figure 6.5: The x-velocity profiles at $x = -50$ mm.

A close up of the area in the middle of the channel, $y = 12.5$ mm, would have shown only small differences between the different cases, but nearly no differences between the first order scheme and the higher order scheme are noted. The measured x-rms velocities are compared with the simulations in Figure 6.6. The RSM gives the individual stresses directly, but for the k - ϵ model an assumption must be made. If isotropic turbulence is assumed, the turbulent kinetic energy can be converted into a single rms velocity, which represents all three directions. Equation (6.1) shows the expression of k as function of the individual stresses.

$$k = \frac{1}{2}(\overline{u'^2} + \overline{v'^2} + \overline{w'^2}) \quad (6.1)$$

It is assumed that the individual stresses are equal in all directions and then the stresses are summed together, and the rms velocities can then be expressed by

$$u' = v' = w' = \sqrt{\frac{2k}{3}} \quad (6.2)$$

For the profiles located at $x = -50$ mm the performance between the different turbulence models should be minimal. The non-isotropic nature of the turbulence is modest, and hence the drawback for the k - ϵ model is minimal. The profiles show satisfactory predictions for the majority of the cases, although some deviations are noted for the un-structured cases.

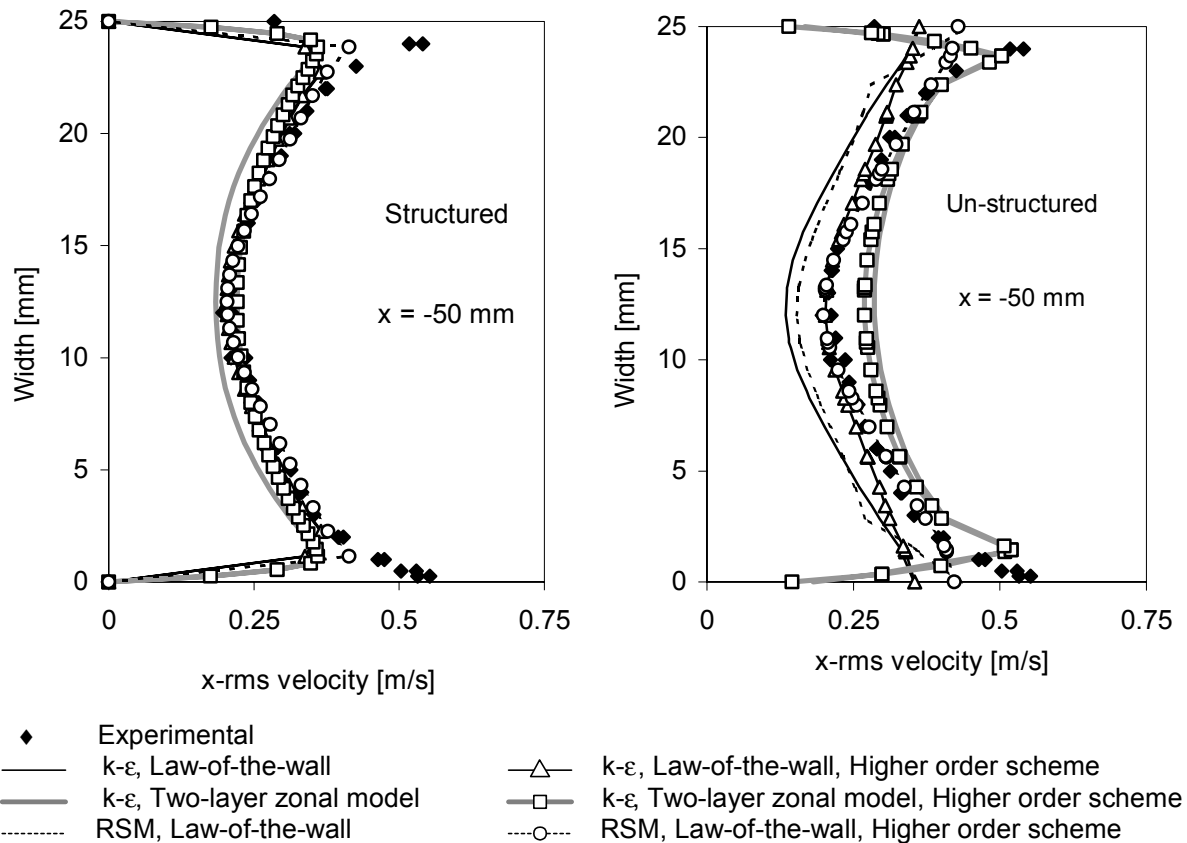


Figure 6.6: The x-rms velocity profiles at $x = -50$ mm.

6.3.3 The profiles at $x = 50$ mm

The velocity profiles are shown in Figure 6.7. The different cases differ little in the prediction of the velocity for the structured cases. For the un-structured cases some deviation exists near the upper wall. The coarse grid for the 'Law-of-the-wall' cases causes the first value to be relatively far away from the wall, and some deviation is noted in this point. A slight overprediction in the predicted velocity is noted near the upper wall, while a relative constant velocity is measured. The influence of the obstacle, the big hook, upstream is overpredicted. It is quite clearly that the mass is not conserved in this location. All the simulated velocity profiles are some higher than the measured profiles, and hence a higher mass flux seems to be used in the simulations. The mass flux is not manipulated for the simulations, and the explanation to the overprediction in the mass flux is in-accuracy between the physical model and the computational model.

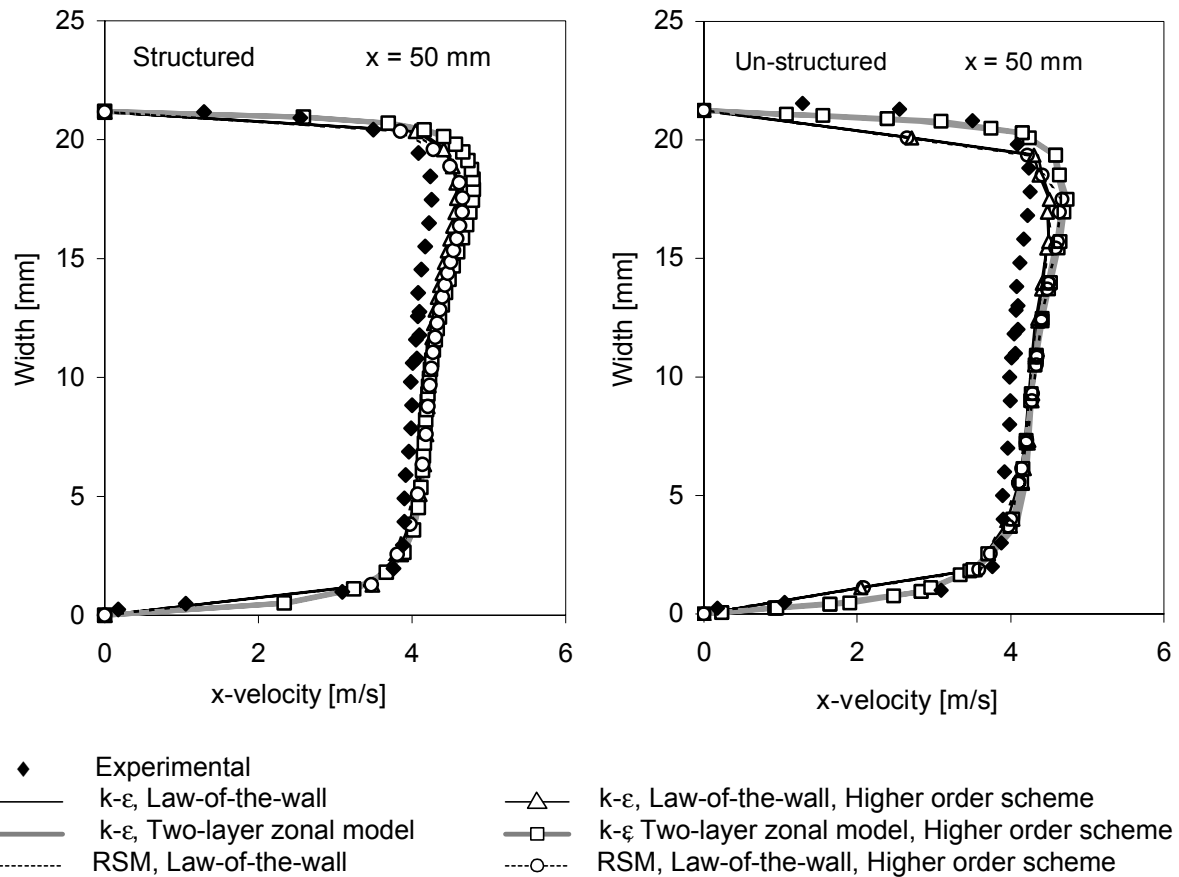


Figure 6.7: The x-velocity profiles at $x = 50$ mm.

The results from the simulations for the x-rms velocities are shown in Figure 6.8. The measured x-rms velocities suggest an s-shaped profile, and this tendency is predicted for most of the cases. For the upper part of the profile, RSM predicts the measured turbulence level very accurate, but the quality of the prediction decreases towards the lower wall. The $k-\epsilon$ predicts well in the lower part of the profile for the structured grid, but towards the upper wall, an increase in the deviation occurs. This was for the structured cases, but some other features are noted for the un-structured cases. For the un-structured cases the $k-\epsilon$ model along with the Two-layer zonal model predicts higher values of the rms velocity near the upper wall. Close to the lower wall, a satisfactory prediction of the rms velocity is noted. Using a higher order scheme increases the quality of the predictions for the un-structured cases, while for the structured cases small differences are noted. Overall it can be stated that the rms predictions are better for the structured cases than for the un-structured cases, and the un-structured predictions have larger variation.

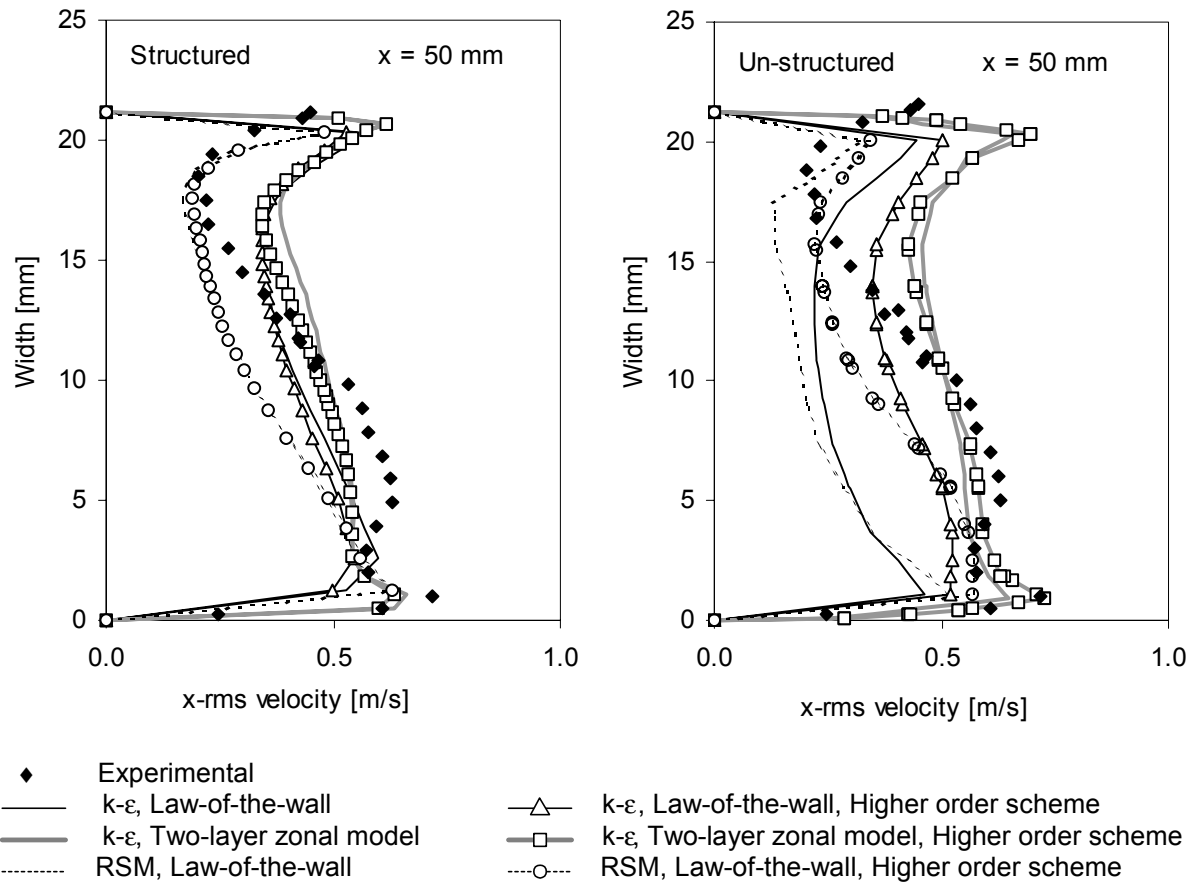
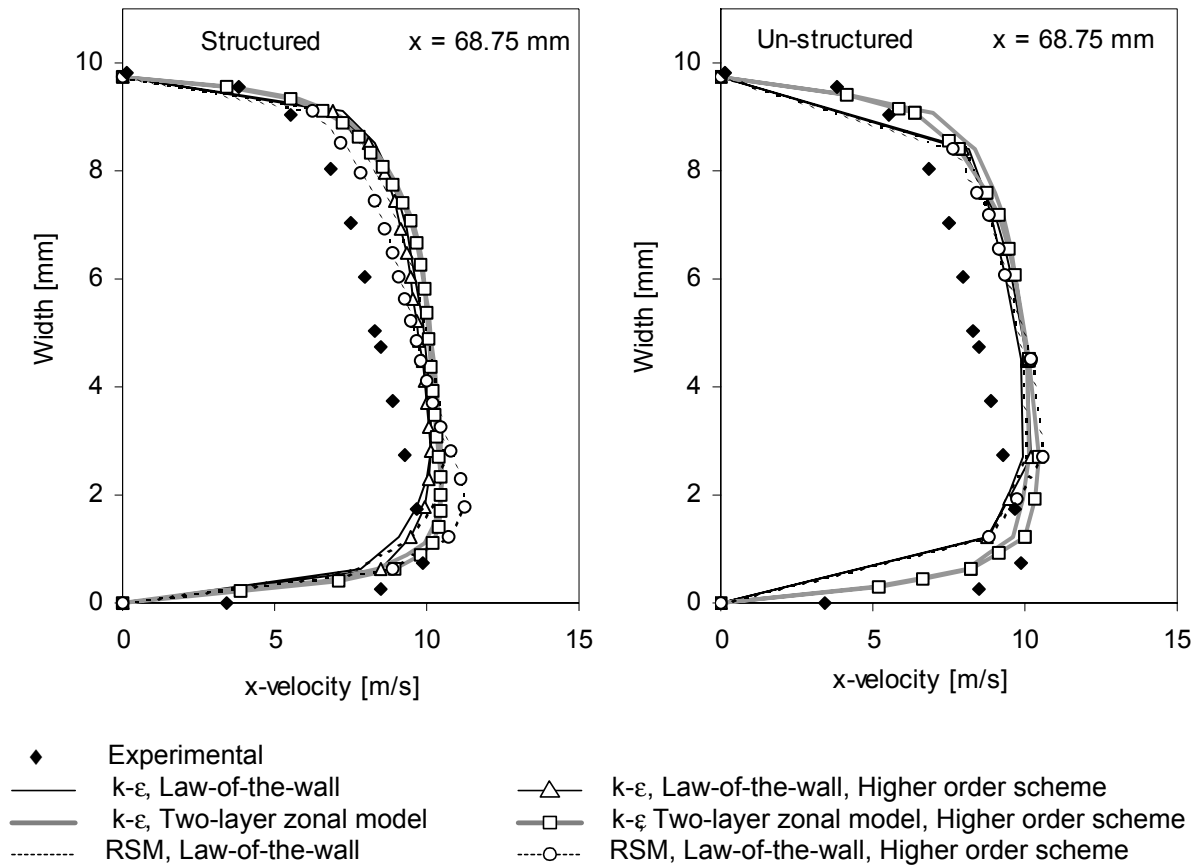


Figure 6.8: The x-rms velocity profiles at $x = 50$ mm.

6.3.4 The profiles at $x = 68.75$ mm

The predicted velocity for this position is shown in figure 6.9. A slight overprediction of the velocity is noted for all the cases. It seems that the mass is not correct simulated, and some deviation in the mass flow is present. This is doubtful because of the good agreement between measurement and simulation in the $x = -50$ mm position. The explanation to the deviation between the measured and simulated x-velocity is found in the geometric model of the vane. A difference in the channel width for the simulation model and the geometrical model may be the cause of this deviation. The difference is in the scale of less than a millimetre, but can nevertheless influence the properties of the flow. For the structured cases the RSM-'Law-of-the-wall' is slightly better than the rest. For the un-structured cases the velocity near the walls is somewhat insufficient because of the grid requirement. The same requirement is valid for the structured cases, but in the un-structured cases more conservative level of the y^+ was chosen. The prediction of the un-structured cases is of same quality as the structured cases.

Figure 6.9: The predicted profiles at $x = 68.75$ mm.

The x-rms velocity is presented in Figure 6.10. For the structured cases the RSM predictions are superior in comparison with the $k-\epsilon$ cases. The RSM predicts the x-rms velocity satisfactorily in major parts of the profile, and only some deviation is noted near the upper wall. For the $k-\epsilon$ cases an overprediction occurs, and the predicted shape of the profile does not match with the measured profile. For the un-structured cases, the RSM shows again good prediction of the x-rms velocity. But the $k-\epsilon$ model along with the 'Law-of-the-wall' shows a better prediction than the three other $k-\epsilon$ cases. In this position, the RMS model is necessary to accomplish good predictions of the rms velocity.

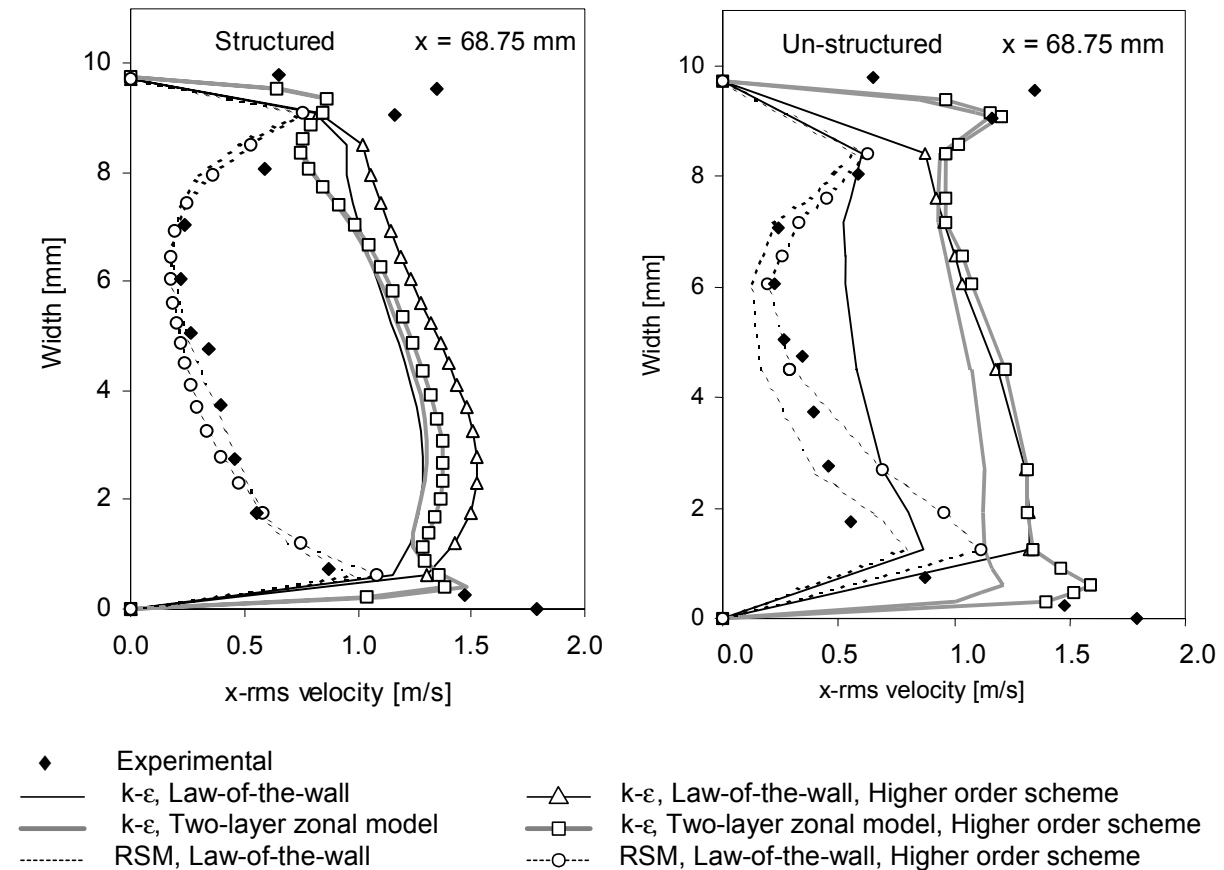


Figure 6.10: The predicted x-rms velocity profiles at $x = 68.75$ mm.

6.3.5 The profiles at $x = 87.5$ mm

The x-velocity profiles for the $x = 87.5$ mm position are shown in Figure 6.11. The predictions are generally satisfactory in the areas where the x-velocity is large and positive. For the negative values of x-velocity, the prediction is not good enough. Many of the different cases predict a linear variation of the x-velocity into the area of the negative x-velocities. This is not like the measured profile, which suggests an s-shaped profile. The RSM and higher order case predicts this S-shape, but the magnitude is not completely predicted. The differences between the structured and un-structured predictions are of minor character, and no obvious differences are commented.

For the y-velocities the measured profile only exists in the middle of the channel, but an idea of the quality of the predictions can be achieved. The results from the comparisons for the y-velocity are shown in Figure 6.12. The RSM and the higher order scheme seems again to be the case, and deviates from the other cases. In addition, the structured RSM and first order scheme case is close to the RSM and higher order scheme, but this is not the case for the un-structured grid.

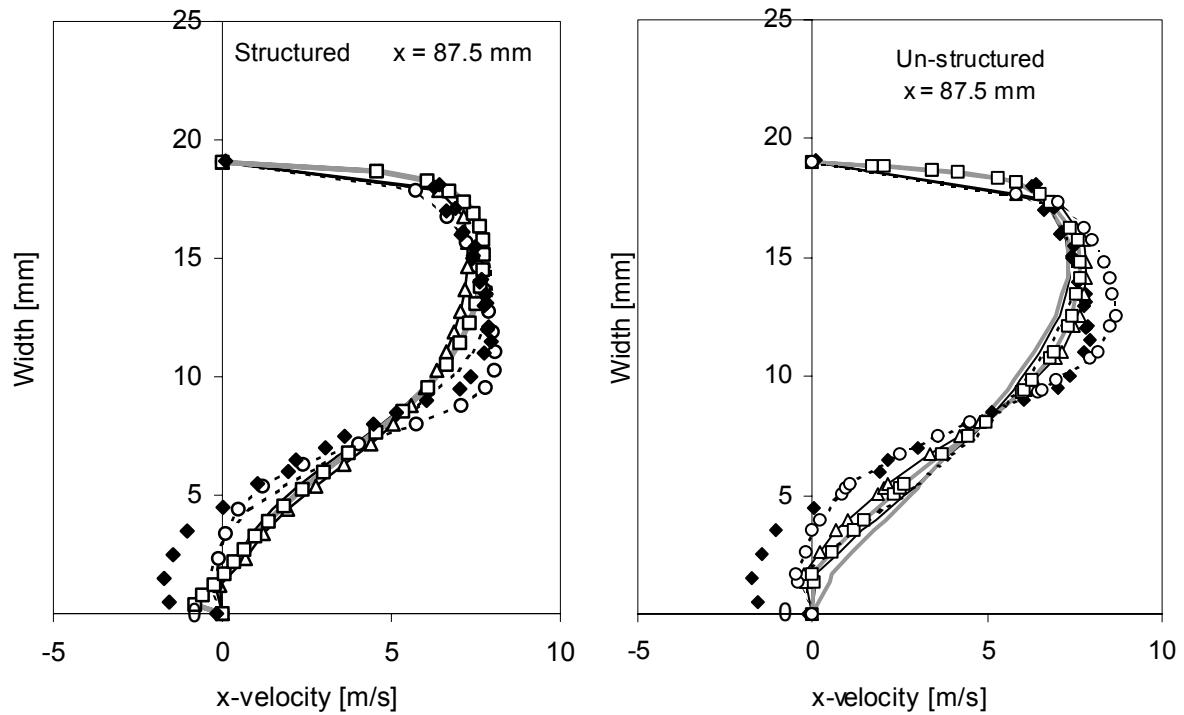


Figure 6.11: The x-velocity profiles at $x = 87.5$ mm, (same legend as Figure 6.12).

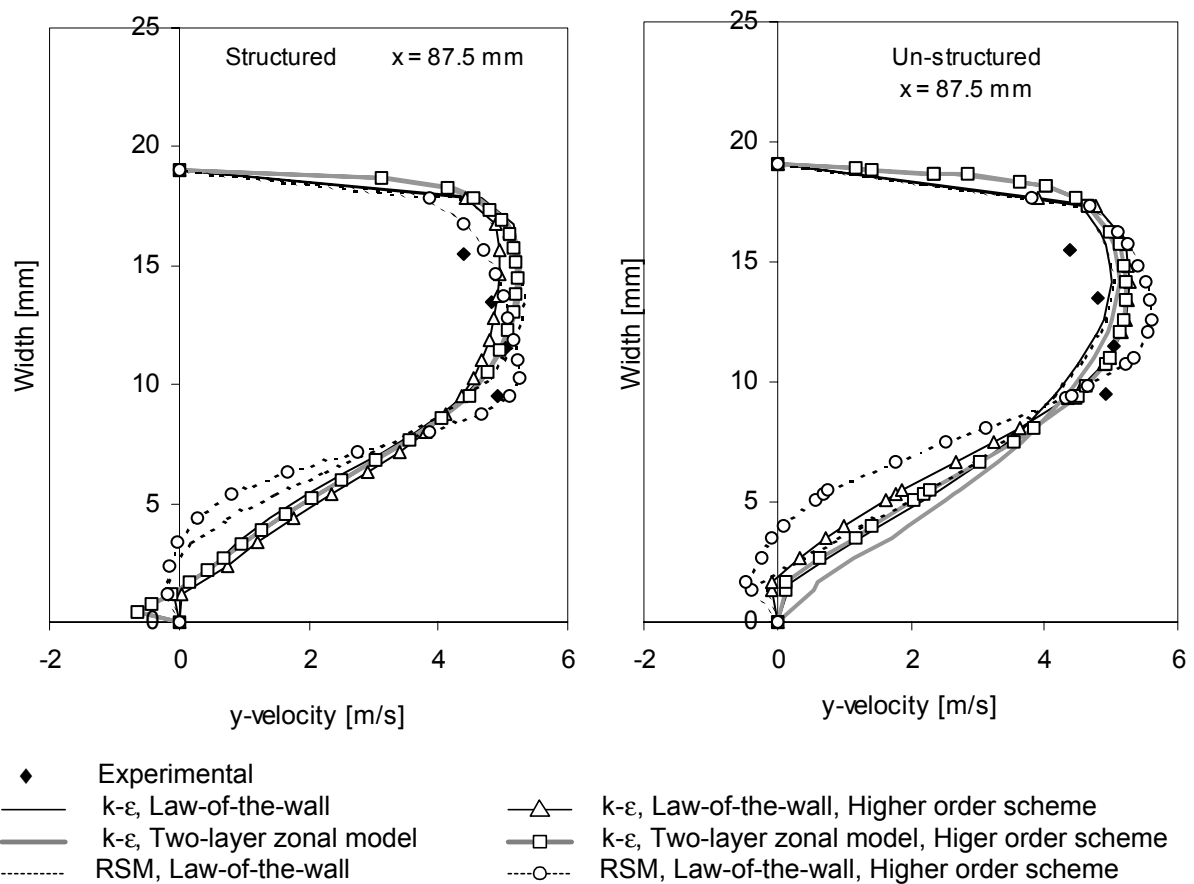


Figure 6.12: The y-velocity profiles for the $x = 87.5$ mm position.

The x-rms velocities show large differences in the predictions, and the predictions are shown in Figure 6.13. There exists also a difference between the predictions from the structured cases contra the un-structured cases. The quality of the prediction varies from area to area for the different cases. For the structured cases the RSM model predicts well in the upper part of the profile, while an underprediction exists in the lower part. For the other cases the situation is the other way around. The prediction for the lower part is far better than at the upper part, where a major overprediction of the x-rms velocity exists. The prediction for the un-structured approach is quite similar as for the structured approach, but the RSM and first order scheme performs better on the structured than on the un-structured approach.

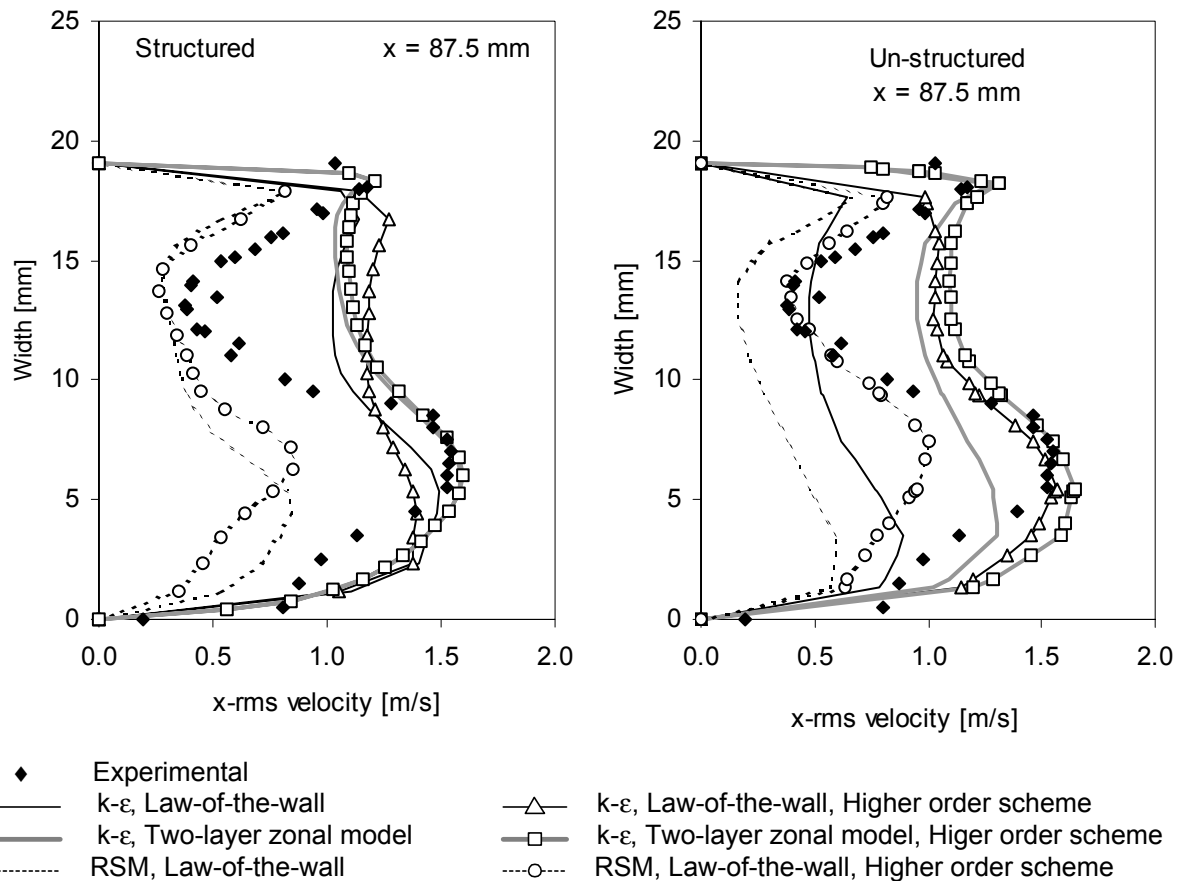


Figure 6.13: The x-rms velocity profiles at $x = 87.5$ mm.

The y-rms velocities are presented in Figure 6.14. The measured profile for the y-rms velocities contains few measurements, but anyway the comparison is carried out. The prediction of the y-rms velocity shows the same trends that were noted for the x-rms velocity predictions.

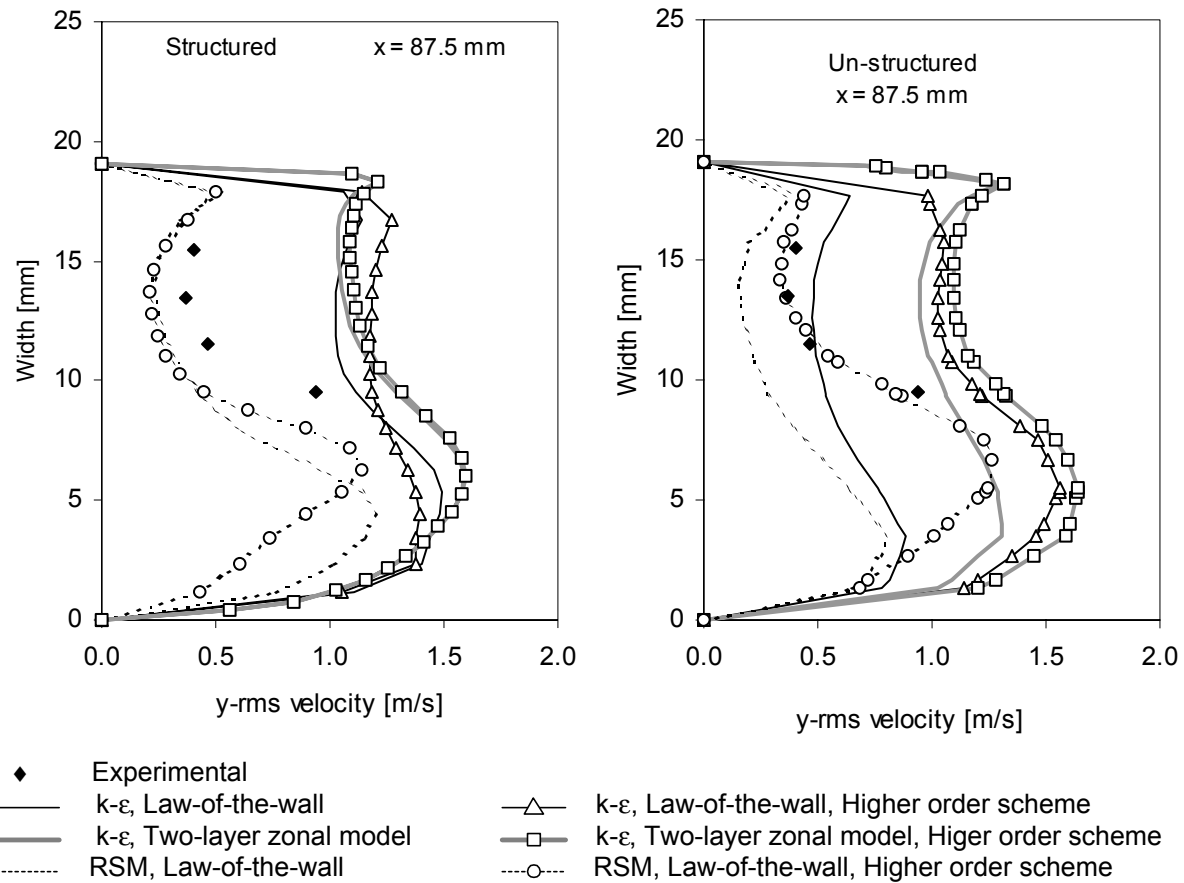


Figure 6.14: The y-rms velocity profiles at $x = 87.5$ mm.

6.3.6 The profiles at $x = 112.5$ mm

The x-velocity profiles from $x = 112.5$ mm are presented in Figure 6.15. The effect of the resirculation zone one position upstream, $x = 87.5$ mm, is over estimated by the RSM model. The measured profile indicates that only a slight effect of the resirculating zone is present. The results from the RSM model show that the x-velocity is underestimated near the resirculating zone and overestimated in the other part of the passage. For the $k-\epsilon$ model the predicted velocity agrees well over large parts of the profile. However, near the lower wall some deviation exists. It seems that the effect from the upstream resirculating zone at $x = 87.5$ mm is underestimated for the $k-\epsilon$ model, while overestimated by the RSM model. While the RSM model with the first order scheme and the higher order scheme produce similar results for the structured grid, the same model combinations produce slightly different results on the un-structured grid.

For the y-velocities, shown in Figure 6.16, the same trends are seen for the x-velocity for this position exist. The RSM model overpredicts the effect from the upstream resirculating zone, while the $k-\epsilon$ model predicts satisfactorily.

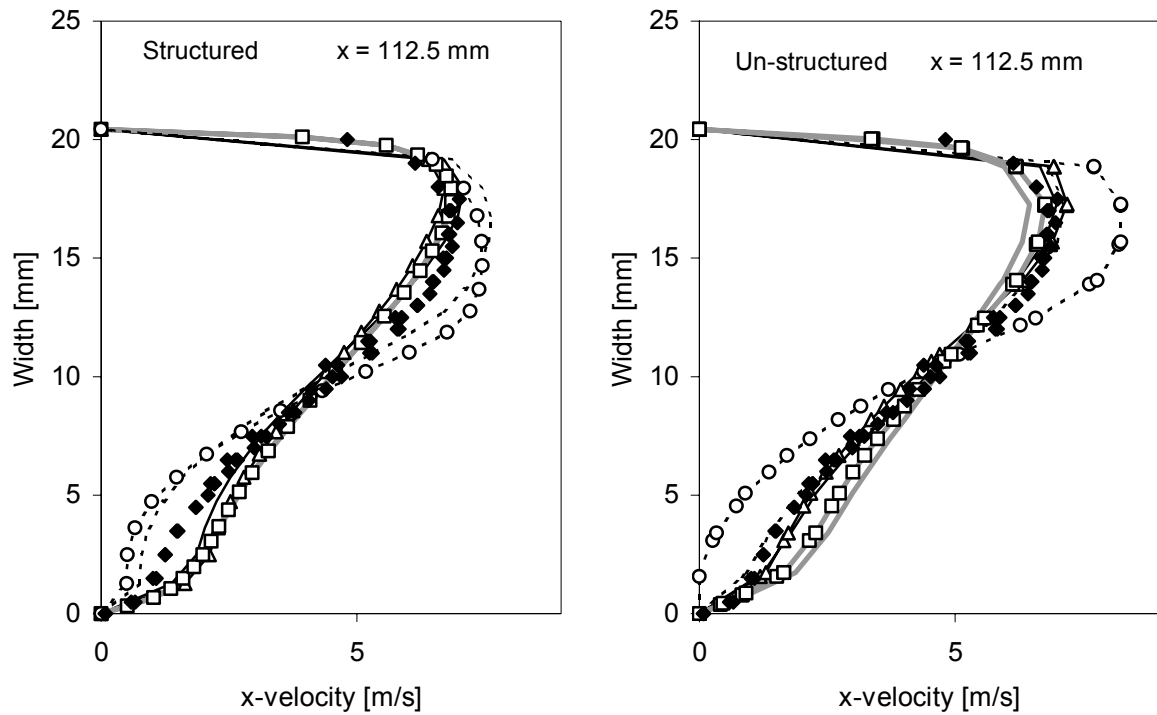


Figure 6.15: The x-velocity profiles in $x = 112.5$ mm position (same legend as Figure 6.16).

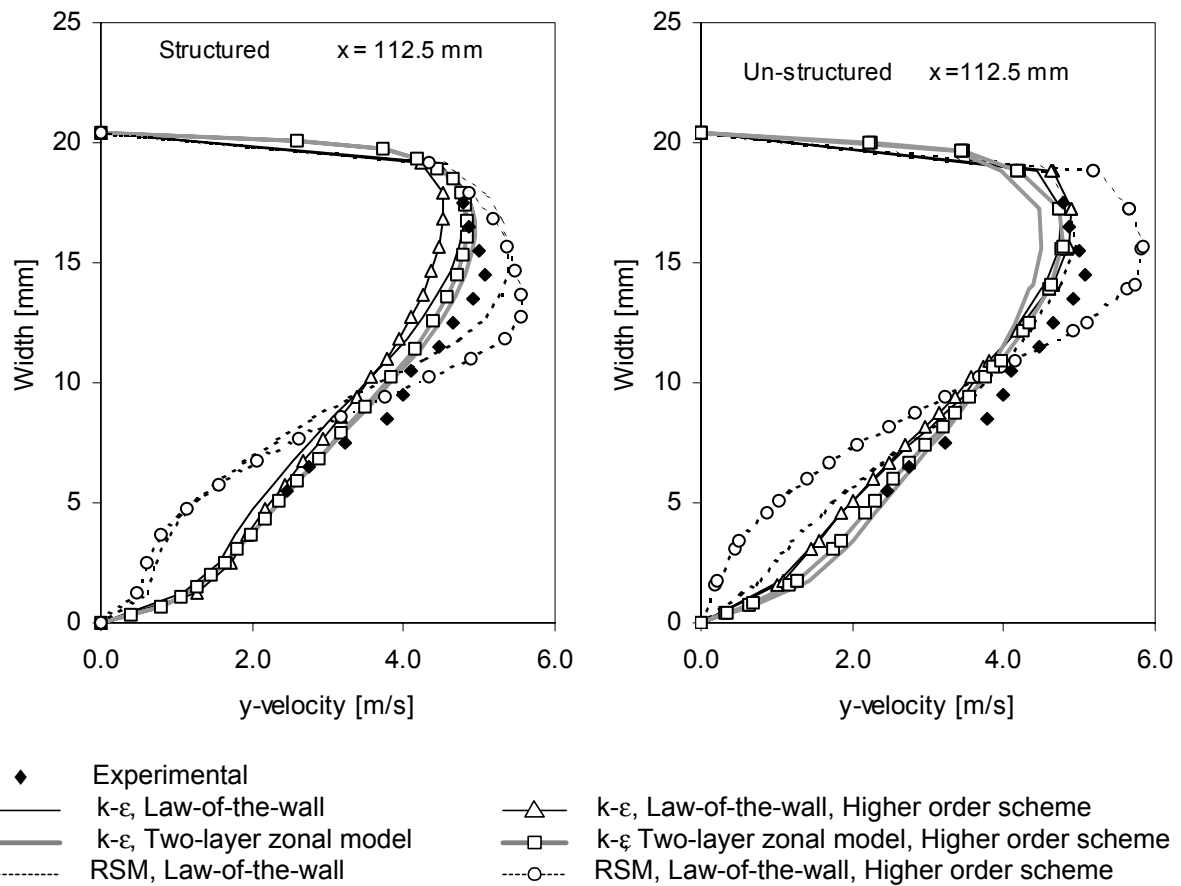


Figure 6.16: The y-velocity profiles for the $x = 112.5$ mm position.

The x-rms velocities for $x = 112.5$ mm are presented in Figure 6.17. For the x-rms velocities some differences between the structured and un-structured cases are noted. For the structured cases the prediction of the x-rms velocities are satisfactory for the k- ϵ cases, while the RSM cases underpredict the x-rms velocity throughout large parts of the profile. For the un-structured cases some deviations between the different k- ϵ cases are seen, and the quality of the predictions is not so high as for the structured cases.

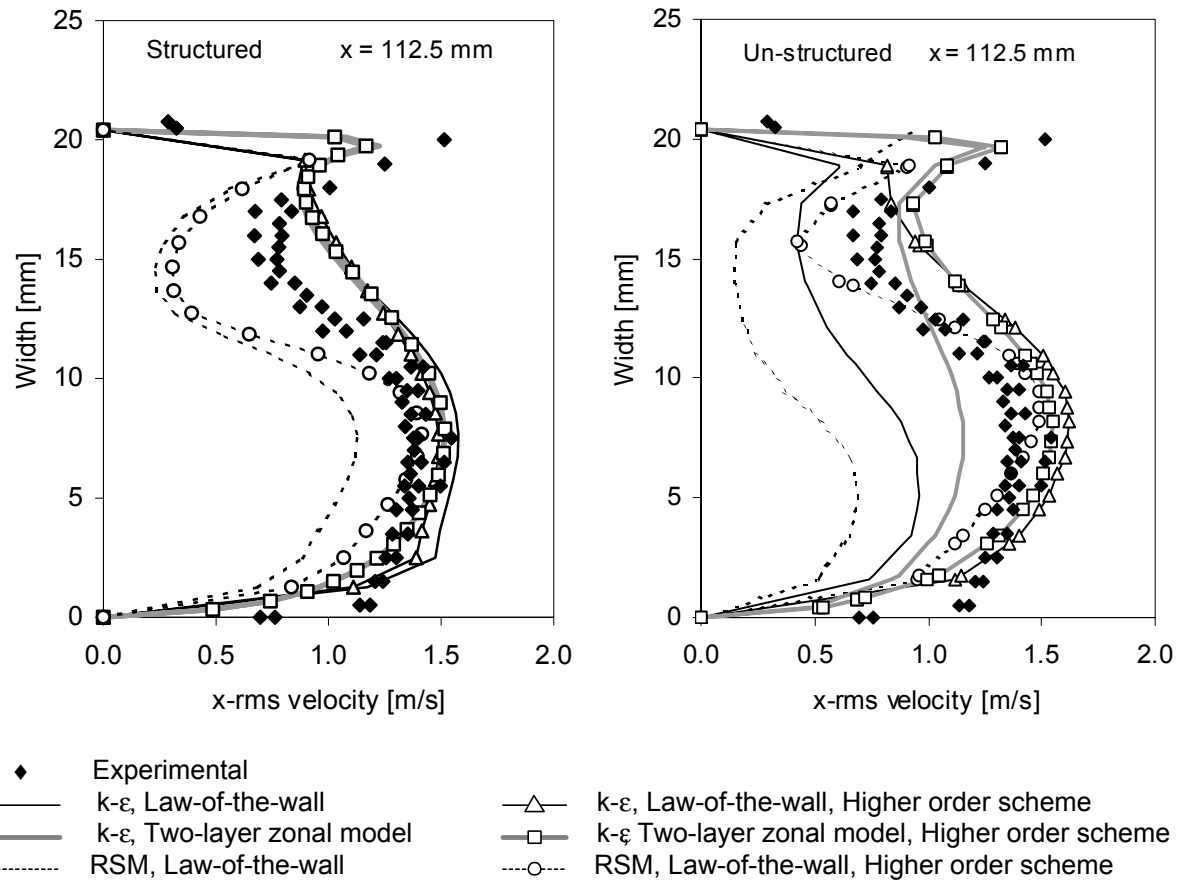


Figure 6.17: The x-rms velocity profiles for the $x = 112.5$ mm profile.

The y-rms velocity profiles are presented in Figure 6.18. The structured cases show a more homogenous prediction of the y-rms velocity than the un-structured cases. In the un-structured cases more deviation between the different cases exists. But the prediction of the y-rms velocity in the lower part of the profile is well predicted by the RSM model together with the higher order scheme. For the upper part of the profile the k- ϵ model performs better, with some exceptions for the un-structured cases.

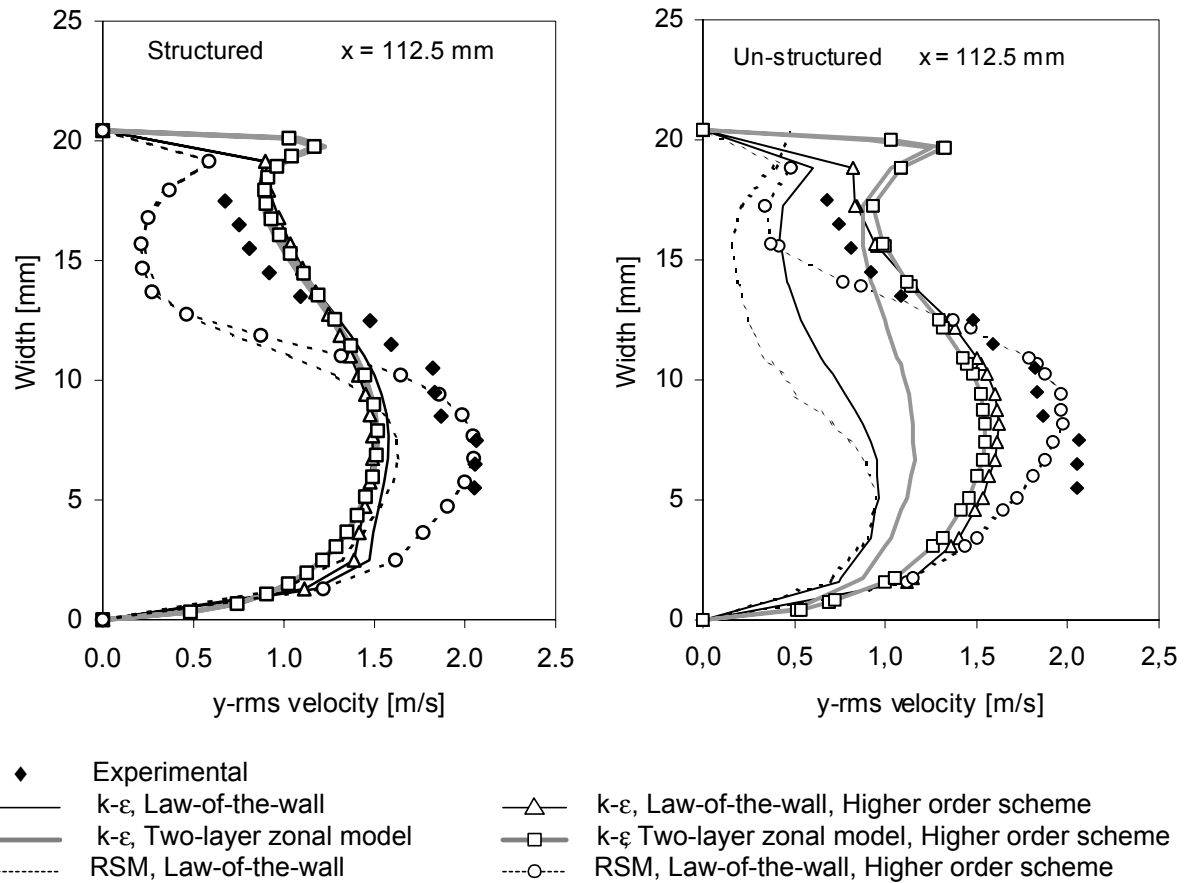
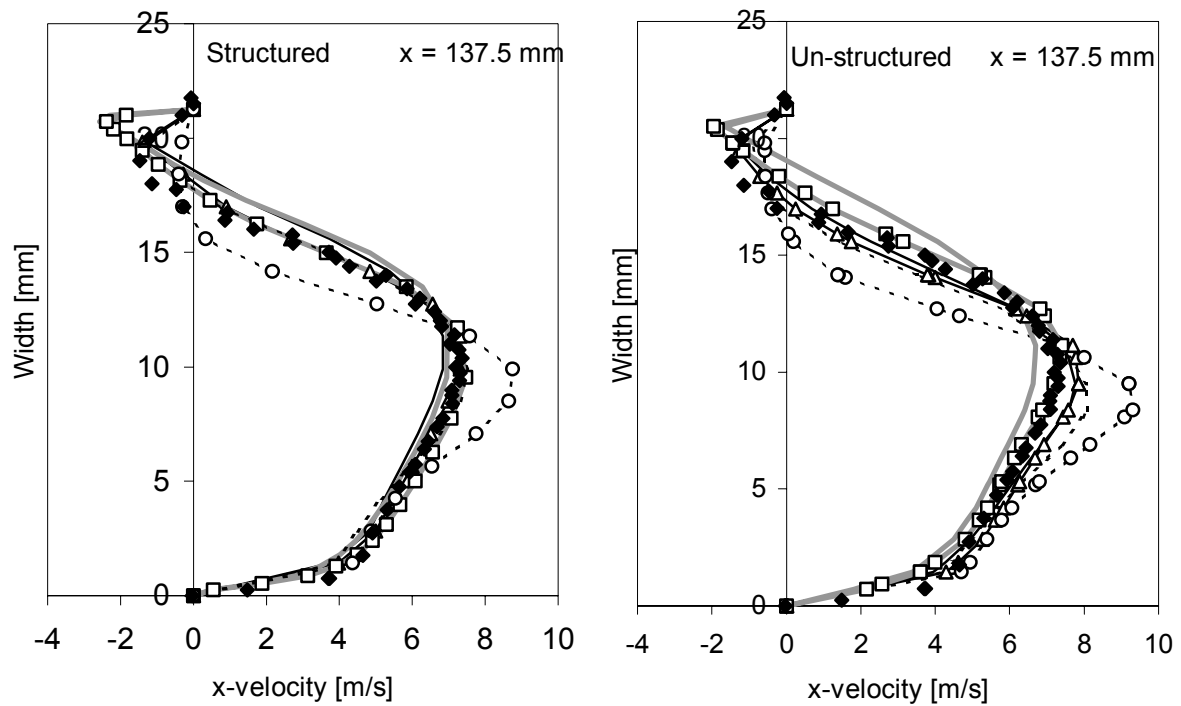
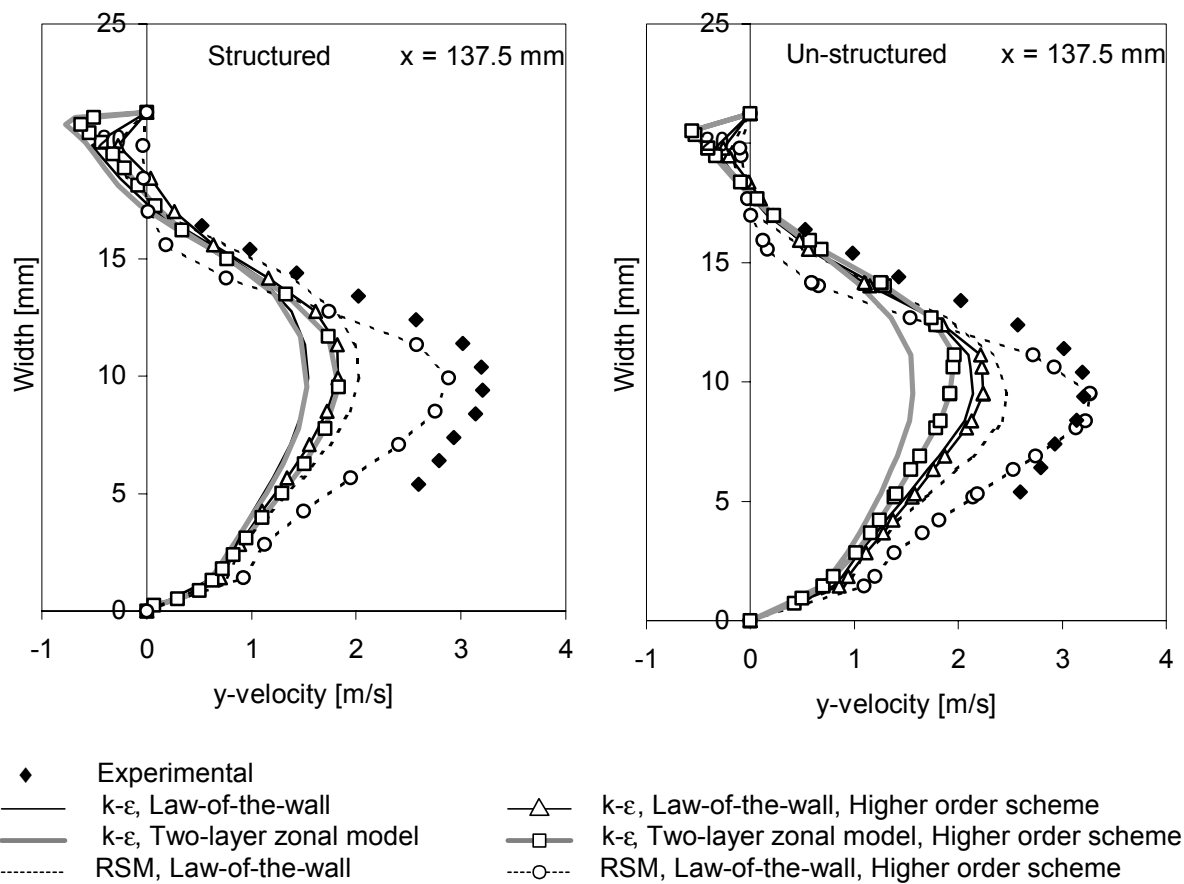


Figure 6.18: The y-rms velocity profiles in the profile located at $x = 112.5$ mm.

6.3.7 The profiles at $x = 137.5$ mm

The x-velocity profiles for the $x = 137.5$ mm position are presented in Figure 6.19. The majority of the cases perform satisfactorily for the x-velocity profile. The deviation from case to case is greater for the un-structured cases than for the structured cases. There is one case that performs different from the others. The RSM together with the higher order scheme overpredicts the magnitude of the maximum velocity. In the backflow area an overprediction of the width of the resirculating zone is noted.

The y-velocity profiles at $x = 137.5$ mm are shown in the Figure 6.20. The y-velocity is best predicted by the RSM and higher order scheme case. This is exactly opposite from the x-velocity, where this case predicts the largest deviations. The other cases underpredict the y-velocity in large parts of the profile, but for the upper part of the profiles the predictions are satisfactorily.

Figure 6.19: The x-velocity profiles for $x = 137.5$ mm (Same legend as Figure 6.20).Figure 6.20: The y-velocity profiles at $x = 137.5$ mm.

The x-rms velocity is presented in Figure 6.21. The structured k- ϵ cases are quite similar in their prediction of the x-rms velocity. Minor deviations between the cases exist, but the overall prediction gives an impression of correct level of the x-rms value. The measured profile indicates a maximum x-rms value at 16 mm, but this maximum is not predicted. The structured RSM cases predict a lower minimum value of the x-rms velocity in the middle of the channel, otherwise the RSM cases are equal to the k- ϵ cases. The un-structured k- ϵ cases vary much more than the structured k- ϵ cases. The k- ϵ model together with first order scheme underpredicts the x-rms velocity, while the other cases overpredict the x-rms velocity for large parts of the channel. An underprediction exists only in the parts where the x-rms velocity is large. The RSM model on an un-structured grid show a large variation between the first order scheme and the higher order scheme. The RSM model together with the first order scheme underpredicts the x-rms velocity in the channel, while the RSM model and the higher order scheme overpredicts the x-rms velocity in the lower part of the channel, and underpredicts in the upper part of the channel.

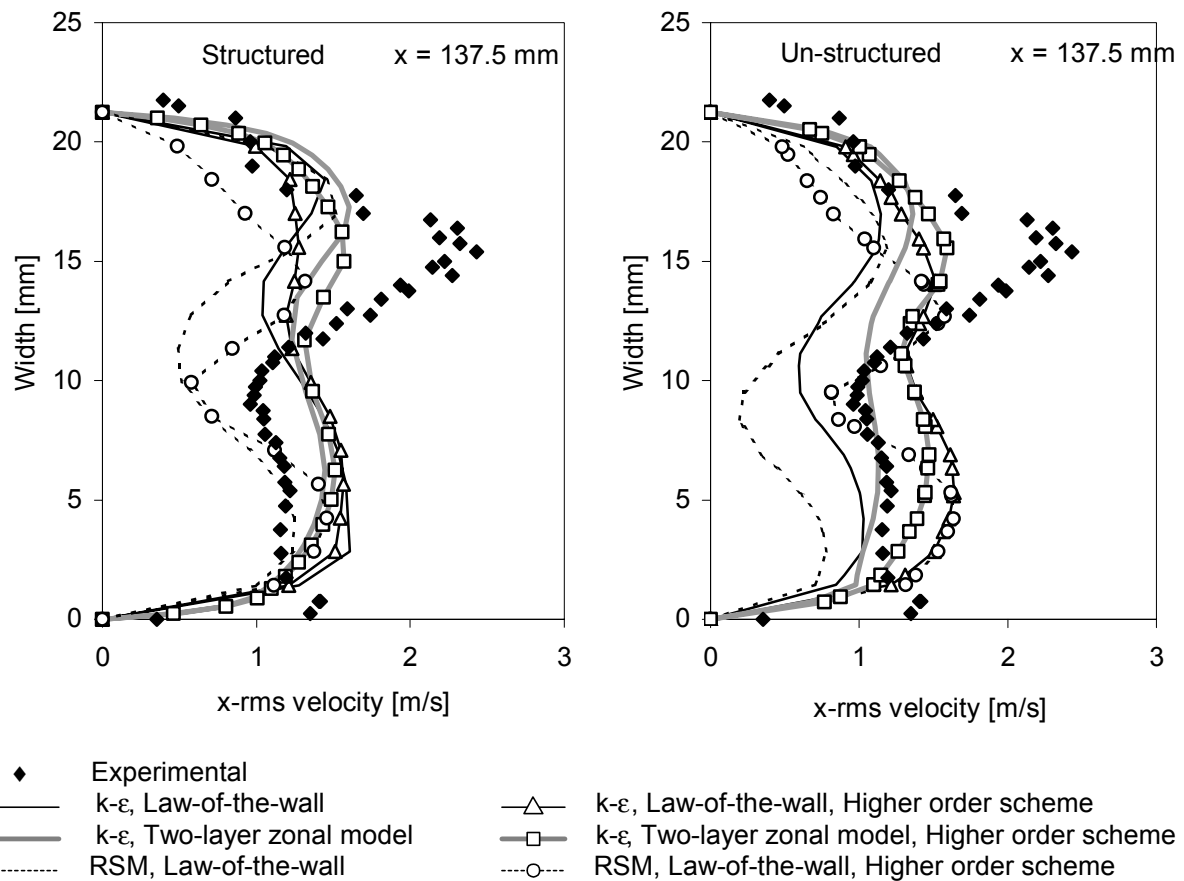


Figure 6.21: The x-rms velocity profiles at $x = 137.5$ mm.

The y-rms velocities at $x = 137.5$ mm are presented in Figure 6.22. For the structured cases the y-rms values are satisfactorily predicted by the k- ϵ cases, while the RSM cases show large discrepancies in middle of the profile and towards the upper wall. For the un-structured cases, the same trends are noted, but the k- ϵ cases show deviations, which were not present at the structured grid.

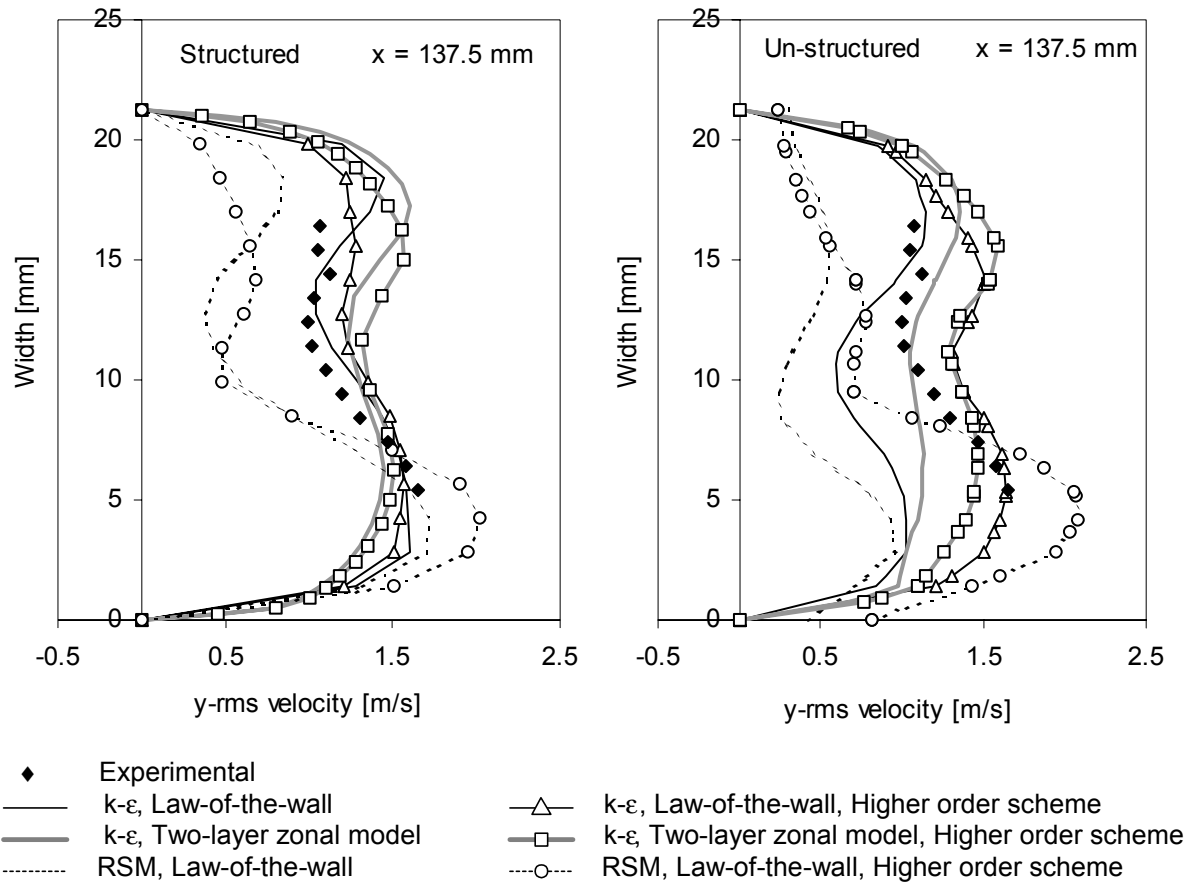


Figure 6.22: The y-rms velocity profile at $x = 137.5$ mm.

6.3.8 The profiles at $x = 165$ mm

The x-velocity profiles at $x = 165$ mm are presented in Figure 6.23. The predicted velocity is satisfactory for nearly all cases, but one exception is the RSM and higher order cases. Both in the structured and in the un-structured case the RSM and higher order case shows deviation. For the un-structured grid the RSM and first order case also shows some deviation. Otherwise the predictions are satisfactory.

The results from the y-velocity are shown in Figure 6.24. For the y-velocity at $x = 165$ mm the $k-\epsilon$ model predicts satisfactorily, while the RSM cases predict more deviation. Especially, the positive y-velocity in the upper part of the profile is not well predicted by the RSM model.

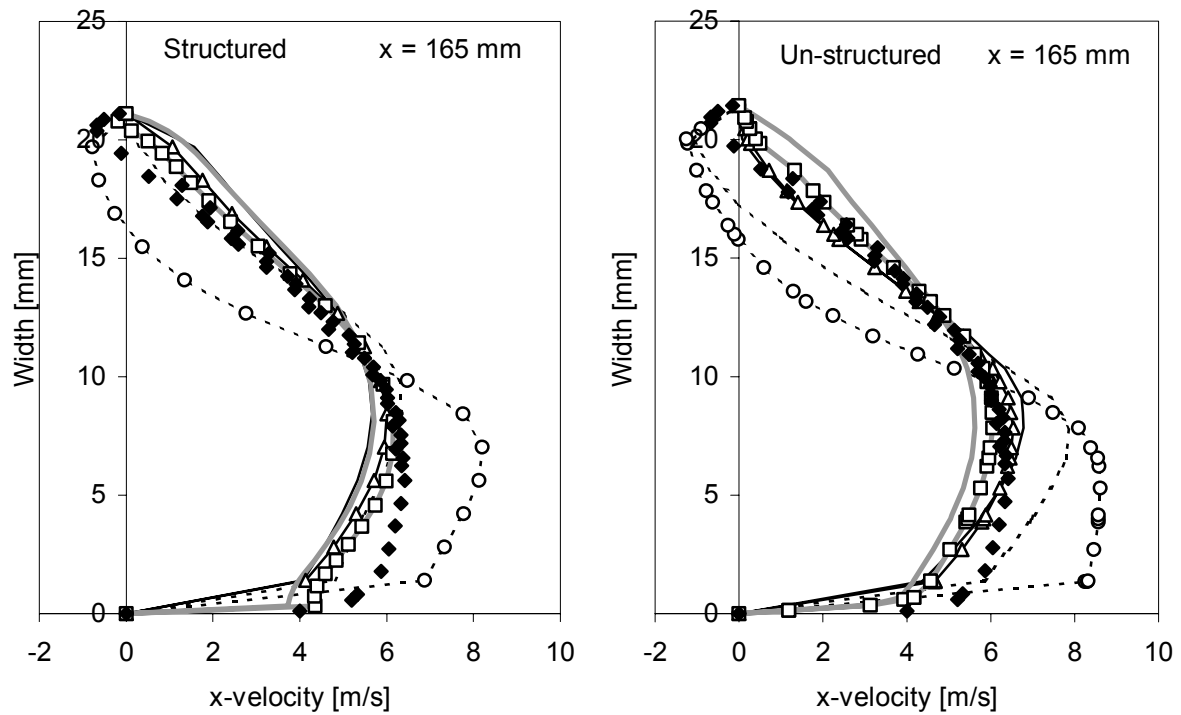


Figure 6.23: The x-velocity profiles at $x = 165$ mm (same legend as Figure 6.24).

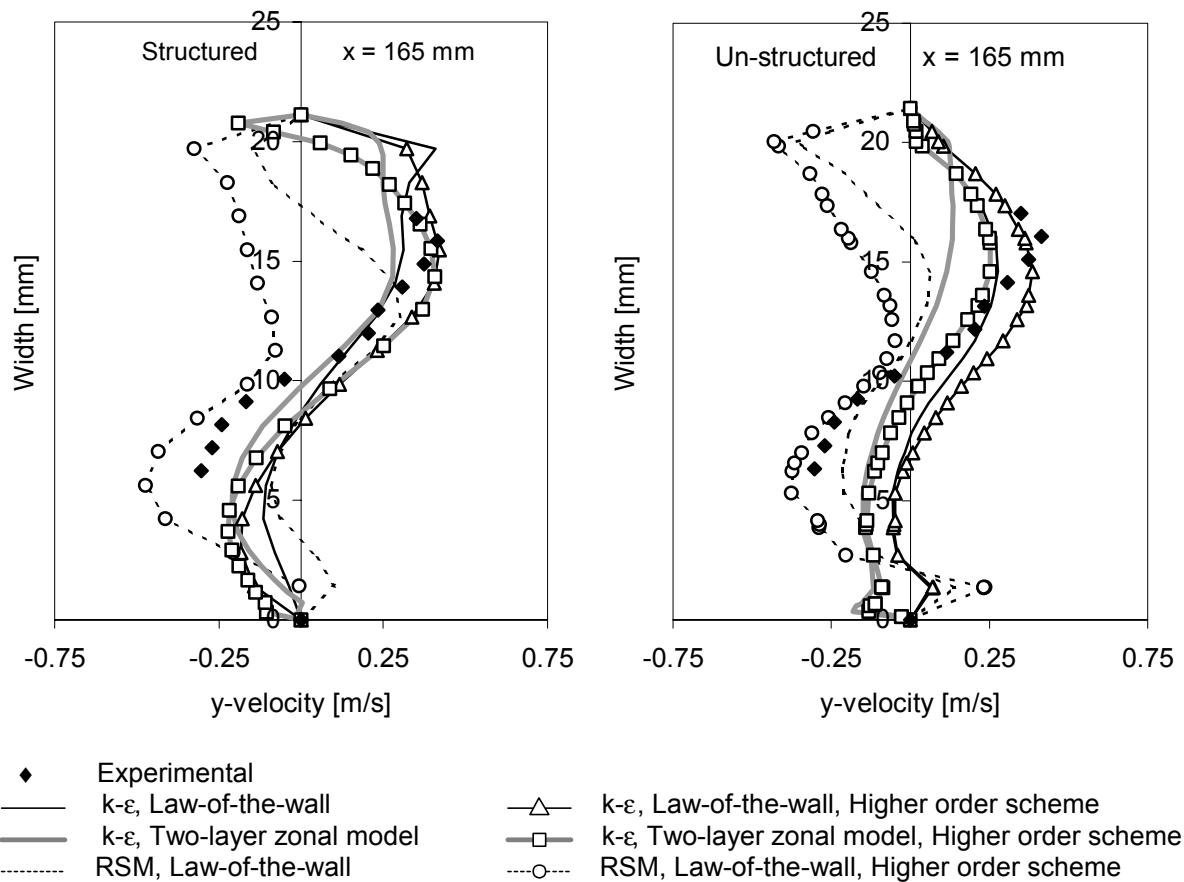


Figure 6.24: The y-velocity profiles at $x = 165$ mm.

The x-rms velocity profiles are shown in Figure 6.25. The predicted x-rms velocities from the structured cases are nearly the same for all the k- ϵ cases, while the RSM cases differ. For the un-structured cases the different models differ more.

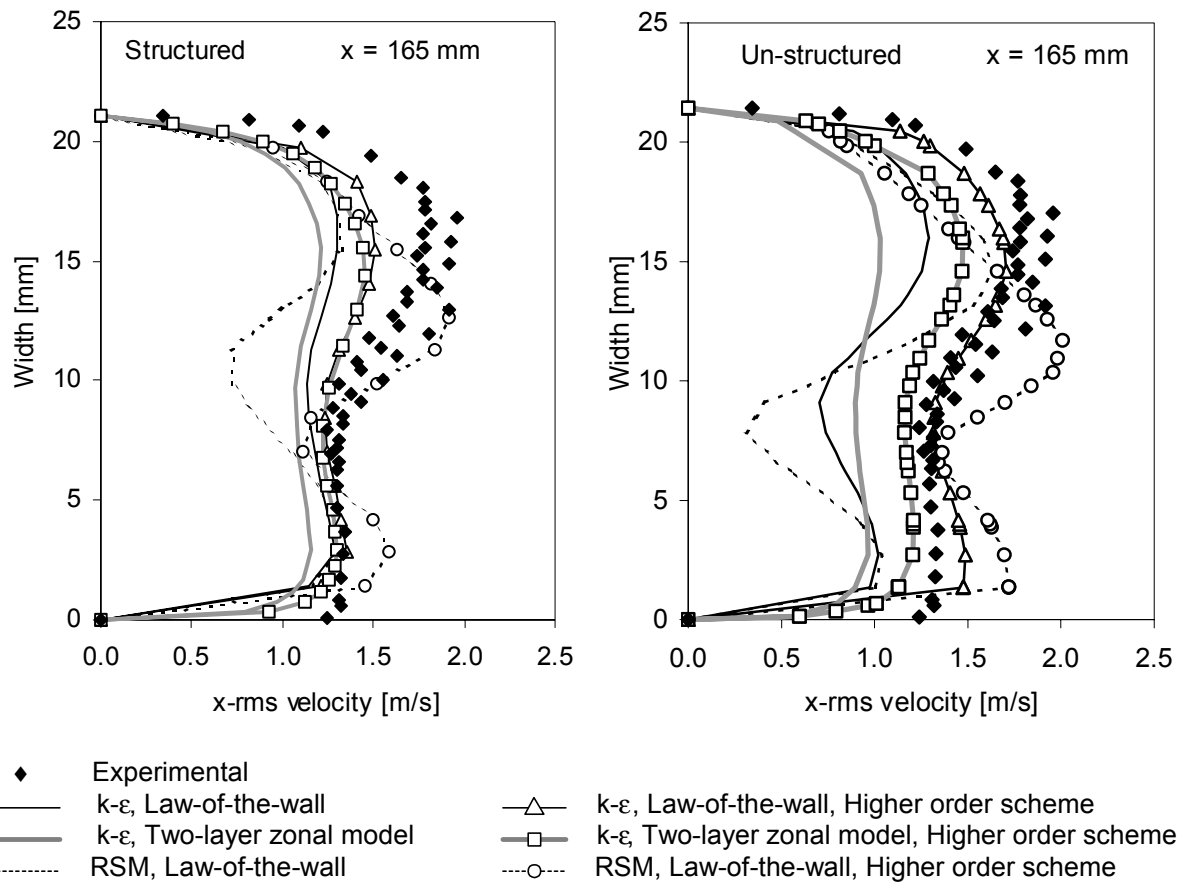


Figure 6.25: The x-rms velocity profiles at $x = 165$ mm.

The y-rms velocities for the $x = 165$ mm position are presented in Figure 6.26. The same trends as observed for the x-rms velocity are also found for this velocity. Both in the structured and the un-structured cases the RSM model shows deviation depending on the first order scheme or the higher order scheme is used.

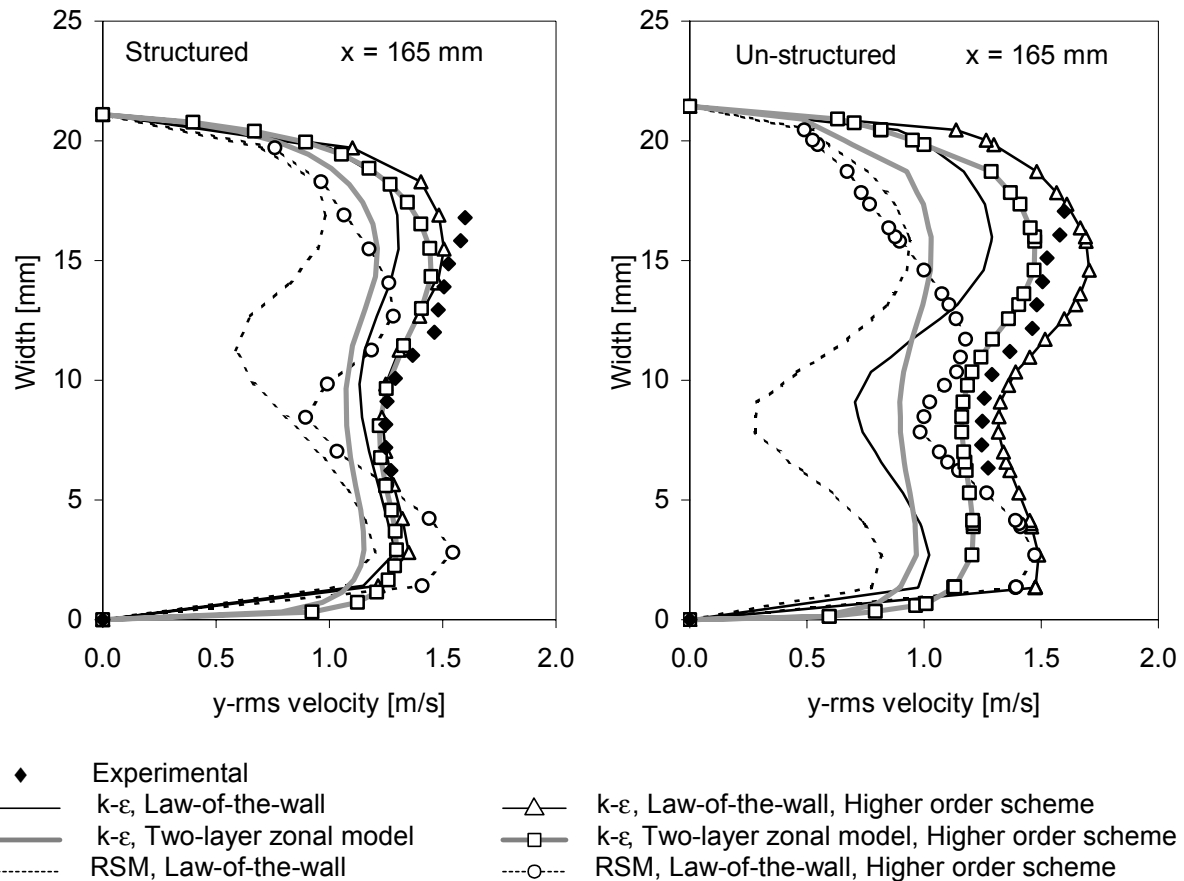


Figure 6.26: The y-rms velocity profiles at $x = 165$ mm.

6.4 Discussion and conclusions from the predicted profiles

The first obvious and important observation is the performance of the RSM model used together with a higher order scheme. The first glimpse of the poor prediction for this case is already noted in the pressure drop table, Table 6.1. A deviation up to 53 % is noted for the RSM model, and this can be verified in the velocity profiles. In the end of the vane, in positions $x = 137.5$ mm and $x = 165$ mm, the RSM model together with the higher order scheme overpredicts the s-shape in the profile. An overprediction of the resirculating zone width is also present. For $x = 165$ mm it is worth noting that the backflow region is not predicted with the first order scheme in the structured grid, but only with the higher order scheme. The reason for why the predictions are not so good for this case is not completely understood. Normally the RSM model is better than the $k-\epsilon$ model in predicting separated flow. In fact, the $k-\epsilon$ model is known to be weak in separating flows, due to the overprediction of the turbulent viscosity. In addition, the use of a higher order scheme should further increase the quality of the predictions. The velocity profiles presented in the previous section, tells a different story. The turbulence level is although not so poorly predicted. At present time there is no good explanation for this phenomena.

For the comparison between the predictions from the structured and un-structured cases only minor differences are noted. A general difference is that the un-structured cases shows more spread in the prediction of the rms velocities. The grid used for the structured and un-structured simulations consists of approximately same number of control volumes. It is known

that the un-structured grid has a higher requirement on the number of control volume than the structured grid, and this can explain the difference in the predictions.

The variation in the different cases concerning the two near wall treatments of the turbulence is negligible. Since the grid used in the simulations is matched with the current near wall model, this is not surprising. It is anyway nice to achieve an anticipated result.

The effect of using a higher order scheme instead of a first order scheme is not a clear issue. The numerical diffusion should be minimal, since a bfc grid is used in the structured case. The flow alignment should then theoretical, be good. But in regions of flow separation, some numerical diffusion might occur. The higher order scheme seems therefore to be the best choice. In some positions for certain combinations of turbulence model and numerical scheme an improvement is noted when using a higher order scheme, but for the same case in a different position in the same profile, it might happen that the first order scheme is better. It seems to be difficult to predict the correct choice of numerical scheme would be in a given position in the separator.

Overall conclusion becomes that the RSM overpredicts the recirculation zone, and hence leads to an overprediction of the pressure drop. As long as the grid matches the proper near wall treatment of the turbulence, the two near wall methods show to be equal. For the k- ϵ model, a satisfactorily prediction is noted throughout the domain, even though the turbulence is anisotropic and some deviations for the backflow areas are noted.

Chapter 7

Droplet generation mechanisms and existing models

In Chapter 5 it was shown that many small droplets were generated in the vane separator. The generated droplets vary in diameter from a couple of microns to an upper limit that is difficult to identify. The upper limit is difficult to identify because the smallest droplet diameter at the inlet corresponds to the largest diameter out of the separator. It is hence not possible to know exactly whether these droplets are generated in the vane separator or if they were present at the inlet. This chapter contains descriptions of the possible mechanisms and existing models for predicting droplet generation. The main objective for this chapter is to point out which mechanism or mechanisms that generate the new droplets. It is also an objective to find existing models that can be used to predict the generated droplet sizes. The structure of the chapter is straightforward, starting off with a short description of possible mechanisms, and then descriptions of possible models are given.

7.1 Introduction to droplet generation mechanisms

Several mechanisms that cause the droplet generation are proposed in the literature [2, 21, 27, 46, 47, 51, 60]. The mechanisms can be classified into 4 groups representing the origin of the new droplets. These groups are:

- 1) Droplet-droplet interaction
- 2) Droplet break up
- 3) Splashing of impinging droplet
- 4) Re-entrainment from liquid film

The names of the groups describe more or less the nature of the mechanism in each group. The four mechanisms are visualised in Figure 7.1.

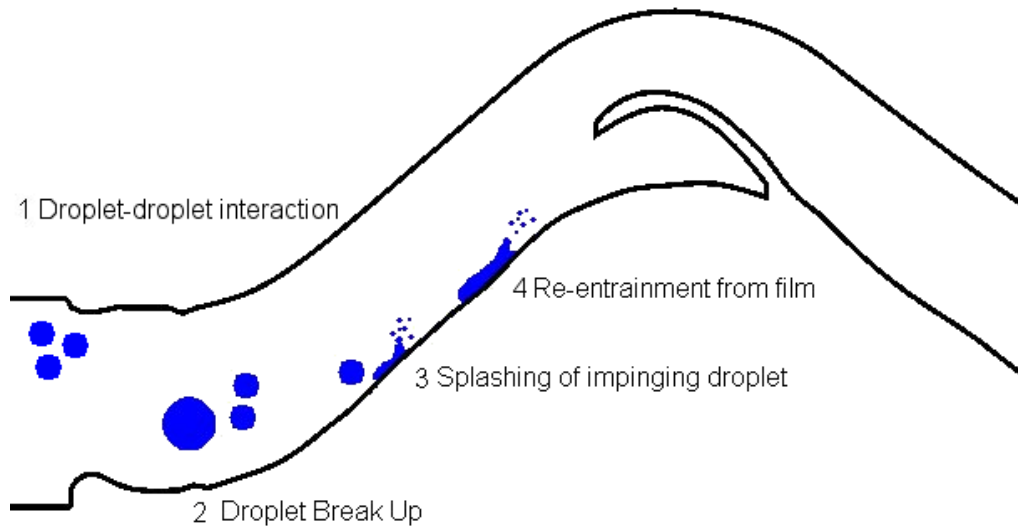


Figure 7.1: A visualisation of the possible generation mechanisms inside the vane separator.

These mechanisms will now be discussed, and seen in light of the experiments carried out in Chapter 5. Typical operational conditions are used in the discussions in order to verify or show that the current mechanisms can be neglected.

7.1.1 Droplet-droplet interaction

This mechanism requires that the concentration of the droplets is relatively high, so that collisions between droplets can occur. This mechanism leads most probably to coalescence between the two colliding droplets. However, if the collision between the droplets is energetic enough a fragmentation of the resulting droplet might be possible. The volume fraction of water used in the experiment is 0.1 % for the low mass flow experiment, so that it can be safely assumed that droplet-droplet interactions do not occur.

7.1.2 Droplet break up

Droplet break up happens when the droplet is broken into smaller fragments as a result from deformation forces. Details concerning the droplet formation process are suggested in various references. The suggested mechanisms span from few to several mechanisms. Tsouris and Tavlarides [60] refer to the literature for several droplet break up mechanisms in turbulent flow, which includes drop elongation in a shear flow field, turbulent pressure fluctuation, relative velocity fluctuations, drop-eddy collisions, thorough breakage, erosive breakage, and binary drop breakage. From Hinze [21] a list of three different kinds of drop break up mechanisms can be found: flattening type, cigar shaped, and bulgy deformation. In Narasimhamurty and Purushothaman [47] a short and informative review of the phenomena is given. In this thesis, the focus will be drawn to the mechanisms suggested in Azzopardi [2]. Only two classes of mechanisms are defined, and these are bag break up and shear break up.

Bag break up

The flow will deflect a droplet in a gas stream. A gas pressure will build, and flatten the drop, and finally turn the drop into a bag. At a certain pressure, this bag will burst, and give birth to many small droplets. The rim will result in few large droplets.

Shear break up

At higher gas velocity the droplet will be dragged to an elongated shape. At a certain air velocity the shear exerted by the gas will be big enough to tear small parts off the main drop. This will result in many small droplets. The deformation forces can be shear from passing gas or turbulence effects. The surface tension of the droplet is damping the influence from these forces. From these two competing forces a Weber number, We , is defined. This Weber number represents the ratio between the deformation forces and the damping action from the surface tension. The Weber number is then

$$We = \frac{\rho_g (u_g - u_d)^2 D_d}{\sigma} \quad (7.1)$$

where D_d is the droplet diameter, ρ_g is the density of the gas, u_g is the gas velocity, u_d is the droplet velocity, and σ is the surface tension [27, 46, 47]. However, the conditions inside the separator are quite different from the experimental conditions used in the literature. Typical a falling droplet is used in order to determine the stable We number. Turbulence effects, gradients in the air stream and geometrical effects can alter the critical We number. Intuitively this change will lower the critical We number. In Table 7.1 different definitions and applications are listed for the critical We number, We_c .

Table 7.1: Some critical We numbers found in the literature [27].

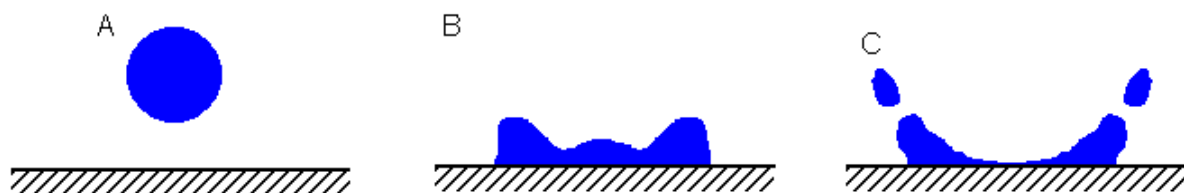
Description	We_c
Large, free falling droplet	22
Large, free falling droplet, based on droplet diameter observations	8~17
A droplet suddenly exposed into a gas stream	$12[1+(\frac{\mu_f}{\rho_f D_d \sigma})^{0.36}]$
Some modifications on the above mentioned equation	$12+14(\frac{\mu_f}{\rho_f D_d \sigma})^{0.8}$
Disintegration due to strong turbulent motions	1.2~2.5

From the table it can be seen that the critical We number, We_c , varies from 22 and to a minimum at 1.2. For a droplet suddenly exposed into an air stream, the critical We number is altered, and a model that contains a viscosity group is added. This model gives values for the critical We number ranging from 12, with no influence from the viscosity group, to a higher value. A modified model for this is also included, and the minimum value for the critical We number is still 12. The last critical We number listed is a We number in a strong turbulent field. This is believed to be the most appropriate for the use inside the separator. Kataoka et al. [27] adds a comment to these criterions: "It is noted that these critical Weber numbers are sensitive to flow conditions. For example, in a pulsating flow the value of We_c can be reduced by as much as 50 percent of the one given in the equation."

The We number is dependent on the relative velocity between the droplet and the carrier gas, in addition to the droplet diameter. The We number is also dependent on physical properties, such as the gas density and the surface tension. These physical properties are however fixed, and not unique for the separator. For a typical droplet in the present application, the diameter is between 20 μm to 100 μm , and the relative velocity is low. The low relative velocity leads to a very small We number. Thus, the critical We numbers mentioned above are never reached in the flow, and hence droplet break up does not happen.

7.1.3 Splashing of impinging droplet

Splashing may occur when a droplet hits a wall. A deformation of the droplet occurs, and small droplets may splash directly from the collision. The physics of the impingement process is shown in the sketch in Figure 7.2. Some nice photos of a droplet impact on a liquid film are given in Chandra and Avedisian [8].



A - The droplet before the collision with the wall.

B - After the collision, crown formation.

C- The jetting of new droplets from the crown.

Figure 7.2: A sketch of the splashing process.

When the impinging droplet hits the wall, a crown starts to form. If the impact contains enough energy, the momentum of the crown is big enough to get detached from the rest of the liquid. Then splashing occurs. The crown is also formed for less energetic impacts, but then the momentum of the crown is too small to detach the ligament, and the movement is finally damped out. Many models for predicting the splashing from an impinging droplet are found in the literature, and the models for this type of impact are discussed in detail in Section 7.2.

7.1.4 Re-entrainment from the liquid film

The fourth mechanism is droplet generation from the liquid film present at the walls. The shear from the passing gas creates waves on the liquid film, and from the wave crests, a re-entrainment can occur. The film is generated from deposited water from earlier impacts of water droplets. In Azzopardi [2] two mechanisms are proposed to explain the re-entrainment. These mechanisms are shown in Figure 7.3.

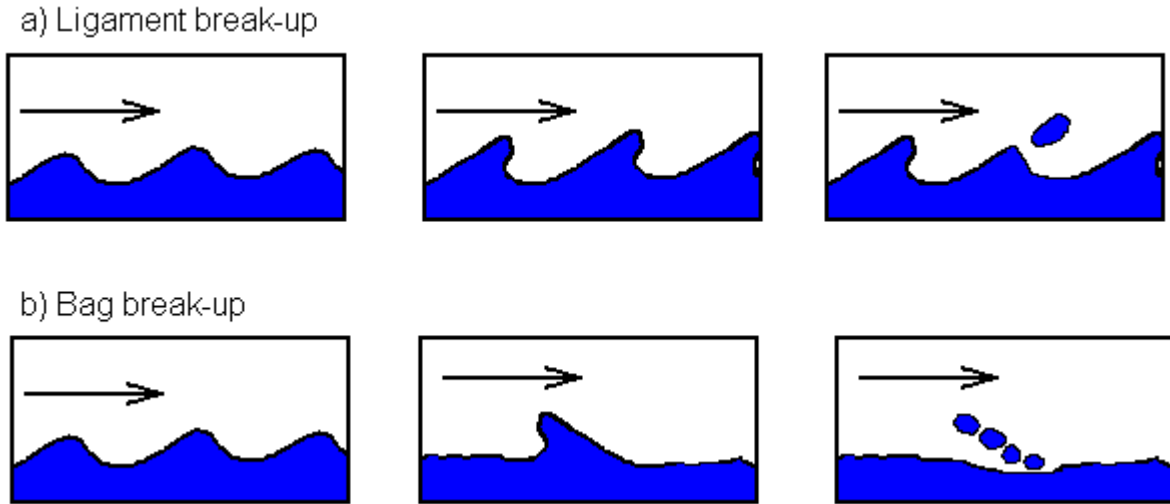


Figure 7.3: Two different mechanism of atomisation.

In the upper three figures the ligament mechanism is shown. A thin ligament is developed from an elongated crest of a wave. The passing gas finally drags off this elongation. The lower three figures show the bag break-up. The bag break-up occurs at lower flow rates than the ligament break-up. For the bag break-up the passing gas undercuts a wave, and the result is an atomisation of the wave.

The vane separator is constructed so that the liquid film drains downwards while the air flows cross-wise passing the liquid film. Some models exist for the re-entrainment of the liquid film, but deviations between the operational conditions in the model and the operational conditions in this vane separator are big. However, these models are tested in Section 7.3.

7.2 Models for splashing of impinging droplet

The splashing of impinging droplet seems to be the most probable mechanism, and many models are presented in the literature. Some of the models are studied and tested in this section, and the first to be presented is the model of Park & Watkins [48].

7.2.1 The model from Park and Watkins

The first impact energy models tested are the models from Park and Watkins [48]. In the reference two models are shown. The models use a Weber number, We , as a threshold between the splashing and the deposition fates. The We number is in this model defined as

$$We = \frac{\rho_l u_{dn}^2 D_{db}}{\sigma} \quad (7.2)$$

where ρ_l is the liquid density, u_{dn} is the component of the drop velocity normal to the surface just before impact, and D_{db} is the drop diameter just before the impact. The model uses the We number as a threshold to predict the outcome of a droplet collision. The original model uses the threshold $We = 80$. When $We < 80$, low We cases, the droplets which strikes the surface, rebound with a reduced velocity. The reduced velocities after the impact are for the normal and tangential velocity u_{dan} and u_{dat} , and the expression for calculating the value of these reduced velocities are shown in Table 7.2. For low We cases, the diameter of the droplet

is equal before and after the impact, $D_{db} = D_{da}$. At high We , $We > 80$, the drops break and divide into lots of smaller ones. The velocities after the impact in the high We cases are modelled as shown in Table 7.2.

Table 7.2: The original model to Park & Watkins [48]

	For $We < 80$	For $We > 80$
u_{dan}	$-\alpha u_{dbn}$	0
u_{dat}	αu_{dbt}	u_{dbt}
D_{da}	D_{db}	$C_{wb} D_{db}$

where α is the energy loss coefficient, u_{dan} is the normal velocity of the droplet after the splash, u_{dbn} is the normal velocity of the droplet before the splash, sub-script t is tangential direction, and C_{wb} is assumed to be 1/3. The energy loss coefficient, α , is calculated from

$$\alpha = \sqrt{1 - 0.95 \cos^2 \theta} \quad (7.3)$$

where θ is the impinging angel to the normal. If we assume a droplet diameter of 140 μm , which is the largest droplet diameter in the experimental work, and a normal velocity of 3 m/s, the We -number is 17.3. This is a conservative guess for the normal velocity, and simulations show that the normal velocities are in the order of 1-1.5 m/s. The calculated We numbers are well below the threshold of 80, and hence all droplets bounces off, with a reduction in the droplet velocity. To reach the threshold of 80, the 140 μm droplet, should impinge with a normal velocity of ~ 6.5 m/s. This is an artificial high normal velocity, since only minor parts of the separator contain velocity magnitudes, above this limit.

A second model is presented in the same reference [48], and this is referred to as the new model. Instead of a fixed threshold, the threshold in this model is calculated according to the equation

$$We = 1320 La^{-0.18} \quad (7.4)$$

and the La is defined as

$$La = \frac{\rho_l \sigma D_{db}}{\mu_l^2} \quad (7.5)$$

The La coefficient is calculated for the experimental conditions in the separator, and for a 140 μm droplet the calculated threshold will be at $We = 60$. This threshold is too high, and all the droplets are predicted to rebound.

The conclusion from these two models is that the models are not useful for explaining the droplet generation. Suggested reasons for this can be found in the experimental material that is used to derivate the We -threshold for the models. The material is based on the works from Wachters and Westerling [64], and this work focuses on hot wall impingement. The experimental work carried out in this thesis operates at room temperature, and deviations are likely to be present.

7.2.2 The model from Mundo et al.

The model from Mundo et al. [42, 43, 44] uses a correlation between the Ohnesorge number, Oh , and the Reynolds number, Re , for the impinging droplet. The correlation is

$$K = Oh Re^{1.25} = \left(\frac{\rho_l^3 u_{dn}^5 D_{db}^3}{\mu_l \sigma^2} \right)^{1/4} \quad (7.6)$$

where:

$$Oh = \frac{\mu_l}{\sqrt{\rho_l \sigma D_{db}}} \quad \text{and} \quad Re = \frac{\rho_l u_{dn} D_{db}}{\mu_l} \quad (7.7) \text{ and } (7.8)$$

When $K > 57.7$ splashing occurs, and for $K < 57.7$ completely deposition occurs. These models or correlations are based on normal velocities, and hence the influencing factor is the normal momentum, and not the total momentum. An analysis of the K values reached in a simulation of the experimental rig shows that the maximum K reached was 10. This is well below the splashing threshold, and hence all droplets are deposited. Further analysis shows that a 140 μm water droplet must impinge with a normal velocity of ~ 7.3 m/s in order to reach a value of $K = 57.7$. This is not likely considering the operational conditions in the separator. This model leads to deposition for all the droplets in all the regions of the separator, and is not able to predict the generation of the small droplets.

7.2.3 The model from Cossali et al.

In this model from Cossali et al. [11] a correlation similar to the model from Mundo et al. is used, but a modification for the liquid film is included. The threshold is

$$K_L = (Oh^{-0.4} We) = 2100 + 5880 \delta^{1.44} \quad (7.9)$$

where Oh is defined in Equation (7.7), and We is defined in Equation (7.2), and δ is the non-dimensional film thickness, (h/D_d) where h is the film thickness. This correlation holds for $0.1 < \delta < 1$ and $Oh > 7 \cdot 10^{-3}$. This correlation is within 10 % accuracy, and correlates adequately with other available experimental results. An analysis of the impacts identified inside the vane separator is made. The calculated K_L is shown in Table 7.3.

Table 7.3: K_L according to the model from Cossali et al. [11].

Diameter [μm]	Normal velocity [m/s]	K_L predicted [-]	K_L threshold [-]
140	3	109.5	$2100 + 5880 \delta^{1.44}$
140	13.2	2105	$2100 + 5880 \delta^{1.44}$
50	3	31.84	$2100 + 5880 \delta^{1.44}$
50	24.4	2106	$2100 + 5880 \delta^{1.44}$

Seen from Table 7.3 the threshold is never reached, and the deviation is relatively big. A velocity of 13.2 m/s for 140 μm diameter droplet gives a value over the threshold. This is a normal velocity that is not present in the separator, and hence the threshold is never reached, and all droplets are deposited. An explanation to why all the droplets are modelled to deposit, can be found in the basis of the model. The model is based on measurements of droplets, which are from 2 - 5.5 mm in diameter. The droplets in this application are far smaller than this, and this has probably a large influence on the splashing threshold.

7.2.4 The model from Schmehl et al.

The model from Schmehl et al. [57] is based on the Reynolds number, Re , and the Laplace number, La . Splashing is predicted when

$$Re > 24La^{0.419} \quad (7.10)$$

where La is defined in Equation (7.5), and Re is defined in Equation (7.8).

The Table 7.4 shows the calculated values from an analysis carried out on the droplets found in the separator.

Table 7.4: The calculated values for the model of Schmehl et al. [49].

Diameter [μm]	Normal velocity [m/s]	Re [-]	$24 \cdot La^{0.419}$ [-]
140	3	418.7	1144
140	8.2	1145	1144
50	3	150	743
50	14.9	743	743

The right hand side of Equation (7.10) is always greater than Re , hence the splashing regime is never reached, and deposition always occurs. The La number seems to be too large. The calculated velocities for the threshold Re numbers are too high, because such high numbers are never achieved. This model is not appropriate to predict the droplet generation inside the separator.

7.2.5 The model from Stanton and Rutland

Stanton and Rutland [58] divide the fate of the impact into four regimes; stick, rebound, spread, and splashing. The model uses different sources in the literature to set the threshold between the different regimes. The summary of the model is found in Table 7.5.

Table 7.5: The model from Stanton and Rutland [58].

Regime	Name	Criterion
1	Stick	$We < 5$
2	Rebound	$5 < We < 10$
3	Spreading	$10 < We < 18^2 D_d (\frac{\rho_l}{\sigma})^{1/2} u_{dn}^{1/4} f^{3/4}$
4	Splashing	$18^2 D_d (\frac{\rho_l}{\sigma})^{1/2} u_{dn}^{1/4} f^{3/4} < We$

The Weber number is defined in the same way as Equation (7.2), and f is the frequency. The introduction of the frequency is noted in the threshold for spreading and splashing. The frequency is a bit troublesome to define in the simulations. However, Mundo et al. [44] give a suggestion of how to rewrite the frequency in terms of velocity and diameter. According to Mundo et al.

$$f = \frac{u_{dn}}{D_d} = \frac{1}{\tau_k} \quad (7.11)$$

where τ_k is the characteristic kinematic time scale. The threshold that sets the start of the splashing regime, is written

$$18^2 D_d (\frac{\rho_l}{\sigma})^{1/2} u_{dn}^{1/4} (\frac{u_{dn}}{D_d})^{3/4} \quad (7.12)$$

The calculated threshold for a 140 μm droplet impinging at 3 m/s is then 298. In order to reach the splashing limit, the We number must be equal to 298. This We number is never reached, and hence the model is not suitable to predict the droplet generation in the separator.

7.2.6 Conclusions from splashing models

Several models for splashing are tested, and none of the tested models was able to predict splashing. The models have a too high threshold for the start of the splashing regime, and this threshold is never reached and deposition appears. However, an exception exists for the model of Park and Watkins, where rebound was predicted for every impact. The reason why the tested models is not suitable to predict the droplet generation inside the separator, is believed to arise from the differences in the basis of models and the operational conditions in the separator. The droplets in the separator are small, and for some of the models the experimental basis is for bigger droplets. For other models the experimental work considers warm droplets, with non-negligible mass transfer from the surface.

Other reasons for the lack of prediction may arise from the fact that the experimental basis for the models is more or less quiescent environment, while for the vane separator turbulent effects exist. Al-Roub and Farrell [1] found that the droplet spacing is a variable to include when the threshold between splash and deposition is to be determined. An interference pattern of the waves created at the droplet surface was formed. It was then shown that if the spacing

between two droplets was perfect, addition of two waves could occur, and an atomisation could be the result. This observation is useful, and can explain why these models fail in predicting the splashing.

The main conclusion is, however, that the splashing mechanism cannot explain the generation of the new droplets.

7.3 Models for re-entrainment from the liquid film

In the previous section it was shown that the droplet does not splash directly, but other mechanisms must explain the generation of droplets inside the vane separator. Small droplets can be generated from the liquid film by the mechanism known as atomisation or re-entrainment. In the rest of the thesis, the re-entrainment term is used, since all water exist initially as droplets. Models for the re-entrainment mechanism are developed from several authors, but these models are mostly designed for annular gas/liquid flows in pipes. This is not directly comparative with the flow conditions in the separator. In the separator the liquid film is drained by the gravity, and the air is flowing horizontal over the film. Not much useful information is found on such types of flow. Some re-entrainment models are tested, with varying quality, and these models are discussed in the next sections.

7.3.1 The model from Zaichik et al.

The model from Zaichik et al. [70] calculate a critical We number, We_i^* , according to

$$We_i^* = [2.5 \cdot 10^{-5} + 6 \cdot 10^{-4} (Re_f - 160)^{-0.6}] Re_f \quad (7.13)$$

where the film Reynolds number are defined according to

$$Re_f = \frac{4h\bar{U}_f}{\nu_l} \quad (7.14)$$

where h is the mean film thickness, \bar{U}_f is the mean film velocity, and ν_l is the kinematic liquid viscosity. We_i is found through the following relation:

$$We_i = \frac{\tau_i h}{\sigma} \quad (7.15)$$

where τ_i is the interfacial stress. The re-entrainment takes place if We_i exceeds We_i^* . The major drawback with this model is the requirement on the liquid Reynolds number, Re_f . No re-entrainment is present until the liquid Reynolds number has reached a value of 160. To reach a value of 160 on the liquid Reynolds number is very hard for the operational conditions inside the vane. For water at 20°C, the kinematic viscosity is $1.003 \cdot 10^{-6} \text{ m}^2/\text{s}$. If the kinematic viscosity is inserted into the equation above, the product between the mean film thickness, h , and the mean film velocity, \bar{U}_f , is $4.012 \cdot 10^{-5}$. However, the mean film thickness is not easy to achieve. Patches of water are spread around, and many ways of calculating the mean of this can be applied. In addition, the film has actually no steady state velocity, but varies strongly in time and place. The effect of the crosswind is notable, and causing the film to drain slantwise. Sometimes the film does not drain at all, and then suddenly it starts to drain. However, if these two parameters are approximated in the case when the film drains, the values of the variables are given in Table 7.6.

Table 7.6: Approximated values for calculating the film Reynolds number.

Variable	Value
Mean film thickness	$5 \cdot 10^{-4}$ m
Mean film velocity	0.1 m/s

The resulting Reynolds number for the film is ~ 200 . The We_i^* can now be calculated as a fixed value, $We_i^* = 1.82 \cdot 10^{-2}$. Then the We_i can be calculated by the use of equation (7.15), where the τ_i in the equation is calculated as

$$\tau_i = \mu_l \frac{du_l}{dy} \quad (7.16)$$

If typical values of the velocity gradient found along the walls in the simulations are inserted in these models, re-entrainment is predicted at certain places. The velocity gradient is the only dependent variable, since the thickness and the velocity of the film are assumed. These values are fixed in order to bring the liquid film number over 160, which is required in the model to calculate a critical We number. Considering the requirement on the liquid Reynolds number this model is thought to be not appropriate in the prediction of the re-entrainment from the film. The assumed liquid Reynolds number is conservative, and a liquid Reynolds number exists only during drainage. When the water patch is at still, the liquid Reynolds number is zero. It is hard to believe that droplets only are generated when drainage occurs. It is therefore concluded that this model is not appropriate to predict the generation of the new droplets. On the other side it can be stated that this mechanism may contribute to the droplet generation during drainage.

7.3.2 The model from Woodmansee and Hanratty

This model is based on a We criterion from Woodmansee and Hanratty [67], but the model uses a modified We number definition. The We number in this model is defined as

$$We = \frac{\rho_g (U_g - C)^2 h}{\sigma} \quad (7.17)$$

where U_g is the superficial gas velocity, C is the wave velocity, and h is the characteristic height of the film. The critical We number, which defines the threshold between re-entrainment and no re-entrainment, is based on two different characteristic film heights. A critical We number based on the height of the roll waves gives a threshold of 5.5. If the base film height is used, the threshold is 1.5.

From the simulations the velocity magnitude near the walls is used as the relative velocity between the gas and the wave velocities. In order to achieve a conservative guess, the maximum value is used. The We number from the experiments becomes then, with the use of correct density and surface tension

$$We = 1055h \quad (7.18)$$

If a film height of 1 mm is inserted, the We number becomes 1.055, which is below the threshold independent of the characteristic height used. Re-entrainment is not predicted, and hence this model is unable to predict the generated droplets.

7.3.3 Conclusions from the re-entrainment models

The re-entrainment models tested in this section suggest that the generated droplets in the separator cannot be explained from this mechanism. The models give either a too high threshold or use a film Reynolds number that is probably not obtainable in the separator. There is however a difference in the physics between the models tested and the separator. The models consider experiments performed on horizontal pipe flows. So for the experimental basis for the models, the gravity acts stabilising, and cause the threshold to be set at a higher level. For the separator the gravity acts in a different direction, so the influence from the gravity is assumed small in terms of stabilising the surface. In addition, the experiments on the separator showed that the film consisted of patches of water, which drained at certain times, leaving an almost dry track behind its way. The crosswind also influenced, and made the drainage slantwise. The water injection trials in Section 5.1.4 indicate that the re-entrainment cannot be explained in light of a mechanism arising from the existing film. The conclusion becomes then that the re-entrainment from the film is not the mechanism that generates the new droplets inside the vanes.

Chapter 8

Complete description of the new models

In the previous chapter, it was shown that the four proposed mechanisms could not predict the generation of the new droplets. In this section, alternative mechanisms are suggested, and modelled. The generation of the droplets inside the vane may be caused by disturbances created by impact of a droplet on some of the already deposited water. The impacts are not energetic enough to create splashing directly, but under influence of geometric factors, shear of passing gas, and turbulent effects the disturbance waves can be the origin of the new droplets.

Al-Roub & Farrel [1] found that the droplet spacing is a variable to include when the threshold between splash and deposition is to be determined. An interference pattern on the waves was formed and, if the spacing between two droplets was perfect, addition to the wave caused by a second impact was the case, and an atomisation occurred. This observation is useful, and can explain why some of the models presented in the previous chapter failed in predicting the splashing. This observation implies that the continuous impact of droplets on the film can cause re-entrainment. In the work of Nakao et al. [46] a mechanism for the generation of the new droplets present at the outlet, is suggested to origin from the break-up by impingement on the liquid film.

In addition, in order to obtain better quality of the predictions in the simulations, the film is shifted from a continuous film, to a non-continuous film type. This is according to the experimental observations, and is described in Section 8.1. Three models are given, and these three models are presented individually in each sub-section. As a short introduction, it can be stated that model 1 – ‘An empirical approach’ is far different from the other two; model 2 – ‘Based on the stable We number’ and model 3 – ‘Variation of the critical We number’. The difference between the models is mainly the re-entrained droplet definition and the stability criterion. This is given in detail in later sections, but first some overall improvements of the simulations.

8.1 Some general improvements used in the simulations

In order to achieve better quality of the simulations, some additional features were added. These features are presented in this section. The first is to account for the non-continuous behaviour of the liquid film on the vanes, and the second improvement is to include the effects of the boundary layer on an impinging droplet with small collision angle.

8.1.1 Droplet description on the wall instead of a continuous film

The continuous film, which was approximated in the re-entrainment models in Section 7.3, seems a bit arbitrary in light of experimental observations. The deposited water formed patches or droplets of water at the vane, and not a continuous film. It is quite possible that for higher water loads a continuous film can be present, but for the current operational conditions

this was not the case. The water patches drain at certain time, and leave an almost dry track after drainage. This drainage occurs at different half droplet diameters depending on the position in the separator. For higher flow just past the droplet, increased turbulence, or geometrical conditions the maximum stable diameter for the deposited water vary. In the experimental work it is done little effort to measure these different effects on the stable diameter of the deposited water. It is instead used a crude estimation of a stable diameter of the deposited water. A calliper rule is used on a wetted vane in order to achieve the crude estimation, and the used maximum diameter is 1 mm. The models then approximate the deposited water in terms of a half droplet attached to the vane, termed non-continuously film approach. This is in contrast to the previous method, where the deposited water was converted into a mean film height, where the film covered the complete area of the current cell. The difference between these two approaches is shown in Figure 8.1.

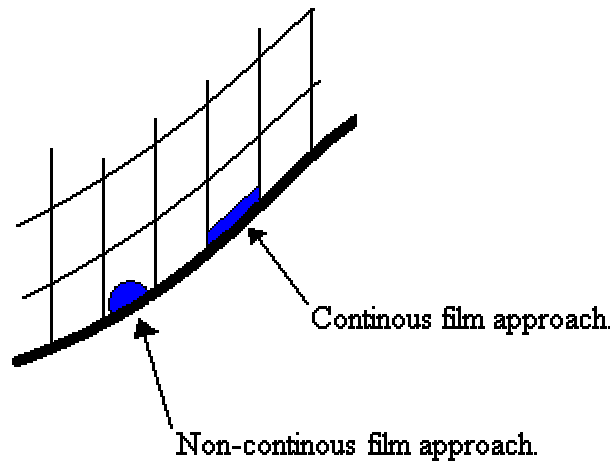


Figure 8.1: A sketch showing the difference between the non-continuous and the continuous approach.

The following relation converts the deposited mass into a diameter:

$$D_w = \sqrt[3]{\frac{12M_D}{\pi\rho_l}} \quad (8.1)$$

where M_D is the amount of deposited fluid in the current cell, D_w is the calculated diameter and ρ_l is the fluid density. The M_D accumulates as the particle tracking carries on. The incoming particle stream has an associated mass flow, and this mass flow is added to the M_D . Then D_w is calculated, and tested for drainage. The critical deposited water diameter is assumed to be 1 mm, and if D_w is bigger than 1 mm drainage occurs. Drainage means that D_w and M_D are reset to 0.

8.1.2 Reflection at small angles

In Lee and Hanratty [38] a reflection regime is identified based on the impinging angle of the droplet. The authors state that for low We number droplets at glancing angles, $< 3^\circ$, the small droplets are likely to reflect. The improvements were small, but still included on the simulations.

8.2 Model 1 - Empirical model

The first model presented is termed ‘Model 1 – Empirical model’. In this model the calculated diameter from the non-continuous approach for the deposited mass is used in the re-entrainment criterion. This is an analogy to a normal view on a stable droplet in an air stream. The We number is used as a threshold, and the half droplet used as the current droplet. The re-entrainment criterion is formulated as

$$We_{1/2-droplet} = \frac{\rho_g u_d^2 D_w}{\sigma} \quad (8.2)$$

where u_d is the impact velocity for the incoming droplet and D_w is the diameter according to Equation (8.1). As a first approach critical We numbers in the range 10-20 were tested. These We numbers were however too high, and produced only deposition. The critical We number for a highly turbulent flow was tested. It seems more correct to include turbulent effects on the critical We number, and the threshold was set according to Kataoka [27]. This gives a $We_{critical}$ number of 1.2. Table 8.1 shows the model for predicting re-entrainment.

Table 8.1: The formulation of the re-entrainment criterion.

Condition	Outcome
$We_{1/2-droplet} < We_{critical}$	Deposition
$We_{1/2-droplet} > We_{critical}$	Re-entrainment

The improvements according to the tested models in Chapter 7 are mainly the droplet description at the wall. The droplet description at the wall corresponds to the experimental observations. Even though that more than one droplet may exist in each cell, and that interactions between two droplets in a neighbouring pair of cells are not included. This introduces some discrepancy to the experimental observations.

When the droplet hits the vane, the test listed in Table 8.1 is performed. If the outcome from the test is that the droplet is stable, $We_{1/2-droplet} < We_{critical}$, then deposition occurs. The particle track for this injection stops here, and all the associated mass to this injection is added to the M_D . When the $We_{1/2-droplet} > We_{critical}$, re-entrainment occurs. The re-entered droplet diameter, and its associated mass flow, must be modelled. This model contains some empirical based assumptions, and both the re-entered droplet diameter and the deposited mass are assumed in this model.

The re-entered droplet diameter is based on the measurements, which indicates that droplets are generated in the range from close to 0 μm to 20 μm . The variation inside this range is assumed to follow a triangle shaped frequency. In Figure 8.2 the distribution of the triangle frequency is shown. In the same plot, a flat distribution is shown as a comparison.

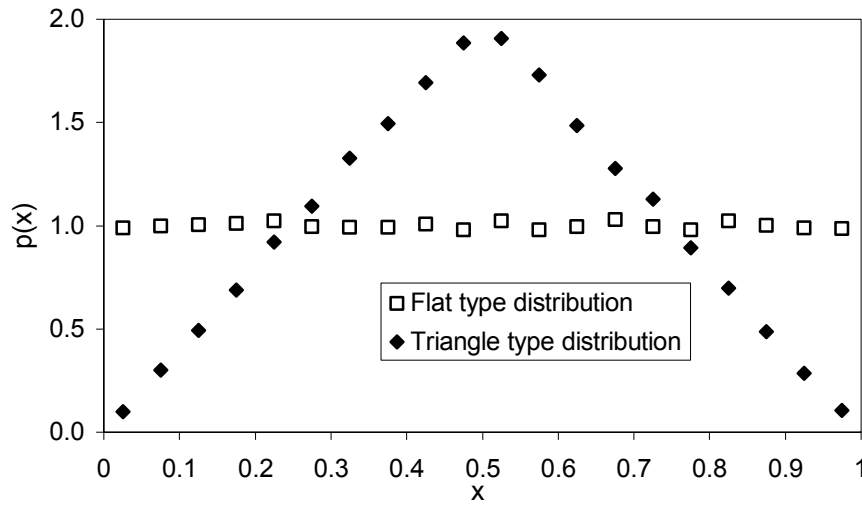


Figure 8.2: This figure shows the difference between the flat and the triangle random number distribution.

The flat distribution is given, and the random numbers from the flat distribution are transformed into the triangle distribution. For a random x between 0 and 0.5 from the triangle distribution, a line is drawn from 0 to 2.0. The equation for this line is

$$y_1 = \frac{2}{0.5} x = 4x \quad (8.3)$$

The gradient of the curve arises from the fact that for $x = 0.5$, the relative frequency must be 2.0. This is in strong contrast to the flat distribution, where the relative frequency is 1.0 (according to Figure 8.2) for $x = 0.5$. The line that is given by Equation (8.3) represents the analytical view, and the triangle, which is given by the two lines, shall have an area of 1. From this it follows that the height, or relative frequency must be twice as high as for the flat distribution. The integral of this line from 0 to $x_{\text{triangle}} < 0.5$ is:

$$F_1(x_{\text{triangle}}) = \int_0^{x_{\text{triangle}}} y_1 dx = 2x_{\text{triangle}}^2 \quad (8.4)$$

To find the corresponding x_{triangle} from a given x_{flat} , Equation (8.4) is set equal to the x_{flat} . The $F(x_{\text{flat}})$ is:

$$F(x_{\text{flat}}) = \int_0^{x_{\text{flat}}} y_{1,\text{flat}} dx = cx_{\text{flat}} \quad (8.5)$$

where $c = 1$. Equation (8.4) is set equal to Equation (8.5), and the only unknown is the x_{triangle} , which is wanted. This is shown in Equation (8.6).

$$x_{\text{flat}} = 2x_{\text{triangle}}^2 \quad (8.6)$$

This equation is only valid until x_{flat} reaches 0.5. Beyond this point a different line is valid, and is given by

$$y_2 = -4x + 4 \quad (8.7)$$

This line is valid from $0.5 < x_{\text{triangle}} < 1.0$. The integrated equation for this line is:

$$F_2(x_{\text{triangle}}) = 4x_{\text{triangle}} - 2x_{\text{triangle}}^2 - 1 \quad (8.8)$$

This equation is used to determine the x_{triangle} when the x_{flat} exceeds 0.5.

The droplet size from these equations is then given by multiplying the x_{triangle} with $20\text{E-}6$ m, and hence $20\text{E-}6$ is the maximum diameter.

In addition, the deposited mass is needed. It is assumed that 90 % of the associated mass is deposited in cases of re-entrainment. This gives 10 % as the re-entered mass from a re-entrainment occurrence.

8.3 Model 2 – Constant We number model

This model is based on the re-entrainment from a thin ligament on the deposited water patch. The ligament is generated from droplet impacts, shear, or turbulence effects. The droplet impact is used to set the dimension of the size of the ligament. The size of the ligament, or the diameter, is used in the determination whether re-entrainment occurs or not. Figure 8.3 shows a sketch of the re-entrainment of the ligament.

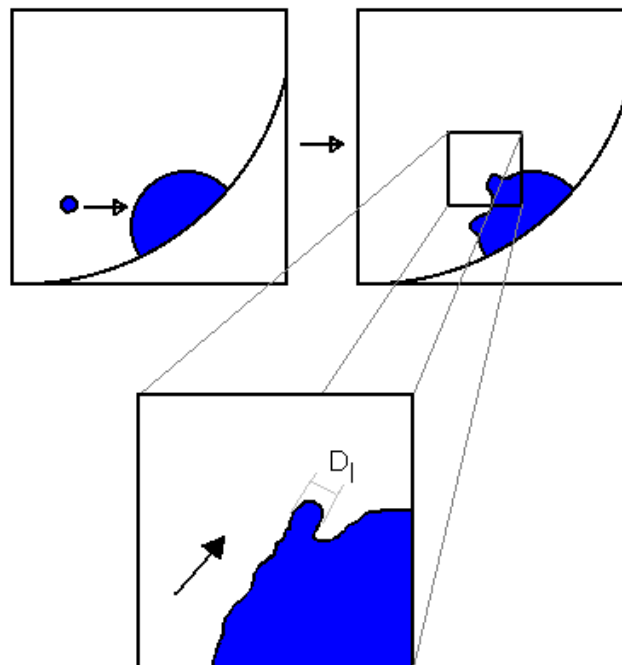


Figure 8.3: An impinging droplet causes waves on the surface, and ligament can be torn off.

In Figure 8.3 a droplet impinges on the film, or already deposited water, and causes some waves on the surface of the big droplet. If the impact is vigorous enough a ligament can be

created. This ligament can if the velocity is high enough, be torn off. To establish a criterion for the ligament to be torn off, a force balance on the ligament is written [27], and showed by

$$\pi D_l \sigma = \frac{\pi}{4} D_l^2 C_D \frac{1}{2} u_g^2 \rho_g \quad (8.9)$$

The left side of the Equation (8.9) is the surface force that has to be overcome by the drag force exerted by the air. The drag force is the right side of the equation. If the definition of the We number is used, Equation (7.1) the equation for the We number can be written as [27]:

$$We = \frac{8}{C_D} \quad (8.10)$$

The Stokes drag law is used, which is [10]:

$$C_D = \frac{24}{Re} \quad (8.11)$$

If Equation (8.11) is inserted into Equation (8.10), the result is:

$$We = \frac{Re}{3} = \frac{\rho_g u_g D_l}{3 \mu_g} \quad (8.12)$$

where D_l is shown in Figure 8.3. This equation can be used to describe the re-entrainment process. A We number threshold is then required. The We number used is the value according to Kataoka et al. [27], which gives $We_{critical} = 1.2$. This We number describes the maximum stable droplet size in a turbulent stream. Table 8.2 give a short summary for the re-entrainment test in the particle tracking routine.

Table 8.2: The re-entrainment test for ‘Model 2 – Constant We number model’.

	Fate of the ligament
$We_{critical} > 1.2$	Re-entrainment
$We_{critical} < 1.2$	Unchanged

The D_l used in the definition of the We number in this test, is a matter of discussion. The D_l should ideally represent the width of the ligament, which is the origin of the new droplet. This value is estimated from the impinging droplet, and it is assumed that the created ligament or wave is of the same size as the original droplet. It may seem that this is a kind of overestimation of the size of the ligament. But it is done this way, in order to include multi collisions on a droplet. Multiple collisions on a droplet caused by other droplets may lead to a positive interference, and a summation of the wave crests. It is therefore assumed that a higher value for the wave diameter can compensate for the many droplet impacts.

In cases where a re-entrainment happens, the re-entering droplet diameter is predicted from Equation (8.12). This gives the following equation for the re-entered droplet diameter

$$D = \frac{3We_{critical}\mu_g}{\rho_g u_g} \quad (8.13)$$

8.4 Model 3 – Varying We number model

The results from model 2, which will be presented in the next chapter, were not satisfying. The model predicts a sharp droplet distribution. The variation of the droplets generated inside the separator is somewhat under predicted. According to various authors the critical We number for a droplet varies. This leads to the idea of varying the We number threshold. The critical We number used in the determination of the re-entrainment, and the prediction of the droplet size generated, is varied within the limits suggested in Kataoka et al. [27]. In this reference, the stable We number varies for a strong turbulent flow from 1.2 to 2.5. In addition, it is mentioned that if the flow are pulsating the We number can be lowered by 50 %. It is assumed that the pulsation and turbulence level inside the vane separator are high, so the variation is according to

$$We_{Critical} = 0.1 + 2.4 \cdot N_{Random} \quad (8.14)$$

where N_{Random} is a random number between zero and one. The limits for the $We_{critical}$ are then between 0.1 and 2.5.

The only difference between model 3 and model 2 is the variation of the critical We number, otherwise these models are identical.

Chapter 9

Results from the new droplet models

The models developed and presented in the previous chapter, are used in the simulations and the results are presented in this chapter. The simulations consist of several cases, which will be described in separate subsections of this chapter. The results will be presented for each of the models independently of each other. Comparisons are made between the measured droplet size distribution and the predictions from the different models. In addition, the results are further analysed in order to obtain as much information as possible from the predictions. Some relevant information for the different cases, the particle tracking procedure, the inlet droplet distribution and set up for the simulations are next to follow. Then the results from the new models are presented.

9.1 Particle tracking procedure, properties and inlet conditions

Four subsections are presented in this section. The comparisons of the droplet size distributions consist of three cases for each model. These cases is discussed and described in the first subsection. Then the two representations of inlet droplet size distributions are described. The final subsection consists of a short summary of some properties concerning the simulations.

9.1.1 The different cases

The particle tracking are conducted in the following way. First, the film was initiated to zero, and the 'dry wall prediction' could be performed. The 'dry wall prediction' is then a simulation with no film present in the separator at the start of the particle tracking. After the 'dry wall prediction' the film was constructed. The film was constructed by injecting lots of particles, until no change in the outlet droplet conditions was noted. The case for particle tracking that includes the film inside the separator is termed the 'wet wall prediction'. The last and third case was a reference case, where a trap condition was used on the wall. In this case no effects from the different models are included.

9.1.2 The Rosin-Rammler representation

Two different representations for the experimental droplet distribution are used in the simulations. In this subsection the Rosin-Rammler representation is described and the theory of the Rosin-Rammler is presented in Subsection 2.6.3. The values of the coefficients used in the representation of the experimental distribution are given in Table 9.1

Table 9.1: The coefficients used in the model for the Rosin-Rammler distribution.

Variable		
D_{mean}	60	μm
n	2.25	-

When the coefficients presented in Table 9.1 are used in the theoretical equation for the M_D -variable, the quality of the cumulative representation is seen in Figure 9.1. Figure 9.1 shows the experimental dots, and Equation 2.63 gives the solid line. The variable M_D is the mass fraction of droplets with diameter greater than the particle diameter D .

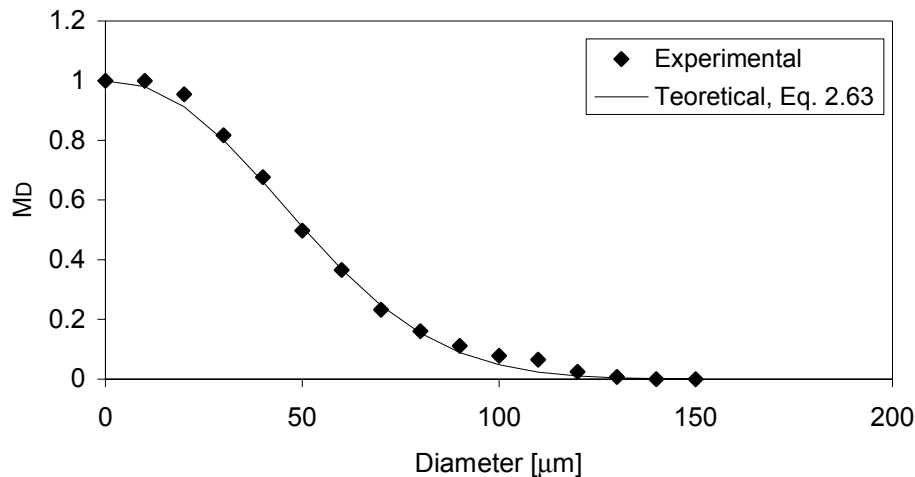


Figure 9.1: The Rosin-Rammler distribution for the inlet condition.

Each injection contains a droplet diameter, and an associated mass. The total mass flow of the droplet distribution matches the measured mass flow of water. The droplet distribution is injected in 10 discrete points evenly distributed across the width of the channel. Each of the injections consists of 100 droplets, and hence a total of 1000 droplets are injected each particle tracking, and the effect of turbulence is included. The injections are shown in Figure 9.2.

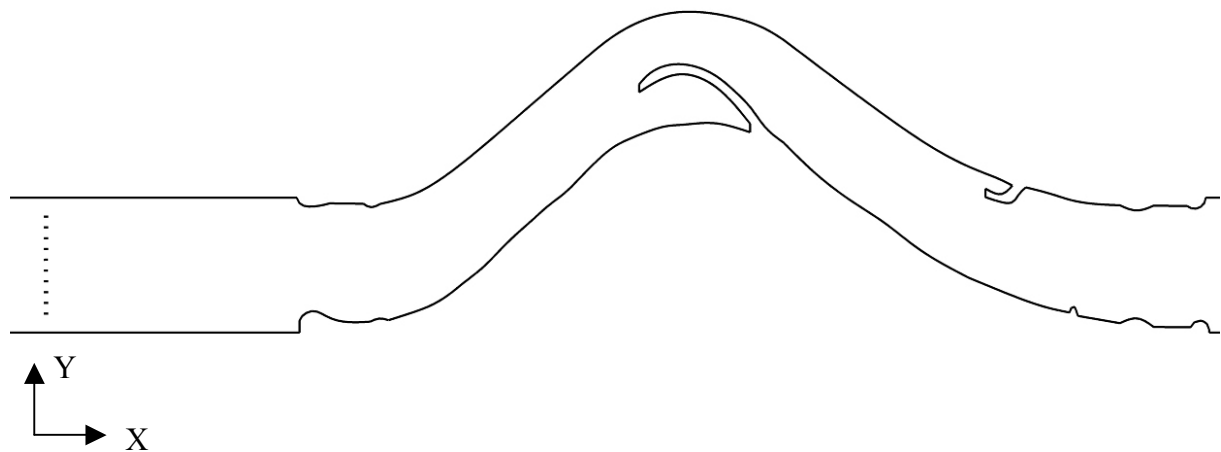


Figure 9.2: The injections 50 mm prior to the vanes.

9.1.3 The discretized droplet distribution

A second way of representing the experimental droplet size distribution is included. This method discretizes the continuous probability density function for the experimental droplet distribution. A histogram based on size-ranges of 1 μm was used as a basis for the development of the discretized droplet distribution. The relative frequency is calculated for each size-range. The value for the relative frequency was then calculated, and a droplet is defined at each time the relative frequency pass a 0.01 interval. This will give a total of 100 droplets in the discretized droplet distribution. The discretized droplet distribution constructed this way, together with the experimental droplet size distribution, is shown in Figure 9.3.

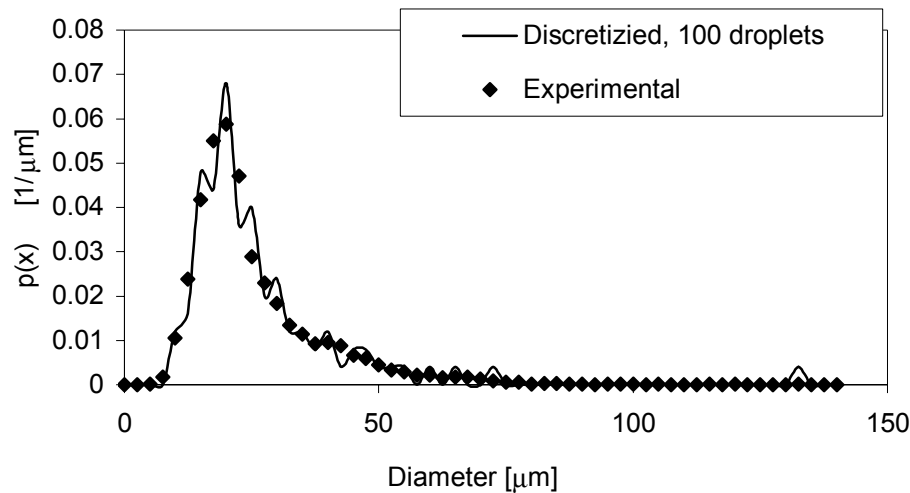


Figure 9.3: The discretized droplet distribution at the inlet.

The mass of the droplet distribution is given as the product between the measured mass flow of water and the mass fraction for the current droplet diameter. The injections are analogue to the injections defined for the Rosin-Rammler distribution, and are shown in Figure 9.2. This gives a total of 1000 droplets for the complete injection.

9.1.4 Different properties

The force balance given in the theory section, Subsection 2.5.1, gives the mean tracks of the droplet trajectories. In order to achieve a better quality of the predictions the turbulence is included. The theory of including turbulence to the particle tracks is given in Subsection 2.5.3, and the effect on the simulations of the outlet distribution is shown in Figure 9.4. Figure 9.4 shows the difference between a simulation based on mean tracks, and a simulation with turbulence included. To make the simulation as simple as possible, the trap condition is used as boundary conditions on the wall. The trap condition at the wall means that when the droplet hits the wall, it is removed from the simulation and reported as trapped.

For the Rosin-Rammler droplet distribution improvements can be seen for the biggest droplets. For droplet diameters bigger than approximately 16 μm the case with turbulence predicts more realistic than the case with mean tracks. For droplets smaller than 16 μm the deviation compared to the experimental distribution is slightly better. The smallest droplet diameters are not present at the inlet, and since the droplet generation models are not included in these simulations, none are generated. This explains the deviation for the smallest droplet diameters.

For the discretized droplet distribution the same effects are seen as for the Rosin-Rammler droplet distribution. For large droplets the separator works less efficient when the turbulence is included in the particle tracks. An overprediction of the efficiency for the separator is noted for droplet diameters between 9 μm to 16 μm . Again, droplets smaller than 9 μm are totally absent. The effect on the predications when including the turbulence is positive, and hence the turbulence is included in the simulations. The number of tries needed is statistically based, but some minor trouble was noted on the workstation when the number of tries exceeded 20. Hence, 15 tries were used in the simulations. The results from the various models are

presented in separate sections. The predictions from the particle tracking are carried out on the 'k- ϵ law-of-the-wall' cases.

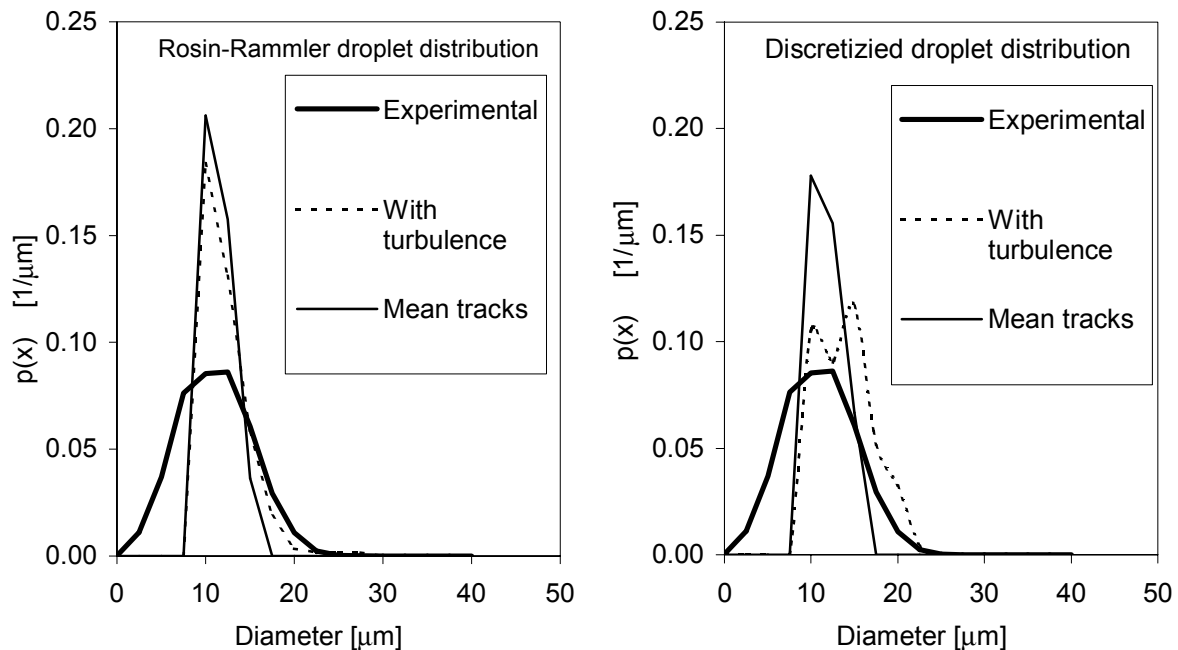


Figure 9.4: The effect when the turbulence is included in the droplet tracking.

9.2 Results from model 1 – Empirical model

The results from the particle tracking using model 1 are presented in this section. Droplet distribution at the outlet is analysed, and the simulated distribution is compared with the experimental distribution. Subsections covering each of the inlet distributions are presented. In addition, the mass trapped and the number of particles trapped will be presented and discussed. But first a figure of the film inside the separator will be shown. Figure 9.5 shows the simulated film inside the separator. The figure shows a contour plot of the mass of water in each cell. The areas of high water load are predicted just right where intuitively these areas should be. The curvature towards the hook separates the most of the water. Some patches of water are noted near the outlet, and this is in accordance to measurements. Some activity in the deposition was noted right after the separator. The amount of water allowed in each cell is limited by the measured maximum size showed in Chapter 5.

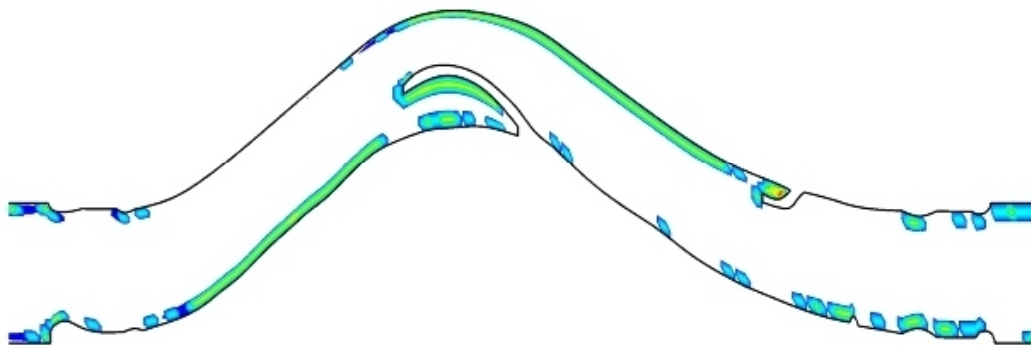


Figure 9.5: The distribution of the film, model 1.

9.2.1 Results from the Rosin-Rammler distribution

The droplet distribution defined according to a Rosin-Rammler distribution is simulated with model 1, which is described in Chapter 8. The droplet size distribution for the different cases is shown in Figure 9.6. Model 1 uses the re-entrainment criterion based on the $\frac{1}{2}$ -droplet at the wall. A We-number of 1.2 is used as the threshold. For re-entrainment an empirical approach is used. Experiments show that droplets less than $20\ \mu\text{m}$ are generated. Model 1 predicts the re-entrained droplets between 0 and $20\ \mu\text{m}$ according to the description in Chapter 8.

The reference case is the trap case, which shows the performance of the simulations with no effect from the droplet-wall interactions. A sharp increase in the droplet distribution is noted for droplets at $\sim 9\ \mu\text{m}$. The small droplet diameters are totally absent. The reason for this is that no droplet is generated in the separator for this case. The trap condition only traps the droplets, and do not create new smaller droplets. The droplet size distribution for the larger droplets is well predicted, but a large deviation exists for the droplets in the range from $9\ \mu\text{m}$ to $12.5\ \mu\text{m}$.

For the dry wall case, the effect of model 1 is included, and small droplets are found at the outlet. The predicted distribution out of the separator is for this case well predicted. Small deviations are noted, and are maximized in the droplet diameter range from $9\ \mu\text{m}$ to $12.5\ \mu\text{m}$. An overprediction of the probability is predicted in this area. Only small deviations between the dry wall case and the wet wall case are noted, and hence the effect of the film seems to be negligible. However, the measured droplet distribution represents the wet wall case. The droplet size distribution for the dry wall case where not measured.

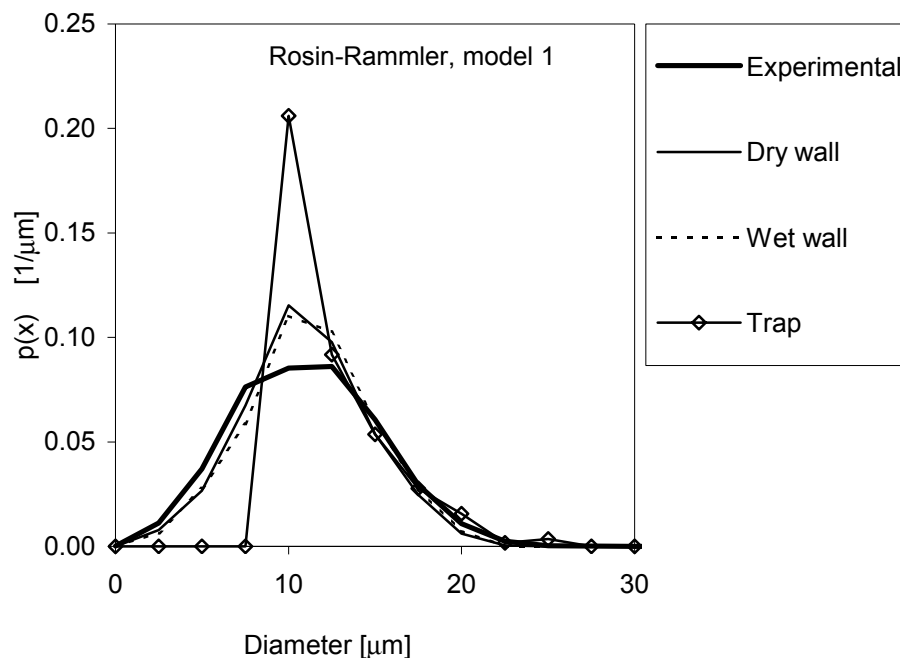


Figure 9.6: The droplet distributions at the outlet for model 1 when using the Rosin-Rammler droplet distribution.

The prediction of the droplet size distribution at the outlet was satisfactorily. The amount of droplets removed and the mass removed in the separator are shown in Table 9.2. The number of droplets removed is nearly 99 % for the trap case. For the two other cases approximately 60 % of the droplets are removed. The number of droplets removed is not measured, and hence it is difficult to conclude anything about the number removed. It is only stated that it seems that the trap case removes too many droplets. This is based on the fact that for each droplet that hits the wall, it will be removed. Physically this droplet may be the origin of several others, and number of droplets removed will be overpredicted for the trap case. For the two other cases the droplets, which fulfils the re-entrainment criterion, will be re-entered and the number of droplets will be lowered. It is still a weakness that the re-entered droplet is only one droplet, because physically it can be many. This is however difficult to predict with the Euler-Lagrange method. Each injection cannot multiply into several trajectories, so the number of re-entrained droplets is bound to be only one. The predicted droplet diameter out of the separator is well predicted. But considering the basis for this model, this is not surprising. The model predicts some loss of water due to re-entrainment of the newly generated droplets, and this can explain the decreased mass removed predictions. This also implies that the mass fraction assumed to be re-entered, 10 %, is set to high. It seems that a lower value than 10 % would be more appropriate to use.

Table 9.2: The number and mass removal for model 1 when Rosin-Rammler distribution is used.

Case	Number removed [%]	Mass removed [%]	Diameter D_{10} [μm]
Experimental		99.85	9.8
Trap	98.47	99.17	10.8
Dry	67.26	96.90	9.8
Wet	57.35	95.98	10.0

9.2.2 Results from the discretized distribution

Model 1 is then simulated with a different set of droplet injections, the discretized distribution. Model 1 is identical as for the Rosin-Rammler injection, and the only difference is the other droplet distribution injected into the separator. The predicted droplet size distributions are shown in Figure 9.7.

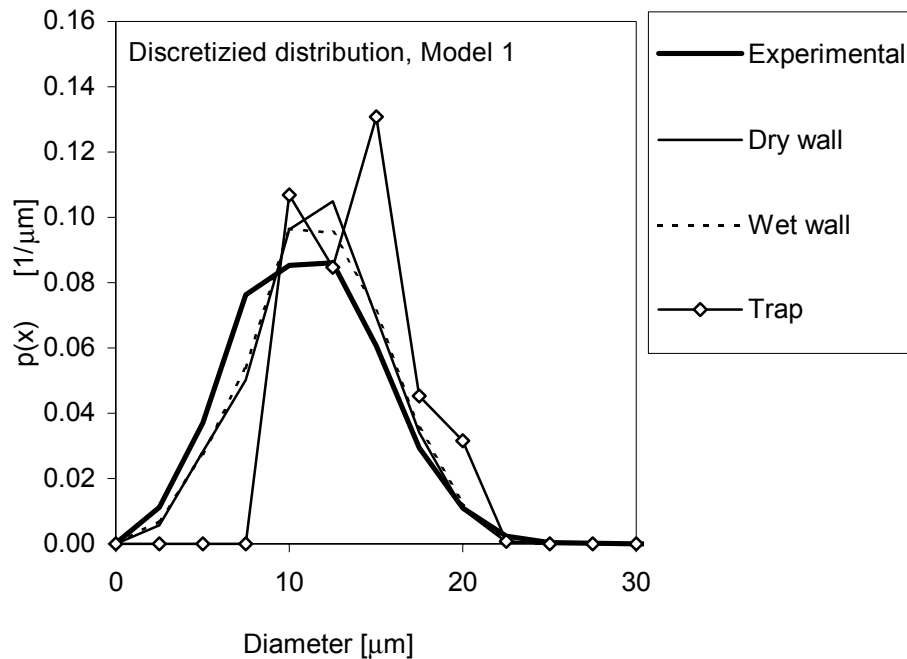


Figure 9.7: The droplet distributions at the outlet for model 1 when using the discretized droplet distribution.

The droplet size distribution for the trap case consists of two tops, localized at 10 μm and 15 μm . This is probably caused by the discretization of the inlet conditions, where the droplets are discretized in ranges of 1 μm . The trap case lacks the small droplets, and hence the curve for the trap case lies over the curves for the other cases. This follows from the fact that all curves shall have an area of 1.

For the Rosin-Rammler distribution the larger droplets in the distribution are well predicted, but some deviation exists for the discretized distribution. The dry wall case predicts satisfactorily the measured droplet distribution. Some deviations exist, and the largest deviation exists in the area approximately at 15 μm . The effect of the film is slightly notable for this distribution. A certain lowering of the probability for the droplet sizes around 12.5 μm is noted.

The Table 9.3 shows the performance of the model 1 for different properties. The same constrictions and discussion that were mentioned for the Rosin-Rammler cases are valid in these cases. The mass trapped is satisfactorily predicted. The mean diameter out of the separator is predicted within 6 % for this model.

Table 9.3: The number and mass removal for model 1 when discretized distribution is used.

Case	Number removed [%]	Mass removed [%]	Diameter D_{10} [μm]
Experimental		99.85	9.8
Trap	96.57	99.83	13.0
Dry	56.81	98.69	10.4
Wet	48.45	98.40	10.5

9.2.3 Conclusions from model 1 – Empirical model

It has been shown that model 1 predicts satisfactorily the droplet distribution out of the separator. The model manages to generate small droplets, less than 9 μm . These droplets do not exist at the inlet, and hence improvements have been done. It is however important to remember that model 1 is empirical, and hence the performance was expected. The mass trapped in the separator coincides well with the experiments, even though the deposited mass is estimated from an experience level. Some tests of the effect of changes in the deposited mass constant were carried out, but had a minor effect on the trapped mass. The trap case shows that the predictions for the droplet with the largest diameters are satisfactorily, but major deviations exist for the smallest droplet diameters. The difference between the dry and wet cases is negligible, and the influence of the film present in the separator is zero. It is impossible to support this view from the experiments since measurements only exist for the wet case. Physically the influence of the film will probably be present, and this is a weakness of the model.

9.3 Results from model 2 – Constant We number model

The model 1 is based on some empirical experiences. The droplet size generated inside the separator is measured, and implemented as a variation between 0 and 20 μm . In model 2, which is used in this section, the re-entrainment criterion and the estimated droplet size from a re-entrainment are more bounded to the theory. The re-entrainment criterion is based on a disturbance wave on the $\frac{1}{2}$ -droplet surface, and the droplet size generated is determined by the We number.

The same cases that were presented for model 1, are also presented for this model. This involves the dry wall case, wet wall case, and the reference case with trap as a boundary condition at the walls. In addition, the Rosin-Rammler distribution and the discretised distribution are used as inlet conditions.

9.3.1 Results from the Rosin-Rammler distribution

The results from model 2 when the Rosin-Rammler injections are employed are shown in Figure 9.8. The reference case, which uses a trap condition on the walls, shows a narrow droplet size distribution out of the separator. The droplets less than 7.5 μm are totally absent, while an overprediction exists for the next droplet sizes. The upper tail of the curve, that is for droplets greater than 15 μm , are good predicted. The difference in the predictions from the dry wall and the wet wall cases are of negligible character. Small droplets are generated, but not completely into the smallest diameters. In comparison to the trap case, the dry and wet wall predicts a lowering in the predicted diameters out of the separator. An overprediction of the middle range droplet sizes exists. If a closer look is taken on the numerical details of the droplet distribution, it can be discovered that the predicted droplet sizes do not contain the same spread as the experimental distribution. The predicted droplet size is dependent on the velocity in the current cell, and this velocity is the mean velocity. The fluctuations in the velocity, which leads to fluctuations in the droplet size, are hence ‘meaned’ out. The predicted droplet diameter is hence the mean droplet diameter, and variations in the predicted droplet size are excluded.

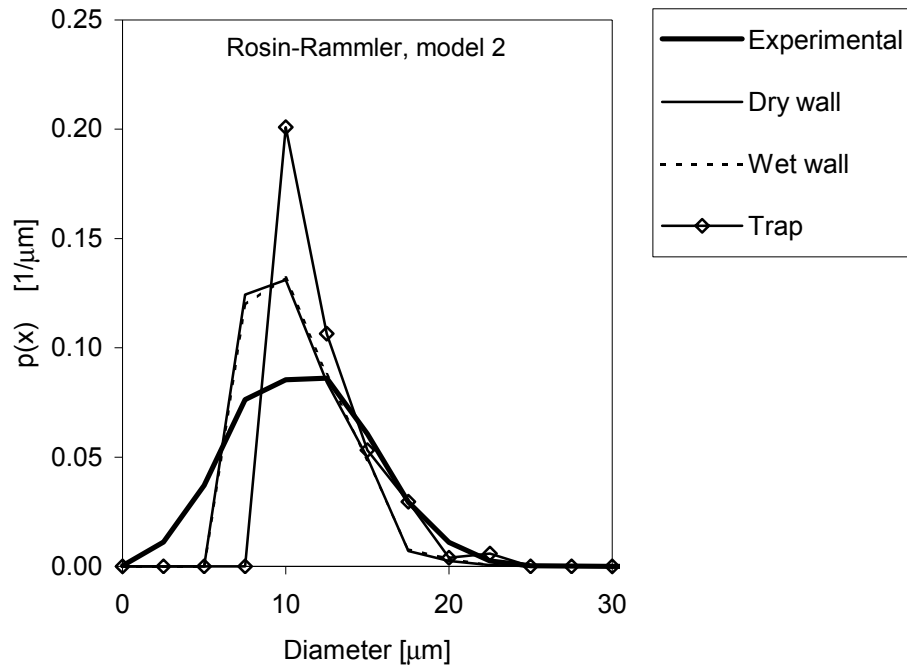


Figure 9.8: The droplet distributions at the outlet for model 2 when using the Rosin-Rammler droplet distribution.

The Table 9.4 shows the performance of the model 2 for different properties. The mass trapped are satisfactorily predicted.

Table 9.4: The number and mass removal for model 2 when Rosin-Rammler distribution is used.

Case	Number removed [%]	Mass removed [%]	Diameter D_{10} [μm]
Experimental		99.85	9.8
Trap	98.65	99.28	10.7
Dry	75.58	98.53	9.5
Wet	75.82	98.51	9.5

9.3.2 Results from the discretized distribution

The results from the different cases with the discretized distribution are shown in Figure 9.9. The trap case shows deviations to the experimental droplet distribution. The small droplets are absent, but this is in accordance with the boundary conditions. No droplets smaller than $9 \mu\text{m}$ are injected, and no new droplets are generated in the trap case. For the dry wall case the droplet distribution is narrow and staggered. An overprediction exists for the droplets in the range around $10 \mu\text{m}$, while the larger droplets generate a staggered and underpredicted distribution. It is also an underprediction of the smallest droplets. The difference between the wet wall and the dry wall cases are only minor. If the droplet diameters are studied in detail, the generated droplets predicted from the model, are too narrow in its distribution. The same problems encountered for the Rosin-Rammler distribution are also found in this distribution.

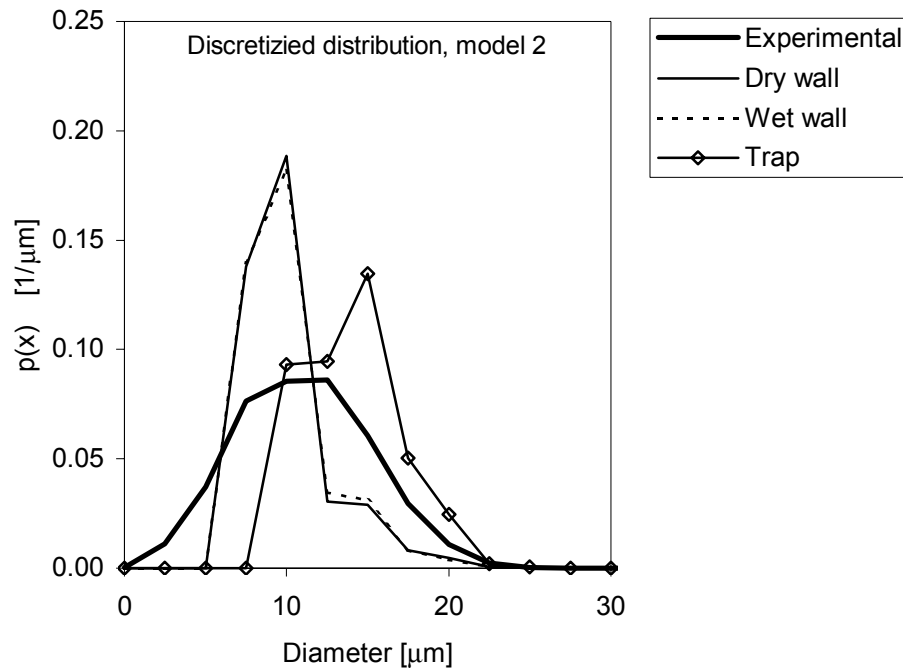


Figure 9.9: The droplet distributions at the outlet for model 2 when using the discretized droplet distribution.

Table 9.5 shows the performance of the model 2 for different properties. The mass trapped is satisfactorily predicted. The mean droplet size is better for the dry and wet cases, than for the trap case.

Table 9.5: The number and mass removal from model 2 when discretized distribution is used.

Case	Number removed [%]	Mass removed [%]	Diameter D_{10} [μm]
Experimental		99.85	9.8
Trap	96.31	99.82	13.0
Dry	69.83	99.47	8.8
Wet	69.86	99.47	8.9

9.3.3 Conclusions from model 2 – Constant We number model

Model 2 increases the quality of the droplet distribution of the separator compared to the trap case, even though there seems to be a need for improvement. The droplet size distribution has, however, some discrepancies to the experimental distribution. The generated droplet size does not spread in the same area as the experimental distribution does. Model 1 gave a much better droplet size distribution, but that model is empirical. Model 2 is based on theory and physical linked to the re-entrainment process, and hence the prediction from model 2 is more general. The velocity that is used to estimate the re-entered droplet size is the mean velocity in the current cell. This cell velocity is the same all through the simulation, and hence no fluctuation in the velocity is included in the estimation of the re-entered droplet size. The next model presented, model 3, includes improvements in order to include some kind of fluctuations in the velocity or the re-entered droplet size.

9.4 Results from model 3 – Varying We number model

The model 3 is a simple and effective modification of model 2. The major improvement of this model is the ability to create wider droplet distribution than model 2. The We number criterion is the only change in comparison to model 2.

9.4.1 Results from the Rosin-Rammler distribution

The results from model 3 for the Rosin-Rammler cases are presented in Figure 9.10. The trap case is nearly identical as for the two other models. This is not surprising since when the trap condition is used at the wall, no effects from the models are included. The largest droplet diameters in the distribution are well predicted, while an overprediction exists for the middle-sized diameters. The droplets smaller than 9 μm are totally absent. The predicted droplet distribution for the dry wall case is given by the thin solid line, and follows the experimental distribution almost perfectly. Small deviation is noted for the small diameters, which gives an overprediction. A slight overprediction also exists for the middle ranged diameters. From 12 μm and towards the larger droplet diameters a slight underprediction is shown. The predicted droplet distribution from this model is definitely better than the equivalent case for model 2. The difference between the wet wall and dry wall cases is of negligible importance, and only small changes are noted in the distribution.

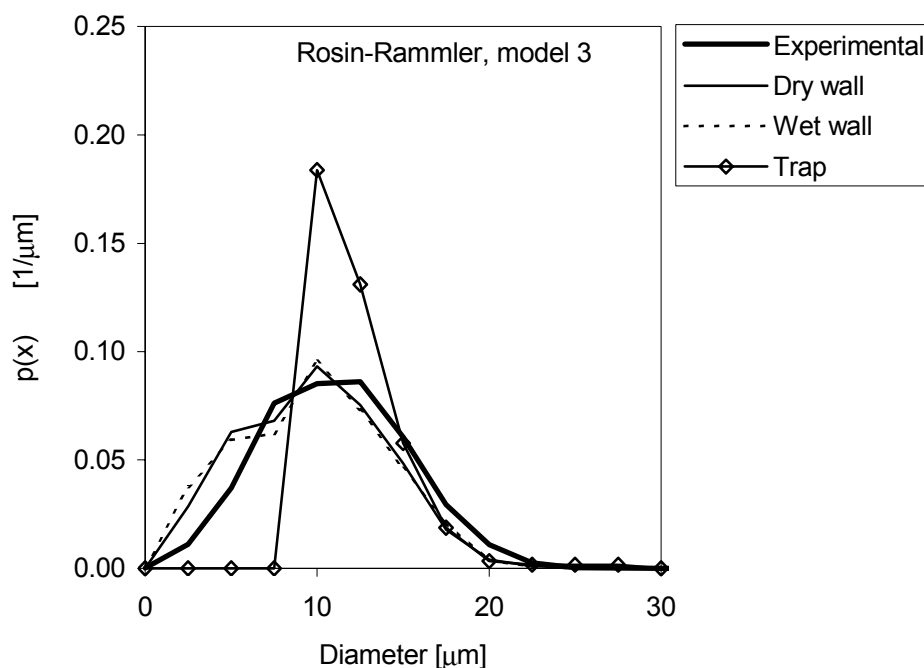


Figure 9.10: The droplet distributions at the outlet for model 3 when using the Rosin-Rammler droplet distribution.

Table 9.6 shows the performance of model 3 for different cases. The mass trapped is satisfactorily predicted. The mean diameter is slightly worse than for model 2, even though the droplet distribution is better.

Table 9.6: The number and mass removal for model 3 when Rosin-Rammler distribution is used.

Case	Number removed [%]	Mass removed [%]	Diameter D_{10} [μm]
Experimental		99.85	9.8
Trap	98.43	99.17	10.7
Dry	84.05	98.63	8.6
Wet	83.43	98.67	8.5

9.4.2 Results from the discretized distribution

The results from the discretized distribution cases for the model 3 are presented in Figure 9.11. The trap case is similar the trap cases for the other models, and small droplets are absent. The dry wall case represents well the measured droplet size distribution. Some deviations are noted, especially on the small and middle ranged diameters. For the larger droplets the droplet distribution is well represented. The deviation noted on the small sized droplets is an overprediction of the probability. An underprediction is noted for the middle ranged diameters. There are only negligible differences between the dry and wet cases.

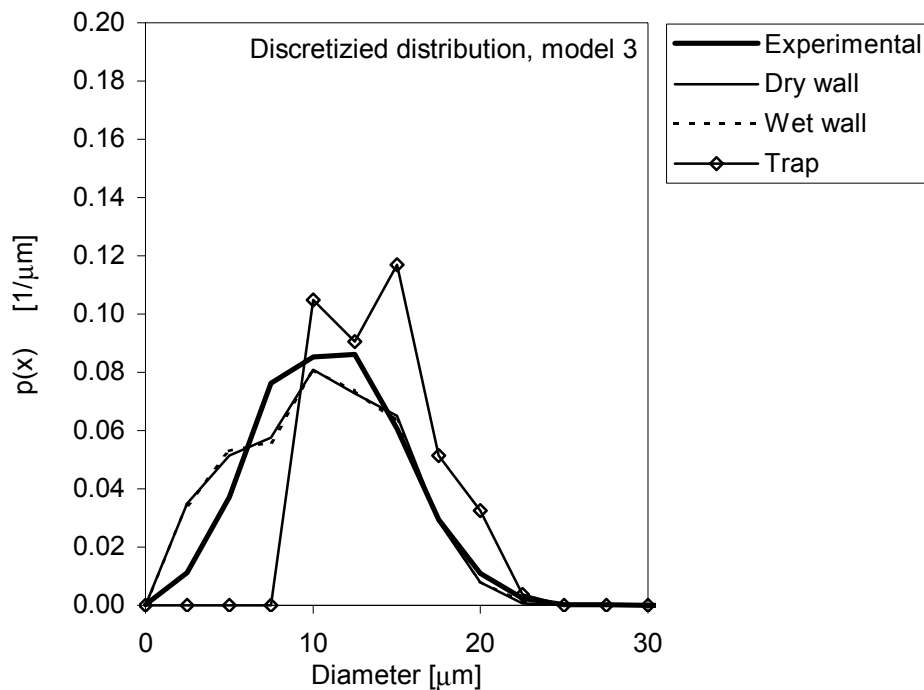


Figure 9.11: The droplet distributions at the outlet for model 3 when using the discretized droplet distribution

Table 9.7 shows the performance of model 3 for different properties. The mass removed is satisfactorily predicted. The mean droplet size is better for model 3 than model 2 for the discretized distribution.

Table 9.7: The number and mass removal for model 3 when discretized distribution is used.

Case	Number removed [%]	Mass removed [%]	Diameter D_{10} [μm]
Experimental		99.85	9.8
Trap	96.48	99.82	13.1
Dry	78.84	99.45	9.2
Wet	79.25	99.45	9.2

9.4.3 Conclusions from model 3 – Varying We number model

The variation in the We number criterion generated a better droplet distribution at the outlet, compared to model 2. Small sized droplets absent in the trap case, became present. The mean diameter is slightly lower than the experimental value, and the mean diameter is better predicted for the discretized cases than for the Rosin-Rammler cases. The difference between the dry wall cases and the wet wall cases are of negligible character.

9.5 Conclusions from new droplet models

The new models generate new droplets inside the separator. Model 1 is primarily based on observations and experiments, but this model shows that it is possible to create models with capabilities to predict droplets that are generated inside the separator. The models 2 and 3 are based on a theoretical analysis including a few assumptions. Model 2 works to a certain extent, but shows that improvements are needed. Model 1 performs better than model 2, but model 2 is based on theory about the re-entrainment process and hence more general. Even though the randomisation of the We number in model 3 can seem a bit simple, it produces good results. It is a fact that the We number threshold for any droplet is not a sharp line, and varying the We number includes these effects. For model 3 the prediction of the droplet size distribution out of the separator is satisfying. The major limitation for the models lies in the Lagrangian particle tracking, which makes it difficult to create more than one droplet from the ligament.

Chapter 10

Cyclone simulations

In this chapter, some work concerning the simulation of cyclones is presented. The simulations of cyclones are not trivial. The complex flow field, involving radial pressure gradients and strong coupling between the pressure and velocity distribution, makes these kinds of problems difficult to simulate. In addition, the most robust and used turbulence model in CFD codes, the standard k- ϵ model, is not appropriate to use in the simulation of the cyclone. The standard k- ϵ model produces best results for isotropic turbulence, which means that the turbulence fluctuations are equal in all directions. In a typical cyclone, this is not the case, and other turbulence models have to be used. The predicted flow field is compared with measurements, and the quality of the simulations is checked. The simulations are divided into several parts. First, the effect of changing from Cartesian velocity components in the momentum equations to the cylindrical components in the momentum equations is tested for a structured CFD code. The CFD code used is Fluent v4.5 and v5.0 [18]. In addition, an Euler-Lagrangian method is used to create the fractional collection curve. Then an un-structured version of Fluent is used to test a multiblock grid of the cyclone. A fractional collection curve is also developed based on the multiblock simulation.

10.1 Cyclone information

The numerical methods that exist today can cope with many of the complex flow fields in common process equipment. However, the flow field inside a flow cyclone is quite of a challenge to a numerical code. The swirling flow sets up a radial pressure gradient, and this coupled with turbulence, and different phases further complicates the simulations of cyclones. In the literature, CFD simulations of cyclones are common, and in newer publications 3D simulations can be found [20]. These simulations however, do not make a point of which velocity formulation they are using. The simulations performed in this work, showed large differences in the solutions depending on which velocity formulation that was used, and hence such information is believed to be important. In addition, new publications present multiblock simulations of cyclones, and a multiblock simulation is shown in the end of this chapter. For the structured simulations presented in this chapter, the main findings are presented in [25].

10.1.1 Additional challenges when simulating cyclones

There are certain aspects that are not considered or mentioned in the theory section, which must be discussed. The first issue is the turbulence model. The standard k- ϵ model is known not to handle the anisotropic nature of the turbulence inside the cyclone very well. It is therefore necessary to use other turbulence models, and for these simulations the RNG k- ϵ model and the RSM model are used.

The solution process for the structured RSM cases was a tough challenge. The initialisation with a near converged solution of the standard k- ϵ model was necessary. In addition, the under-relaxation parameters had to be changed during iteration. When these steps were followed a converged solution was achieved. The outlet of the cyclone causes some additional problems. The swirl creates low pressure near the axis, and some fluid can be dragged into the

cyclone over the outlet. This is not desirable, and the solution to this problem was to extend the outlet tube so far that the suction did not produce any further problems.

10.2 Results from the structured cases

The main objective for this work is to study the CFD-method usefulness on cyclones. The conclusions for the CFD code are made on the basis of velocity, pressure drop, and efficiency comparisons between simulated and experimental results. From the literature two sources containing experimental work on cyclones are collected. These cyclones are named ‘Qing cyclone’ and ‘High efficiency Stairmand cyclone’. For the Qing cyclone detailed measurements of the velocity distribution in the cyclone and the pressure drop exist [52]. Dirgo and Leith [14] performed efficiency studies on the high efficiency Stairmand cyclone, and the CFD generated collection curve is compared with these experiments, along with the pressure drop. The physical dimensions of the cyclones are listed in Table 10.1, with the dimensions noted according to Figure 10.1. The flow medium was air at 20°C for both cyclones. For the Qing cyclone the inlet velocity was 7.1 m/s, and for the high efficiency Stairmand the inlet velocities were 5.1, 10, 15, 20 and 25 m/s.

Table 10.1: Physical dimensions for the two cyclones.

		Qing Cyclone	High efficiency Stairmand Cyclone
Diameter main body [mm]	D	288	305
Diameter vortex finder [mm]	D_e	126	152
Vortex finder length inside cyclone [mm]	S	130	152
Cylinder height [mm]	h	230	457
Cyclone height [mm]	H	500.2	1220
Dust outlet diameter [mm]	B	36	114
Inlet height [mm]	a	130	152
Inlet width [mm]	b	80	61

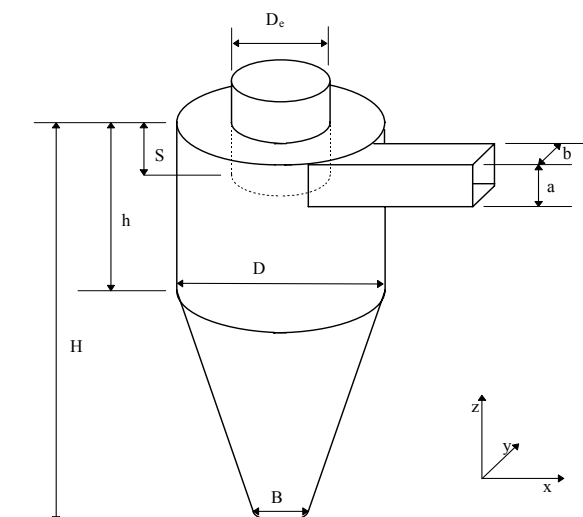


Figure 10.1: Dimensions for the two cyclones.

Both cyclones have a tangential inlet, but the Qing cyclone is not completely tangential. The inlet box is somewhat displaced from the centre of the cyclone. From a tangential position the inlet box is moved 25.5 mm away from the centre of the cyclone in both the x- and y-

direction. According to Figure 10.1 this is 25.5 mm in positive x-direction, and 25.5 mm in negative y-direction. The outer wall of the inlet box is extended with an arch, where its centre is at -25.5 mm in x-direction and zero in the y-direction, and the radius of the arc is 84.75 mm. The arc starts at the outer wall of the inlet box, and ends on the cyclone wall.

10.2.1 The Qing cyclone

In the Ph.D. thesis of Qing [52], pressure drop, velocity in different heights and turbulence quantities are presented. These are compared with predicted values from the simulations. One major drawback is the lack of measured efficiency of the cyclone.

Table 10.2 shows that there is only one satisfactory prediction of the pressure drop, the cylindrical RSM case. The term cylindrical means that cylindrical velocity components are used in the momentum equation while the term Cartesian means that Cartesian velocity components are used in the momentum equation. All cases use a first order scheme, except where else are noted. The cylindrical RSM case predicts the pressure drop to -8.6 %, while the cylindrical RNG k- ϵ case overpredicts the pressure by 29.8 %. The Quick scheme does not improve this solution. The two Cartesian cases give an underprediction of the pressure drop with 80 %.

Table 10.2: Static pressure drop for the Qing cyclone, inlet velocity is 7.1 m/s.

Case	Static pressure drop [Pa]	Deviation [%]
Experimental	436.0	
Cartesian, RNG k- ϵ	88.2	-79.8
Cartesian, RSM	87.3	-80.0
Cylindrical, RNG k- ϵ	566.1	29.8
Cylindrical, RNG k- ϵ , Quick	557.1	27.8
Cylindrical, RSM	398.3	-8.6

For the Qing cyclone the velocity distribution was measured in four different levels in lines from the axis towards the cyclone wall. The line is in positive y-direction and starts in the centre of the cyclone. The velocity was measured by using a backscatter LDA system. These four levels were from the top of the cyclone: 50 mm, 100 mm, 150 mm, and 200 mm [52].

In Figure 10.2 the velocity profiles for the position 50 mm below the top are presented. The measured profile does not contain any data inside the vortex finder, but the predicted profiles are presented anyway. The prediction of the measured velocities in the cyclone is satisfactorily for the cylindrical RSM case for the tangential and axial direction. For the radial direction major deviations exist. None of the cases obtains a good prediction for the radial velocity, and the cylindrical RSM case is the only case with the correct direction of the velocity. For the tangential velocity overprediction exists for the cylindrical RNG cases, while a significant underprediction exists for the Cartesian cases. The magnitude of the axial velocity is small, outside the vortex finder, and only the cylindrical RSM is able to predict the velocity satisfactorily.

In Figure 10.3 the velocity profiles from 100 mm below the top are presented. The velocities are not measured inside the vortex finder, but the predicted profiles inside the vortex finder are included. The same trends noted for the profiles located at 50 mm below the top, are also found in this position. The tangential velocity is overpredicted for the cylindrical RNG cases, and a severe underprediction exists for the Cartesian cases. There is one exception, however,

the cylindrical RSM case predicts very good for the tangential velocity. The axial velocity is small, and again the cylindrical RSM case is performing best. For the radial velocity, which is very small, the cylindrical RSM case seems best. But all in all, none of the cases impress with the prediction of the radial velocity.

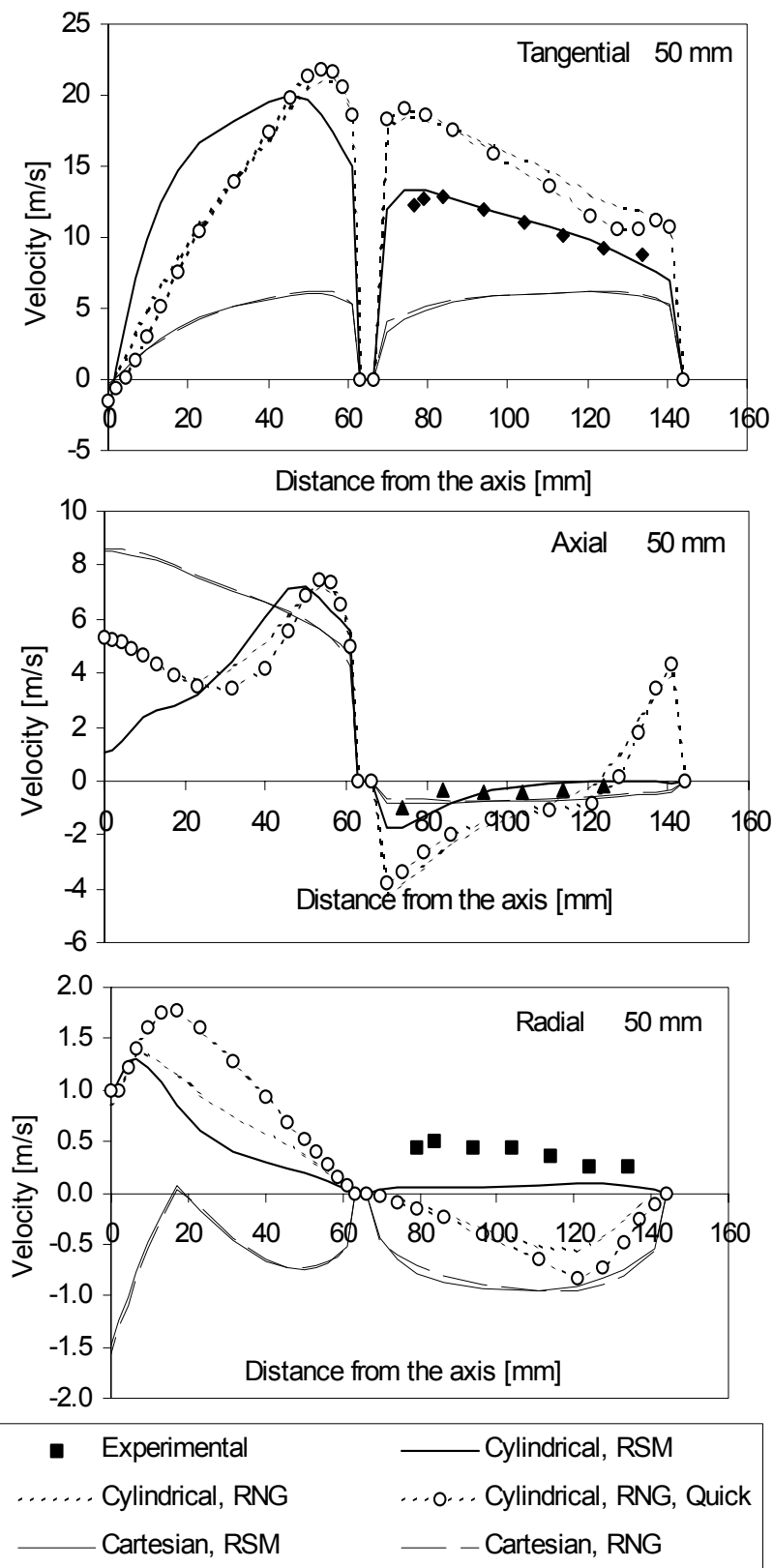


Figure 10.2: The velocity distribution in the Qing cyclone at 50 mm below the top.

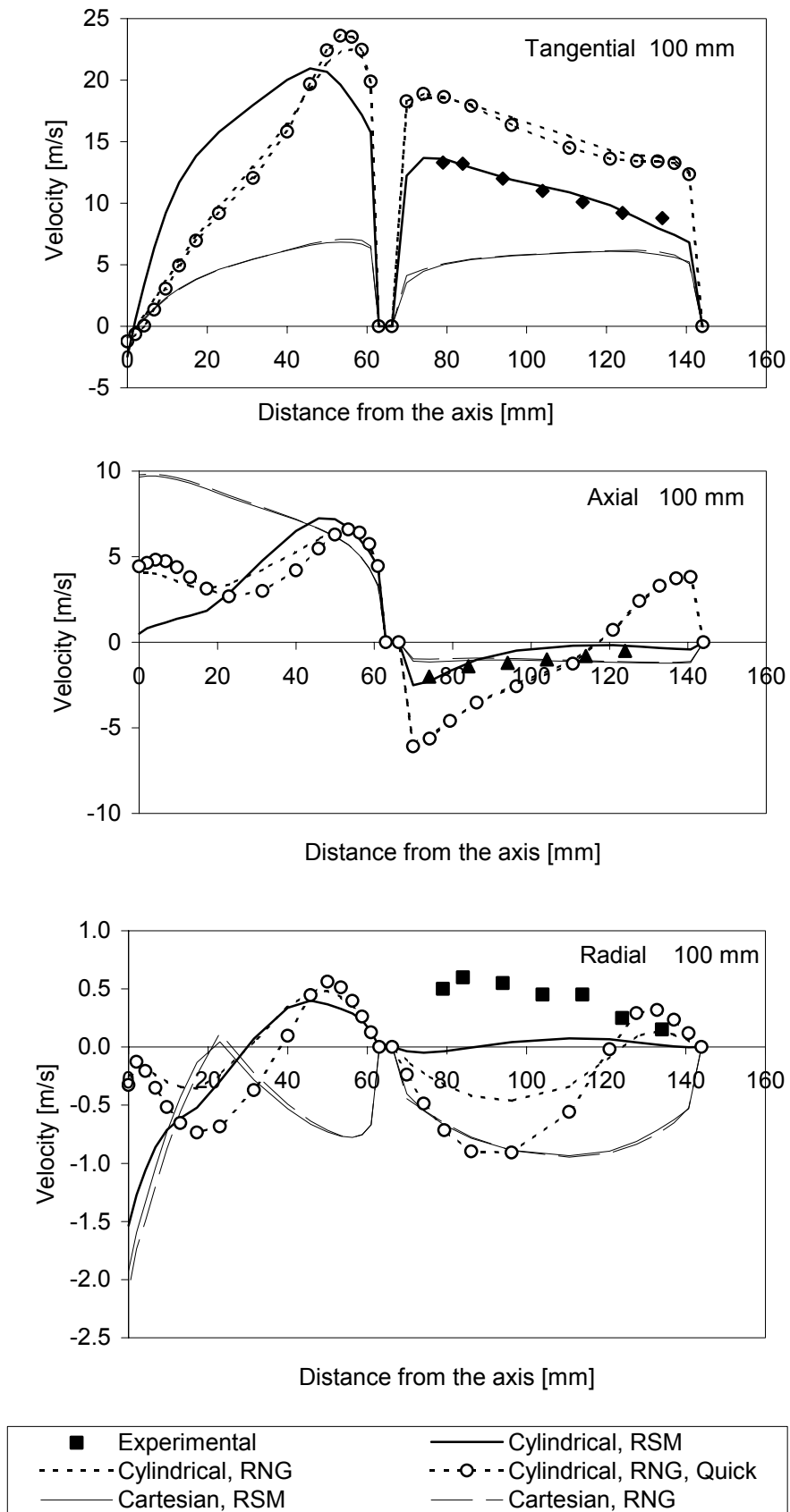


Figure 10.3: The velocity profiles for the Qing cyclone at 100 mm below the top.

In Figure 10.4 the velocity distributions at 150 mm from the top are presented. The vortex finder is not present at this level, and hence the measured data are all the way from the axis to the cyclone wall. The tangential profile shows that the cylindrical RSM case is superior in comparison with the other cases in the prediction of the tangential velocity. The tangential velocity is for this case very well predicted, and only some deviations exist. For the other cases deviations exist. The two cylindrical RNG cases overpredict the tangential velocity in certain places in the cyclone. Near the axis underpredictions exist, while further towards the cyclone wall overpredictions of the magnitude of the tangential velocities exist. For the Cartesian cases underprediction exist over the whole profile. For the axial velocity a negative velocity is measured near the axis. The cylindrical RSM case is the only case which predicts this negative velocity. The other cases overpredict the axial velocity near the axis. Negative or downward velocities are also noted near the cyclone wall. The Cartesian cases and the cylindrical RSM case predict this downward flow. The Cartesian cases predict badly near the axis, where a high overprediction of the axial velocity exists. For the radial velocity the measured data suggests a radial velocity near the axis in the order of 6 m/s. None of the cases is able to predict this high radial velocity. For minor parts of the predicted profiles from the Cartesian cases the quality of the predictions are good, but for the rest of the profiles large deviations exist. All in all the radial velocity is not very well predicted, and it is difficult to point out which case which is the better, but the cylindrical RSM is among the best.

In Figure 10.5 the velocity profiles from the Qing cyclone at 200 mm are presented. The cylindrical RSM case proves to be the best case in the prediction of the tangential velocity. The cylindrical RSM case predicts nearly perfect, while the other cases show deviations. For the Cartesian cases a major underprediction of the tangential velocity is present, and an overprediction occurs for the other cylindrical cases. The different cases give different axial velocities, but still the cylindrical RSM case is the best. The low velocity near the axis is only predicted by the cylindrical RSM case, but the model gives negative values while measurements only have positive values. Near the cyclone wall the negative velocity is predicted by the cylindrical RSM case and the Cartesian cases. The cylindrical RNG cases predict a positive velocity near the cyclone wall. The large magnitude in the radial velocity near the axis is not predicted by any of the cases, but towards the cyclone wall the prediction of the radial velocity is more or less satisfactorily.

All in all it is shown that Cartesian velocity components in the momentum equation give a low pressure, only 1/5 of the experimental, and large deviations in the velocity distribution. The deviations are biggest in the tangential velocity, where the magnitude is underpredicted, and for the axial velocity, where the low or negative velocity near the axis is not predicted. The cylindrical cases improve the predictions of the cyclones, but the improvement for the RNG cases are small. The RSM model used with cylindrical velocity components produces the best predictions, considering both the velocity distributions and the pressure drop.

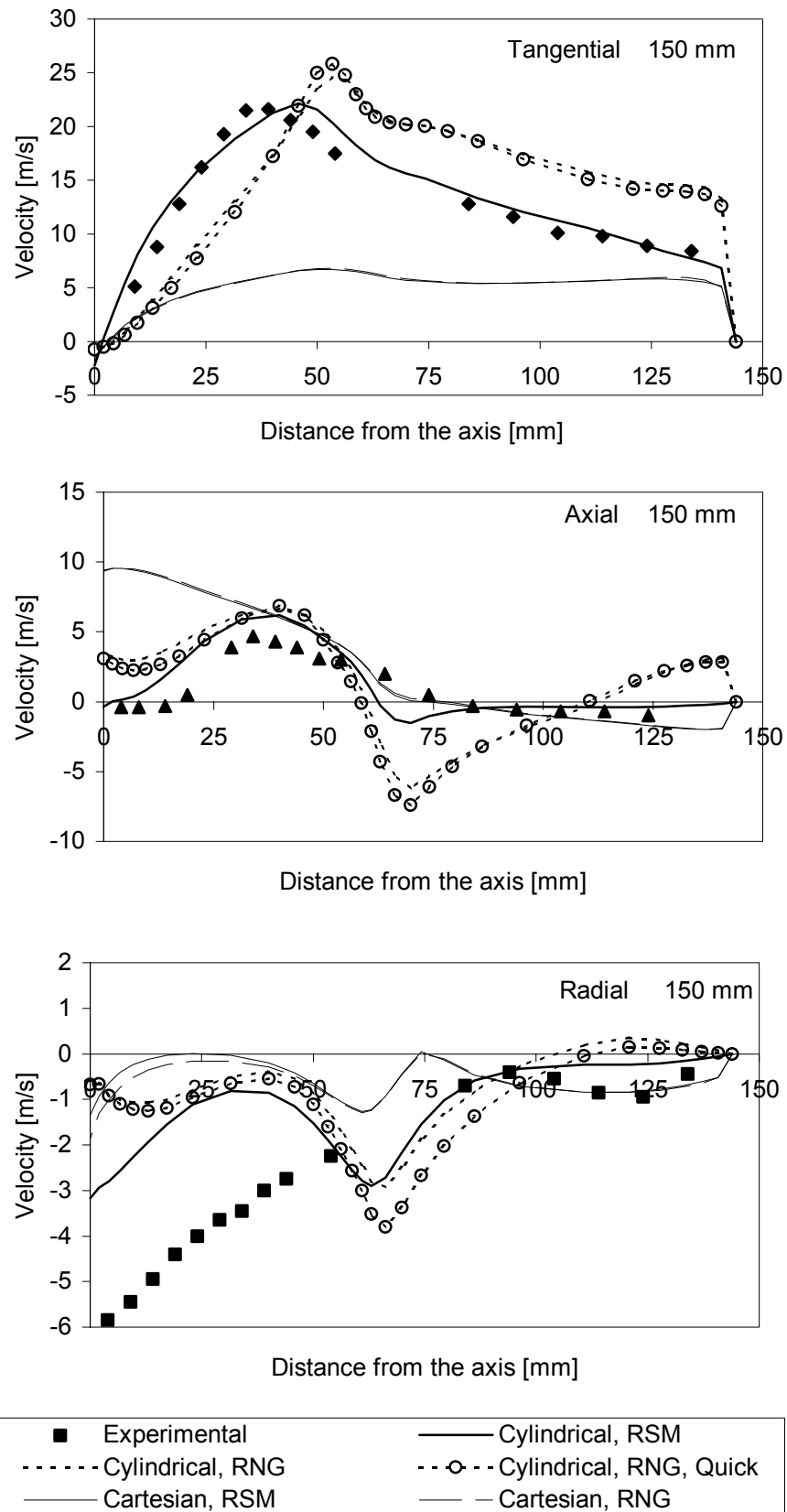


Figure 10.4: The velocity profiles for the Qing cyclone at 150 mm.

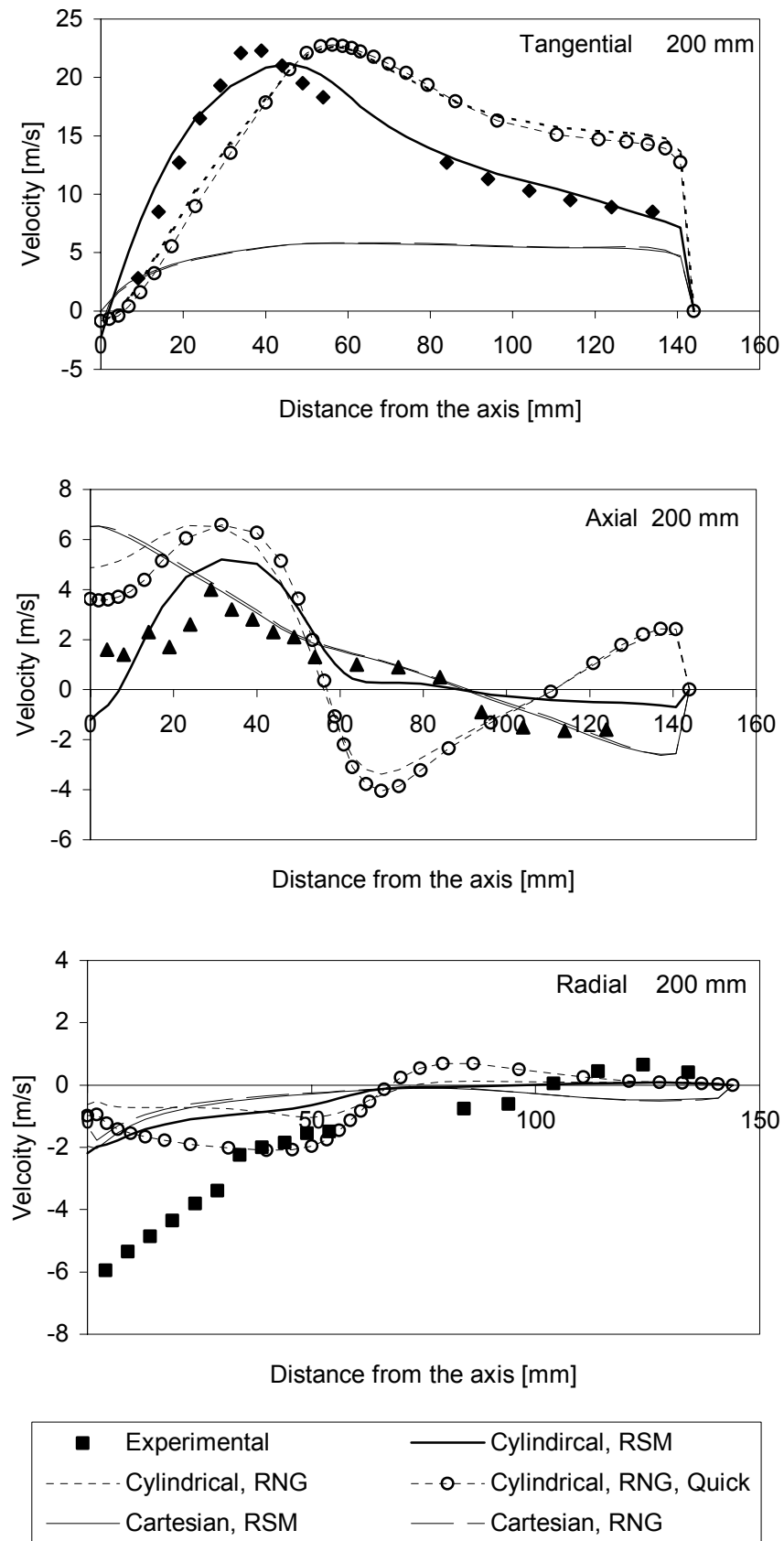


Figure 10.5: The velocity profiles for the Qing cyclone at 200 mm.

10.2.2 The Stairmand cyclone

For this cyclone, efficiency was measured for several mass flows along with the pressure drop [12]. No information about the flow field inside the cyclone is presented. The collection curves are produced by the use of an Euler-Lagrangian particle tracking method. For this cyclone five different inlet velocities are simulated: 5.1, 10, 15, 20, and 25 m/s. The predicted and measured pressure drops for various mass flows are presented in Table 10.3. First order scheme is used for all cases, except for the cylindrical RNG case where a higher order scheme is used, QUICK. From the table it can be seen that the trends from the Qing cyclone are confirmed. The cylindrical simulations are clearly better than the Cartesian, and the RSM model is better than the RNG model. However, for the Cartesian simulations nearly no difference appears between RSM and RNG model. For the Cartesian simulations the deviation is nearly constant at -80 %. For the cylindrical simulations the pressure drops are much better predicted, but variations exist. For the RNG k- ϵ model the predicted pressure drops vary between 10 to 38%, but for the RSM model variations between -4 to 12 % are noted.

Table 10.3: Static pressure drops for the high efficiency Stairmand cyclone.

Inlet velocity [m/s]	Static pressure drop [Pa]				
	5.1	10	15	20	25
Experimental	87.0	337.0	785.0	1407.0	2205.0
Cartesian, RNG k- ϵ	17.1	65.7	148.4	264.7	414.4
Cartesian, RSM	17.3	66.8	150.6	268.1	419.5
Cylindrical, RNG k- ϵ , Quick	95.3	416.8	984.1	1875.5	3058.2
Cylindrical, RSM	83.4	339.2	880.6	1359.0	2300.7

Figure 10.6 shows the normalized static pressure drops for the high efficiency Stairmand cyclone. The predicted pressure drop is divided by the experimental pressure drop for normalization. The figure shows clearly the underprediction of the Cartesian cases. The prediction of the cylindrical RSM cases is superior and the deviation of the cylindrical RNG k- ϵ increases with increasing mass flow.

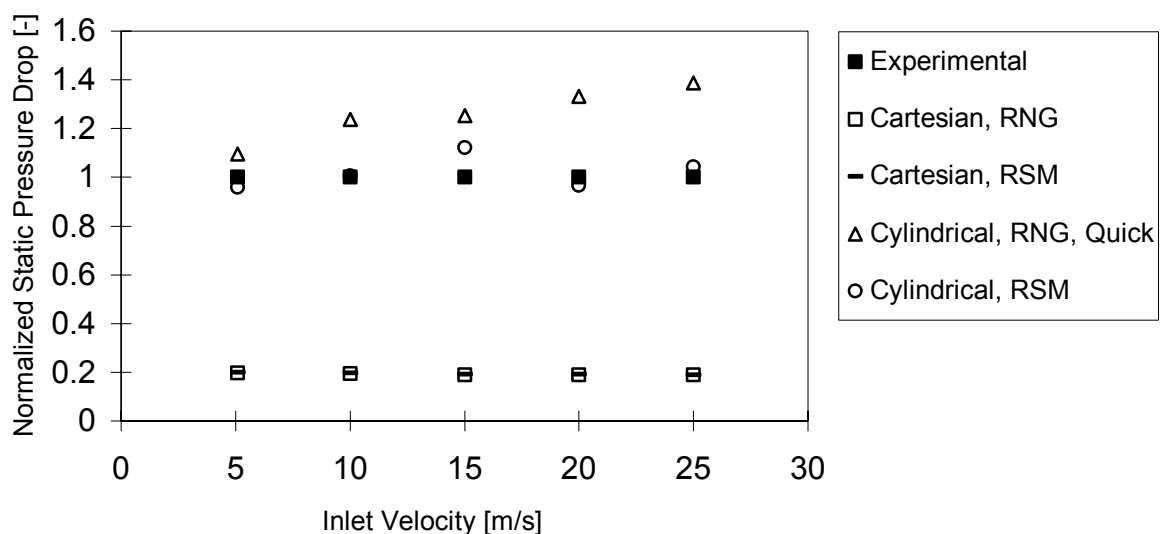


Figure 10.6: The normalised pressure drops for the different mass flows for the high efficiency Stairmand cyclone.

The fractional collection curve is based on the best case, the cylindrical RSM case. The fractional collection curve for inlet velocity of 5.1 m/s is shown in Figure 10.7, and for inlet velocity of 20 m/s is shown in Figure 10.8. The fractional collection curves are well predicted for 5.1 m/s, but the collection efficiency is overpredicted. For 20 m/s the fractional collection curve is very well predicted, and only minor deviations exist between the predictions and the measured values.

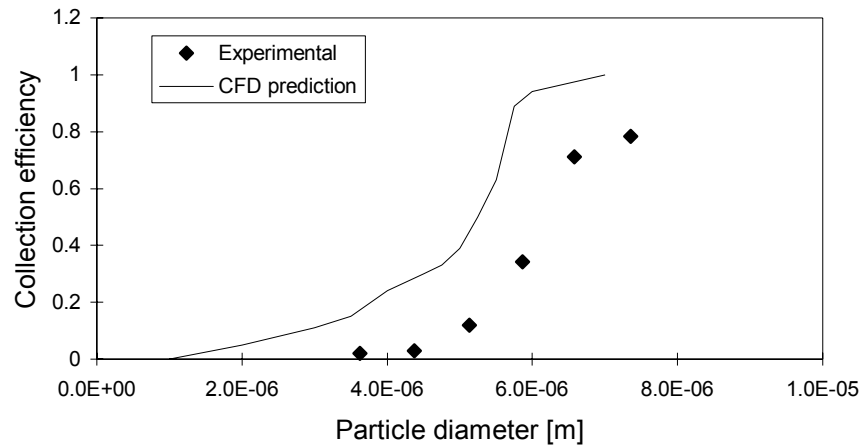


Figure 10.7: Fractional collection curve for the high efficiency Stairmand cyclone, 5.1 m/s.

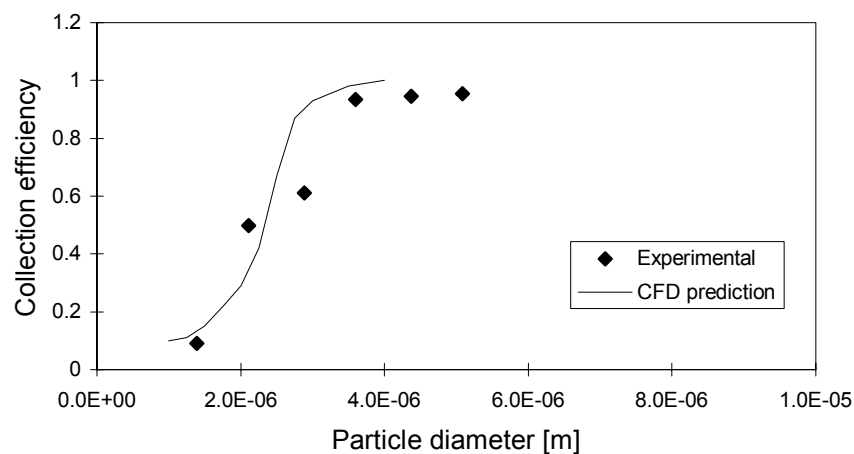


Figure 10.8: Fractional collection curve for the high efficiency Stairmand cyclone, 20 m/s.

10.3 Multiblock grid simulation

A multiblock simulation is carried out in order to achieve comparisons between the structured grid and the multiblock grid simulation. The structured grid used in the previous simulations is based on cylindrical velocity components. The multiblock grid is shown in Figure 10.9.

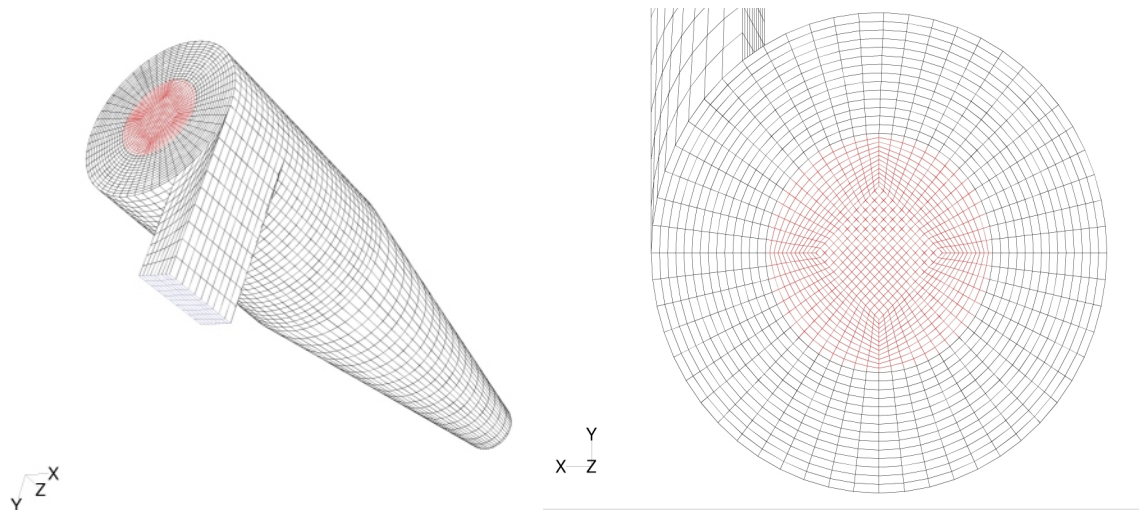


Figure 10.9: The multiblock grid of the Stairmand cyclone.

The solver used together with the multiblock grid is the Fluent v5.0. The multiblock grid used on the cyclone is often called butterfly grid. Instead of the earlier body fitted structured grid of the cyclone, two different cell types are used. Square cells are near the axis, and body fitted near the walls. The CFD technique is the same, but only Cartesian velocity formulation is valid. In addition the PRESTO scheme is used for the pressure-velocity coupling. PRESTO (PREssure STaggering Option) scheme uses the continuity balance for a staggered control volume about the face to compute the staggered (actual the face) pressure, similar proposed by Patankar for structured grids in [49].

10.4 Results from the multiblock cases

The two cyclones simulated in the previous section are simulated again with the multiblock grid. This makes the basis for interesting comparisons between the performance of the two types of grids. The results for the Qing cyclone are presented first.

10.4.1 The Qing cyclone

Two cases are simulated, and these are compared with the matching structured cases. For the structured cases the cylindrical velocity components are used in the momentum equations, while for the multiblock cases the Cartesian velocity components are used. The static pressure drop over the cyclone for the four cases and the experimental value are shown in Table 10.4. The inlet velocity is 7.1 m/s. The prediction of the pressure drop for the RNG k- ϵ case increases in quality when using a multiblock grid rather than the structured grid. The RSM model gives similar results for the multiblock and structured simulations.

Table 10.4: The static pressure drop over the cyclone is compared with the experimental.

	Static pressure drop [Pa]	% deviation
Experimental	436	
Structured, RNG k- ϵ	566.1	29.8
Structured, RSM	398.3	-8.6
Multiblock, RNG k- ϵ	496.2	13.8
Multiblock, RSM	399.1	-8.5

For the Qing cyclone velocity profiles are known for several heights, and comparisons between structured and multiblock for the RSM cases are shown. Figure 10.10 shows the velocity profiles at 50 mm from the top of the cyclone. The tangential velocity between the cyclone wall and the vortex finder are well predicted in both cases. The tangential velocity is quite different inside the vortex finder. For the structured approach it was necessary to increase the length of the outlet section in order to avoid suction of mass to the centre of the cyclone. For the multiblock approach it was not necessary to increase the length of the outlet section. This is the explanation for the great difference between the velocity predictions in the vortex finder. For the axial velocity between the vortex finder and the cyclone wall, the deviations are small. The radial velocity is better predicted by the multiblock approach near the cyclone wall, while near the vortex finder the predictions are not so good. In the vortex finder it is lack of measurements, but the two cases predict slightly different.

The measurements at 100 mm below the top of the cyclone are presented in Figure 10.11. The tangential and the axial velocities are well predicted for both of the approaches, while the radial velocities contain deviations between the predicted and measured velocities. The difference in the prediction of the velocity inside the vortex finder is still present at this location.

Velocity profiles at 150 mm below the top of the cyclone are given in Figure 10.12. The tangential velocity is better predicted by the structured approach. The multiblock approach predicts a lower magnitude of the tangential velocity, and the maximum velocity is moved towards the cyclone wall. For the axial velocity the multiblock approach predicts slightly better. The radial velocity is only satisfactorily predicted in parts of the region, and as seen before, near the axis the predicted velocity cannot match the measured velocity.

Figure 10.13 shows the velocity profiles located at 200 mm from the top of the cyclone. The predictions from this level show the same trends as for the 150 mm position.

The overall conclusions are not easy to make. The differences in the quality of the predictions of the velocity distributions are small. But there is one aspect which counts in favour of the multiblock grid, and that is that the work used to obtain a converged solution is much less than for the structured case. Less iteration is needed, common under-relaxation factors are used, and stable convergence is quickly achieved for the multiblock approach. The structured solution process involves reduced under-relaxation factors, two sets of under-relaxation factors, harder to build a grid, and slow convergence. All this favours the multiblock approach, and taking into account that the quality is nearly the same for the two approaches, it seems safe to suggest that the multiblock is to be preferred in future analysis.

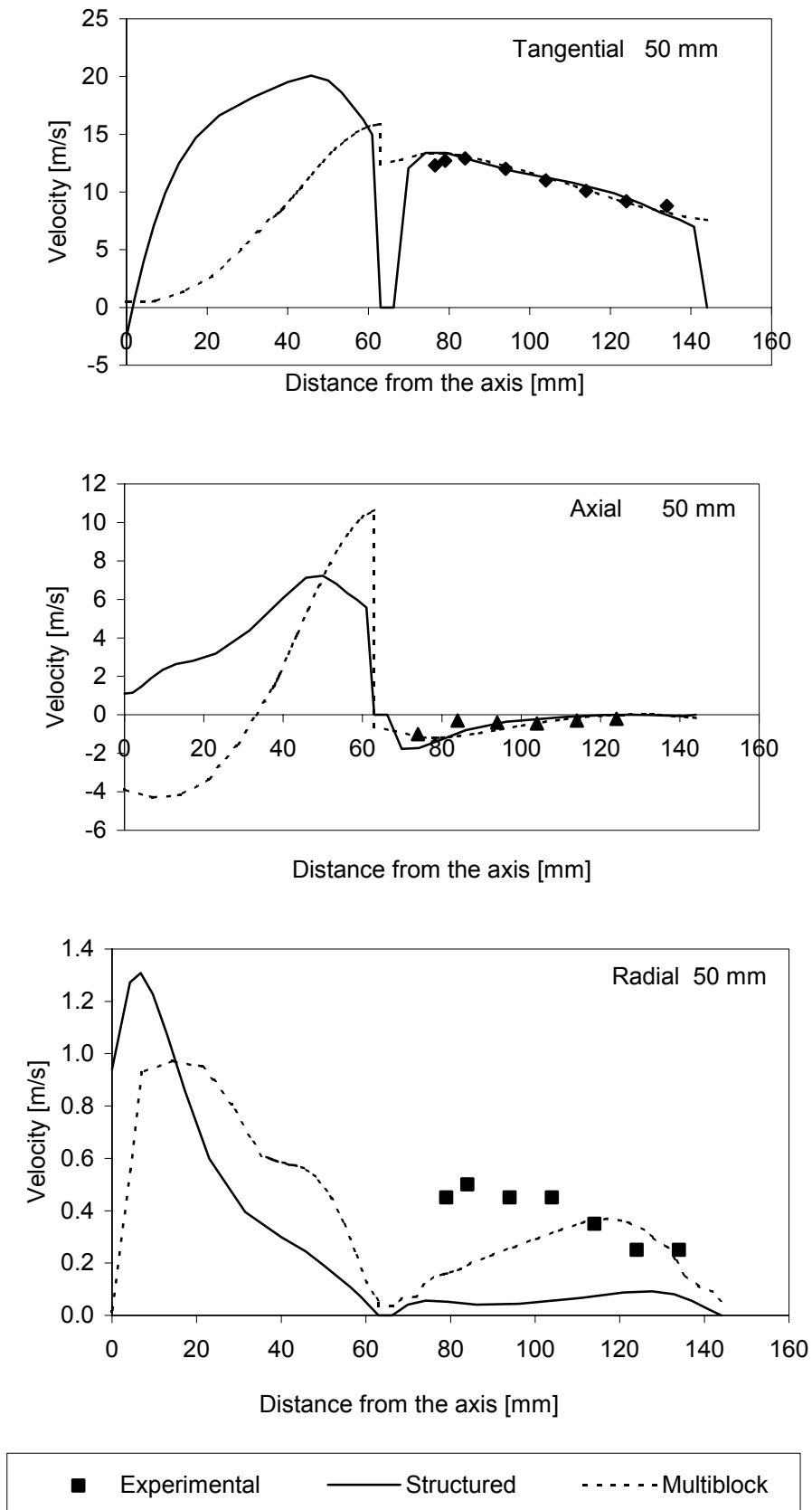


Figure 10.10: The velocity profiles for the Qing cyclone at 50 mm below the top.

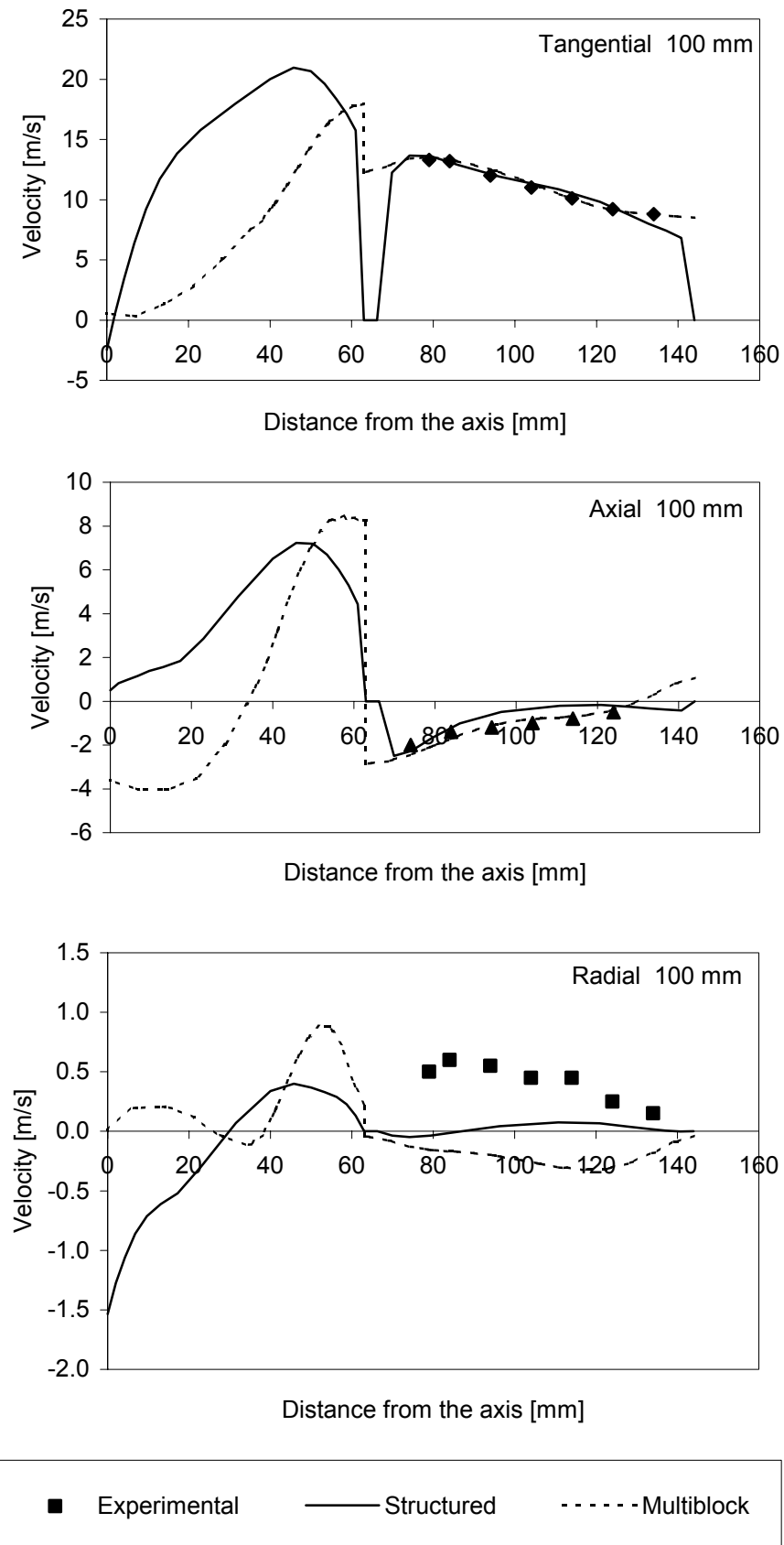


Figure 10.11: The velocity profiles for the Qing cyclone at 100 mm below the top.

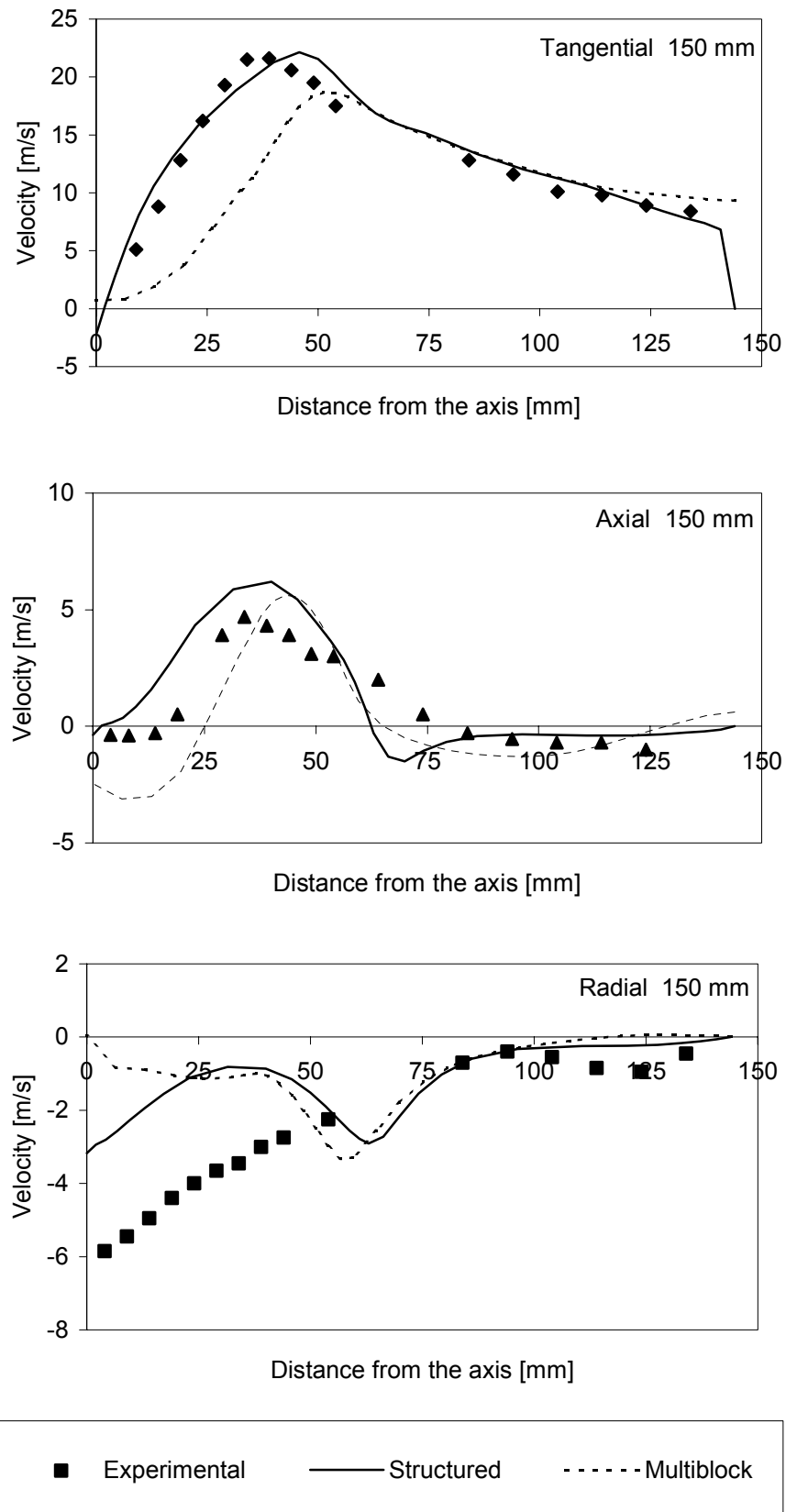


Figure 10.12: The velocity profiles for the Qing cyclone at 150 mm below the top.

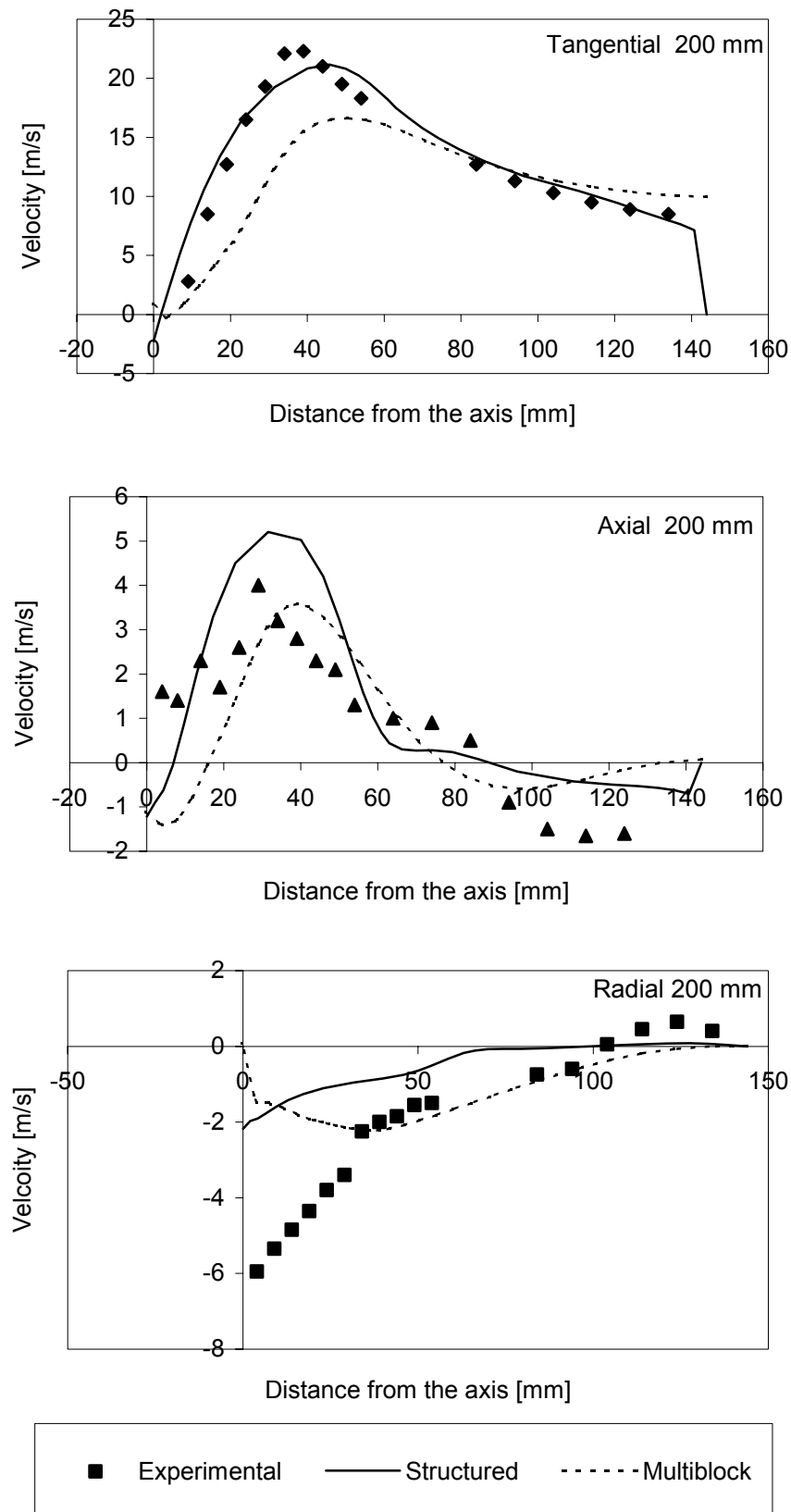


Figure 10.13: The velocity profiles for the Qing cyclone at 200 mm.

10.4.2 The Stairmand cyclone

The Stairmand cyclone is simulated with the multiblock grid with an inlet velocity of 5.1 m/s. The pressure drop comparisons are shown in Table 10.5.

Table 10.5: Pressure drops for the multiblock and the structured simulations.

Case	Static pressure drop	Deviation
	[Pa]	[%]
Experimental	87	
Structured, Cylindrical, RSM	83.4	-4.1
Multiblock	86.4	-0.7

The pressure drop is well simulated for both the structured and the multiblock approach. The efficiency curves are generated similar for the multiblock case as it was for the structured method. The generated curve is shown in Figure 10.14. As seen from the figure the efficiency is overpredicted. Too many of the small particles are trapped in the cyclone, and even so small particles as 0.1 μm have difficulties in leaving the cyclone in the multiblock case.

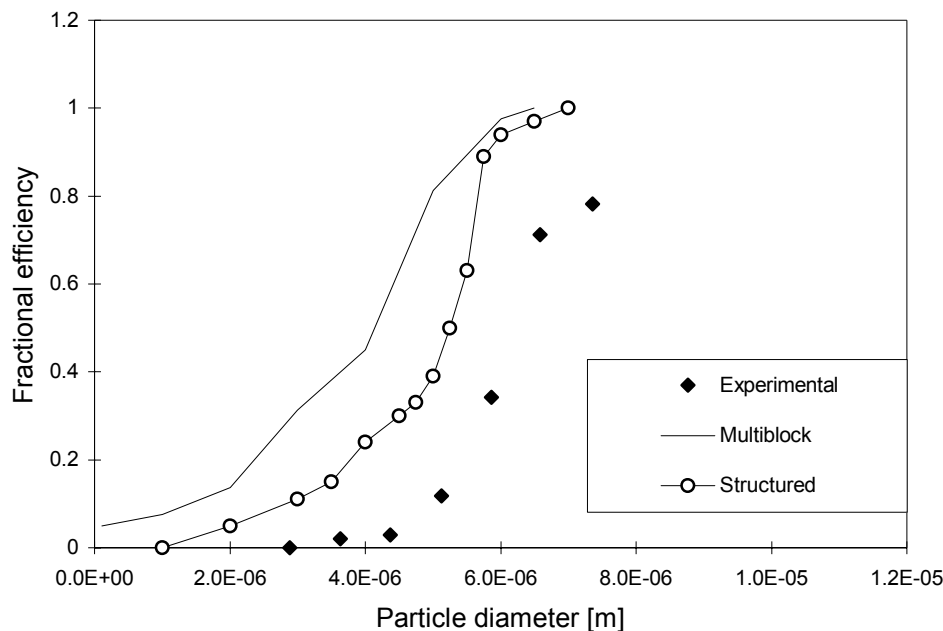


Figure 10.14 Fractional collection curves for the high efficiency Stairmand cyclone.

The reason for the increase in the overprediction of the efficiency for the multiblock case is believed to arise from the fact that the velocity vectors are not complete tangential by the cyclone wall. A small angle towards the wall can be noted, and it is probably this angel that forces small particles to touch the wall and get collected. When performing simulations without the PRESTO scheme, the the angels towards the walls were larger, and made the predicted efficiency of the cyclones even more overpredicted.

10.5 Conclusions from the cyclone simulations

The results showed that to be able to get good results from simulating cyclones with a structured CFD code, one should use the cylindrical velocity formulation along with the RSM model for turbulence. The RSM model predicts better than the RNG k- ϵ model. Cartesian

velocity components in the momentum equations for structured cases should be avoided, because of the low quality of predicting the pressure drop. The simulations of the multiblock cases showed good results on the velocity predictions and on the predictions of the pressure drop, while the particle tracking is yet not so good enough. This leads to a high efficiency, and the reason is believed too be the non-tangential velocity vectors near the walls in the cyclone.

Chapter 11

Conclusions and further work

The conclusions from the work presented in this thesis are divided into two separate parts. The first part considers the work performed on the droplet-gas flow inside the vane separator, and the second part covers the work performed on cyclones.

For the vane separator

For the vane separator we have shown that detailed measurements are possible using LDA. Some minor problems related to achieving optical access to the narrowest cross-sections are solved. The laser beam was given a slight incident angle so the velocity profile is measured from the lower vane wall to the upper vane wall. Full velocity and rms velocity profiles are measured for approximately seven cross-sections throughout the vane for three different mass flow rates. Chapter 5 presents all the measured profiles. The measurements reveal that a slight backflow can be noted near the end of the upper vane wall. Other cross-sections show velocity and rms velocity profiles that are expectable. Each cross-section profile is composed of minimum three parallels. The three parallels coincide very well for most of the cross-sections, and only in exceptional cases it can be seen that the profiles are composed of several parallels. This implies that the measurements have a good quality, and are repeatable and the relative errors are small. In addition, the non-dimensional profiles for the different mass flow rates are compared. This comparison shows that there is a great similarity between the different mass flow rates.

A computational model is made as identical as possible to the experimental model. A structured and un-structured grid was made of the vane by the CFD software from Fluent. The performance of the two different grid approaches was studied, and shows only minor differences in the predictions. The quality of the simulations was hence nearly equal for the structured and un-structured cases. It is, however, less complicated to make a satisfactorily grid using the un-structured approach. In the testing of the CFD predictions numerous models and numerical schemes were tested. The predictions from these cases show mostly divergent trends, but there is a trend, which points out. The case using the RSM model together with the QUICK scheme shows more deviation than the other cases. The resirculation zone behind the two barbs, are overpredicted by the RSM-QUICK case. The RSM used together with a first order scheme does not show the same tendency of overpredicting the resirculating zone. The reason why the predictions are not so good for the RSM and QUICK combination is not completely understood. At present time there is no good explanation for this phenomena. A good thing though, is that the overpredictions are also shown in the prediction of the pressure drop. The overprediction of the pressure drop is then a good signal for further analysis of the solution in future simulations. The other cases perform satisfactorily, and in many of the cross-sections the predictions coincide with the experimental profile. There exists some deviation between the predictions and measurements in the resirculation zones. The k- ϵ model is known to be weak in regions with separation due to the overprediction of the turbulent shear stress in the shear layer.

Droplet size distribution upstream and downstream the vane separator was measured using the PDA technique. These measurements were done in a new modified rig. The channel used in

the velocity measurements influenced the droplet size distribution so much that the mean droplet diameter entering the separator was too small. Another important effect of increasing the dimensions of the inlet channel for the droplet size measurements was the decrease in the deposition rate on the channel walls. This deposition ruins the optical access, and makes measurements impossible. During the PDA measurements some deposition activity was noted on the channel wall, but using a wiping technique enabled the optical access making the measurements possible. However, the deposition activity was considerably less on the outlet of the separator than the inlet. Good diameter measurements depend on much tuning, re-tuning and alteration of the set-up. The measurements are considered good, and typically the number of validated measurements in each measuring point was determined from experience.

The droplet size distributions upstream and downstream the separator are plotted and compared. The comparison shows that, besides removing large droplets, the vane separator generates droplets with smaller diameters than entering the separator. The generated droplets have a diameter less than 20 μm . This is of course not wanted. Possible mechanisms for explaining the generation of the new droplets are found in the literature. These mechanisms are studied, and models for predicting droplet generation based on these mechanisms exist in the literature. These models are tested with the operational conditions, which exist in the separator. This analysis shows that none of the models found in the literature are capable of predicting the droplet generation.

An alternative mechanism is proposed in this work. This mechanism is based on the droplet collisions that are not energetic enough to splash directly. But under the influence of more droplet collisions and turbulent effects a droplet generation occurs. The impacting droplets create disturbances on the surface, and under quiescent conditions no new droplets are generated. But between the vanes the conditions are far from quiescent, and shear from the passing gas, turbulence fluctuations, and additional droplet impacts contribute to the disturbances.

Three new models for describing the droplet generation are made. ‘Model 1 – Empirical model’ is based on the experimental findings, and is purely empirical. ‘Model 2 – Constant We number model’ is based on a force balance on a ligament; which is sheared off from the passing gas. The force balance is manipulated to an expression containing the Weber number. The Weber number in this model is constant. ‘Model 3 – Varying We number model’ is based on ‘Model 2 – Constant We number model’ but a variation on the We number is included. The Weber number used contains contributions from the turbulent level. These three models are used together with the CFD code to predict the droplet size distribution leaving the separator. The models give an improvement in the prediction of the droplet size distribution.

To round off the conclusions from the vane separator work, it seems appropriate to come with suggestion about further work. The new models are capable of improving the quality of the droplet size distribution leaving the separator. There is however some limitations in the models. The model is not capable of capturing multiple generation of droplet. For each control volume, only one droplet is generated if the We number reaches the threshold. This is of course also due to the limitation from the Euler-Lagrangian method that is used. Further work could reveal information about the number of generated droplets. For example, it would be interesting to start with a droplet size distribution that has only droplets larger than the largest droplet measured at the outlet. Then one would know that all the leaving droplets are generated inside the separator, and one would be able to say something about the number of droplets generated or the mass they represent. Another feature of the model, which could be

altered in order to improve the model, is to include the calculation of a local We number. The local We number could, for example, be connected to the current turbulence level, shear level and geometrical conditions of the surroundings. Since the model is tested for Euler-Lagranigan technique, is would be wise to include this model in an Euler-Euler simulation. Further testing in different applications and comparisons against other experimental data is also suggested.

For the cyclones

For the cyclones it is shown that a CFD analysis requires cylindrical velocity components in the momentum balance for a structured grid. The simulations show satisfactory prediction of the flow field inside the cyclone if cylindrical velocity components are used. The RSM model is better than the RNG k- ϵ model. If Cartesian velocity components were used, the predicted pressure drop was underpredicted by 80 %. The efficiency of the cyclone is satisfactorily predicted by an Euler-Lagrange method, and the fractional collection curve is shown.

It is also shown that the multiblock technique together with Cartesian velocity components performs just as well as the structured technique with cylindrical velocity components. The velocity profiles are of the same quality, and the pressure drops are in the same order of deviation. The efficiency is overpredicted some by the multiblock method.

For the cyclones, further work would be to compare the models presented in Chapter 8 to measurements performed on a droplet-gas cyclone. If good and reliable measurements are hard to find, which they often are, it should be considered to carry out the measurements. The combined effort of both numerical and experimental measurements could lead to design improvements, and increased understanding of droplet-gas flow. Future versions of the CFD code should be tested, and the efficiency prediction be investigated.

12 References

- [1] Al-Roub, M. and Farrell, P.V. *Atomization of thin liquid films by droplet impact*. Atomization and Sprays, Vol. 7, pp. 531-547, 1997.
- [2] Azzopardi, B.J. *Drops in annular two-phase flow*. Int. J. Multiphase Flow, Vol. 23, Suppl., pp. 1-53, 1997.
- [3] Basset, A. B. *Hydrodynamics*, New York, Dover, USA. 1961.
- [4] Bradshaw, P. *An introduction to turbulence and its measurements*. Pergamon Press, Oxford, 1971.
- [5] Brayton, D.B, Kalb, H. T. and Crosswy, F. L. *Two Component Dual-Scatter Laser Doppler Velocimeter with Frequency burst Signal Readout*. Applied optics, Vol. 12, No. 6, June 1973.
- [6] Brunazzi, E., Nardini, G. and Paglianti, A. *An experimental study of gas-liquid separation in vane-type demisters*. The 1996 IchemE event/Second European conference for young researchers, 1996.
- [7] Bürkholz, A. *Droplet separation*. VCH publishers, New York, NY(USA), ISBN 0-89573-879-1, 1989.
- [8] Chandra, S. and Avedisian, T. C. *On the collision of a droplet with a solid surface*. Proc. R. Soc. Lond. A, 432, pp. 13-41, 1991.
- [9] Chen, H.C. and Patel, V.C. *Near-wall Turbulence Models for Complex Flows Including Separation*. AIAA J. Vol. 26, No. 6, pp. 641-648, 1988.
- [10] Clift, R., Grace, J.R. and Weber, M.E. *Bubbles, Drops, and Particles*. Academic Press, New York, 1978.
- [11] Cossali, G.E., Coghe, A. and Marengo, M. *The impact of a single drop on a wetted solid surface*. Experiments in Fluids, Vol. 22, pp. 463-472, 1997.
- [12] Crowe, C., Sommerfeld, M. and Tsui, Y. *Multiphase flows with droplets and particles*. CRC Press, 1998.
- [13] Dantec *Particle Dynamics Analyser*. Dantec Measurement Technology A/S, P. O. Box 121, Tonsbakken 18, DK-2740 Skovlunde, Denmark, April 1999.
- [14] Dirgo, L. and Leith, D. *Cylone collection efficiency : comparison of experimental results with theoretical predictions* Aerosol Sci, Technol., Vol. 4, pp. 401-415, 1985.
- [15] Durst, F., Melling, A. and Whitelaw, J. H. *Theory and Practice of Laser Doppler Anemometry*. G. Braun, Karlsruhe, 1981.

- [16] Durst, F. and Zaré, M. *Laser Doppler measurements in two-phase flows*. In: "The Accuracy of flow measurements by Laser Doppler Methods", Proceedings of the LDA-Symposium, Copenhagen 1975, P. Buchhave et al., Copenhagen (1976).
- [17] Elseth, G. *An experimental study of Oil/Water flow in horizontal pipes*, PhD-thesis, NTNU Trondheim, Høgskolen i Telemark, Doktor Ingeniøravhandling, 2001:102, 2001.
- [18] *Fluent User's Guide*, Volume 1-4, Release 4.5 (June 1996), Release 5.0 (July 1998).
- [19] Gaskell, P.H. and Lau, A.K.C. *Curvature-compensated convective transport: smart, a new boundedness-preserving transport algorithm* International Journal for Numerical Methods in Fluids, Vol. 8, pp. 617-641, 1988.
- [20] Griffiths, W.D. and Boysan, F. *Computational Fluid Dynamics (CFD) and empirical modeling of the performance of a number of cyclone samplers*. J. Aerosol Sci., Vol 27, No. 2, pp. 281-304, 1996.
- [21] Hinze J.O. *Fundamentals of the Hydrodynamic Mechanisms of Splitting in Dispersion Processes*, AIChE Journal, Vol. 1, No. 3, pp. 289-295, September 1955.
- [22] Hinze, J.O. *Turbulence*, McGraw-Hill Publishing Co., New York, 1975.
- [23] Jakobsen, H.A. *On the Modelling and Simulation of Bubble Column Reactors Using a Two-Fluid Model*, Dr.Ing. thesis, Trondheim, Norway, 1993.
- [24] Johansen, S.T. *On the modelling of Disperse Two-phase Flows*, Dr. Tech. Thesis, Trondheim, Norway, 1990.
- [25] Jøsang, A.I. and Melaaen, M.C. *Numerical predictions of cyclones*, Relpowflo III, Porsgrunn, August, 1999.
- [26] Kallio, G.A and Reeks, M.W. *A numerical simulation of particle deposition in turbulent boundary layers* Int. J. Multiphase Flow, Vol. 15, No. 3, pp. 433-446, 1989.
- [27] Kataoka, I., Ishii, M. and Mishima, K. *Generation and Size Distribution of Droplet in Annular Two-phase Flow*. Transactions of the ASME, Vol. 105, pp. 230-240, June 1983.
- [28] Kays, W.M and Crawford, M.E. *Convective Heat and Mass Transfer*. McGraw-Hill Book Company, New York, 3rd edition, 1993.
- [29] Keshava Iyer, V., Dasgupta, A., Venkat Rao, B. and Srivastava, R. *Some investigation on flow through chevrons of moisture separator and reheater used in nuclear power plants*. Proceedings of the ASME Fluids Engineering Division, FED-Vol. 244, pp. 381-386, ASME 1997.
- [30] Kudo, Y., Tanaka, N. and Miyano, H. *An analytical study on the moisture separation performance in dryers*. International Conference on Nuclear Engineering, Volume 1 - Part A, pp. 123-129, ASME 1996.
- [31] Kuo, K.K *Principles of Combustion*. John Wiley & Sons, New York, 1986.

- [32] Launder, B.E., Reece, G.J. and Rodi, W. *Progress in the development of a Reynolds-stress turbulence closure* J. Fluid Mech., Vol. 68, part 3, pp. 537-566, April 15, 1975.
- [33] Launder, B.E and Spalding, D.B. *Lectures in Mathematical Models of Turbulent Flows*, Academic Press, London, England, 1972.
- [34] Launder, B.E. and Spalding, D.B. *The Numerical Computation of Turbulent Flows* Computer Methods in Applied Mechanics and Engineering, Vol. 3, pp. 269-289, 1974.
- [35] Launder, B.E. *Second-moment closure: Present... and future?* Int. J. Heat Fluid Flow, Vol. 10, No.4, pp. 282-300, 1989.
- [36] Layton, J.S., Walters, J.K., Azzopardi B.J. and Zaidi S.H. *Droplet motion in wave-plate demisters*. The 1997 jubilee research event, IchemE, 1997.
- [37] Layton, J.S., Zaidi S.H., Altunbas, A., Walters, J.K. and Azzopardi, B.J. *Study of droplet size distribution in Wave-plate demisters using Optical Techniques*. Proc. SPIE, Vol. 3172, pp. 45-54, 1997.
- [38] Lee, M.M. and Hanratty T.J. *The inhibition of droplet deposition by the presence of a liquid wall film*. Int. J. Multiphase Flow, Vol. 14, No. 2, pp. 129-140, 1988.
- [39] Leonard, B.P. *A stable and accurate convective modelling procedure based on quadratic upstream interpolation*. Computer methods in applied mechanics and engineering, North-Holland publishing company, 19, pp. 59-98, 1979.
- [40] Mazumder, M.K. and Wankum, D.L., *SNR and Spectral Broadening in turbulence structure measurement using a cw laser*. Applied optics, Vol. 14, 1970.
- [41] Morsi, S.A. and Alexander, A.J *An investigation of particle trajectories in two-phase flow systems* Journal Fluid Mech. Vol. 55 (part 2), pp. 193-208, 1972.
- [42] Mundo, C., Sommerfeld, M. and Tropea, C. *Experimental studies of the deposition and splashing of small liquid droplets impinging on a flat surface*. ICLASS -94, Rouen, France, July 1994, Paper I-18, pp. 134-141.
- [43] Mundo, C., Sommerfeld, M. and Tropea, C. *Droplet-wall collisions: Experimental studies of the deformation and break-up process*. Int. J. Multiphase Flow, Vol. 21, No. 2, pp. 151-173, 1995.
- [44] Mundo, C., Sommerfeld, M. and Tropea, C. *On the modelling of liquid sprays impinging on surfaces*. Atomization and Sprays, Vol. 8, pp. 625-652, 1998.
- [45] Monat, J. P., McNulty J., Michelson, I.S. and Hansen O.V. *Accurate evaluation of chevron mist eliminators*. Chemical engineering progress, December 1986.
- [46] Nakao, T., Nagase, M., Aoyama, G. and Murase, M. *Development of Simplified Wave-type Vane in BWR Steam Dryer and Assessment of Vane Droplet Removal Characteristics*. Journal of Nuclear Science and Technology, Vol. 36, No. 5, pp. 424-432, May 1999.

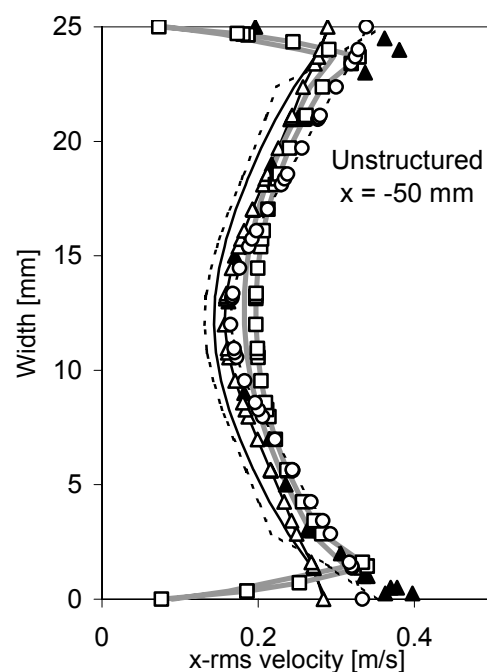
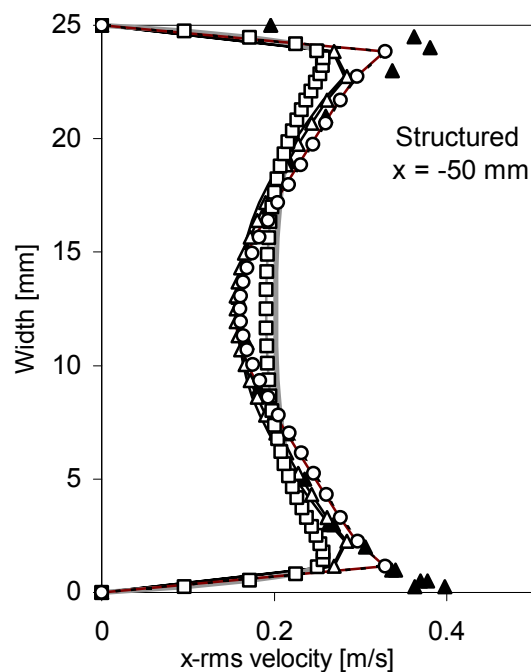
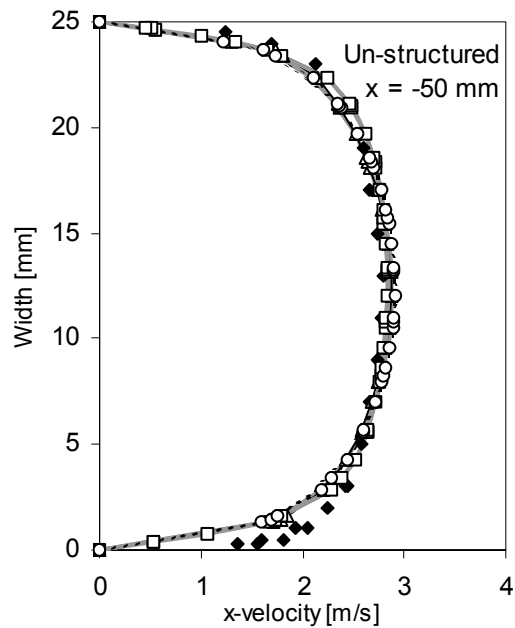
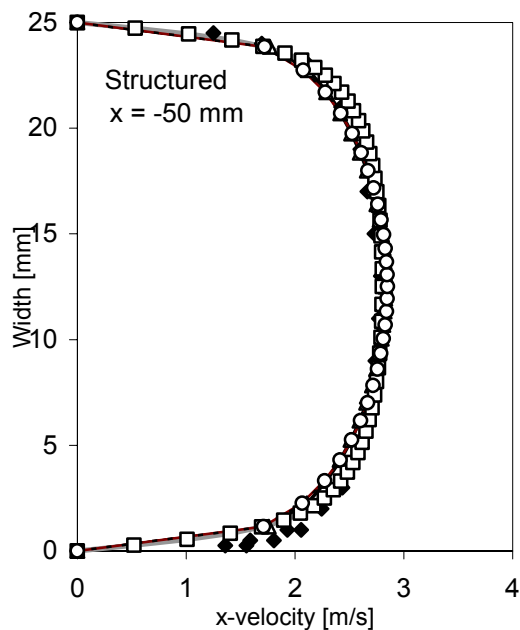
- [47] Narasimhamurty, G.S.R. and Purushothaman, A. *Hydrodynamics in of liquid drops in air*. Encyclopaedia of fluid mechanics, Vol. 3 Gas-Liquids flows.
- [48] Park, K. and Watkins, A.P. *Comparison of wall spray impaction models with experimental data on drop velocities and sizes*. Int. J. Heat and Fluid flow 17:424-438, 1996.
- [49] Patankar, S.V. *Numerical heat transfer and fluid flow* McGraw-Hill Book Company, New York, 1980.
- [50] Phillips, H.W. and Deakin, A.W. *Measurements of the collection efficiency of various demister devices*. Proceedings of the 4th Annual Meeting of the Aerosol Society, Loughborough, 1990.
- [51] Qian, J. and Law, C.K. *Regimes of coalescence and separation in droplet collision*. J. Fluid Mech, 1997, vol 331, pp 59-80, fig1 and 2.
- [52] Qing, X. H. *Velocity and turbulence distributions in cyclone* Ph.D. thesis, Department of Fluid Mechanics, Technical University of Denmark, 1983.
- [53] Rodi, W. *Turbulence Models and their Application in Hydraulics*. Delft, The Netherlands, IAHR, 1984.
- [54] Rubinow, S. I. and Keller, J.B. *The transverse force on a spinning sphere moving in a viscous fluid*. Journal Fluid Mech., Vol 11, pp. 447-459, 1961.
- [55] Saffman, P. G. Journal Fluid Mech., Vol 22, pp. 385, 1965.
- [56] Schlichting, H. *Boundary-layer Theory*. 7th edition, McGraw-Hill Book Company, New York, 1979.
- [57] Schmehl, R., Roskamp, H., Willmann, M. and Wittig S. *CFD analysis of spray propagation and evaporation including wall film formation and spray/film interactions*. Int. J. of Heat and Fluid Flow, 20, pp. 520-529, 1999.
- [58] Stanton, D.W. and Rutland, C. J. *Multi-dimensional modelling of thin liquid films and spray-wall interactions resulting from impinging sprays*. Int. J. Heat Transfer 41, pp. 3037-3054, 1998.
- [59] Thompson J.F. J. Fluid Mech, Vol. 180, pp. 529-556, 1987
- [60] Tsouris, C. and Tavlarides, L.L. *Breakage and Coalescence models for drops in turbulent dispersions*. AIChE Journal, Vol. 40, No. 3, pp 395-406, March 1994.
- [61] Ushiki, K., Nishizawa, E., Beniko, H. and Iiinoya, K. *Performance of a droplet separator with multistage rows of flat blades*. Journal of Chemical Engineering of Japan, Vol. 15, No. 4, pp. 292-295, 1982.

- [62] Van Kampen, N.G. *Stochastic Processes in physics and chemistry* North-Holland, Amsterdam, 1987.
- [63] Verlaan, C. *Performance of novel mist eliminators*. Ph.D. thesis, Delft University of Technology, Faculty of Mechanical Engineering and Marine Technology, ISBN 90-370-0054-1, 1991.
- [64] Wachters, L.H.J. and Westerling, N.A.J. *The heat transfer from a hot wall to a impinging water drops in spheroidal shape*. Chem. Eng. Sci., 21, pp. 1047-1056, 1966.
- [65] Wang, Y. and James, P.W. *The calculation of wave-plate demister efficiencies using numerical simulation of the flow field and droplet motion*. Third International Conference on Multiphase flow, ICMF'98, Lyon, France, June 8-12, 1998.
- [66] Wolfstein, M. *The Velocity and Temperature Distribution of One-dimensional Flow with Turbulence Augmentation and Pressure gradient*. Int. J. Heat Mass Transfer, Vol. 12, pp. 301-318, 1969.
- [67] Woodmansee, D. E. and Hanratty, T. J. *Mechanism for the removal of droplets from a liquid surface by a parallel air flow*. Chem. Eng. Sci., Vol. 24, pp. 299-307, 1969.
- [68] Yakhot, V. and Orszag, S.A., *Renormalization Group Analysis of Turbulence. I. Basic Theory* Journal of Scientific Computing, Vol. 1, No. 1, pp. 3-51, 1986.
- [69] Yeh, Y. and Cummins, H. Z. *Localized Fluid Flow Measurements with a He-Ne Laser Spectrometer*. Applied Physics Letters, Vol. 4, No. 10, 1964.
- [70] Zaichik, L.I., Nigamtulin, B.I. and Aplichenkov, V.M. *Droplet deposition and film atomization in gas-liquid annular flow* Third International Conference on Multiphase Flow, ICMF'98, Lyon, France, July 1998.

Appendix 1

Comparison for the low mass flow

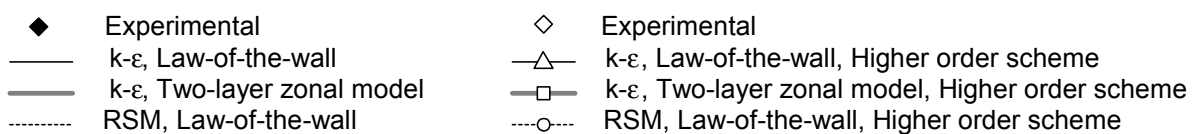
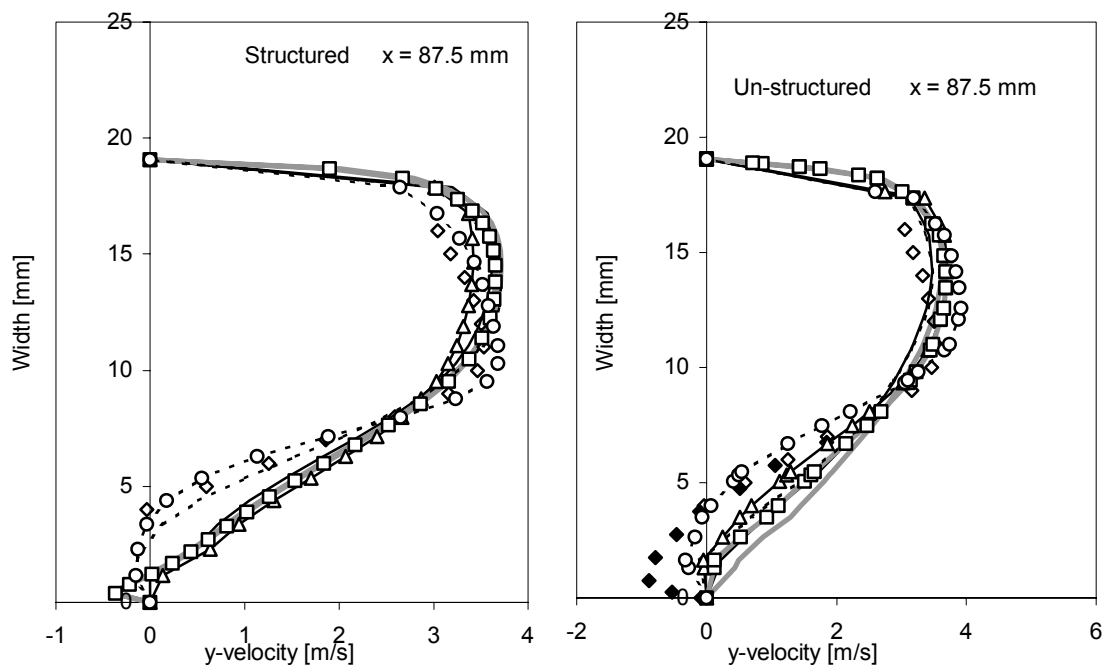
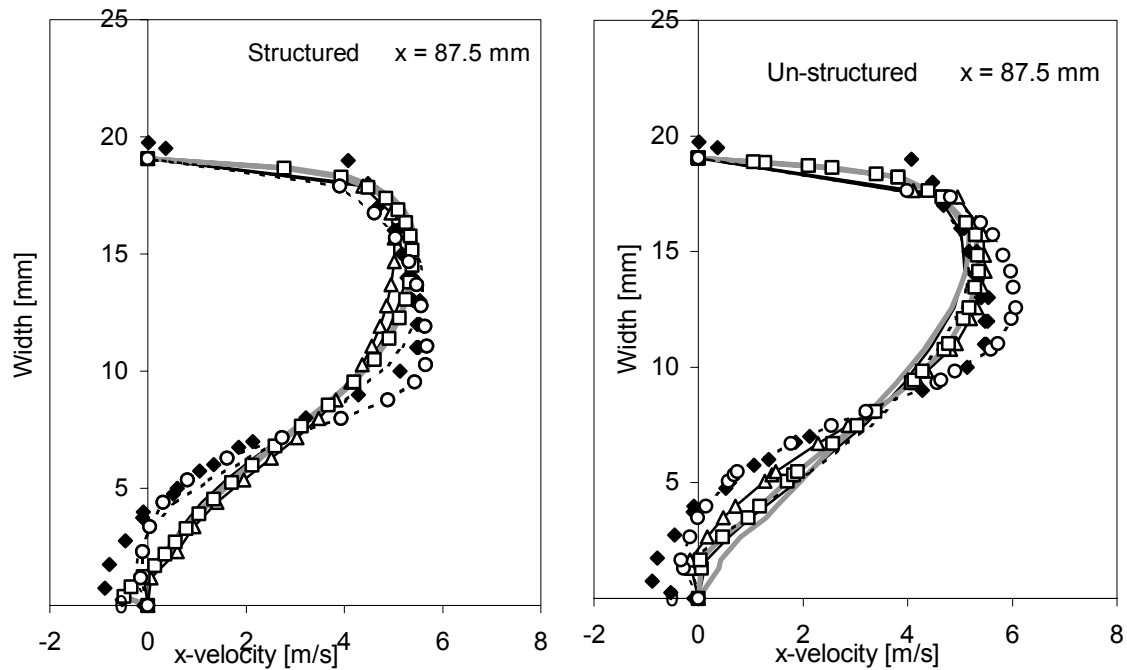
A1.1 $x = -50$ mm

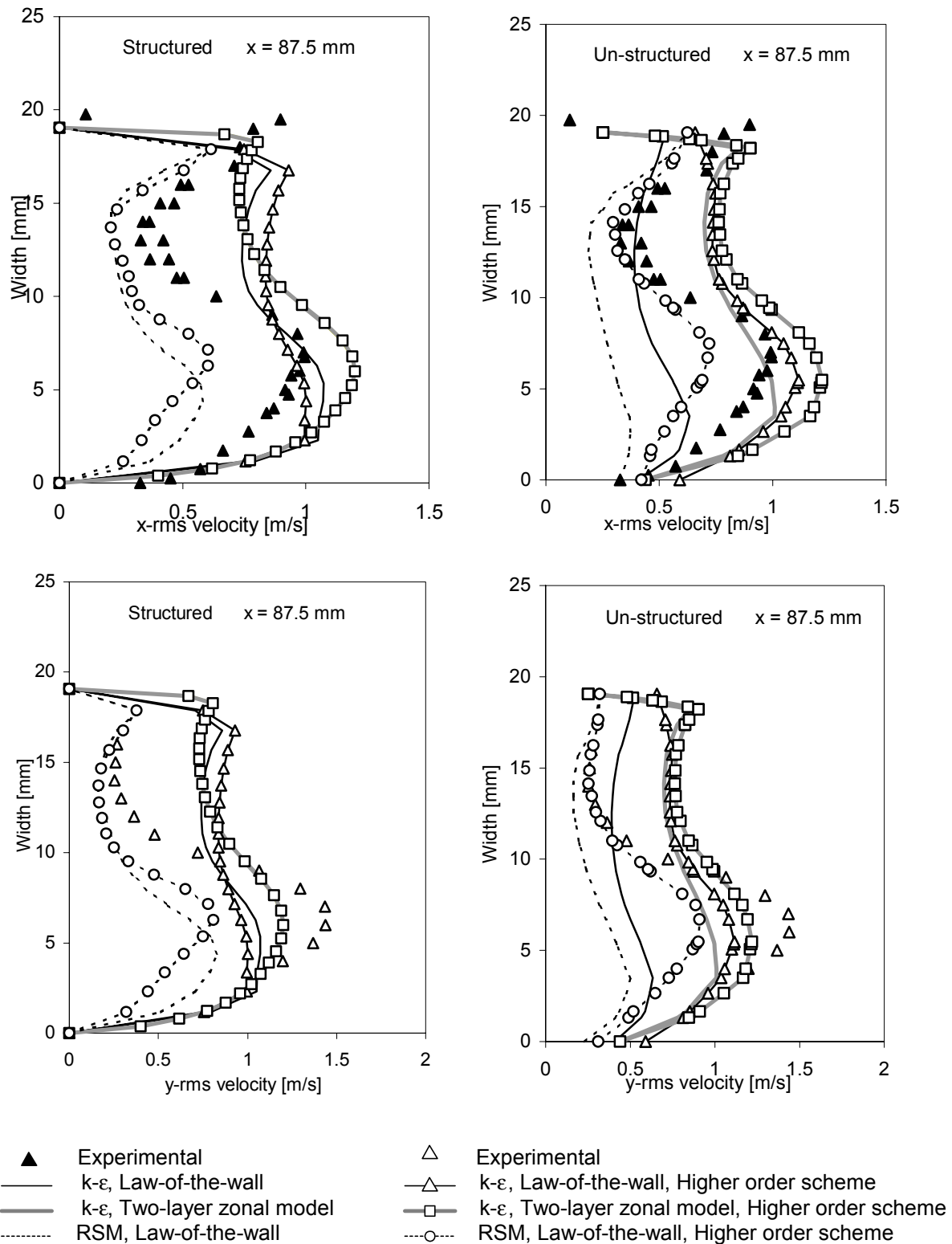


- ◆ Experimental
- $k-\epsilon$, Law-of-the-wall
- $k-\epsilon$, Two-layer zonal model
- RSM, Law-of-the-wall

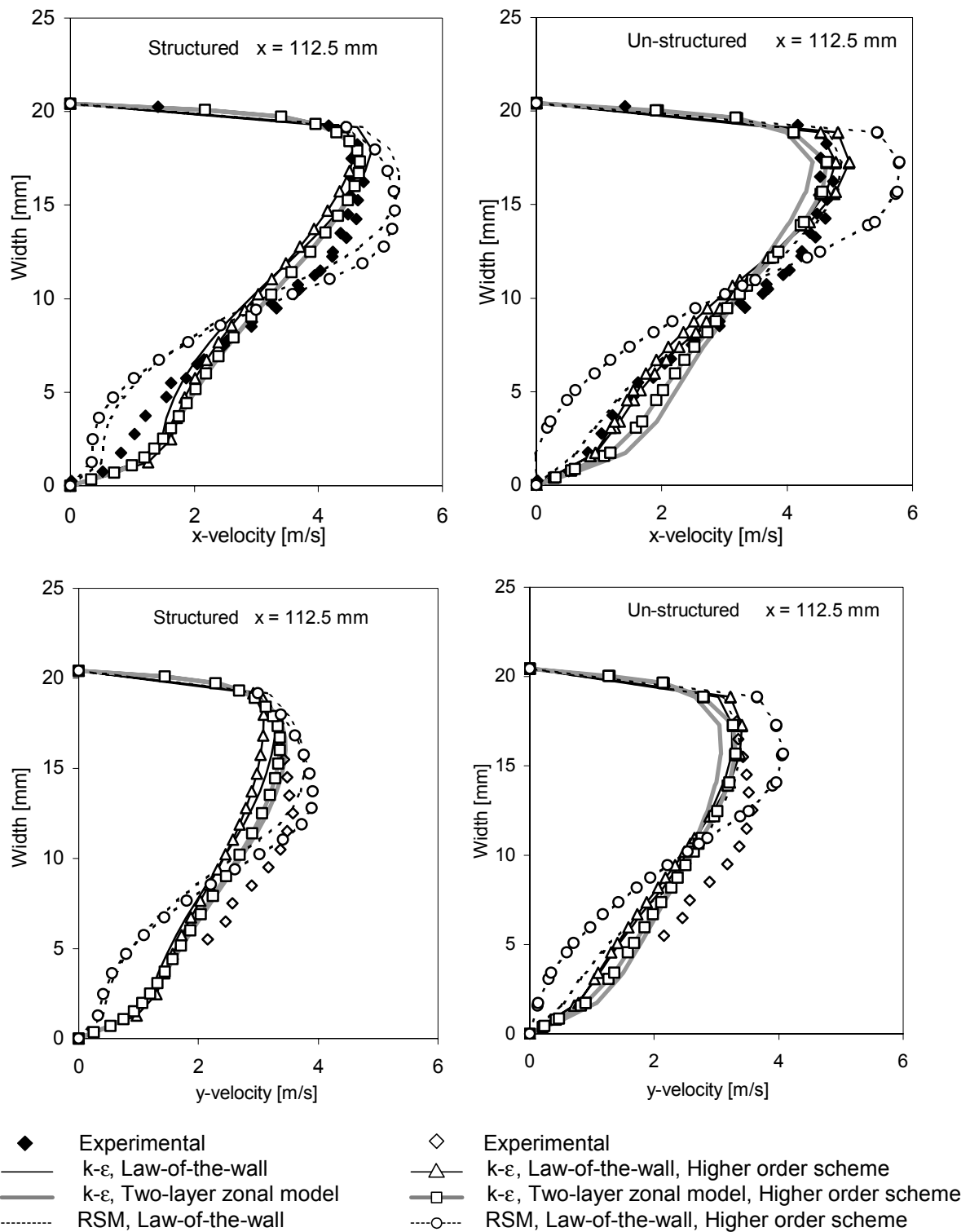
- ▲ Experimental
- △ $k-\epsilon$, Law-of-the-wall, Higher order scheme
- $k-\epsilon$, Two-layer zonal model, Higher order scheme
- RSM, Law-of-the-wall, Higher order scheme

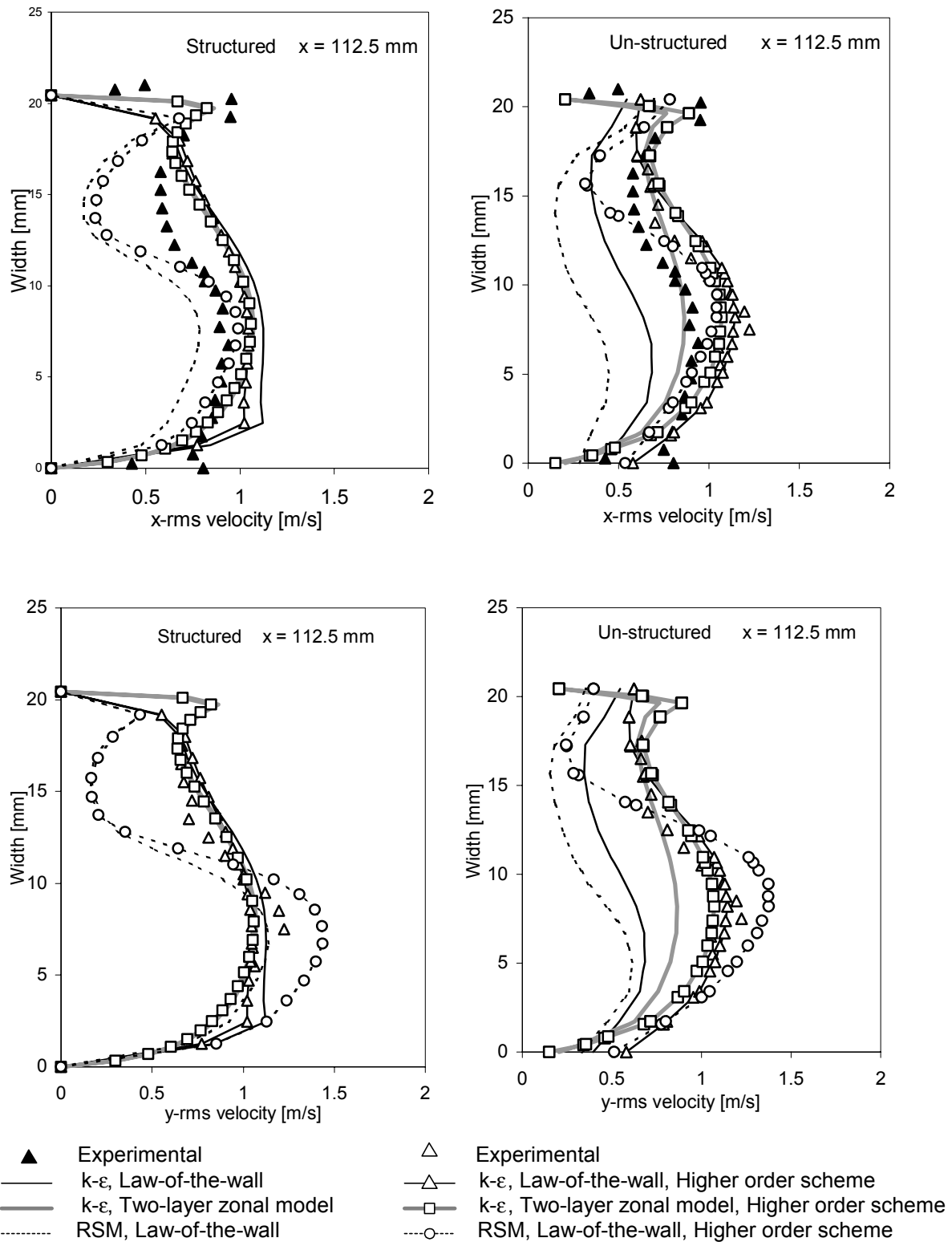
A1.2 $x = 87.5$ mm



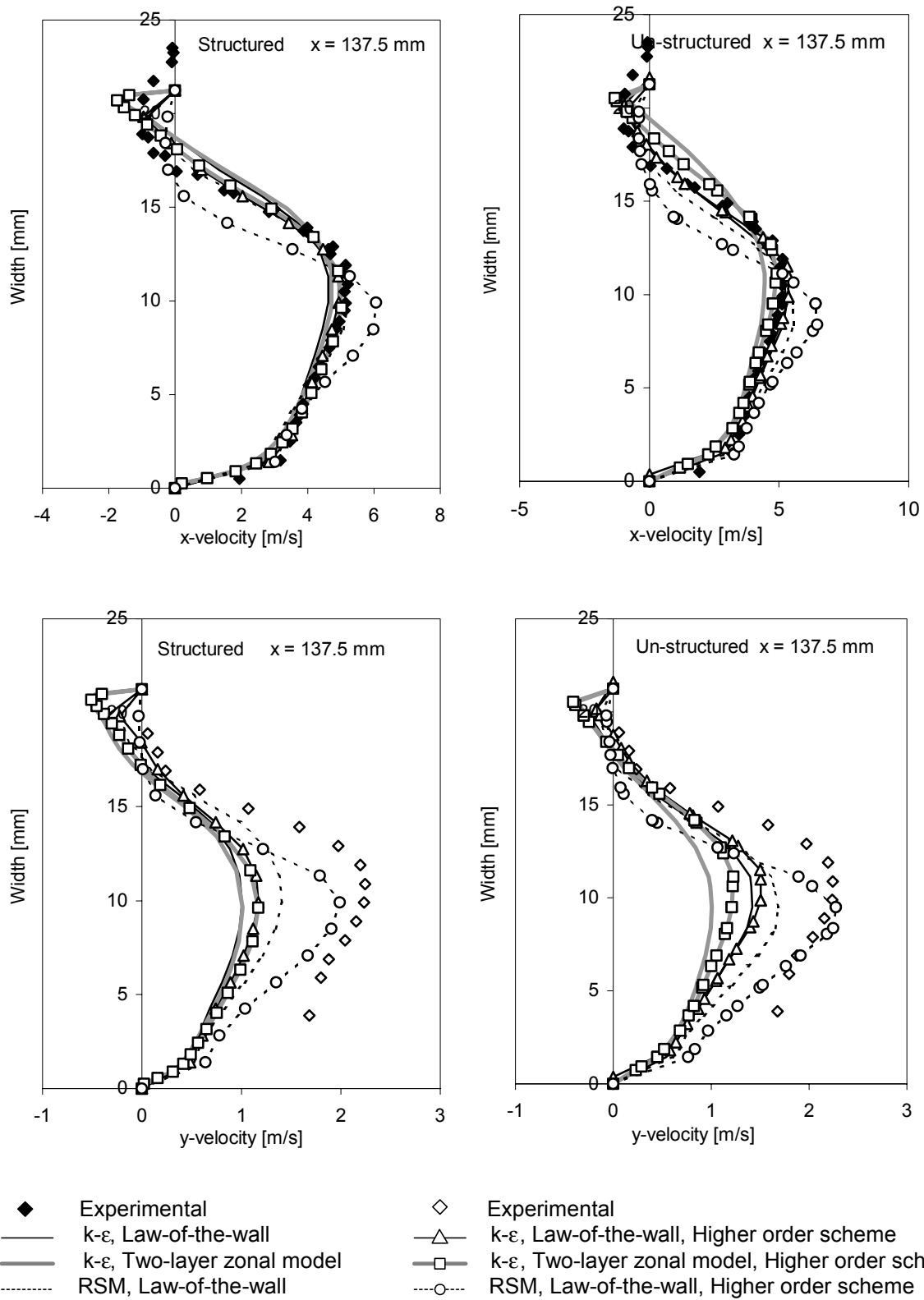


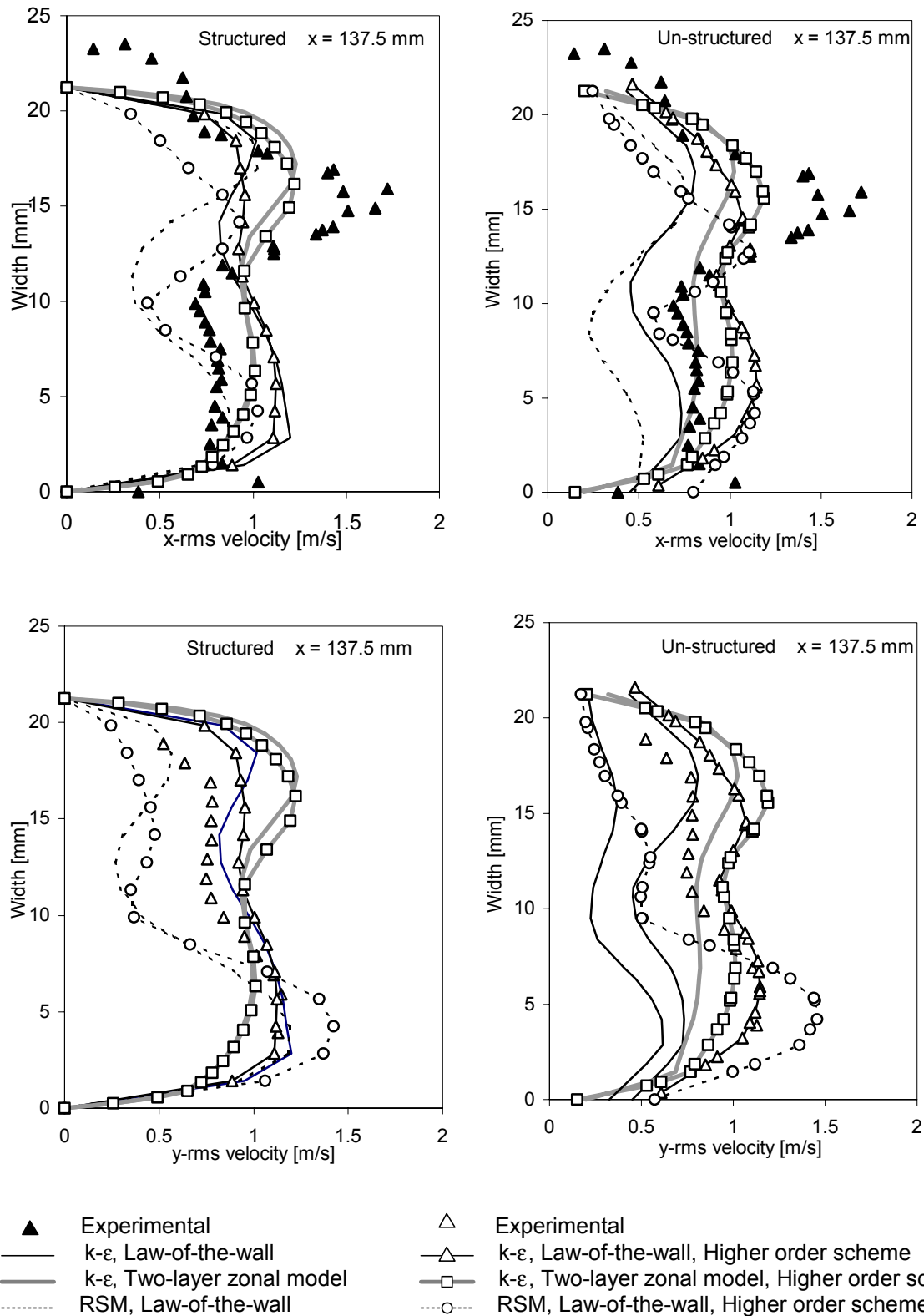
A1.3 $x = 112.5$ mm



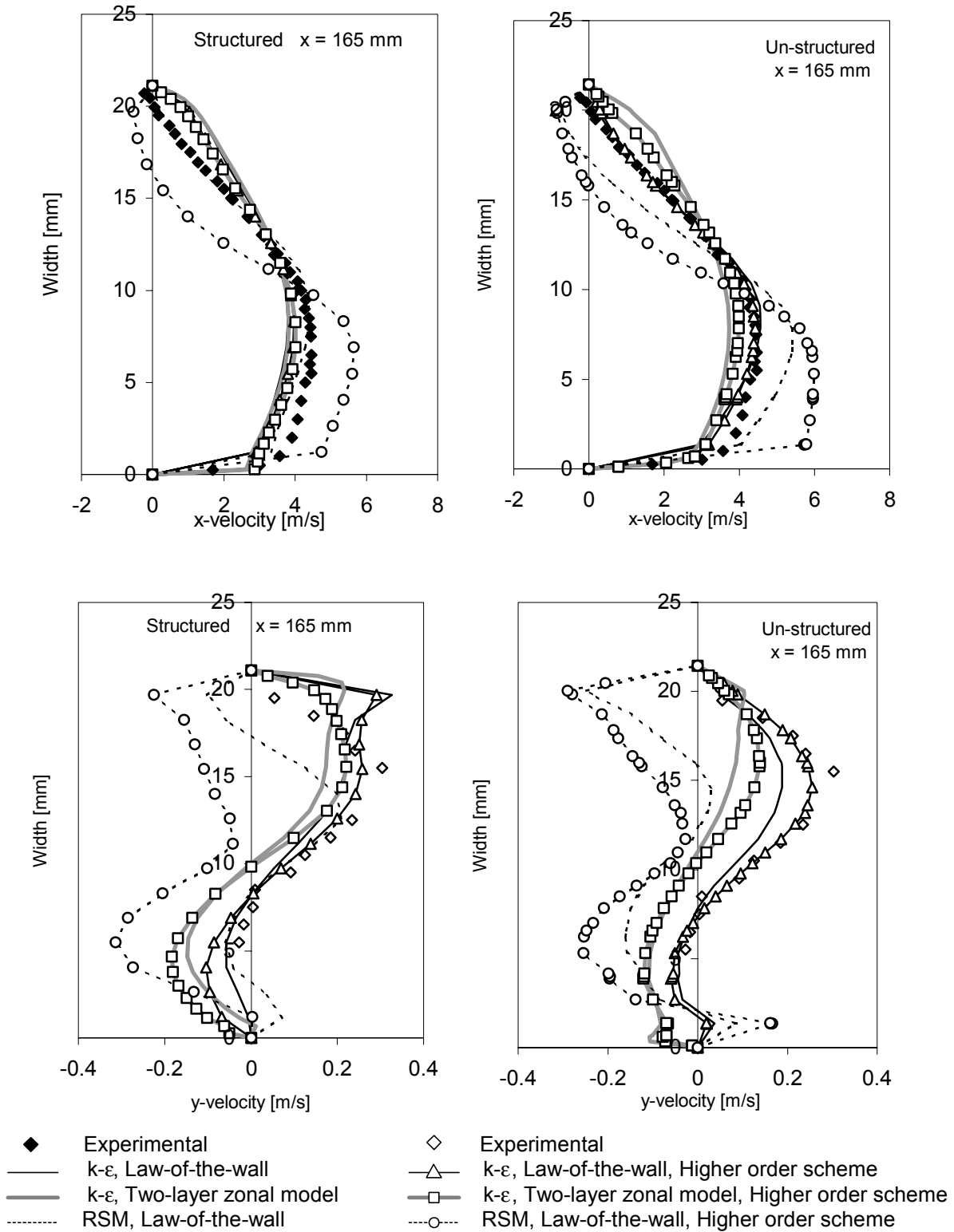


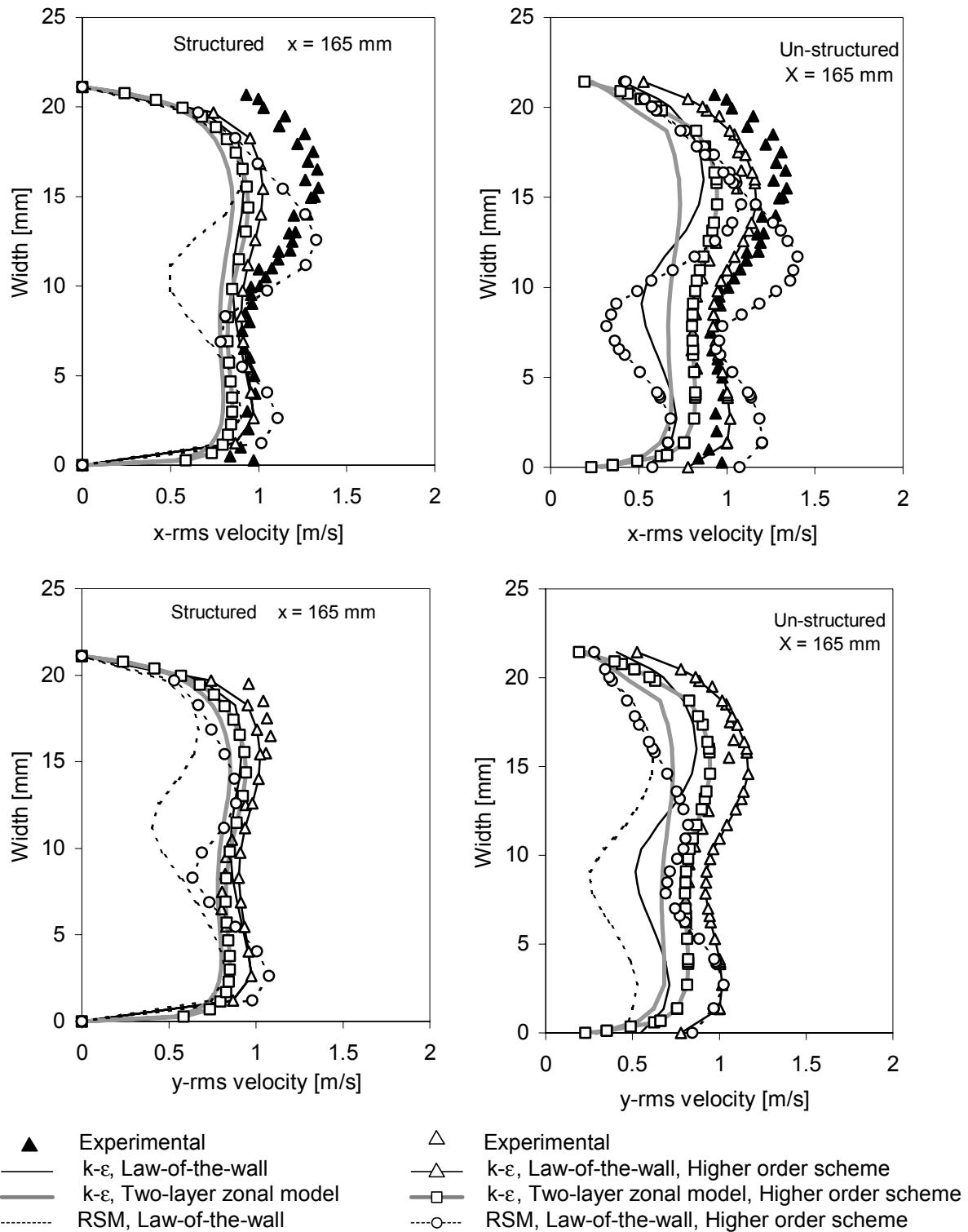
A1.4 $x = 137.5$ mm



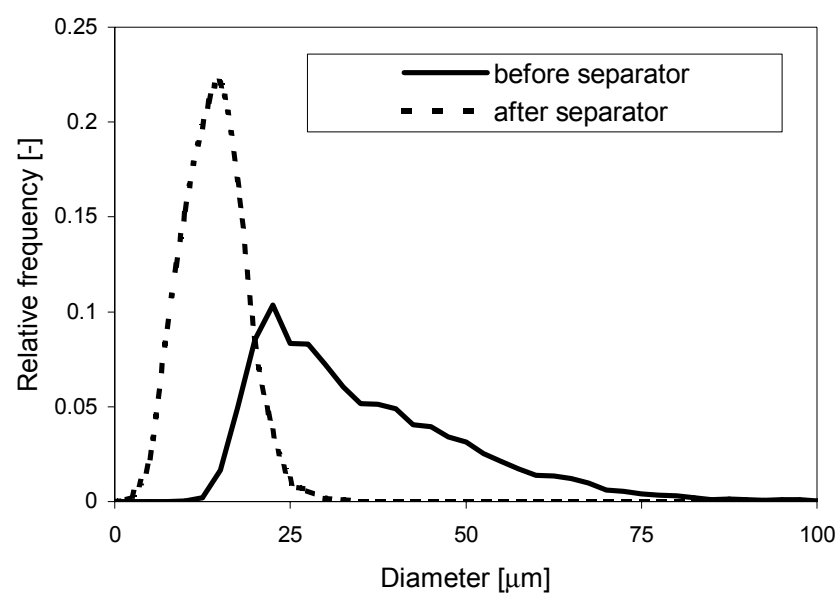


A1.5 $x = 165$ mm





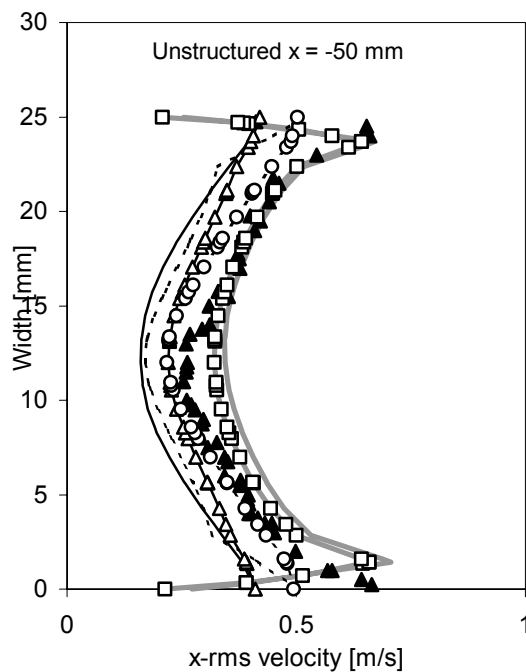
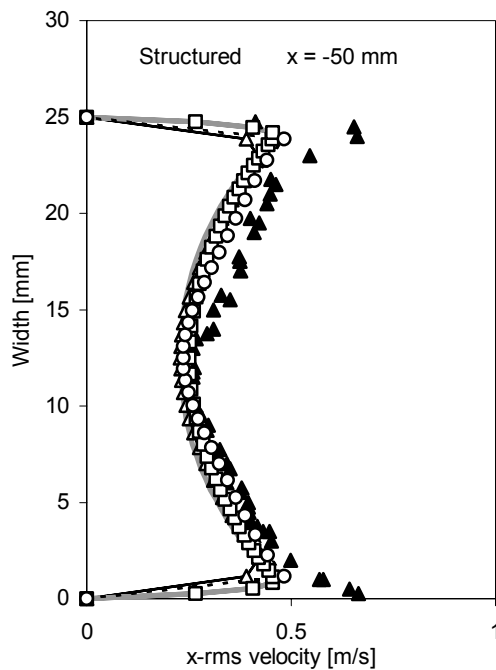
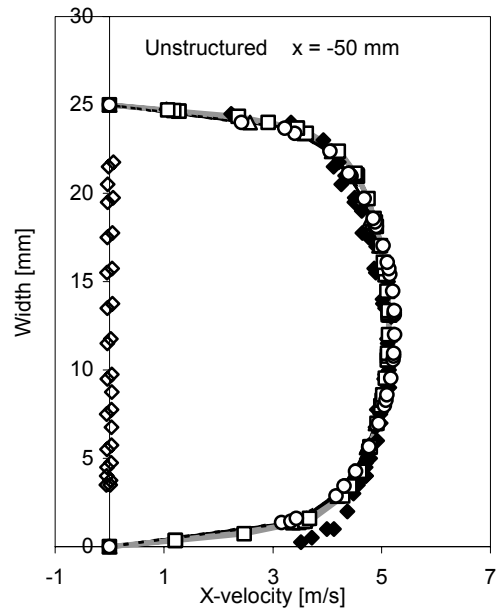
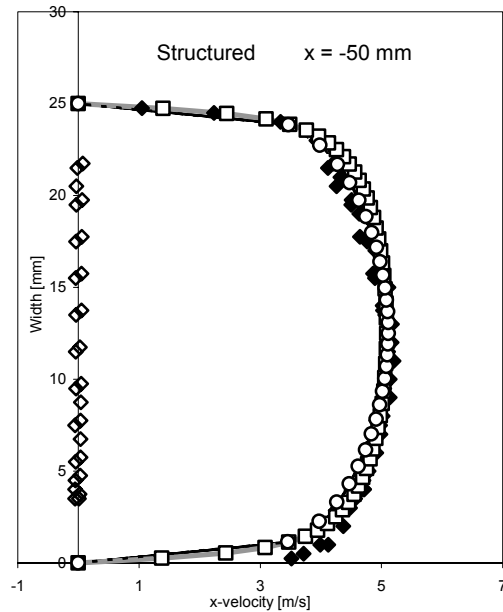
A1.6 The droplet size distribution in and out of the separator



Appendix 2

Comparison for the large mass flow

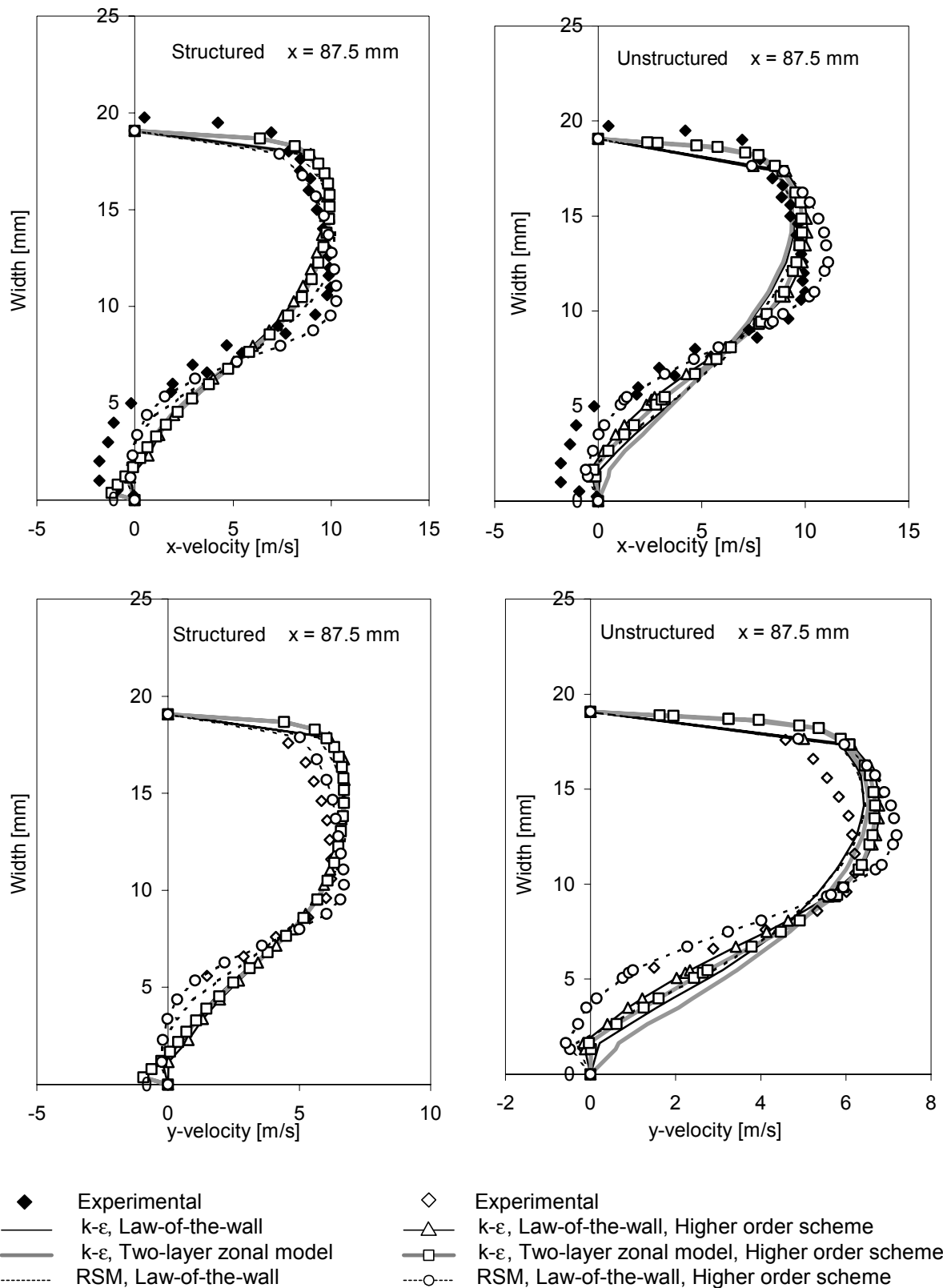
A.2 $x = -50$ mm

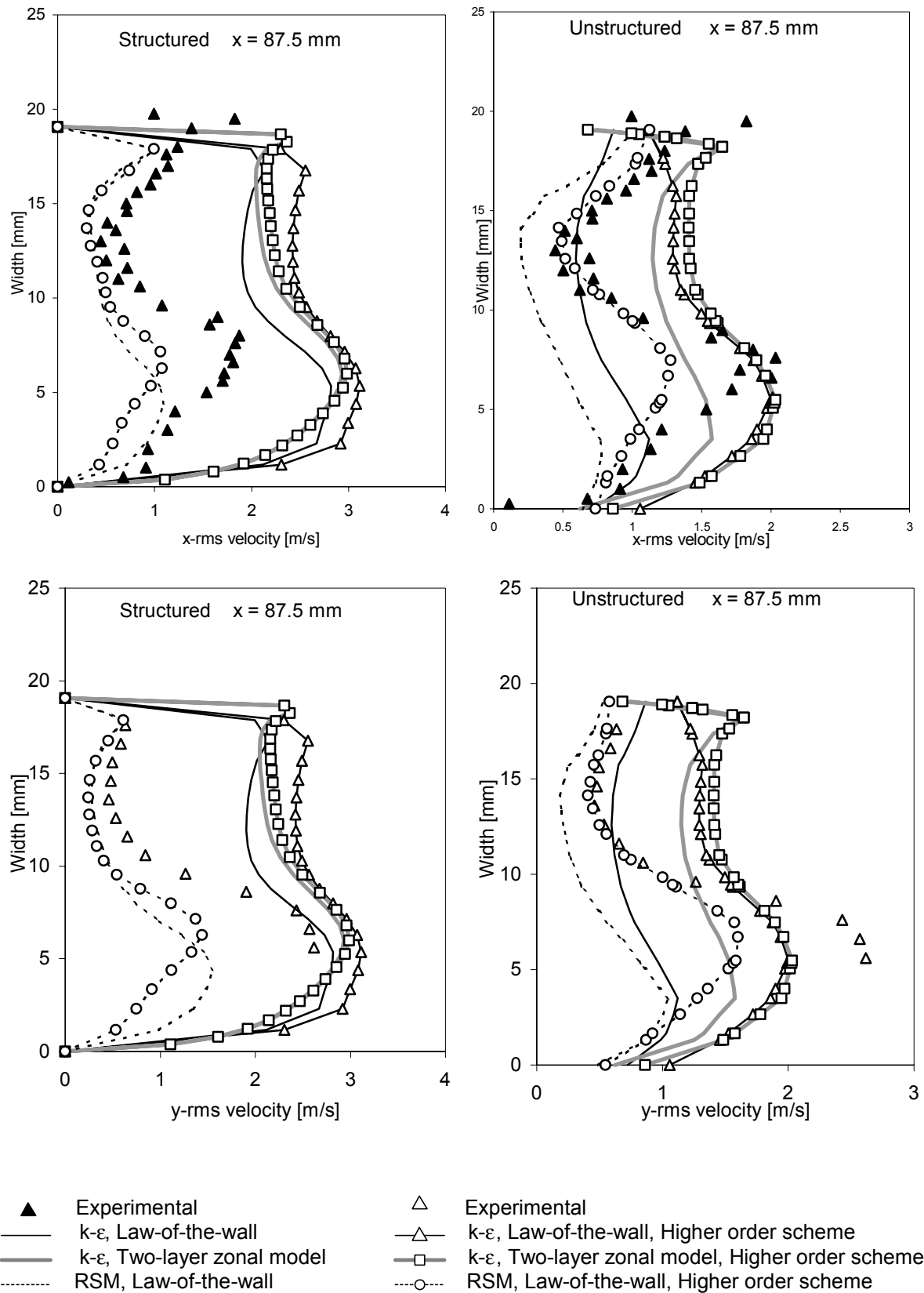


▲ ◆ Experimental
 — k- ϵ , Law-of-the-wall
 — k- ϵ , Two-layer zonal model
 RSM, Law-of-the-wall

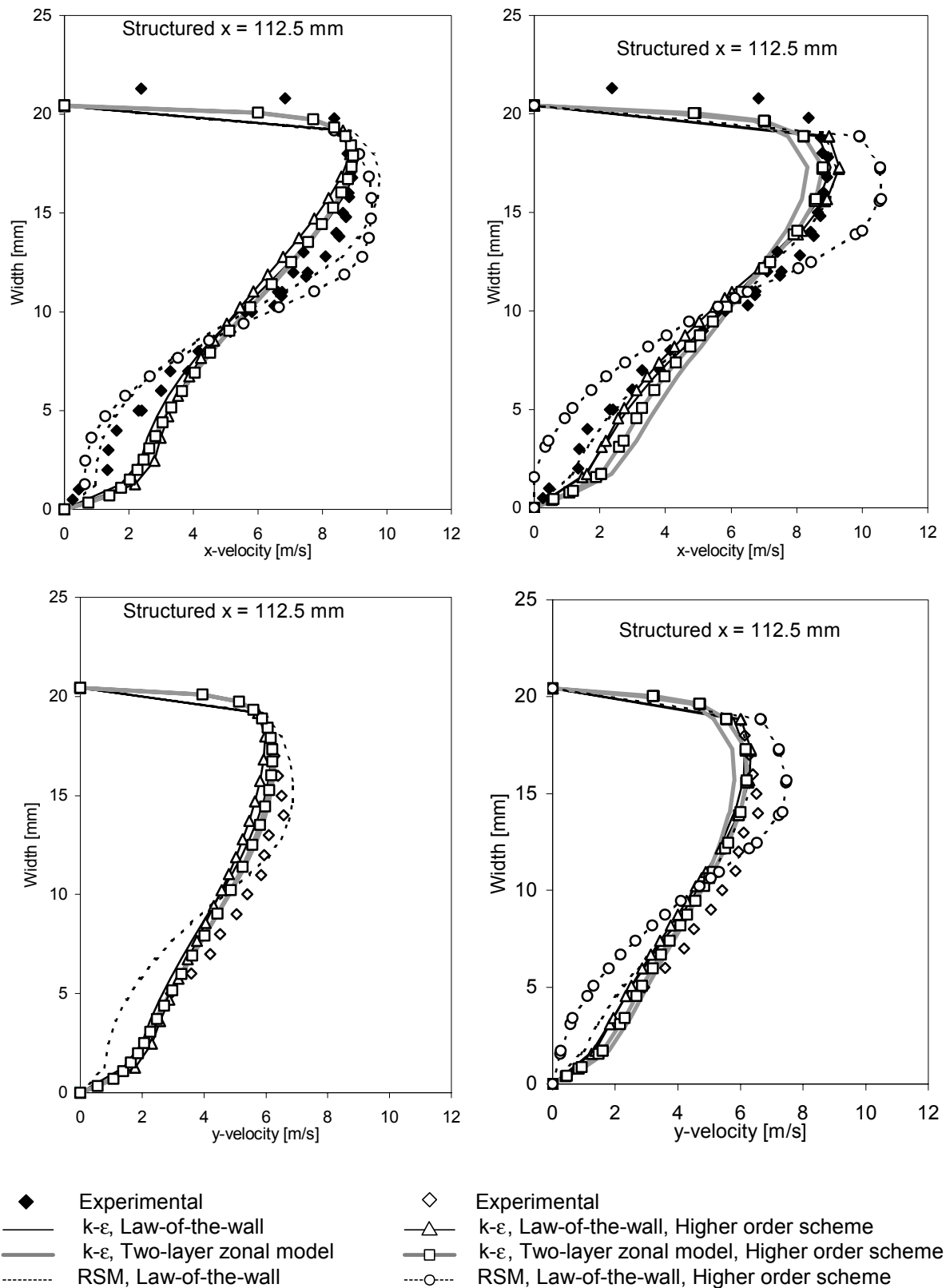
△ Experimental
 —△ k- ϵ , Law-of-the-wall, Higher order scheme
 —□ k- ϵ , Two-layer zonal model, Higher order scheme
 -○- RSM, Law-of-the-wall, Higher order scheme

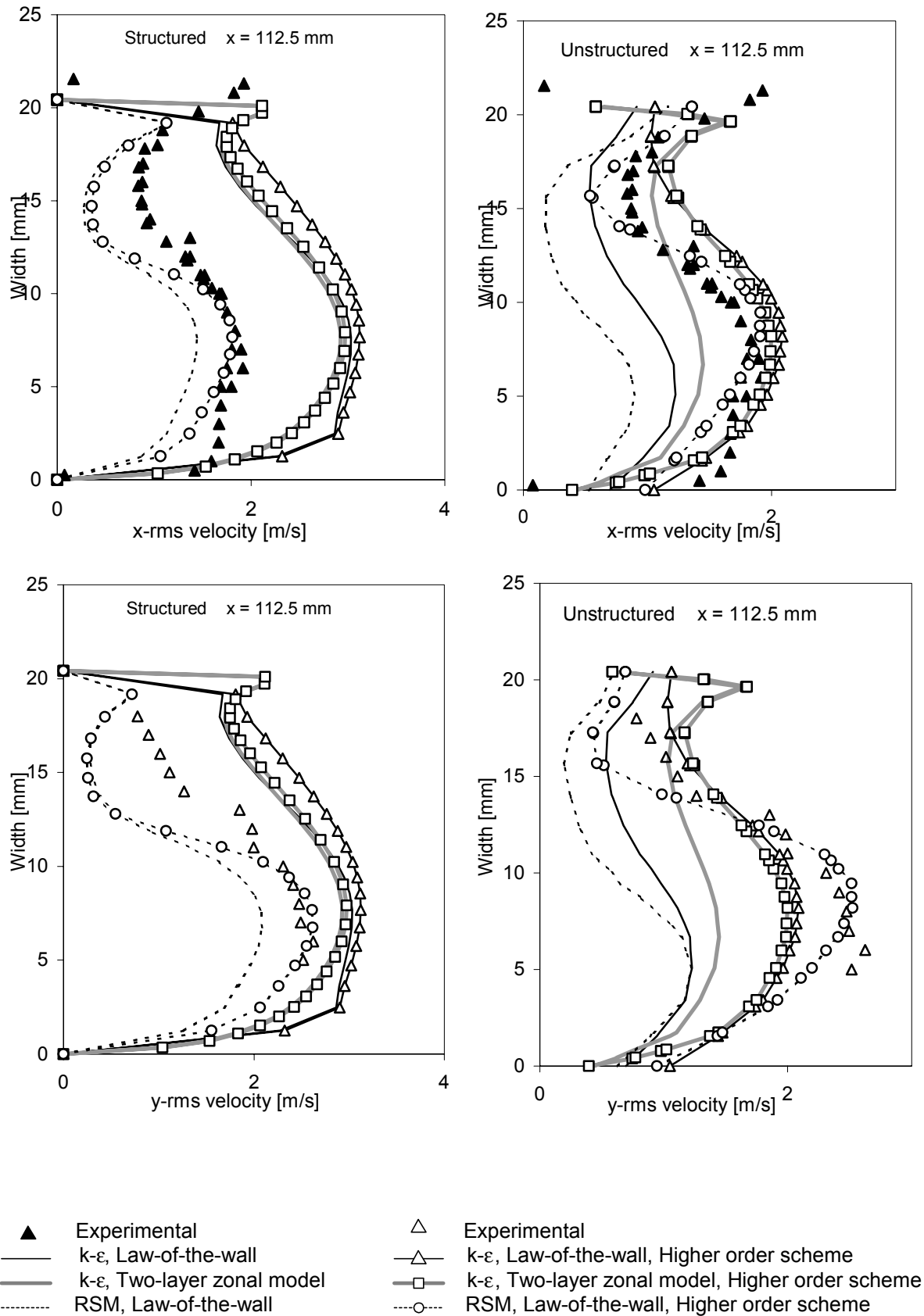
A2.2 $x = 87.5$ mm



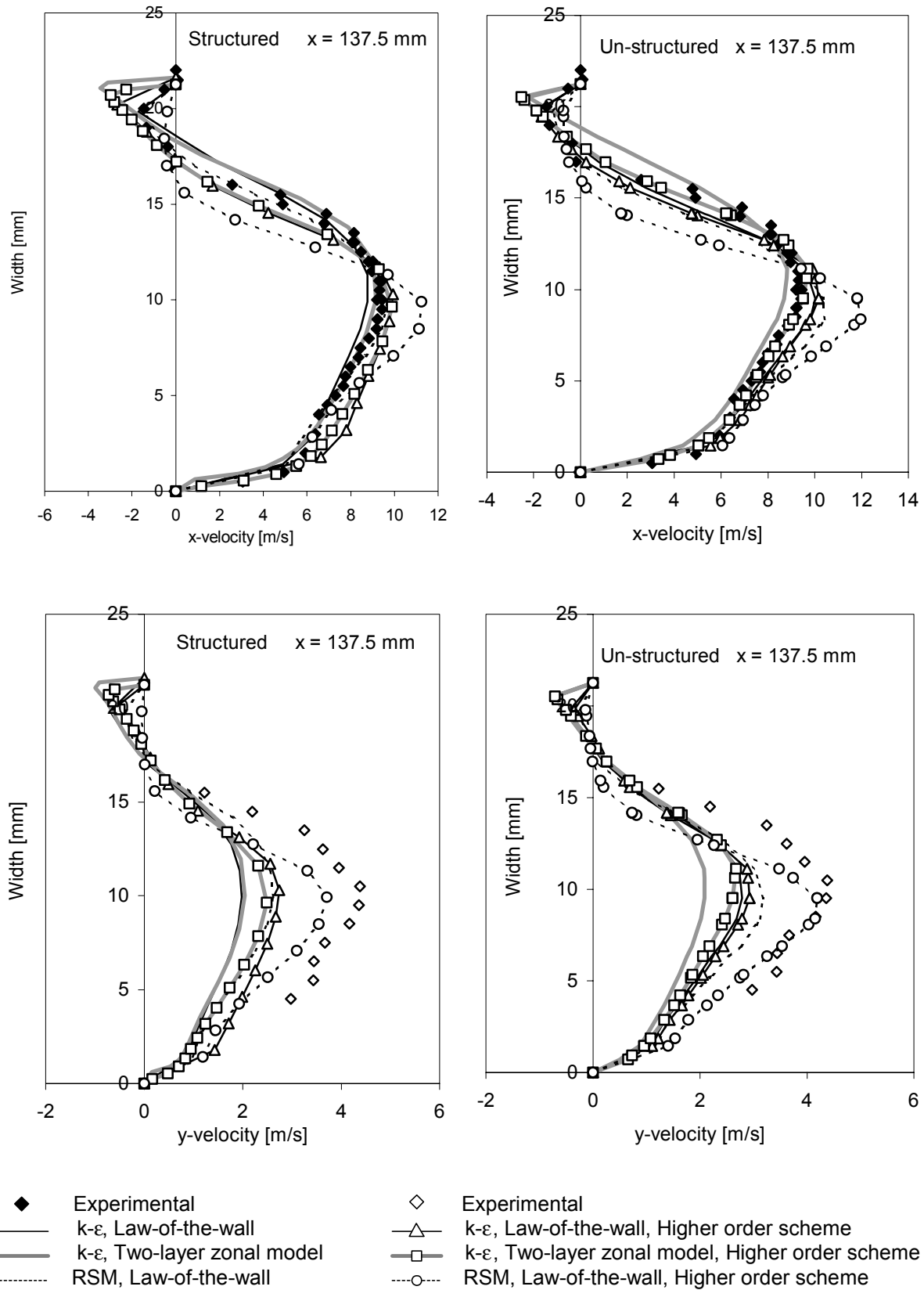


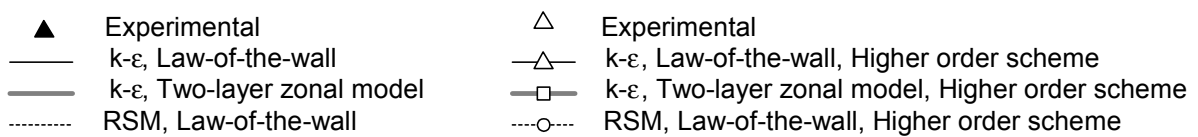
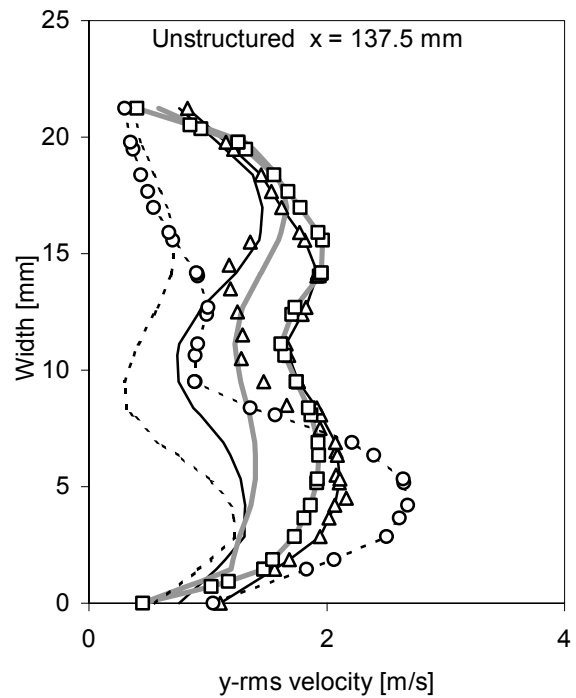
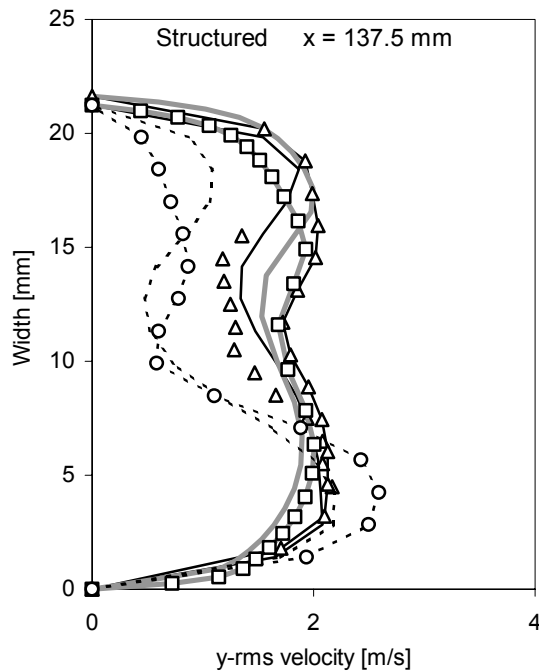
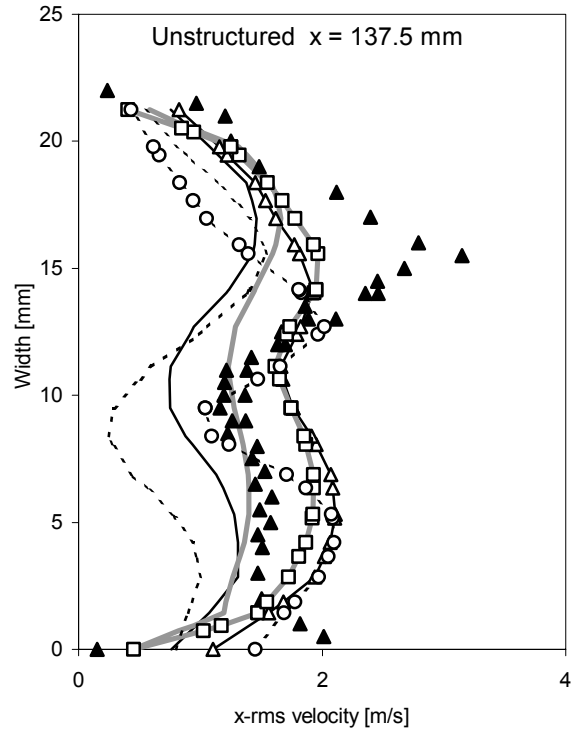
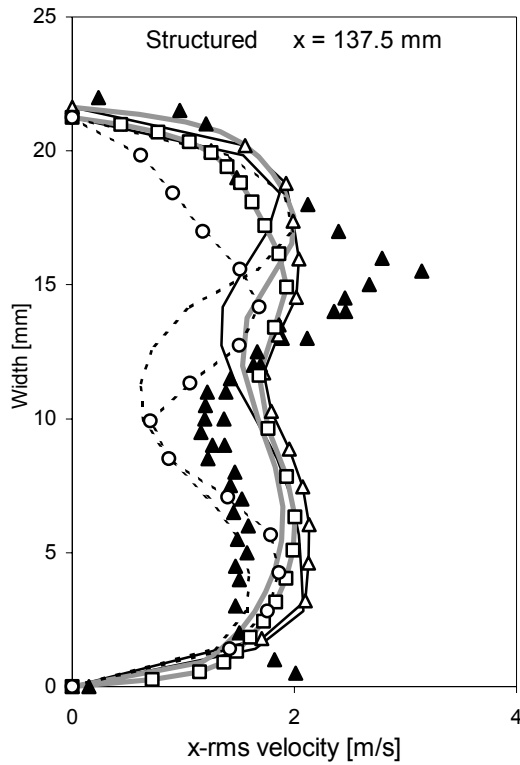
A2.3 $x = 112.5$ mm



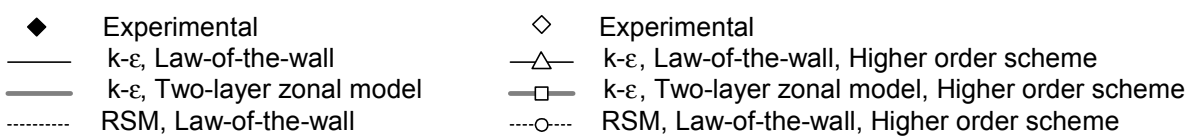
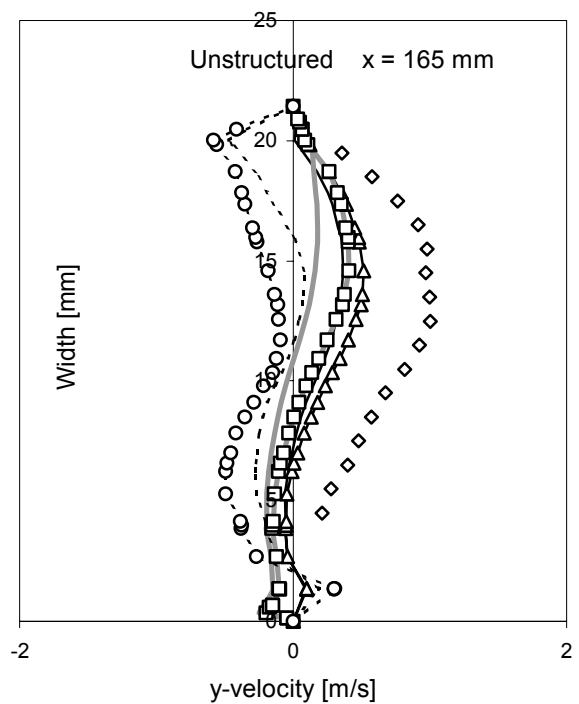
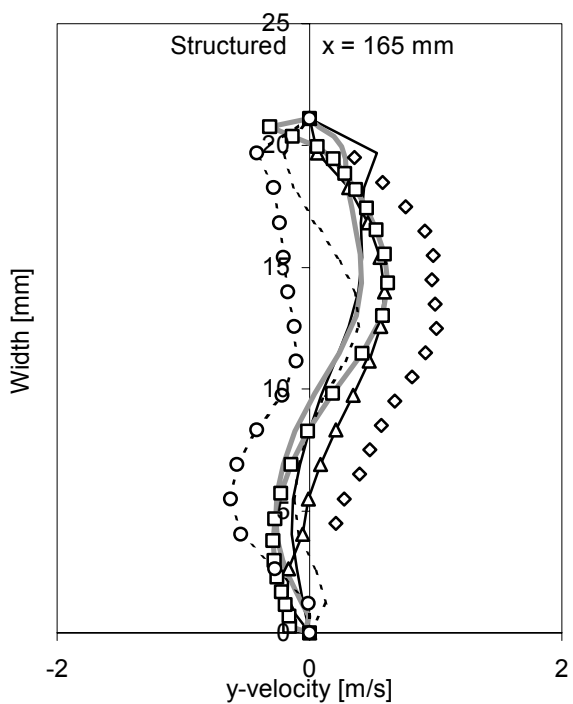
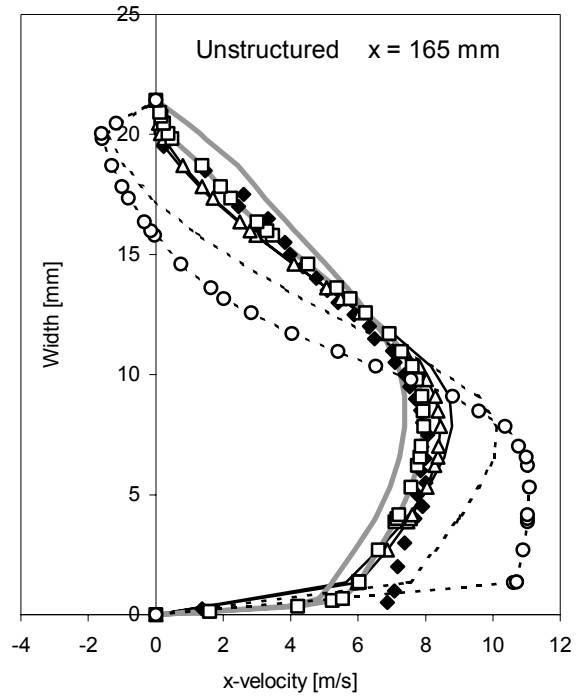
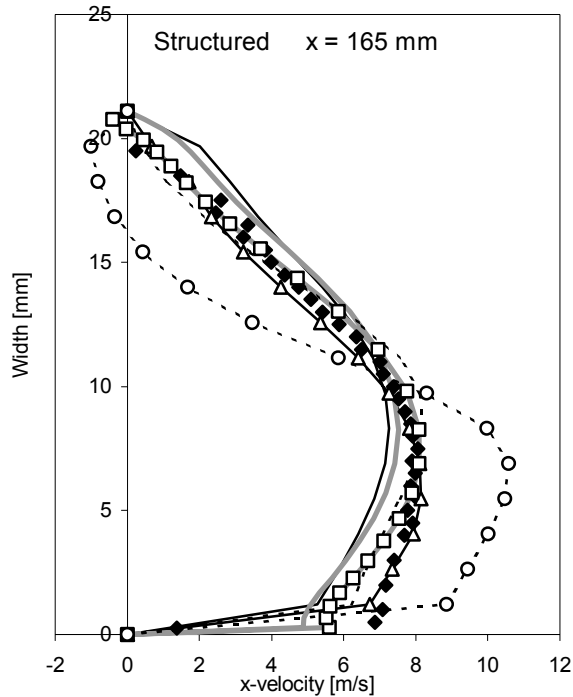


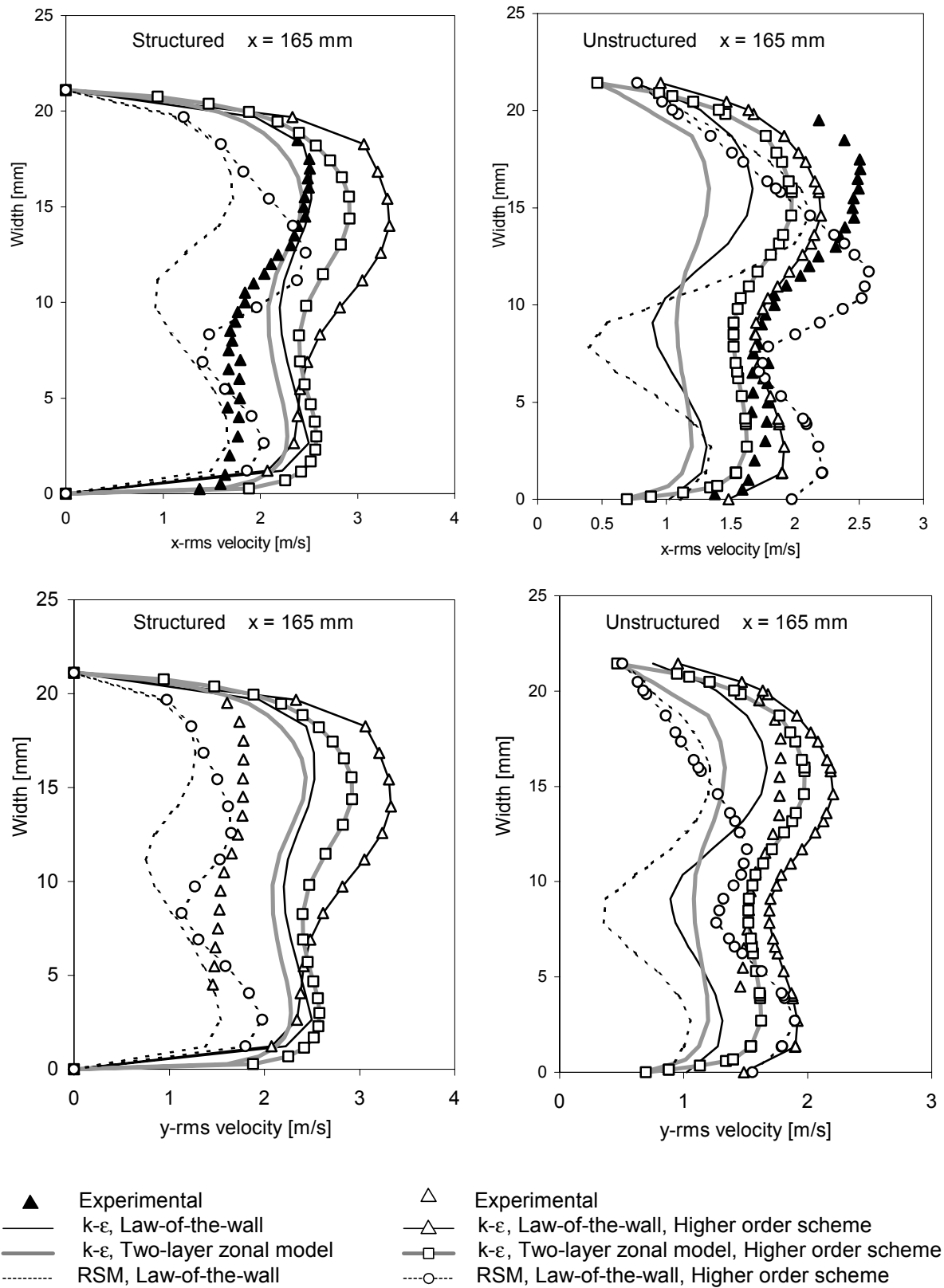
A2.3 $x = 137.5$ mm



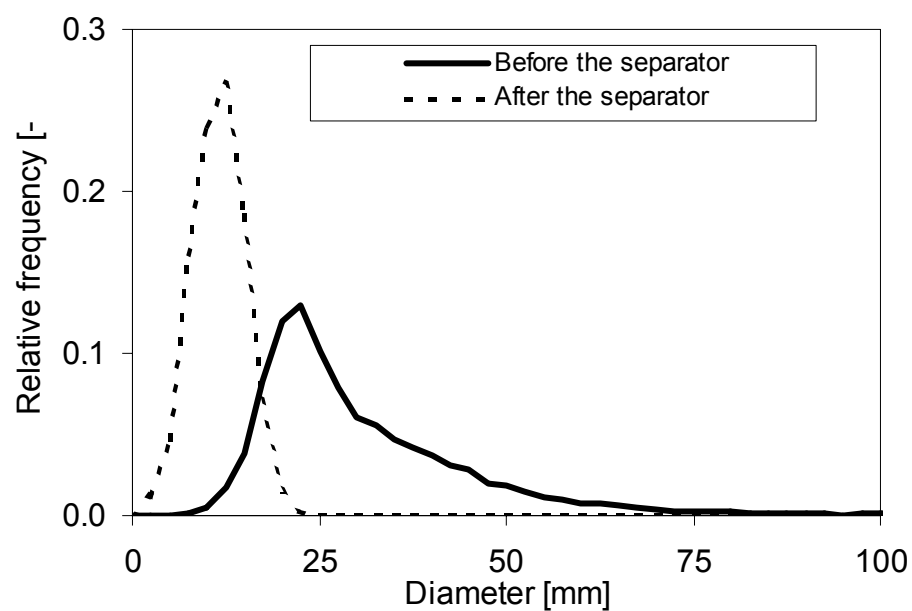


A2.4 $x = 165$ mm





A2.5 The droplet size distribution in and out of the separator



A3.1 The vane

Some dimensions of the vane are shown in Figure A3.1. The length of a single vane is 171 mm, and the height is 52 mm. The vanes are made of talcum improved Polypropylene (PPTV). The detailed coordinates used to generate the computational grid are shown in Table A3.1. The coordinates are read off a copy of the vane on a millimetre paper. The copy of the vane is zoomed 160 %, so the values read off has to be transformed to the real value. The values are read off to the accuracy of nearest 0.5 mm, and the values given in Table A3.1 are a result of the transformation into real values.

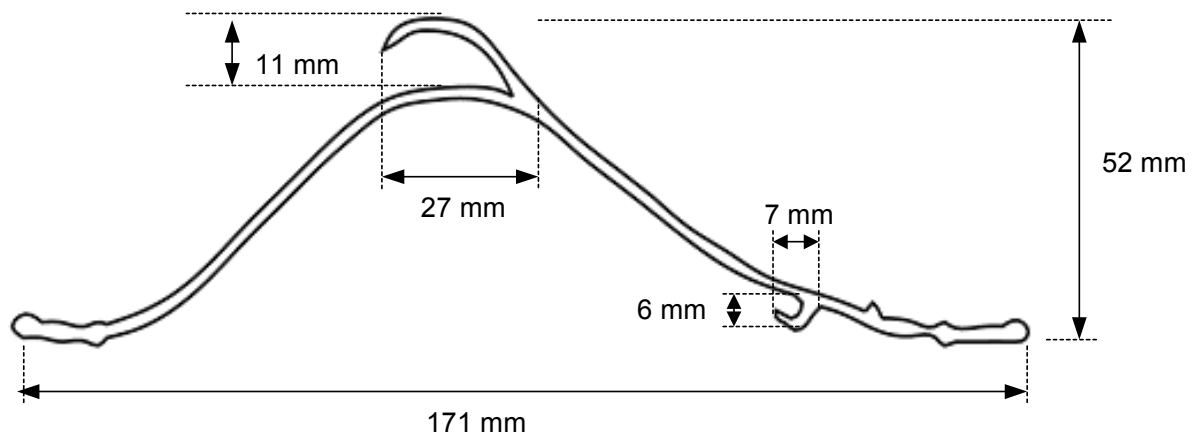


Figure A3.1 The vanes with some dimensions.

Table A3.1: The complete list of coordinates for the vane.

x-coordinate	y-coordinate
-1.875	-1.875
0.000	0.000
0.000	-3.750
1.250	-0.625
3.125	-1.250
3.125	-3.750
6.250	-1.250
6.250	-4.375
10.625	-1.875
10.625	-4.375
12.500	-1.250
12.500	-5.000
14.063	-1.563
14.063	-3.750
18.750	0.000
18.750	-2.500
25.000	3.125
25.000	0.625
31.250	8.125
31.250	5.625
37.500	14.375

x-coordinate	y-coordinate
37.500	11.875
43.750	20.313
43.750	17.813
50.000	26.250
50.000	23.750
56.250	31.563
56.250	29.063
60.000	43.125
60.625	42.500
62.500	45.625
62.500	43.438
62.500	35.000
62.500	33.125
65.625	45.313
65.625	47.188
68.750	47.500
68.750	45.625
68.750	36.250
68.750	34.375
75.000	46.563
75.000	44.063
75.000	36.563
75.000	34.688
81.250	40.625
81.250	37.500
81.250	35.625
81.250	33.438
82.500	35.000
87.500	33.750
87.500	30.625
93.750	28.125
93.750	25.625
100.000	23.438
100.000	20.938
106.250	18.750
106.250	16.250
112.500	13.750
112.500	11.563
118.750	7.500
118.750	10.000
125.000	4.688
125.000	6.250
126.875	0.625
126.875	-0.625
128.125	0.000
128.125	-1.250
129.375	-0.625
130.000	3.125
130.000	-2.500

x-coordinate	y-coordinate
130.625	0.000
131.250	4.063
131.250	-2.188
131.250	1.875
133.125	0.000
134.375	1.250
137.500	0.313
137.500	2.188
141.875	0.500
143.125	0.000
143.750	1.250
143.750	-2.500
144.688	-0.625
150.000	-3.438
150.000	-1.250
153.750	-1.875
153.750	-3.750
155.313	-1.250
155.313	-5.000
156.250	-4.688
156.250	-1.875
157.188	-2.188
157.188	-4.375
162.500	-1.875
162.500	-4.375
165.000	-1.875
165.000	-4.375
167.500	-0.938
167.500	-4.375
168.750	-1.563
168.750	-4.063
169.375	-2.813